Free Vibration Analysis of Rotating Porous Functionally Graded Conical Shell in Thermal Environment based on Polynomial and Trigonometric Shear Deformation Theory

Thesis submitted by

SUBHENDU PAL

Doctor of Philosophy (Engineering)

Department of Mechanical Engineering
Faculty Council of Engineering & Technology
Jadavpur University
Kolkata, India

2025

JADAVPUR UNIVERSITY
KOLKATA - 700 032, INDIA

INDEX NO.: 199/19/E

1. Title of the thesis:

Free Vibration Analysis of Rotating Porous Functionally Graded Conical Shell in Thermal Environment based on Polynomial and Trigonometric Shear Deformation Theory

2. Name, Designation & Institution of the Supervisors:

Dr. Amit Karmakar,

Professor,

Department of Mechanical Engineering,

Jadavpur University, Kolkata -700032.

&

Dr. Mrutyunjay Rout,

Assistant Professor,

Department of Mechanical Engineering,

Government College of Engineering, Kalahandi, Bhawanipatna, Odisha, Pin- 766003.

3. List of Publication:

I. Pal, S., Rout, M., & Karmakar, A. (2023). Thermoelastic free vibration analysis of functionally graded conical shell based on trigonometric higher-order shear deformation theory. ***International Journal of Solids and Structures***, *284*, 112505.

II. Pal, S., Rout, M., & Karmakar, A. (2024). Thermoelastic free vibration of rotating tapered porous functionally graded conical shell based on non-polynomial higher-order shear deformation theory. ***Mechanics of Advanced Materials and Structures***, *31*(25), 7469-7485.

III. Pal, S., Rout, M., Deb Singha, T., & Karmakar, A. (2024). Free vibration response of rotating pretwisted porous exponential and sigmoid functionally graded conical shells in thermal environment. ***Mechanics of Advanced Materials and Structures***, *31*(27), 8745-8763.

IV. Pal, S., Rout, M., Deb Singha, T., & Karmakar, A. (2024). Thermoelastic free vibration of rotating pretwisted porous p-FGM, e-FGM, and s-FGM conical shells in nonlinear temperature distribution. ***Journal of Vibration and Control***, 10775463241240625.

4. List of Patents: NIL.

5. List of Presentations in National/International/Conferences/Workshops:

I. Pal, S., Rout, M. Free Vibration Analysis of Rotating Porous Power-Law Functionally Graded Conical Shell in Thermal Environment. International Conference on Mechanical Engineering, January, 5-6, 2024, Jadavpur University, Kolkata, India.

II. Das, A., Pal, S., Ziyi, S., Rout, M., Inaba, K., Karmakar, A. Natural Frequency and Resonance Study of FGM Turbo-Machinery Blade Using Campbell Diagram. In Gas Turbine India Conference, December 2-3, 2021, Bengaluru, Karnataka, India.

III. Das, A., Pal, S., Agarwal, G., Inaba, K., Deb Singha, T., Karmakar, A. A study on low velocity impact behaviour of functionally graded sandwich conical shell under thermal environment. In Gas Turbine India Conference, December 2-3, 2021, Bengaluru, Karnataka, India.

"Statement of Originality"

I, **SUBHENDU PAL** registered on **28.06.2019** do hereby declare that this thesis entitled **"Free Vibration Analysis of Rotating Porous Functionally Graded Conical Shell in Thermal Environment based on Polynomial and Trigonometric Shear Deformation Theory"** contains literature survey and original research work done by the undersigned candidate as part of Doctoral studies.

All information in this thesis have been obtained and presented in accordance with existing academic rules and ethical conduct. I declare that, as required by these rules and conduct, I have fully cited and referred all materials and results that are not original to this work.

I also declare that I have checked this thesis as per the "Policy on Anti Plagiarism, Jadavpur University, 2019", and the level of similarity as checked by iThenticate software is 6 %.

Signature of Candidate: Subhendu Pal

Date: 16/09/25

Certified by Supervisors:

(Signature with date, seal)

1. Amit Karmakar 16/09/25

Professor
Mechanical Engineering Dept.
Jadavpur University
Kolkata – 700 032

2. Mrutyunjay Rout 16/09/25

Dr. Mrutyunjay Rout
Asst. Professor
Govt. College of Engineering, Kalahandi
Bhawanipatna- 766002

CERTIFICATE FROM THE SUPERVISORS

This is to certify that the thesis entitled **"Free Vibration Analysis of Rotating Porous Functionally Graded Conical Shell in Thermal Environment based on Polynomial and Trigonometric Shear Deformation Theory"** submitted by **Shri Subhendu Pal,** who got his name registered on **28.06.2019** for the award of Ph. D. (Engg.) degree of Jadavpur University is absolutely based upon his own work under the supervision of **Dr. Amit Karmakar, Professor, Department of Mechanical Engineering, Jadavpur University, Kolkata-700032 & Dr. Mrutyunjay Rout, Assistant Professor, Department of Mechanical Engineering, Government College of Engineering, Kalahandi, Bhawanipatna, Odisha** and that neither his thesis nor any part of the thesis has been submitted for any degree or any other academic award anywhere before.

1. Amit Karmakar 16/09/25

Signature of the Supervisor
and date with Office Seal

Professor
Mechanical Engineering Dept.
Jadavpur University
Kolkata – 700 032

2. Mrutyunjay Rout 16/09/25

Signature of the Supervisor
and date with Office Seal

Dr. Mrutyunjay Rout
Asst. Professor
Govt. College of Engineering, Kalahandi
Bhawanipatna- 766002

ACKNOWLEDGEMENT

First and foremost, I pay reverence to God, the almighty for providing me this opportunity and granting me the capability to proceed successfully. This thesis appears in its current form due to the assistance and guidance of several persons. I, therefore, would like to offer my sincere thanks and gratitude to each and every one of them.

I express my profound gratitude to my supervisors Prof. (Dr.) Amit Karmakar and Dr. Mrutyunjay Rout for their keen interest, cherished guidance and constant inspiration during the course of the research work. I am greatly indebted to them for their valuable time and methodical guidance in the course of this work. Above all, without their moral support I could not have completed the present research work.

I also owe my sincere thanks to Dr. Tripuresh Deb Singha, Assistant Professor, GCETT, Serampore for assisting me to the field of functionally graded materials (FGM) during the initial stages of my Ph.D work. I admire his great qualities and feel happy to be associated with him.

The excellent cooperation and support provided by Dr. Tanmoy Bandopadhyay, Assistant Professor, Jadavpur University and Dr. Apurba Das, Assistant Professor, IIEST, Shibpur are thankfully acknowledged. I would also like to express my heartiest thanks to my friend Dr. Pabitra Maji for his vital favour and valuable suggestions.

I am extremely grateful to Prof. (Dr.) Sumanta Neogi, Prof. (Dr.) Arghya Nandi, Prof. (Dr.) Himadri Chattopadhyay, Prof. (Dr.) Nipu Modak for their encouragement and advice. I would also like to thank all the faculty members of the Mechanical Engineering Department, Jadavpur University, for their unwavering support and fondness.

I am very much thankful to Jalpaiguri Government Engineering College, Jalpaiguri and the Department of Higher Education, Govt. of West Bengal for granting the necessary permission to do this research work. I owe my gratitude to Dr. Amitava Ray, Principal of my parent institute, Jalpaiguri Government Engineering College, Jalpaiguri and Dr. Soupayan Mitra, Professor and Head, Department of Mechanical Engineering, Jalpaiguri Government Engineering College, Jalpaiguri for their constant encouragement and moral support to complete this research work.

I express my sincere gratitude to my family members for their blessings and standing by me with lots of encouragement.

Subhendu Pal

Subhendu Pal

LIST OF PUBLICATIONS

The following research publications are based on the present research work:

I. Pal, S., Rout, M., & Karmakar, A. (2023). Thermoelastic free vibration analysis of functionally graded conical shell based on trigonometric higher-order shear deformation theory. *International Journal of Solids and Structures*, 284, 112505.

II. Pal, S., Rout, M., & Karmakar, A. (2024). Thermoelastic free vibration of rotating tapered porous functionally graded conical shell based on non-polynomial higher-order shear deformation theory. *Mechanics of Advanced Materials and Structures*, 31(25), 7469-7485.

III. Pal, S., Rout, M., Deb Singha, T., & Karmakar, A. (2024). Free vibration response of rotating pretwisted porous exponential and sigmoid functionally graded conical shells in thermal environment. *Mechanics of Advanced Materials and Structures*, 31(27), 8745-8763.

IV. Pal, S., Rout, M., Deb Singha, T., & Karmakar, A. (2024). Thermoelastic free vibration of rotating pretwisted porous p-FGM, e-FGM, and s-FGM conical shells in nonlinear temperature distribution. *Journal of Vibration and Control*, 10775463241240625.

V. Pal, S., & Rout, M. (2024, January). Free Vibration Analysis of Rotating Porous Power-Law Functionally Graded Conical Shell in Thermal Environment. In *International Conference on Mechanical Engineering* (pp. 641-658). Singapore: Springer Nature Singapore.

ABSTRACT

Turbomachinery blades are frequently subjected to gaseous or fluid impact in high-temperature aviation engines and power plants. Therefore, this blade material needs to be able to withstand impacts with high pressure and high velocity while being subjected to significant thermal loading. Nowadays, the development of diverse advanced materials with improved material properties is a major concern. Functionally graded material (FGM) is a high-tech composite material that is ideal for meeting this requirement. The application of FGM can avoid the frequent results of delamination, debonding, and fiber breakage in composite materials at very high temperatures. FGMs are composed of metal and ceramic constituents, with the metal part contributing to the material qualities of the FGM and the ceramic part providing protection against severe temperature and pressure . As a result, studying the free vibration characteristics of rotating turbomachinery blades built of FGMs under thermal gradient is quite important. Earlier the researchers have thought of the blades of turbomachinery as cantilevered twisted beams, however, this is quite inaccurate if the blade has a small aspect ratio, or if more than the first few frequencies and mode shapes are required. A beam representation totally eliminates chordwise bending modes. Other modes, particularly higher frequency modes, tend to be mixed rather than pure spanwise bending or torsion. A two-dimensional analysis is thus required for accurate description of such modes. A pretwisted conical shell having thickness variation along the longitudinal direction and cantilever boundary condition may be a better alternative. The twisted tapered conical shell made of FGM having some degree of porosity will make the model very practical and realistic.

The free vibration response of rotating pretwisted functionally graded (FG) conical shells in nonlinear thermal conditions is investigated using a finite element approach with the purpose of application in turbomachinery blades. The pretwisted conical shell with one metal and one ceramic constituent is functionally graded in its transverse direction with the aid of power, exponential, and sigmoid laws. In addition, the FG conical shell with one ceramic and two metal constituents is graded in both the thickness and longitudinal directions by following power-law function. Porosity distributions in FGMs can be categorized as even or uneven and temperature-dependent properties of materials are also functions of porosity distributions. The one-dimensional Fourier heat conduction equation is used to assess the nonlinear temperature distribution across the thickness of the FG conical shell. Finite element method (FEM) is introduced to discretise the conical shell in eight-noded isoparametric elements having seven degrees of freedom at each node. Two different mathematical models

based on trigonometric and polynomial higher order shear deformation theory is employed for evaluating element mass matrix, element stiffness matrices, and the equations of general dynamic equilibrium. Lagrange's equation is applied to kinetic and potential energy based formulations to derive the governing equation of motion of the cantilevered FG conical shell.

The mathematical analysis based on finite element formulations are employed to develop an in-house computer code to evaluate the natural frequencies of pretwisted porous FG conical shell in thermal environment. The results are validated with the available benchmark publications and the convergence study is also carried out to establish the exactitude of the model. A parametric study is explored to analyse the effect of porosity, power-law indexes, top surface temperature, pretwist angle, taper ratio and rotational speed on the natural frequency. The findings reveal that the porosity volume fraction has a significant influence on the natural frequency. The nonlinear temperature difference and pretwist angle both cause stiffness reduction to the FG conical shell upon increasing, whereas the presence of rotational speed inducts geometrical stiffness resulting in centrifugal stiffening. Moreover, mode shapes are developed to illustrate the modal displacements under the impacts of aforementioned parameters.

CONTENTS

NOMENCLATURE

s, L	Cone length and span length of the conical shell
ϕ_v, ϕ_0	Vertex angle and base subtended angle
β_0, α_0	Minor and major radii of the reference elliptical cross-section
β , α	Minor and major radii of any elliptical cross-section
Ψ	Pretwist angle
b_0	Reference width
r_{xy}	Pretwist radius
r_x , r_y	Curvature radii in *x* and *y*-directions
Ω', Ω	Actual rotational speed and non-dimensional rotational speed
ω_n	Natural frequency
h	Conical shell thickness at a distance
h_0	Fixed end thickness of the conical shell
C_r	Tapper ratio
E	Young's modulus
α_t	Thermal expansion coefficient
υ	Poisson's ratio
ρ	Mass density
K	Thermal conductivity
V_c , V_m	Volume fractions ceramic and metal
z	Distance in the thickness direction from the mid-plane
N	Power-law index
P_{eff}	Effective material properties
P_m , P_c	Material properties of metal and ceramic
α_p	Volume fraction of porosity
P_i	Temperature-dependent coefficients
T	Temperature
$K(z)$	Thermal conductivity at any plane
K_m, K_c	Thermal conductivity of metal and ceramic
V_{m1}, V_{m2}	Volume fractions of metal-1 and metal-2
P_{m1}, P_{m2}	Material properties of metal-1, metal-2

K_{m1}, K_{m2}	Thermal conductivities of metal-1, metal-2
ξ , η	Natural coordinates
$\{\delta_e\}$	Nodal displacement vector
N_i	Shape function at i^{th} node
$\{\delta\}$	Generalized displacement vector
u_0, v_0, w_0	Mid-surface displacement variables along x,y, and z directions
θ_x, θ_y	Rotations of the normal to the mid-surface about y- and x-axes
ξ_x, ξ_y	Higher-order displacement variables
$[Z]$	Transformation matrix
$\{\varepsilon\}, \{\gamma\}$	Linear bending and shear strain components
$[Z_b]$, $[Z_s]$	Mid-plane bending and shear thickness co-ordinate matrices
$\{\bar{\varepsilon}\}, \{\bar{\gamma}\}$	Mid-plane strain vector of bending and shear
$[Q_{ij}]$	On-axis reduced elastic constants
$[\bar{Q}_{ij}]$	Off-axis reduced elastic constants
$[D_b], [D_S]$	Elasticity matrices due to bending and shear
$[B_b]$,$[B_s]$	Strain-displacement matrix for bending and shear
E_{11}, E_{22}	Young‟s moduli in material coordinates 1 (longitudinal) and 2 (transverse)
G_{12}, G_{23}, G_{13}	Shear moduli of a lamina in the 1-2, 2-3 and 1-3 planes
ν_{12}, ν_{21}	Poison‟s ratios
θ	Inclination angle of the layer
$[K_b]$, $[K_S]$	Stiffness matrix due to bending and shear
T_1, T_0	Applied and reference temperatures
$N_x^{Th}, N_y^{Th}, N_{xy}^{Th}$	Thermal stress resultant vector
$[m]$	Inertia matrix
$[M]$	Element mass matrix
$\{\varepsilon_{nl}\}$	Non-linear strain components
$\{\sigma_0\}_{Th}, \{\sigma_0\}_R$	Stress resultants due to thermal and rotational load
$[K_{GThe}], [K_{GRe}]$	Geometrical stiffness matrices due to and rotational effect
x′, y′, z′	Inertial or fixed frame of reference
x, y, z	Shell coordinate system
θ_y, θ_x	precone angle and skew angle

h_x, h_y, h_z	Fixed translational offsets
$\Omega'_x, \Omega'_y, \Omega'_z$	Components of angular velocity in the shell coordinate system
$[C_e]$	Element Coriolis matrix
$[K_R]$	Element rotational stiffness matrix
$\left[F_{cfe}\right]$	Element centrifugal force vector
$[M]$	Global mass matrix
$[K]$	Global elastic stiffness matrix
$[K_{GR}]$ and $[K_{GT}]$	Global geometric stiffness matrices due to thermal and rotation load
$\left[F_{cf}\right]$	Nodal equivalent centrifugal load vector
T_t, T_b	Top surface and bottom surface temperature

LIST OF TABLES

LIST OF FIGURES

Dedicated

to

My Past and Present Colleagues

CHAPTER 1

INTRODUCTION

1.1 GENERAL

1.1.1 Preamble

Advanced materials are crucial to the advancement of contemporary technology and society. The scientific application of existing base materials into diverse inorganic and organic compounds has facilitated the development of sophisticated polymers, engineered alloys, structural ceramics, and more. Functionally graded materials (FGMs) are sophisticated engineered composites composed of two or more constituent phases with a continuous and gradually varied composition throughout their thickness. These advanced materials, with tailored gradients in composition, structure, and/or specialized qualities in a selected direction or orientation, surpass homogeneous materials consisting of comparable constituents. The mechanical parameters, including Young's modulus, Poisson's ratio, shear modulus, and material density, exhibit smooth and continuous variation in designated directions within FGMs. FGMs have been created by integrating advanced engineering materials in the forms of particles, fibers, whiskers, or platelets. In the ongoing pursuit of enhanced structural performance, functionally graded materials (FGMs) are being engineered to customize material architecture at the microscopic level to optimize specific functional aspects of structures.

These materials are being utilized across many fields of engineering and technology to optimize the advantageous features of available resources. This has been achieved through research and development in the mechanics of functionally graded materials for applications in specialized nuclear components, spacecraft structural elements, and high-temperature thermal barrier coatings, among others. These materials have various benefits that render them suitable for future applications. It encompasses a possible decrease in in-plane and through-thickness transverse stresses, enhanced thermal characteristics, and increased toughness, among other factors. Conventional FGMs, comprising metallic and ceramic elements, are recognized for improving the characteristics of thermal-barrier systems, as they eliminate cracking or delamination commonly seen in traditional multi-layer systems through a seamless transition between the properties of the components. By spatially altering the volumetric

percentages of two or more materials, functionally graded materials can be created to exhibit a desired gradation of properties in certain spatial directions.

Delamination appears as a significant issue in the dependable design of modern fiber-reinforced composite laminates. In laminated composites, delamination of layers caused by increased local inter-laminar stresses disrupts the load transfer mechanism, reduces stiffness, and jeopardizes structural integrity, ultimately leading to structural and functional failure (Reddy, 2004). FGMs address issues of delamination and debonding, acquiring significant importance as sophisticated materials for creative engineering applications. The components of FGMs may include metal-ceramic, ceramic-ceramic, and metal-metal combinations. Metal-ceramic is the most prevalent composition of functionally graded materials (FGMs), with the ceramic component providing excellent thermal resistance and the metallic component supporting mechanical loads. Functionally Graded Materials (FGMs) have established a significant role as structural components relative to conventional metals and ceramics, consequently presenting new opportunities for designers in aerospace, civil, marine, and automotive industries since their introduction during the past two decades.

Due to curved shape, a shell structure may support functional loads primarily through in-plane direct stresses, while also accounting for bending action. The curvature of shells produces a non-coplanar surface that generates both axial and flexural (bending and shear) forces, leading to increased structural stiffness in shell structures. Shell structures' exceptional strength and resistance to deformation make them suitable for a wide range of engineering applications, including roofs, bridges, water and oil tanks, aircraft and spacecraft fuselages, ship hulls, automobile bodies, turbomachinery, fan blades, and defence structures. The shell action comprises membrane action from in-plane direct stresses and bending action from flexural stresses, contributing to the high strength of shell structures. A pretwisted conical shell is a specific instance where the curvature of the mid-surface in one orthogonal direction is non-existent (r_x=∞), yet the curvature in the other orthogonal direction and the curvature resulting from twist are of non-zero values ($r_y \neq 0$ and $r_{xy} \neq 0$). Consequently, the resultant surface of the pretwisted shell is conical helicoids. The pretwisted FGMs shells are structurally significant components in engineering. The majority of turbomachinery blade configurations employed in practice, such as those found in fans, compressors, gas turbines, steam turbines, water turbines, marine propellers, windmills, helicopters, and flow guiding vanes, are often intricate due to their geometry. The cross-sectional area and planforms of such structures are not precisely

rectangular. Consequently, the geometric parameters may fluctuate along the length. The design requirement mandates that a blade must have a specific degree of pretwist, whereas the functional requirement stipulates the necessary rotational speeds. The conical shell profile is the most practical geometry commonly utilized in turbomachinery blades. Therefore, the pretwisted functionally graded materials shallow conical shell with a low aspect ratio may be modeled as a turbomachinery blade.

A turbomachinery blade is affixed to a revolving disk or hub, with the blade root chord rotating around the blade axis. The pretwist angle of the blade induces coupling in bending planes. The disc and its affixed blades revolve around an axis that is perpendicular to the disc's plane. Blade failure in turbomachines frequently arises due to issues related to blade vibration. Consequently, understanding these frequencies is essential. The blades experience centrifugal body forces due to rotation. The initial stress system significantly influences natural frequencies due to centrifugal force. Therefore, all these complex factors must be examined to accurately anticipate the dynamic characteristics of the turbomachinery blades. This work aims to analyze the free vibrations of functionally graded conical shell structures.

1.1.2 FGMs and Its Application

In recent years, FGMs have proven to be more advantageous than conventional structural materials and layered composites because to their continual variation in characteristic properties. Despite their extensive uses across multiple sectors, certain challenges must be addressed through future research in this domain. The mathematical modeling of graded materials is essential for accurately predicting the behavior of functionally graded materials (FGM) structures. While experimental methods exist to forecast individual thermo-physical material qualities, microscopic analyses must be conducted, and quantitative relationships created for precise assessment of the physical and thermal properties of graded materials. These linkages are employed with diverse hypotheses for the analytical or numerical assessment of various responses in FGM structures.

FGMs possess significant promise for applications under extreme working circumstances, such as spacecraft heat shields, heat exchanger tubes, biomedical implants, flywheels, and plasma facings for fusion reactors. Different combinations of typically incompatible characteristics can be utilized to develop novel materials for aircraft, chemical facilities, nuclear energy reactors, and similar applications. A separate layer of ceramic material is affixed to a metallic structure in a traditional thermal barrier coating for elevated temperature

applications. The sudden change in material characteristics at the interface between different materials can result in significant inter-laminar stresses, potentially causing plastic deformation or breaking (Reddy, 2004). The detrimental impacts can be mitigated through the gradual spatial variation of the material components. In certain instances, substantial amounts of ceramic material are situated in corrosive, high-temperature environments, whereas significant quantities of metal are positioned in areas requiring elevated mechanical qualities. Subsequently, its applications have been extended to include components of chemical plants, solar energy generators, heat exchangers, nuclear reactors, and high-efficiency combustion systems. The principle of FGMs has been effectively utilized in thermal barrier coatings to enhance thermal, oxidation, and corrosion resistance.

In the initial phases of the space-plane project, FGMs such as SiC/C, Ni-based alloy/ZrO_2, and TiC/Ni demonstrated the ability to endure significant temperature variations, thermal shocks, and stress concentrations at the interfaces (Reddy, 2004). FGMs can function as a thermal barrier system and are utilized in the insulation of combustion chambers, components of rocket engines, and exhaust wash structures of spacecraft. Fiber-reinforced composites using TiAl/SiC fibers are utilized in heat exchange panels, rocket nozzles, spacecraft truss structures, nose caps, and the leading edges of missiles and space shuttles. FGMs in spacecraft truss structures capable of supporting a substantial mass of 200 metric tons, exhibiting high-temperature resistance and a pronounced gravity gradient. Carbon nanotube (CNT) reinforced functionally graded materials demonstrate thermal stability and possess superior mechanical properties, including high toughness, hardness, abrasion resistance, and flexural strength, suitable for application in both high and low temperature environments. The majority of helicopters, fighter planes, armoured tanks, weaponry, and protective suites are constructed using functionally graded materials. These materials have excellent damping characteristics along with thermal and chemical inertness, making them suitable for usage in fuselage tanks, stabilizers, rotor blades, aircraft wings, cryogenic propellant tanks, gas turbine engines, nozzles, and compressor components of fighter jets and helicopters. Extremely lightweight weights FGMs are utilized in the defence sector for the development of weapon platforms, armour plates, barrier materials, and bulletproof vests, among others. Components of military submarines, such as sonar domes and composite piping systems, are constructed using Glass/Epoxy functionally graded materials, propulsion shafts utilize Carbon/Glass fiber FGM, cylindrical pressure hulls are manufactured from Graphite/Epoxy FGM, and diving cylinders are fabricated with Aluminium/Silicon Carbide FGM. Medical applications

encompass the substitution of biological tissues in the human body with biopolymer functionally graded materials.

Orthopaedic and dental implants are often made of collagen hydroxyapatite (HAP) and titanium alloys. High-density polyethylene with a graded biopolymer coating is utilized in orthopaedic implants such as total hip, shoulder, and knee joint replacements (Watari et al., 1997; Pompe et al., 2003). Nano hydroxyapatite-reinforced polyvinyl alcohol (nano HA/PVA) gels serve as a material for artificial articular cartilage regeneration (Bharti et al., 2013). Ti-29Nb-13Ta-4.6Zr (TNTZ) with a graded microstructure is employed as dental implants to restore masticatory function following the full loss or extraction of a tooth root (Li et al., 2014). In photo electronic devices, features such as refractive index modulation, diffusion length, and energetic band gap can be optimized by material gradation techniques, consequently improving absorption capacities and generation efficiencies. Consequently, these materials are extensively utilized in antireflective coatings, optical fibers, lenses, photodetectors, solar cells, optical sensors, semiconductor devices, computer circuit boards, and mobile phones.

Functionally graded materials integrated with piezoelectric layers are utilized in shape memory alloys. Automotive components necessitate superior strength and resistance to cracking, fracturing, and thermal shock. FGM with Al/SiC is utilized in engine cylinder liners, flywheels, drive shafts, and racing car brakes. Diesel engine pistons are constructed from SiCw/Al-alloy and leaf springs utilizing Al/C functionally graded materials. Additional components encompass motorcycle drive sprockets, pulleys, shock absorbers, radiator end caps, among others. The majority of forming tools, cutting tools, forging tools, and machine tools are produced with functionally graded materials. Examples include a lathe, drill press, broaching machine, gear shaper, and hone. FGM serves as a coating material that diminishes heat loss from engine exhaust system components, such as turbocharger casings, exhaust headers, exhaust manifolds, tailpipes, and downpipes, thus reducing coolant consumption (Bohidar et al., 2014; Kohli and Singh, 2015). The turbine wheel blades of a gas turbine engine, operating at 40,000 rpm, are coated with a TiAl/SiC functionally graded material to serve as a thermal barrier. Additionally, anti-abrasion sports equipment such as tennis rackets, baseball cleats, sports shoes, and racing bicycle frames are designed based on the principle of stress relaxation. Commonly utilized FGMs encompass razor blades, cutting instruments, eyeglass frames, helmets, X-ray tables, vehicle fuel tanks, pressure vessels, wind turbine blades, MRI

scanner components, cryogenic tubes, laptop casings, titanium timepieces, window panes, and camera tripods.

1.1.3 Present Study - Its Relevance in Research

Recently, functionally graded materials (FGMs) have been preferred in turbomachinery blades due to their performance in extremely high temperature circumstances, especially in the automotive, aerospace, and marine sectors. A substantial body of research is available in several scholarly journals, monographs, and reviews concerning FGM structures exposed to high-temperature environments. The literature encompasses a wide range of works on the analysis, design, and modeling of FGM plates and shells. Compared to the other dimensions of the shell, the shallow shell is thinner and demonstrates less deformations in relation to its thickness. In the domain of mechanical structural components, shell structures featuring variable thickness and twisted geometries have numerous applications. The literature extensively addresses the design, modeling, analysis, and construction of shell structures, which is particularly pertinent to the current study. The utilization of functionally graded materials has advanced considerably since their inception

Shell forms have a longstanding history of extensive applications as turbo-machinery blade structures, despite several studies into the properties of shell structures commencing about a century ago. Rotter (1998) gave a historical review of shell research and design, whereas Meirovitch (1997) discussed the principles and techniques of vibration. Rao (1991) presents the vibration characteristics of turbomachinery blade profiles. Isotropic shells were initially utilized for study; subsequently, attention shifted to composite laminated shells. However, at elevated temperature gradients, delamination poses a significant challenge for composite shells. Consequently, since the inception of FGMs throughout the past two decades, considerable focus has been directed towards FGM shells and structures. Functionally graded materials are increasingly utilized across diverse engineering and technological fields to optimize the advantageous qualities of existing materials. This has been achieved through research and development in the mechanics of functionally graded materials for contemporary technologies involving specialized nuclear components, spacecraft structural elements, and high-temperature thermal barrier coatings, among others. De-bonding or delamination represent the primary issues in advanced fiber-reinforced composite laminates, as the separation of layers due to elevated local inter-laminar stresses diminishes stiffness and compromises structural integrity. FGMs possess the capability to resolve these issues, and

owing to these benefits, they have attained significant prominence as a sophisticated material. The predominant functionally graded materials consist of metal-ceramic components, wherein the ceramic portion exhibits excellent thermal resistance, while the metallic portion provides superior structural support. The turbo-machinery blade materials with functionally graded materials possess numerous benefits over composite and traditional materials in terms of both thermal and structural properties.

1.2 LITERATURE REVIEW

The literature concerning the study, design, and modeling of functionally graded materials (FGM) plates and shells encompasses a broad spectrum of research. The shallow shell possesses a reduced thickness relative to its other dimensions, wherein deformations are minimal in comparison to the thickness. Shell structures with twisted geometry possess significant applications in mechanical structural components. The literature concerning the design, modeling, analysis, and building of shell structures encompasses a wide range of research, particularly in relation to the current study. Substantial advancements have occurred in the utilization of these specialized structures with the advent of functionally graded materials.

Review articles by Birman and Byrd (2007), Liew et al. (2011), Alijani and Amabili (2014), Jha et al. (2013), Thai and Kim (2015), Swaminathan and Naveenkumar (2015), Gupta and Talha (2015), Liew et al. (2015), and Swaminathan and Sangeetha (2017) encompass a significant portion of the research conducted over the past two decades, while minimal focus was directed towards FGM conical shells prior to that, with notable exceptions being Zhao and Liew (2011) and Tornabene et al. (2014). The various shell theories, distinct FGM porous structures, and FEM analysis techniques are reported from Section 1.2.1 to Section 1.2.4. The literature study subsequently concentrates on exploring shell structures based on the pretwist angle and taper ratio, which are presented in Section 1.2.5 and Section 1.2.6, respectively. Section 1.2.7 to Section 1.2.9 discusses the impact of several characteristics, including porosity, rotation, and non-linear temperature distribution. Section 1.2.10 presents a critical analysis of the available literature about the free vibration of various functionally graded material (FGM) shell and plate configurations.

1.2.1 Plate and Shell Theories

Although comprehensive research on the properties of shell structures commenced than a century ago, there has been a prolonged history of substantial application of shell forms in

turbo-machinery blade configurations. Shell structures are defined as three-dimensional forms enclosed by two reasonably proximate curving surfaces. Most shell theories (thin and thick, deep and shallow) simplify the three-dimensional elasticity equations to a two-dimensional framework. This is typically achieved by removing the coordinate perpendicular to the shell surface in the formulation of the shell equations. The precision of thin and thick shell theories can be validated by comparing them to the three-dimensional theory of elasticity. The behaviour of functionally graded plates and shells under mechanical and thermal loads can be anticipated using either three-dimensional (3D) elasticity theory or equivalent single-layer (ESL) theories. The ESL models are formulated from the 3D elasticity theory by applying appropriate assumptions on the kinematics of deformation or the stress state across the thickness of plates and shells (Reddy, 2004). These ESL theories may explain both shear and normal deformation effects contingent upon the degree of assumptions made. The most basic ESL model is the classical plate theory (CPT), commonly referred to as Kirchhoff theory (1850), which disregards both shear and normal deformation forces. Consequently, it is exclusively appropriate for slender FG plates or shells. The subsequent theory in the hierarchy of ESL models is the first-order shear deformation theory (FSDT) established by Mindlin in 1951. The FSDT incorporates the shear deformation effect by employing a linear variation of in-plane displacements over the thickness. A shear adjustment factor is thus necessary. The shear correction factor is challenging to ascertain as it is influenced by both geometric characteristics and the loading and boundary conditions. Higher-order shear deformation theories (HSDTs) were established to eliminate the necessity of the shear correction factor. The HSDT can be formulated by expanding the displacement components into power series of the thickness coordinate. The theories created by this method can achieve any desired level of accuracy by incorporating an adequate number of words in the series.

The HSDTs incorporate higher-order variations of in-plane displacements, as well as both in-plane and transverse displacements (i.e., quasi-3D theory) across the thickness, thereby accounting for the effects of shear deformation and both shear and normal deformations. Higher-order shear deformation theories (HSDTs) can be formulated with either polynomial or non-polynomial (trigonometric) shape functions. Patel et al. (2005) investigated the free vibration properties of functionally graded elliptical cylindrical shells employing a quasi-3D theory and the finite element method. Matsunaga (2008) formulated a quasi-3D theory for the analysis of buckling and free vibrations in functionally graded shallow shells. Pradyumna and Bandyopadhyay (2008) created a four-noded continuous shell element featuring nine degrees

of freedom per node for the free vibration analysis of functionally graded curved panels utilizing a higher-order finite element formulation. They expanded upon the prior research of dynamic instability of FG curved panels conducted in 2009. Levy (1877) initially employed the non-polynomial function alongside a sinusoidal function to formulate an advanced theory for thick isotropic plates. Stein (1986) later utilized the sinusoidal function to formulate a five-unknown sinusoidal shear deformation theory (SSDT) for isotropic plates, while Touratier (1991) introduced it for laminated composite plates. The HSDT was extensively employed to analyze the dynamic behavior of FG structures. Research on the vibration of functionally graded plates is available (Zenkour, 2005), as well as studies on the bending of FG plates (Zenkour, 2006) and the thermal bending of FG plates supported by an elastic base (Zenkour and Sobhy, 2011). Zenkour (2012) determined the bending relationships between the HSDT and CPT values for FG Levy-type plates. Recently, Zghal et al. (2018) conducted a free vibration analysis of carbon nanotube-reinforced functionally graded composite shell structures employing higher-order shear deformation theory (HSDT).

The accuracy of the FSDT is inherently compromised by its reliance on the shear correction factor, whereas the polynomial HSDT integrates shear deformation using Taylor series coefficients. Consequently, this process is relatively intricate and computationally demanding, as each augmentation in the power of the thickness coordinate introduces a new variable. Non-polynomial HSDTs have been introduced, utilizing the shear strain function to represent shear deformation, hence overcoming the previously noted limitations. Non-polynomial functions enable precise predictions of structural behavior, exhibit nonlinear in-plane displacement variations, demonstrate parabolic transverse shear stress variations across the thickness, and satisfy traction-free boundary requirements. Mantari et al. (2012) introduced a non-polynomial shear deformation theory with five variables to examine the flexural bending properties of isotropic, composite, and sandwich structures. The non-polynomial function is more intricate than polynomial functions; however, it is more straightforward and accurate, and the free surface boundary conditions can be guaranteed before application (Mantari et al., 2012a). Hu et al. (2024) reported the magneto-thermo-elastic nonlinear free vibration of FG cylindrical shell by using Galerkin method. Hong (2022) investigated the thermal vibration of thick FG plates-cylindrical shells by using TSDT. Bagheri et al. (2024) presented the large amplitude nonlinear vibration of conical–cylindrical–conical joint shell by applying von Karman assumptions and FSDT.

1.2.2 Functionally Graded Materials

FGMs were fundamentally designed to address the requirements of high temperature gradient applications in the aerospace and energy sectors. FGMs are increasingly being utilized in several areas due to their numerous advantages. The composition of the metal and ceramic elements varies from plane to plane; hence, the material characteristics of FGMs are not constant throughout thickness. Following three continuous functions, the proportions of metal and ceramic constituents change throughout the thickness. When the volume fraction follows a power-law of distribution across the thickness then it is referred to as p-FGM (Reddy and Chin, 1998; Zhao et al., 2009). In the second case, the volume fraction might vary exponentially throughout the thickness and is referred to as e-FGM (Jin and Batra, 1996). Due to the existence of sharp material interfaces, a high value of stress concentration may be seen for p-FGM and e-FGM. The solution offered by Chung and Chi (2001) to get around this issue is a material known as s-FGM, which consists of a volume fraction followed by the union of the two power functions or the sigmoid law of distribution. Chi and Chung (2002) conducted an analysis showing that the s-FGM is devoid of stress intensity factors when applied to cracked structures. The static loading behaviour of all three varieties of FGM (p-FGM, e-FGM, and s-FGM) plates was reported by Lee et al. (2015) applying higher-order shear deformation theory (HSDT) and higher-order normal deformation theory. The static loading of simply supported p-FGM and e-FGM shells in a three-dimensional model was examined by Monge and Mantari (2020) using the Chebyshev–Gauss–Lobatto distribution and Lagrange's interpolation polynomials. To examine the free vibration of e-FGM rectangular plates, Reddy and Kant (2014) provided an analytical strategy based on the 3-D elasticity theory. Utilizing HSDT, Han et al. (2009) investigated the linear and nonlinear vibration of s-FGM in addition to laminated composite plates and shells. The dynamic stiffness technique (DSM) was used by Kumar and Jana (2019) to examine the vibration behaviour of rectangular e-FGM and s-FGM plates.

Loy et al. (1999) investigated the vibrations of functionally graded cylindrical shells with simply supported boundary conditions employing the Classical Plate Theory and the Rayleigh–Ritz method. Arshad et al. (2007) employed a comparable methodology to examine the vibrational properties of FG cylindrical shells under three distinct volume fraction laws. Pradhan et al. (2000) investigated the vibrational properties of functionally graded cylindrical shells under different boundary conditions utilizing the Classical Plate Theory and Rayleigh technique. Naeem et al. (2010) re-evaluated this issue employing the Ritz technique. Alijani et al. (2011) examined the nonlinear forced vibrations of functionally graded doubly curved

shallow shells utilizing the classical plate theory with von Karman assumptions and the multi-modal Galerkin discretization method. Du et al. (2014) investigated the nonlinear vibrations of functionally graded cylindrical shells subjected to stimulation, utilizing the classical plate theory with von Karman assumptions alongside a multiple scale technique. Du and Li (2013) investigated the nonlinear vibrational response of functionally graded cylindrical shells in temperature conditions using a comparable methodology. Ebrahimi and Najafizadeh (2014) investigated the free vibration of functionally graded cylindrical shells employing the classical plate theory alongside the generalized differential quadrature and generalized integral quadrature techniques. Nguyen and Tran (2013) investigated the nonlinear behavior of imperfect eccentrically stiffened functionally graded panels supported by an elastic basis, employing the Classical Plate Theory and the Lekhnitsky smeared stiffener method. Duc and Quan (2012, 2015) performed a nonlinear dynamic study of imperfect functionally graded doubly curved shallow shells on an elastic foundation, subjected to mechanical and thermal loads, employing classical plate theory with von Karman assumptions. The link between stretching and bending in functionally graded plates results from the variation of material properties along the thickness. Consequently, the neutral surface of the FG plate does not align with its central surface. The relationship may be eliminated if the governing equations were established based on the neutral surface. Zhang and Zhou (2008) established the report's validity by formulating the CPT for FG plates based on the neutral surface and deriving the governing equations of motion in the context of isotropic plates. Kar et al. (2017) assessed the impact of varying temperature loads on the thermal post-buckling behavior of functionally graded shallow curved shell panels utilizing the Classical Plate Theory model.

Shahsiah and Eslami (2003, 2003a) formulated analytical solutions for the buckling temperature of functionally graded cylindrical shells with simply supported boundary conditions, addressing two types of thermal loadings, by employing the first-order shear deformation theory (FSDT) and the Navier solution. Arciniega and Reddy (2007) published the geometrically nonlinear analyses of FG shells utilizing the finite element method, with the shell kinematics grounded in the first-order shear deformation theory (FSDT). Barbosa and Ferreira (2009) presented additional investigations on the geometrically nonlinear bending behavior of FSDT shells utilizing the Marguerre shell element, while Sheng and Wang (2011) employed the fourth-order Runge–Kutta numerical approach. Behjat et al. (2009) analyzed the static bending, free vibration, and transient responses of functionally graded piezoelectric cylindrical panels subjected to mechanical, thermal, and electrical loads using first-order shear

deformation theory and the finite element method. Kiani et al. (2012) investigated the static and dynamic bending behavior, as well as the free vibration characteristics, of functionally graded doubly curved panels under combined mechanical and thermal loadings, employing the first-order shear deformation theory (FSDT) and an analytical hybrid Laplace–Fourier transformation. Isvandzibaei et al. (2016) conducted a study on the vibrations of a supported thick-walled cylindrical functionally graded (FG) shell under pressure loading, where the governing equations derived from the first-order shear deformation theory (FSDT) were analytically solved for the natural frequency of FG cylindrical shells across various boundary conditions utilizing the Ritz method. Xiang et al. (2015) employed the meshless local collocation method and FSDT to determine the natural frequency of functionally graded cylindrical shells. Pradyumna and Nanda (2013) examined the transient response of functionally graded plates, deriving the nonlinear governing equations from the first-order shear deformation theory (FSDT) utilizing von Karman assumptions, and solving them using an eight-noded continuous element. The time-dependent dynamic response was resolved using the Newmark integration strategy in conjunction with the modified Newton–Raphson iteration approach. Talebitooti (2018) examined the heat influence on the free vibration of a ring-stiffened, rotating, functionally graded conical shell with clamped boundaries utilizing the first-order shear deformation theory (FSDT).

1.2.3 Bidirectional Functionally Graded Material (BDFGM)

Since the advancement of functionally graded materials, various types of FGMs are developed based on different grading laws to fulfil the desired material properties. When the metal and ceramic constituents are graded unidirectionally based on the simple power law, exponential law and sigmoid law then the FGMs are termed as p-FGM, e-FGM and s-FGM respectively. However, if variation of the constituents follow the aforementioned gradation laws along both the thickness (z- axis) and longitudinal direction (x-axis) then it is termed as bidirectional functionally graded material. The top surface is assumed to have completely ceramic and its volume proportion keeps on decreasing along the depth, where the bottom surface is completely metallic in nature. Subsequently, the metallic volume fraction at one end keeps on changing following the gradation laws with the increase of the length of the structure until the other end. Simsek (2015) studied the free and forced vibration of bidirectional functionally graded beam under four different types of boundary conditions using first order shear deformation theory (FSDT). Here the FGM constituents are graded in both the direction using exponential law and the Lagrange equation is applied to get the equation of motion. Hashemi

and Jafari (2020) analysed the nonlinear free and forced vibration of bidirectional rectangular plates by applying von Karman nonlinearity strain-displacement relation. The time-dependent governing equations of motions are derived by using Galerkin method and FSDT. Chen et al. (2018) employed isogeometric analysis to report the free vibration of bidirectional functionally graded cylindrical shell using FSDT, where the ceramic and metal constituents were graded following power and exponential law in the longitudinal and circumferential direction but significantly not in thickness direction. Ebrahimi and Najafizadeh (2014) used generalized deferential quadrature (GDQ) and general integral quadrature (GIQ) to evaluate the free vibration of bidirectional functionally graded cylindrical shells based on Voigt and Mori-Tanaka models. Xiang et al. (2014) applied a three dimensional consistent approach to present the free vibration and mechanical buckling of in-plane functionally graded plate with material inhomogeneity derived by two-dimensional higher order spectral method. Do et al. (2017) used third order shear deformation theory and reported the static buckling and bending analysis of bidirectional functionally graded plates with finite element model formulations. Using a quasi-3D higher order shear deformation theory, Sekkal et al. (2017) investigated the free vibration and static buckling of FG plates considering thickness stretching influenced by a hyperbolic distribution of displacements. Lakhdar et al. (2024) applied TSDT with the p-version of finite element method to study the free vibration and static bending of porous bi-directional functionally graded sandwich shell. Nguyen and Phan (2023) used NURBS-based isogeometric analysis to report the nonlinear free vibration of porous bi-directional functionally graded plates.

1.2.4 Finite Element Modeling

The advent of computers in the mid-twentieth century significantly eased the resolution of engineering challenges related to the static and dynamic responses of structures. The finite element method (FEM) is a numerical approach used to approximate solutions for boundary value problems that involve partial differential equations. It involves discretizing the domain into smaller sub-domains known as finite elements, developing element equations for each finite element, and combining these equations at selected nodes to produce the global equations, which are then, solved using appropriate solution methods. The vibration of the FGM shells entails several intricate interactions among the shell structures, layer properties in the thickness direction, internal strains, starting loads, and the influence of external bodies. The resolution of such issues is exceedingly intricate, computationally demanding, and involves substantial matrices. The advent of contemporary high-speed computers and finite element

software such as NASTRAN/PATRAN, alongside commercial packages like ANSYS, LSDYNA, ICEM-CFD, COSMOS/M, and ABACUS, has facilitated the resolution of issues in static and dynamic structural analysis, fluid dynamics, thermal analysis, electromagnetic studies, seismic response, and various optimization processes. The selection of an acceptable mathematical model, optimal and localized mesh size, effective solution approach, and appropriate solver is critical for any finite element simulation, as it determines accuracy, dependability, and usefulness for modeling complex engineering issues. The turbomachinery blades experience significant centrifugal loading, leading to steady-state deflections. The turbomachinery blades of FGMs exhibit significant influences from twist angles, rotational speeds, arbitrary cross-sectional area variations along the blade length, and diverse material properties throughout the thickness, all of which must be considered for precise prediction of the blade's dynamic characteristics using the finite element method (FEM). Owing to their complex character, blade dynamic problems can only be precisely resolved in a few specific instances. Given these conditions, finite element methods are suitable for the dynamic analysis of both stationary and rotating turbomachinery blades, as these numerical techniques effectively accommodate blades of various configurations. Analytical approaches facilitate a fundamental comprehension of the problem and assist in preliminary design, whereas finite element methods enable refinement throughout the detailed design phase.

Finite element methods (FEM) have significantly advanced over the past four decades, mostly derived from the Ritz method, utilizing energy minimization or other energy techniques at the element level to derive an element stiffness matrix. The Finite Element approach overcomes the challenges encountered by the Ritz approach in addressing diverse boundary conditions and intricate geometries. The Ritz approach demonstrates superior convergence and reduced processing requirements for simple shell designs. The Finite Element Method (FEM) has demonstrated efficacy for complex shell structures and boundary conditions. The finite element method (FEM) is the most widely employed computer methodology for addressing a range of engineering problems. In FEM, the continuum is divided into a finite number of discrete, non-overlapping segments referred to as elements. The equilibrium conditions for each element are determined by a restricted set of state variables. The universal solution of the entire system is obtained by integrating the results of the different components. A significant array of FEM commercial codes and packages is available to derive vibration findings.

Sundararajan et al. (2005) utilized an eight-nodded shear flexible quadrilateral plate element, applying a consistency technique, to investigate the large amplitude free flexural vibration characteristics of functionally graded material plates according to the first-order shear deformation theory (FSDT). The impact of skew angle was seen to increase the ratio of nonlinear frequency to linear frequency relative to the rectangular arrangement. Pradyumna and Bandopadhyay (2008) utilized an eight-nodded continuity element for the free vibration analysis of simply-supported FGM rectangular curved panels, applying the higher-order formulation established by Kant and Khare (1997). The authors observed that although the higher-order shear deformation theory is computationally demanding, it exhibits effective performance for both thin and thick panels, thus endorsing its use for the free vibration analysis of functionally graded material plates and shell panels of varying thicknesses. Alijani et al. (2011) utilized a p-version of the finite element method in conjunction with a blending function technique for the non-linear free vibration analysis of functionally graded material doubly-curved shallow shells with an elliptical plan, applying the first-order shear deformation theory. FGM plates exhibit hardening behavior dependent on the volume fraction exponent and thickness ratio. Talha and Singh (2010) employed a continuous element featuring 13 degrees of freedom per node to present a higher-order shear deformation theory, incorporating a specific modification in the transverse displacement that improves the displacement freedom throughout the thickness and fundamentally eliminates the over-correction in the static and free vibration analyses of functionally graded material plates. Talha and Singh (2011) conducted an investigation of large amplitude free flexural vibrations of shear deformable functionally graded material plates, employing higher-order shear deformation theory and utilizing a continuous element with 13 degrees of freedom at each node. Malekzadeh and Shojaee (2013) utilized an eight-nodded solid element alongside the Newmark time integration method to examine the transient response of functionally graded material (FGM) plates based on the first-order shear deformation theory (FSDT) under arbitrary boundary conditions and the influence of a moving heat source. Reddy and Chin (1998) investigated the dynamic response of functionally graded cylinders and plates under two distinct thermal loadings employing the first-order shear deformation theory and the finite element approach. Arciniega and Reddy (2007) conducted a geometrically nonlinear analysis of FG shells employing the FSDT and the finite element method. Naghdabadi and Kordkheili (2005) introduced a finite element approach for the study of functionally graded plates and shells. Hosseini and Naghdabadi (2007) conducted a geometrically non-linear thermoelastic analysis of functionally graded shells employing the finite element method. Santos et al. (2009) presented a semi-analytical finite

element model for the examination of cylindrical shells composed of functionally graded materials. Recently, Ansari et al. (2018) conducted a static analysis of a doubly curved, singly ruled, truncated functionally graded material cone utilizing the finite element method. Dey and Bandyopadhyay (2024) used finite element analysis and presented the free vibration behaviour of functionally graded plates in the presence of nonlinear temperature distribution. Marzavan and Nastasescu (2023) employed finite element method to report the free vibration of functionally graded plates by using multilayer plate concept. Zang et al. (2022) applied scaled boundary finite element method to study the free vibration and static bending of functionally graded plates.

1.2.5 Pretwisted Shell Structure

The layer-wise isotropic functionally graded material with continuous ceramic-to-metal transition can be readily customized for turbomachinery blades to achieve certain overall attributes. The blades are typically affixed to the hub region. The blades are typically broad at the root and exhibit a gradual chordwise taper toward the free end. A turbomachinery blade is characterized as a cantilevered open conical shell with a trapezoidal planform and a changeable curvature along the chordwise axis. A thickness fluctuation may also occur along the length of the conical shell. Typically, an initial twist is applied to the blades to adjust the angle of attack for optimal performance, although the pretwist angle is constrained by the decrease in the structural rigidity of the laminates (the pretwist angle is kept between 0° and 45°). Previously, the blades were represented as cantilevered beams and plates, which produced highly erroneous results for low aspect ratio and thin blades due to the omission of curvature effects along the chordwise camber. Subsequent researchers portrayed them as cantilevered conical shells to incorporate the chordwise camber but the studies were limited due to the difficulties in generating the precise geometry of functionally graded material conical shells. Nonetheless, the introduction of high-speed computers facilitated modeling, resulting in results that were more closely related to experimental data. The application of Kirchhoff's theory to shell modeling is valid only when the two dimensions (chord and shell thickness) are minimal in comparison to the third dimension (length of the shell) and when variations throughout the length can be disregarded.

The modeling of turbomachinery blades with a shallow conical shell model produces precise results just in instances of low aspect ratios and low length-to-thickness ratios of the conical shells. Consequently, the FGM turbomachinery blades can be engineered to exhibit specific

static and dynamic characteristics. The FGM blades of a pretwisted shallow conical shell can be produced using a powder metallurgical technique. Consequently, it is feasible to fabricate intricate designs that provide effective aircraft turbopropellers. Therefore, as a forerunner in the utilization of FGMs in the essential components of aeroengines or turbomachinery in general, comprehensive design analysis is necessary in addition to the deformation and vibration properties. The twisted conical shell element is capable of accurately replicating the behavior of functionally graded material (FGM) blade structures in finite element analysis and can be applied to more realistic scenarios. The aerodynamic efficiency of engines can be optimized by incorporating a variable radius of curvature in the blades, achievable with conical shell forms, but such an adaptation is constrained in cylindrical shell geometries.

As the kinetic energy of the gaseous flow will convert into the rotational motion of the turbo machinery blade so the need for pretwist angle becomes an essential criteria for smooth functioning. For any types of turbine blade even including hydro and wind, the presence of pretwist angle is compulsory for high efficiency (Yin et al, 2014). Cao et al. (2017) analysed the free vibration of sandwich blades with thermal barrier coatings having pretwist angle by applying first-order shear deformation theory. Chen et al. (2021) analysed natural frequencies of pretwisted functionally graded sandwich blades in the presence of temperature distribution. Zhang et al. (2020) studied the nonlinear vibration of pretwisted rectangular plates applying third-order shear deformation theory. Rout et al. (2018) worked on pretwisted cylindrical shells considering delamination and stiffener and neglecting Coriolis effect for rotation. Xu and Wang (2024) analysed the nonlinear free vibration of rotating pretwisted functionally graded plates based on von Karman assumptions. Based on three-dimensional elasticity shell theory and Carrera unified formulation, Chen et al. (2022) presented three dimensional vibration of rotating pretwisted functionally graded cylindrical shells.

1.2.6 Shells with Variable Thickness

Li et al. (2020) illustrated the free vibration of FGM beams with variable thickness subjected to hydrodynamic loading by applying Timoshenko beam theory. Kumar et al. (2019) investigated the effect of thickness variations to evaluate the free vibration of FG rotating beams based on differential transform method. Liu et al. (2014) explored the free vibration of ring-stiffened tapered conical shell in submerged condition using Flugge theory. Miao et al. (2022) used Sanders' shell theory to present the free vibration three-layer FG thin cylindrical shell having non-uniform thickness, where the middle layer is formed by two dimensional

FGM. Sivadas and Ganesan (1990) analysed the free vibration of cantilevered isotropic conical shell with variable thickness based on Love's first approximation thin shell theory. Cheung and Zhou (2003) reported the free vibration of tapered rectangular Mindlin plates where the static load is derived by using Timoshenko beam functions. Fang and Zhou (2017) presented the free vibration of rotating rectangular Mindlin plates by using Ritz method where the admissible functions are derived based on Chebyshev polynomials.

Thi (2022) examined the free vibration behavior of porous functionally graded plate with varying thickness based on HSDT, wherein the plate was supported by two-parameter elastic foundations. Kumar et al. (2021) employed the finite strip displacement theory kinematics to investigate the vibrational behavior of a porous tapered rectangular plate situated on an elastic base. In a study, Farsani et al. (2022) employed the Rayleigh-Ritz technique and the FSDT to investigate the vibration characteristics of porous taper FGM plates including its interaction with fluid. The authors Chen et al. (2020) presented a numerical method to examine the characteristics of free vibrations in porous parallelogram plates made of FGM with different thicknesses wherein the displacement field was mathematically expressed as a polynomial function. Tran et al. (2021) proposed a novel triangular element for the analysis of bending and free vibration in variable-thickness plates made of FGM with porosity, based on the FSDT.

1.2.7 Porosity Distribution

The fabrication of porosity-free functionally graded materials utilizing existing production techniques is quite challenging. Consequently, the influence of the porosity factor on the structural behavior of FGM components necessitates the consideration of porosities in FGM. Porosities are classified into two types: even and uneven. Wang and Zu (2017) elucidated the comprehensive theoretical framework of even and uneven porosities. The swift advancement of materials technology has positioned structures with graded porosity as a recent innovation in functionally graded materials (FGMs). The local density of the material accounts for the presence of porosity within its microstructures. Porous materials consist of two components: a solid element (body) and another element that is typically a liquid or gas, commonly seen in nature, such as wood, stone, and dust layers. Currently, researchers focus on the preparation methods of FGMs, which encompass powder metallurgy (Khor and Gu, 2000), vapor deposition (Seifried et al., 2001), self-propagation (Liu et al., 2006), centrifugal casting (Watanabe et al., 1998, 2001), and magnetic separation (Song et al., 2007). Nevertheless, these methods are expensive and entail their own technological intricacies.

Due to the fact that it is impossible to produce an FGM that is pore-free throughout processing and fabrication, the presence of porosity is an essential characteristic of any FGM. Due to the way porosity is distributed in FGMs, there are two main categories that may be classified: even and uneven porosity distributions. Therefore, if the presence of porosity distribution is taken into consideration, one may acquire highly practical and realistic results and conclusions for studying FGM structures. The nonlinear buckling analysis of all three types of shallow FGM panels was analyzed by Rezaiee-Pajand and Masoodi (2022) taking into account porosity in a hygrothermal environment. Amoozgar and Gelman (2022) examined the vibration of rotating FGM beams in three dimensions while taking into account both even and uneven porosity distributions. According to even and uneven porosity, Kumar et al. (2021) investigated the vibration response of p-FGM and e-FGM plates lying on Pasternak's foundation. Based on Carrera's unified formulation, Rahmani et al. (2022) worked on free vibration optimization of the distribution of metal and ceramic elements for porous p-FGM plates by using the Carrera unified formulation (CUF). With regard to all FGM components, including arches, beams, tubes, plates, and shells, Wu et al. (2020) examined the consequences and features of material properties for the existence of porosity. The free vibration of p-FGM shells with double curves was analyzed using first-order shear deformation theory (FSDT) by Zare Jouneghani et al. (2017) while taking the existence of porosity into consideration. In a multi-directional analysis, Sah and Ghosh (2022) took into account even porosity as well as several forms of uneven porosities, such as logarithmic distribution, linear distribution, and sinusoidal distribution. Using first-order shear deformation theory (FSDT), Hamilton's principle, and the variational approach, Rezaei et al. (2017) studied analytically the impact of porosity distributions on the free vibration behaviour of p-FGM plates. Using the von Karman type nonlinear plate theory, Wang and Zu (2018) investigated the natural frequencies and nonlinear forced vibration responses of moving porous s-FGM plates. Zhou (2022) predicted the free vibration response of p-FGM plates with varying porosity distribution and thermal conditions using a dynamic similitude approach.

Previous studies indicate that numerous porosities may develop inside the materials during the non-pressure sintering process of FGM preparation (Zhu et al. 2001), and these porosities can significantly diminish the strength of FGMs. Additionally, the multi-step sequential infiltration approach results in porosities within the intermediate region of the FGMs. This phenomenon arises from the difficulty of perfectly infiltrating the secondary material into the central region, while infiltration into the upper and lower areas is more feasible, resulting in reduced porosity

in these zones (Wattanasakulpong et al., 2012). Given the presence of porosities in FGMs, it is crucial to examine the impact of porosity on the vibrational properties of FGM structures. This study emphasizes the necessity of considering the porosity effect in the design and analysis of FGM constructions.

Wattanasakulpong and Ungbhakorn (2014) examined the linear and nonlinear vibrations of porous functionally graded material beams with elastically constrained ends. Ebrahimi and Mokhtari (2015) investigated the vibrations of rotating Timoshenko functionally graded beams with porosities using the differential transform method. The porosity volume percentage and the type of porosity distribution significantly influence the vibrational response of the FGM beams. Wattanasakulpong and Chaikittiratana (2015) forecasted the flexural vibration of porous functionally graded material beams via Timoshenko beam theory. Additionally, Yahia et al. (2015) investigated the wave propagation of functionally graded porous plates utilizing higher-order shear deformation theory. Ebrahimi and Zia (2015) examined the substantial amplitude nonlinear vibrations of porous functionally graded material beams employing Galerkin and many scales methodologies. Atmane et al. (2017) utilized an efficient beam theory to examine the influence of thickness stretching and porosity on the mechanical responses of functionally graded material beams supported by an elastic base. They asserted that the existence of porosities results in two significant consequences: a decrease in both mass and strength of FG beams. Ebrahimi et al. (2016) examined the thermo-mechanical vibrational response of temperature-dependent functionally graded material beams with porosities. Mechab et al. (2016) have formulated a nonlocal elasticity model for the free vibration of functionally graded porous nanoplates supported by elastic foundations. Zare et al. (2017) conducted an investigation of free vibrations in functionally graded porous doubly-curved shells utilizing the first-order shear deformation theory. Based on FSDT, Tung and Thinh (2025) reported the nonlinear free vibration of functionally graded shell panels in the presence of nonlinear foundations. Thinh and Tung (2024) investigated the nonlinear free vibration of functionally graded plates with porosity incorporating damping effects.

1.2.8 Rotating FGM Shell structures

In the dynamic analysis of tubromachinery blades, rotational speed serves as a critical characteristic that has been examined by numerous researchers. Free vibration evaluations of rotating functionally graded shells of revolution are confined to functionally graded cylindrical shells. Ahmad and Naeem (2009) examined the vibrational properties of rotating functionally

graded cylindrical shells under various boundary conditions. The shell dynamical equations were derived from Budiansky and Sanders' thin shell theory and resolved by a wave propagation method. Malekzadeh and Heydarpour (2012) investigated the free vibration properties of rotating functionally graded cylindrical shells under a thermal environment. Heydarpour et al. (2012) conducted a thermoelastic analysis of rotating laminated functionally graded cylindrical shells utilizing the layer wise differential quadrature method. Malekzadeh and Heydarpour (2013) expanded upon their prior research (2012) about rotating conical shells, conducting a free vibration analysis of rotating functionally graded conical shells under various boundary conditions based on the first-order shear deformation theory. The formulation included the centrifugal and Coriolis forces arising from the rotation of the FG shell. The differential quadrature method (DQM) was employed to solve the thermoelastic equilibrium equations and the equations of motion for free vibrations. Heydarpour et al. (2014) examined the free vibration characteristics of rotating functionally graded carbon nanotube-reinforced composite truncated conical shells. Nguyen and Nguyen (2017) evaluated the dynamic response and vibrations of functionally graded carbon nanotube-reinforced composites (FG-CNTRC) within truncated conical shells supported by elastic foundations, whereas Sheng and Wang (2017) examined the non-linear vibrations of rotating functionally graded cylindrical shells. Aris and Ahmadi (2023) reported the thermoelastic nonlinear vibration of rotating stiffened functionally graded conical shells in the presence of harmonic excitation. Based on FSDT, Mohammadi and Hosseini (2024) investigated the free vibration of rotating functionally graded thin-walled hub-blade systems under aerothermoelastic loading.

1.2.9 Nonlinear Temperature Distribution

The temperature of the surroundings has a significant impact on the vibration characteristics of FGM structures. Uniform, linear, and nonlinear temperature distributions are typically the three distinct forms of temperature distributions on the two opposing surfaces of the FGMs (Huang and Shen, 2004; Lal and Saini, 2020; Parida and Mohanty, 2017; Van Do et al., 2019). The effects of these three forms of temperature distributions on the material properties of the three distinct types of FGMs (p-FGM, e-FGM, and s-FGM) were reported independently by Amine and Abd El Kader (2016). The nonlinear temperature distribution throughout the thickness of the FGM is typically observed in reality among these three types of temperature distributions. The nonlinear vibration of p-FGM plates in nonlinear temperature distribution was described by Alijani et al. (2011). Using the Rayleigh–Ritz approach, Chakraverty and Pradhan (2014) examined the free vibration of e-FGM plates with and without

temperature distribution under a variety of boundary conditions. Using the one-dimensional Fourier's heat conduction equation and the virtual work concept, Fazzolari (2016) investigated the free vibration of p-FGM and s-FGM plates. The free vibration of a completely clamped, ring-stiffened, p-FGM conical shell in a nonlinear temperature distribution was addressed by Talebitooti (2018). Regarding rotating inertia and Reddy's HSDT, Yang and Shen (2003) investigated the free vibration of p-FGM cylindrical panels in thermal environments. In a thermal condition, Duc and Thang (2014) investigated the nonlinear static buckling of an s-FGM cylindrical shell with a stiffener. The vibro-acoustic interaction of s-FGM sandwich plates in thermal environments was studied by Li et al. (2021).

Heat and moisture significantly affect the dynamic characteristics of shell elements. The shell structure exhibits different behavior at high thermal gradients and in humid conditions. Yang et al. (2006) investigated the thermo-mechanical post-buckling behavior of functionally graded cylindrical panels with temperature-dependent characteristics. Shariyat (2009) investigated the vibration and dynamic buckling control of imperfect hybrid functionally graded material plates with temperature-dependent properties under thermo-electro-mechanical loading conditions. Zenkour (2010) documented the hygro-thermo-mechanical impacts on functionally graded material plates supported by elastic foundations. Bouderba et al. (2013) analyzed the thermomechanical bending behavior of functionally graded material thick plates supported by Winkler-Pasternak elastic foundations. Lee and Kim (2013) investigated the hygrothermal postbuckling behavior of functionally graded plates. Lee and Kim (2014) expanded upon prior research by examining the deterioration of thermal postbuckling characteristics of functionally graded materials in aero-hygrothermal conditions. Sobhy (2016) proposed a precise shear deformation theory for the vibration and buckling of functionally graded material sandwich plates in a hygrothermal environment. Beldjelili et al. (2016) examined the hygrothermomechanical bending of s-FGM plates supported by variable elastic foundations through a four-variable trigonometric plate theory. Barati and Shahverdi (2017) examined the aero-hygrothermal stability study of higher-order refined supersonic functionally graded material panels with both uniform and non-uniform porosity distributions. Jiammeepreecha et al. (2024) reported a comparison of FSDT and HSDT for the free vibration of functionally graded spherical and elliptical shells in the presence of nonlinear temperature distributions.

1.2.10 Free vibration behaviour of FGM Shell/Plate

Leissa (1973) conducted a seminal survey on the free vibration of shells, examining the influence of various boundary conditions and semi-vertex angles on the frequency characteristics of conical shells. Numerous researchers have studied the vibrations of homogeneous conical shells under various boundary conditions during the past three decades. Lam and Hua (1999) examined the impact of boundary conditions on the frequency characteristics of a rotating truncated circular conical shell. The vibration effects resulting from various occurrences can significantly impact the strength and safety of functionally graded shell structures. Loy et al. (1999) are pioneers in this domain, having investigated the linear vibration frequency response of a functionally graded cylindrical shell. Subsequently, other researchers examined the free vibration of functionally graded material cylindrical shells employing diverse methodologies. Significant contributions in this domain were made by Pradhan et al. (2000), Ng et al. (2001), Liew et al. (2005), Batra and Jin (2005), Najafizadeh and Isvandzibaei (2007), and Matsunaga (2009). The vibrational characteristics of FGM conical shells are less well documented in the literature compared to FGM cylindrical shells. Naj et al. (2008) investigated the thermal and mechanical instability of functionally graded truncated conical shells. Sofiyev (2009) investigated the vibrational and stability characteristics of flexibly supported functionally graded material conical shells under external pressure. Tornabene (2009) investigated the free vibration properties of functionally graded conical, cylindrical shell, and annular plate structures employing a four-parameter power-law distribution. Zhao and Liew (2011a) employed the meshless approach to ascertain the free vibration characteristics of functionally graded conical shell panels. In addition to the linear vibration analysis of functionally graded materials plates and shells, non-linear vibration analysis is also crucial for various applications of these structures. A comprehensive examination of nonlinear analysis of functionally graded materials (FGM) plates and shells is included in a book by Shen (2016).

In recent years, extensive studies have been conducted on free vibration research, encompassing a broad range of topics including various shell theories, analytical tools, methodological approaches, and diverse shell structures. It also encompasses the examination of various loading types, including the impact effect and diverse boundary conditions. Bich et al. (2011) investigated shallow spherical shells composed of functionally graded material (FGM) subjected to uniform external pressure, considering temperature effects. Su et al. (2014) introduced a thorough methodology for the vibration analysis of functionally graded cylindrical, conical shells, and annular plates under various boundary conditions, while

Kapuria et al. (2015) developed a quadrilateral shallow shell element based on third-order theory for functionally graded plates and shells, overcoming the constraints of the rule of mixtures. Beni et al. (2015) performed a free vibration analysis of size-dependent, shear-deformable, functionally graded cylindrical shells utilizing modified couple stress theory. Sofiyev (2015) investigated the vibration and stability of shear deformable functionally graded material truncated conical shells under axial loading. Sofiyev and Kuruoglu (2016) demonstrated the regions of dynamic instability in functionally graded material (FGM) conical shells subjected to time-dependent periodic loads, Sofiyev (2016) incorporated parametric vibration analysis of functionally graded material conical shells subjected to periodic lateral pressure within the context of shear deformation theory. Van (2016) performed a nonlinear axisymmetric analysis of functionally graded material shallow spherical shells with tangential edge constraints, supported by elastic foundations. In contrast, Ayoubi and Alibeigloo (2017) conducted a three-dimensional transient analysis of FGM cylindrical shells subjected to thermal and mechanical loading. Frikha et al. (2017) presented a four-node shell element for the geometrically nonlinear analysis of thin functionally graded materials plates and shells. Chen et al. (2017) examined the free vibration properties of functionally graded sandwich doubly-curved shallow shells utilizing a novel shear deformation theory that incorporates stretching effects. Han et al. (2017) conducted a vibration analysis of submerged orthogonally stiffened functionally graded material cylindrical shells. Mohammadimehr and Rostami (2018) conducted analysis on the bending and vibration of a rotating sandwich cylindrical shell, incorporating a nanocomposite core and piezoelectric layers, while accounting for thermal and magnetic fields.

1.3 OBJECTIVE AND SCOPE

The comprehensive literature review indicates that research on FGM conical shells is notably limited and sparse. Engineering analyses pertaining to this particular structural element are examined in accordance with existing literature. The objective of this research is to investigate various elements of the dynamic behavior regarding the free vibration analysis of functionally graded pretwisted conical shells. A comprehensive literature overview on shell elements, focusing on the developmental work in the domain of FGM shell structures, is presented in Section 1.2. The dynamic behavior of functionally graded conical shell structures is a promising area for investigation with applications in mechanical systems. The subsequent sub-part evaluates previous research, conducts a gap analysis, and delineates the scope of the current study, while the following section (1.4) outlines the organization of this thesis.

1.3.1 Appraisal of the Past Work

The comprehensive examination of the existing literature on pretwisted shells, within the framework of the current study, reveals the following findings:

(a) The ground-breaking study focused on the vibration properties of FGM stationary and rotational plate and shell structures. Diverse approaches were employed for the vibration analysis of functionally graded materials plates and shells, encompassing analytical, experimental, and numerical methods. The finite element method was utilized as a numerical tool in most assessments because to its adaptability, flexibility, and capacity to address complex issues while adhering to compatibility criteria and boundary conditions. A shallow FGM shell element has demonstrated significant efficacy in addressing the vibration issues of turbomachinery blades.

(b) In contrast, research on the dynamic behavior of FGM pretwisted shells has garnered significantly less focus. Three-dimensional shell components for analyzing functionally graded material shallow conical shells were constructed under the assumption that the Jacobian is independent of the linear coordinate in the thickness direction, allowing for explicit integration through the thickness.

(c) The finite element method utilized to analyze the free vibration of functionally graded material structures focused exclusively on three-noded and six-noded triangular plate finite elements, employing the Ritz method, Galerkin's method, and exact solution techniques to ascertain the natural frequencies of stationary FGM shells. Research on rotating pretwisted functionally graded shells is scarce in the available literature. The influence of rotational speeds on natural frequencies was examined just for composite cylindrical shells/plates within a moderate rotational speed range. Very few analyses have been conducted on rotating pretwisted FGM conical shells without porosity.

(d) A comprehensive and thorough investigation on shells was conducted for both steady-state and transient responses, however it was restricted to composite and functionally graded materials (FGM) plates, excluding conical shells and porosity. No studies have been conducted regarding the dynamic analysis of pretwisted functionally graded porous conical shells in thermal environment, which could be modeled as turbomachinery blades.

(e) Most of the studies listed in literature review analysed the free vibration of rotating pretwisted FGM shells considering FSDT or polynomial HSDT. Few non-polynomial HSDT analyses are restricted to only isotropic and composite shells/plates.

1.3.2 Research Gaps Identified

The primary method for assessing FGM structure should be macro-mechanical, treating each layer as homogeneous. Following the analysis of the fundamental behavior of FGM structures, a micro-mechanical investigation should be undertaken to select appropriate FGM laws with accurate graded material property indices for their intended applications. The macro-mechanical analysis should be prioritized to evaluate the dynamic behavior of functionally graded material pretwisted cantilevered shallow conical shells. To achieve dynamic behavior, it is necessary to address the research gaps found in the review of existing literature.

There has been much research on the free vibration response of functionally graded conical shells, but no studies that account for the porosity and rotating nature of the FG pretwisted conical shell in thermal environment have been reported so far. This challenge has been taken into account using a finite element approach based on polynomial and non-polynomial HSDT to find a free vibration solution. Different functionally graded conical shells (p-FGM, e-FGM, s-FGM and BDFGM) are incorporated with porosities under nonlinear temperature distributions, which will make the study more idealized with the practical scenario.

1.3.3 Scope of the Present Work

The comprehensive evaluation of current accessible literature clearly demonstrates that research on FGM pretwisted shells is incomplete, revealing significant opportunities for further investigation, especially in the domain of dynamic studies of FGM conical shells. A systematic research must be conducted from an engineering perspective. This work aims to investigate certain problem areas to enhance the understanding of the dynamic behavior of pretwisted functionally graded material conical shells. The current study delineates its focus to address the highlighted gaps in the existing literature. The current investigation examines the free vibration behaviour of cantilever porous functionally graded conical shell structures subjected to nonlinear temperature distribution.

(a) A shallow conical shell element is configured in a trapezoidal plan form. The turbomachinery blades can be effectively and precisely represented as pretwisted shallow conical shells to accommodate their geometric complexity. The nonlinear temperature distribution across the thickness is assessed using the one-dimensional Fourier heat conduction equation. The generalized dynamic equilibrium equation is obtained from Lagrange's equation of motion, excluding the Coriolis effect for modest rotational speeds. The study utilizes an eight-noded isoparametric shell element, accounting for transverse shear deformation and

rotating inertia in accordance with FSDT and HSDT theories. The layer of the shell structure in the thickness direction is modeled by altering the composition of the FGM constituents (ceramic and metal) according to various FGM constituent rules. The numerical analyses are executed using the simple power, sigmoidal, exponential and bidirectional law for the gradation of functionally graded conical shell considering even and uneven porosity distribution.

(b) Rotating pretwisted conical shells with a low aspect ratio can be modeled as turbomachinery blades. To guarantee the compatibility of deformation and the equilibrium of consequent forces and moments, a layer-wise isotropic material property is utilized for the computation of the element stiffness matrices. The QR iteration approach is employed to address the conventional eigenvalue problem. A finite element-based computational method is employed to examine the dynamic analysis of pretwisted and tapered functionally graded material conical shells, disregarding the Coriolis effect at moderate rotational speeds. Parametric studies are conducted to derive non-dimensional natural frequencies of functionally graded material (FGM) conical shells, taking into account key parameters such as temperature distribution, twist angles, rotational velocities, taper ratio and the gradation index of material properties across various FGM constituent laws (p-FGM, e-FGM, s-FGM and BDFGM).

(c) An in-house computer code has been created utilizing the current finite element formulation, which has been validated against benchmark published results from the open literature. Numerical solutions are derived for the dynamic analysis of pretwisted functionally graded shallow conical shells concerning their free vibration characteristics. The findings of free vibration analysis of twisted and tapered rotating functionally graded conical shells under thermal environment are compared based on various FGM constituent laws. The distorted mode shapes for each vibrational scenario are provided, along with appropriate reasons.

(d) The findings are thoroughly analyzed, including the impact of primary design parameters on the dynamic behavior of pretwisted and tapered functionally graded rotating conical shells. A series of important results are provided based on key identification and critical discussion. The potential for future study in this domain is also discussed.

1.4 ORGANIZATION OF THE THESIS

This thesis contains of six chapters. The initial chapter provides a comprehensive introduction to FG pretwisted shells, emphasizing their significance concerning free vibration and finite element methodology. This chapter provides a comprehensive survey of the current literature,

focusing on shell theories, shell geometries, dynamic studies of shells, analytical methods, application of thermal environment and porous FGM structures. The scope of the current work is delineated in Chapter 1, informed by a literature review, evaluation of previous research, and gap analysis.

Chapter 2 contains the theoretical formulation employed for the present analyses. The basic elastic equations of FGM conical shell model are discussed, followed by the derivation of governing equations for FGM shell material for different types (p-FGM, e-FGM, s-FGM and BDFGM) of porous FGM structures. The kinematics of the conical shell element is derived based on polynomial and non-polynomial higher order shear deformation theories. The finite element model is based on Lagrange's equation of motion neglecting the Coriolis effect for moderate rotational speeds. An eight noded isoparametric quadratic shell element is employed in the finite element formulation. The standard eigenvalue problem is solved by applying the QR iteration algorithm.

Chapter 3 deals with the free vibration response of rotating pretwisted functionally graded (FG) conical shells under nonlinear temperature distributions, utilizing a finite element method for potential application in turbomachinery blades. The pretwisted conical shell is functionally graded in its transverse direction using power, exponential, and sigmoid laws. The distribution of both even and uneven porosity is examined. The one-dimensional Fourier heat conduction equation is employed to evaluate the nonlinear temperature distribution along the thickness of the functionally graded conical shell. Lagrange's equation is employed to get the dynamic equation of motion for the rotating pretwisted functionally graded conical shell. The suggested finite element model utilizes an eight-noded isoparametric shell element, featuring seven degrees of freedom per node. The influence of several parameters, such as porosity, temperature, twist angle, and rotational speed on the free vibration response of the FG porous conical shell has been examined. The results indicate that the porosity volume fraction substantially affects the natural frequency. The nonlinear temperature difference and pretwist angle both lead to a drop in stiffness of the FG conical shell with an increase, whereas the presence of rotational speed induces geometrical stiffness, resulting in centrifugal stiffening.

Chapter 4 presents the fundamental frequency of a rotating cantilevered porous functionally graded (FG) twisted conical shell with varying thickness along the longitudinal direction is calculated using a trigonometric higher-order shear deformation theory under thermal loading. Finite element method is employed for this purpose. The shell is discretized using eight-noded

isoparametric shell elements with seven degrees of freedom per node. Using a simple power law across the transverse direction, the temperature-dependent material properties of the FG shell are determined. The nonlinear temperature distribution across the thickness direction is calculated using the one-dimensional Fourier heat conduction equation. The dynamic equation of motion is derived using Lagrange's equation. Finally, a parametric investigation of the effects of taper ratio, porosity, pretwist angle, temperature, and rotational speed on the fundamental frequency of the porous FG rotating conical shell is performed. It is also discussed how such characteristics affect mode shapes.

A mathematical model based on trigonometric or non-polynomial higher order shear deformation theory for evaluating the free vibration of rotating porous bidirectional functionally graded conical shell with longitudinally tapered thickness is presented in Chapter 5. The FG conical shell consisting one ceramic and two metal constituents are graded through both the thickness and longitudinal directions following power-law distribution. A finite element method (FEM) is introduced to discretise the conical shell in eight-noded isoparametric elements having seven degrees of freedom at each node. The one-dimensional steady-state heat conduction equation of Fourier is used to assess the nonlinear temperature distribution across the thickness. Lagrange's equation is applied to kinetic and potential energy based formulations to derive the governing equation of motion of the cantilevered FG conical shell. The results are validated with the available benchmark publications and the convergence study is also reported to establish the exactitude of the model. A parametric study is presented to analyse the effect of porosity, power-law indexes, top surface temperature, pretwist angle, taper ratio and rotational speed on the fundamental frequency. Moreover, mode shapes are developed to illustrate the mode-switching phenomenon under the impact of aforementioned parameters.

Chapter 6 systematically enumerates the significant results derived from the current investigation. The primary contribution of this thesis is enumerated. The potential for future research concerning current issues and associated problem areas is also outlined.

The list of references used in the current thesis is presented at the end. A flowchart of the computational procedure adopted is given in Appendix.

CHAPTER 2
THEORETICAL FORMULATION

2.1 INTRODUCTION

In this chapter a detailed theoretical formulation and solution techniques based on finite element method for the present analysis are provided. The basic elastic equations, relevant equations of conical shell model and the derivation of governing equations for the free vibration problems are outlined. The governing equations for different FGM constituent laws along with different porosity factors are portrayedThe one-dimensional Fourier heat conduction equation is employed to evaluate the nonlinear temperature distribution along the thickness of the functionally graded conical shell. Lagrange's equation is utilized to get the dynamic equation of motion for the rotating pretwisted functionally graded conical shell. The suggested finite element model utilizes an eight-noded isoparametric shell element, featuring seven degrees of freedom per node. This study uses a non-polynomial higher-order shear deformation theory to calculate the fundamental frequency of a rotating cantilevered porous functionally graded (FG) conical shell with variable thickness.

2.2 GEOMETRY OF CONICAL SHELL

Figure 2.1 shows an untwisted functionally graded (FG) shallow conical shell with the following dimensions: length L, cone length s, reference width b_0, vertex angle ϕ_v, and base subtended angle ϕ_0. The shallow conical shell's cross-section is thought to be an ellipse and have reference major and minor radii of β_0 and α_0, respectively.

The equation of the ellipse at any cross-section is expressed as

$$\left(\frac{y}{\alpha}\right)^2 + \left(\frac{y+\beta}{\beta}\right)^2 = 1 \tag{2.1}$$

where β and α are the major and minor radii.

The radii of curvature along the x and y direction are denoted by r_x and r_y, respectively. It is clear from the Figure 2.1 that span-wise curvature r_x is infinity and chord-wise curvature $r_y(x, y)$ is a function of x and y. According to Liew et al. (1994)**,** the chord-wise curvature $r_y(x, y)$ can be expressed as

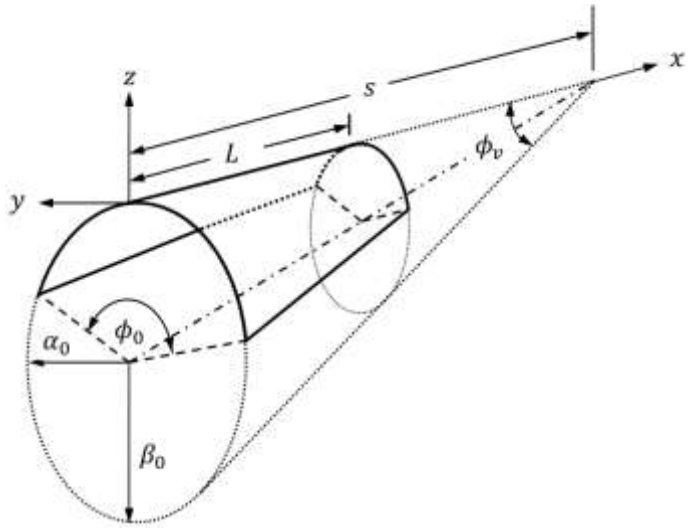

Figure 2.1 Conical shell geometry derived from a cone.

$$r_y = \frac{\left[1+\left(\frac{dz}{dy}\right)^2\right]^{3/2}}{\frac{d^2z}{dy^2}} = \alpha^2\beta^2\left[\frac{1}{\beta^2}+\frac{y^2}{\alpha^2}\left(\frac{1}{\alpha^2}-\frac{1}{\beta^2}\right)\right]^{3/2} \tag{2.2}$$

$$= s\left(\frac{\alpha}{s}\right)^2\left(\frac{\beta}{s}\right)^2\left\{\left(\frac{s}{\beta}\right)^2+\left(\frac{y}{b_0}\right)^2\left(\frac{b_0}{s}\right)^2\left(\frac{s}{\alpha}\right)^2\left[\left(\frac{s}{\alpha}\right)^2-\left(\frac{s}{\beta}\right)^2\right]\right\}^{3/2}$$

where

$$\frac{\alpha}{s} = \frac{\left(\frac{b}{s}\right)\left(\frac{\beta}{s}\right)\tan\left(\frac{\phi_0}{2}\right)}{\sqrt{4\left(\frac{\beta}{s}\right)^2\tan^2\left(\frac{\phi_0}{2}\right)-\left(\frac{b}{s}\right)^2}} \tag{2.3}$$

$$\frac{\beta}{s} = \tan\left(\frac{\phi_v}{2}\right)\left[1-\frac{x}{s}\right] \tag{2.4}$$

$$\frac{b}{s} = \left(\frac{b_0}{s}\right)\left[1-\frac{x}{s}\right] \tag{2.5}$$

$$\frac{b_0}{s} = 2\sin\left(\frac{\phi_v}{2}\right)\sqrt{\frac{\tan^2\left(\frac{\phi_0}{2}\right)}{\cos^2\left(\frac{\phi_v}{2}\right)+\tan^2\left(\frac{\phi_0}{2}\right)}} \tag{2.6}$$

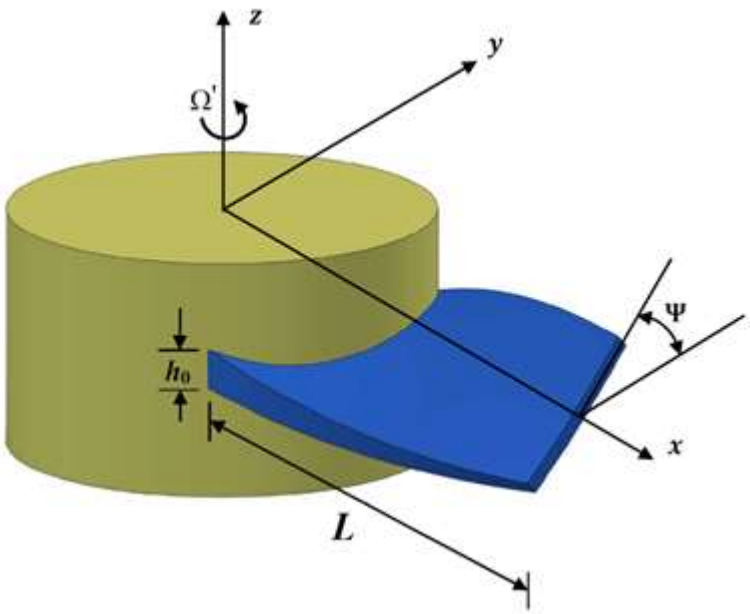

Figure 2.2 The coordinate system position of a tapered pretwisted conical shell.

Figure 2.2 displays the pretwisted rotating FG shallow conical shell with reference width b_0, pretwist angle Ψ, and rotational speed Ω'. The mid-surface of the pretwisted shallow conical shell is defined by

$$z = -\frac{1}{2}\left\{\frac{2xy}{r_{xy}} + \frac{y^2}{r_y}\right\} \tag{2.7}$$

where r_{xy} represents the twisted radius of curvature and can be expressed in terms of span length L and pretwist angle Ψ as given by

$$r_{xy} = -\frac{L}{\tan\Psi} \tag{2.8}$$

The conical shell thickness at a distance *x* from the fixed end is given by

$$h = h_0\left(1 - C_r\frac{x}{L}\right) \tag{2.9}$$

where C_r is the tapper ratio and h_0 is the fixed end thickness.

2.3 MATERIAL PROPERTIES OF POROUS FGM

The conical shells being discussed in this study are formed of both metal and ceramic elements. The distribution of metal and ceramic elements inside the shell's thickness adheres to a straightforward power law. Materials that exhibit a functional gradient, where the constituents are graded based on a simple power law, are sometimes referred to as power-law functionally

graded materials (p-FGM). The material properties of the FG conical shell exhibit a consistent variation pattern, adhering to a power law distribution. The conical shell of the FG material exhibits varying thickness and is characterized by its integrated porosity. The presence of porosity can be observed through two distinct patterns: an even distribution of porosity and an uneven distribution of porosity. Figure 2.3 illustrates the two forms of porosity distributions for the purpose of facilitating comprehension.

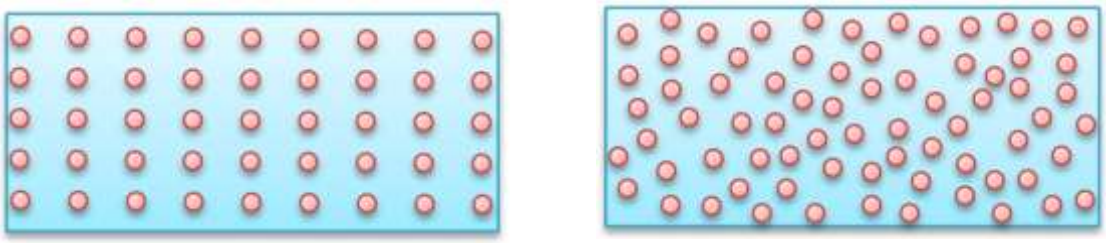

(a) (b)

Figure 2.3 Porosity representation in FG conical shells: (a) Even porosity (b) Uneven porosity

2.3.1 Equations for p-FGM

The FGM shells are composed of two distinct sections, the outer or top half, which contains a ceramic-rich material, and the inner or bottom half, which contains a metal-rich material. This design is based on the specific properties of each component. The ceramic material is utilized for shielding purposes, while the metallic material is chosen for its ability to withstand the core portion. In general, the thickness is partitioned into distinct layers, with the uppermost surface consisting entirely of ceramic material and the lower surface composed entirely of metal. The volume percentage and material qualities exhibit variations due to the presence of different layers, as dictated by various governing principles. The current study utilizes three distinct laws: the simple power law, the exponential law, and the sigmoid law in its formulation. The parameters of Young's modulus (E), thermal expansion coefficient (α_t), and Poisson's ratio (υ) exhibit dependence on both spatial location and temperature. The material properties, such as mass density (ρ) and thermal conductivity (K), are solely contingent upon the layer's position.

The volume fractions and their distributions of the metal and ceramic constituents can be evaluated from the following relations

$$V_c + V_m = 1 \tag{2.10}$$

$$V_c = \left(\frac{z}{h} + \frac{1}{2}\right)^N \tag{2.11}$$

where V_c is the volume fraction of ceramic, V_m is the volume fraction of metal, h is the thickness of the conical shell, z is the distance in z-axis, N is the power-law index, a positive real number that ranges from zero to infinity.

The effective material properties(P_{eff}) of the shallow FG conical shell are expressed by the equation

$$P_{eff}(z,T) = P_m(T) + [P_c(T) - P_m(T)]\left(\frac{z}{h} + \frac{1}{2}\right)^N \tag{2.12}$$

where P_m and P_c are the material properties of metal and ceramic, respectively and both will be the function of temperature in case the property is Young's modulus, Poisson's ratio and thermal expansion coefficient.

When accounting for the porosity factor resulting from various manufacturing implications inherent in the FGM production process, it is essential to consider the effective material properties that incorporate this porosity component. Here two types of porosity distribution i.e. even and uneven have been considered for getting very close realistic approach. The effective material properties, accounting for an even porosity distribution, are derived using the power law distribution and are articulated as follows

$$P_{eff}(z,T) = P_m(T) + [P_c(T) - P_m(T)]\left(\frac{z}{h} + \frac{1}{2}\right)^N - \frac{\alpha_p}{2}\left(P_c(T) + P_m(T)\right) \tag{2.13}$$

When considering uneven porosity distribution, the effective material properties can be articulated as follows.

$$P_{eff}(z,T) = P_m(T) + [P_c(T) - P_m(T)]\left(\frac{z}{h} + \frac{1}{2}\right)^N - \frac{\alpha_p}{2}\left(P_c(T) + P_m(T)\right)\left(1 - \frac{2\,|\,z\,|}{h}\right) \tag{2.14}$$

where α_p denotes the volume fraction of porosities.

The temperature-dependent properties (Young's modulus, Poisson's ratio and thermal expansion coefficient) of ceramic and metal are computed as

$$P_c(T) = P_0(P_{-1}T^{-1} + 1 + P_1T + P_2T^2 + P_3T^3) \tag{2.15}$$

$$P_m(T) = P_0(P_{-1}T^{-1} + 1 + P_1T + P_2T^2 + P_3T^3) \tag{2.16}$$

where P_i ($i = -1, 0, 1, 2, 3$) are temperature-dependent coefficients and their values are different for metal and ceramic.

For a FG pretwisted evenly porous conical shell panel, the change in temperature across the thickness is not uniform, for getting more realistic consequence this temperature distribution has been considered as nonlinear. So the relation of temperature distribution through the thickness of the FG conical shell can be derived by solving the steady-state heat conduction equation of Fourier.

$$-\frac{d}{dz}\left[K(z)\frac{dT}{dz}\right] = 0 \tag{2.17}$$

where

$$K(z) = K_m + [K_c - K_m]\left(\frac{z}{h} + \frac{1}{2}\right)^N - \frac{\alpha_p}{2}(K_c + K_m) \tag{2.18}$$

Using Eq. (2.18) to solve Eq. (2.17) and applying the boundary conditions $T = T_m$ at $z = -h/2$ and $T = T_c$ at $z = h/2$, the equation of temperature distribution is derived as follows

$$\begin{aligned} T(z) = T_m + \frac{\Delta T}{F}\Bigg[&\left(\frac{z}{h} + \frac{1}{2}\right) - \frac{K_{cm}}{(N+1)K_m}\left(\frac{z}{h} + \frac{1}{2}\right)^{(N+1)} \\ &+ \frac{{K_{cm}}^2}{(2N+1){K_m}^2}\left(\frac{z}{h} + \frac{1}{2}\right)^{(2N+1)} - \frac{{K_{cm}}^3}{(3N+1){K_m}^3}\left(\frac{z}{h} + \frac{1}{2}\right)^{(3N+1)} \\ &+ \frac{{K_{cm}}^4}{(4N+1){K_m}^4}\left(\frac{z}{h} + \frac{1}{2}\right)^{(4N+1)} - \frac{{K_{cm}}^5}{(5N+1){K_m}^5}\left(\frac{z}{h} + \frac{1}{2}\right)^{(5N+1)}\Bigg] \\ &- \frac{\alpha_p}{2}(T_c + T_m) \end{aligned} \tag{2.19}$$

where, $K_{cm} = K_c - K_m$, $\Delta T = T_c - T_m$ and

$$F = 1 - \frac{K_{cm}}{(N+1)K_m} + \frac{{K_{cm}}^2}{(2N+1){K_m}^2} - \frac{{K_{cm}}^3}{(3N+1){K_m}^3} + \frac{{K_{cm}}^4}{(4N+1){K_m}^4} - \frac{{K_{cm}}^5}{(5N+1){K_m}^5}$$

Similarly, for uneven porosity distribution the equation for temperature distribution will be

$$T(z) = T_m + \frac{\Delta T}{F}\left[\left(\frac{z}{h}+\frac{1}{2}\right) - \frac{K_{cm}}{(N+1)K_m}\left(\frac{z}{h}+\frac{1}{2}\right)^{(N+1)} + \frac{{K_{cm}}^2}{(2N+1){K_m}^2}\left(\frac{z}{h}+\frac{1}{2}\right)^{(2N+1)} - \frac{{K_{cm}}^3}{(3N+1){K_m}^3}\left(\frac{z}{h}+\frac{1}{2}\right)^{(3N+1)} + \frac{{K_{cm}}^4}{(4N+1){K_m}^4}\left(\frac{z}{h}+\frac{1}{2}\right)^{(4N+1)} - \frac{{K_{cm}}^5}{(5N+1){K_m}^5}\left(\frac{z}{h}+\frac{1}{2}\right)^{(5N+1)}\right] - \frac{\alpha_p}{2}(T_c+T_m)\left(1-\frac{2\,|\,z\,|}{h}\right) \tag{2.20}$$

2.3.2 Equations for e-FGM

According to exponential function, the variation of the effective material properties across the thickness of the pretwisted shallow FG conical shell is expressed as

$$P_{eff}(z,T) = P_m(T)e^{\frac{1}{h}\left(ln\frac{P_c(T)}{P_m(T)}\right)\left(z+\frac{h}{2}\right)} - \frac{\alpha_p}{2}\left(P_c(T)+P_m(T)\right) \tag{2.21}$$

where P_m and P_c are the material properties of metal and ceramic respectively and both are functions of temperature, h is the thickness of the conical shell, z is the distance in z-axis and α is the volume fraction of porosities.

Here the temperature dependent material properties (E, υ and α_t) will follow the same relations as Eq. (2.15) and Eq. (2.16)

The equation of thermal conductivity for e-FGM will be

$$K(z) = K_m e^{\frac{1}{h}\left(ln\frac{K_c}{K_m}\right)\left(z+\frac{h}{2}\right)} = K_m e^{\left(ln\frac{K_c}{K_m}\right)\left(\frac{z}{h}+\frac{1}{2}\right)} = K_m\left(\frac{K_c}{K_m}\right)^{\left(\frac{z}{h}+\frac{1}{2}\right)} \tag{2.22}$$

Putting this relation to the one-dimensional Fourier heat conduction equation, one can get

$$-\frac{d}{dz}\left[K(z)\frac{dT}{dz}\right] = 0 \tag{2.23}$$

Putting the value of $K(z)$ in Eq. (2.23)

$$\frac{d}{dz}\left[K_m\left(\frac{K_c}{K_m}\right)^{\left(\frac{z}{h}+\frac{1}{2}\right)}\frac{dT}{dz}\right] = 0 \tag{2.24}$$

By simplifying Eq. (2.24)

$$K_m ln\left(\frac{K_c}{K_m}\right)\left(\frac{K_c}{K_m}\right)^{\left(\frac{z}{h}+\frac{1}{2}\right)}\frac{1}{h}\frac{dT}{dz}+K_m\left(\frac{K_c}{K_m}\right)^{\left(\frac{z}{h}+\frac{1}{2}\right)}\frac{d^2T}{dz^2}=0$$

$$K_m\left(\frac{K_c}{K_m}\right)^{\left(\frac{z}{h}+\frac{1}{2}\right)}\left[ln\left(\frac{K_c}{K_m}\right)\frac{1}{h}\frac{dT}{dz}+\frac{d^2T}{dz^2}\right]=0$$

$$\frac{d^2T}{dz^2}+\frac{1}{h}ln\left(\frac{K_c}{K_m}\right)\frac{dT}{dz}=0 \tag{2.25}$$

After solving the above differential equation (2.25), the expression of temperature distribution

$$T=c_1e^{0.z}+c_2e^{-\beta z}=c_1+c_2e^{-\frac{1}{h}ln\left(\frac{K_c}{K_m}\right)z} \tag{2.26}$$

Applying boundary conditions $T = T_m$ at $z=-h/2$ and $T = T_c$ at $z=h/2$, one can get

$$T_m=c_1+c_2e^{\frac{1}{2}ln\left(\frac{K_c}{K_m}\right)} \tag{2.27}$$

$$\text{and } T_c=c_1+c_2e^{-\frac{1}{2}ln\left(\frac{K_c}{K_m}\right)} \tag{2.28}$$

From Eq. (2.27) and (2.28), the values of c_1 and c_2 are derived as follows

$$c_2=\frac{T_m-T_c}{\sqrt{\frac{K_c}{K_m}}-\sqrt{\frac{K_m}{K_c}}}=\frac{T_m-T_c}{\sqrt{\frac{K_c}{K_m}}\left(1-\frac{K_m}{K_c}\right)} \tag{2.29}$$

$$\text{and, } c_1=T_m-\frac{T_m-T_c}{\sqrt{\frac{K_c}{K_m}}-\sqrt{\frac{K_m}{K_c}}}\sqrt{\frac{K_c}{K_m}}=T_m-\frac{T_m-T_c}{1-\frac{K_m}{K_c}}=\frac{T_c-T_m\left(\frac{K_m}{K_c}\right)}{1-\frac{K_m}{K_c}} \tag{2.30}$$

Putting the values of c_1 and c_2

$$T=c_1+c_2e^{-\frac{1}{h}ln\left(\frac{K_c}{K_m}\right)z}=\frac{T_c-T_m\left(\frac{K_m}{K_c}\right)}{1-\frac{K_m}{K_c}}+\frac{T_m-T_c}{\sqrt{\frac{K_c}{K_m}}\left(1-\frac{K_m}{K_c}\right)}e^{\frac{z}{h}ln\left(\frac{K_m}{K_c}\right)}$$

$$=\frac{T_c-T_m\left(\frac{K_m}{K_c}\right)}{1-\frac{K_m}{K_c}}+\frac{T_m-T_c}{\left(1-\frac{K_m}{K_c}\right)}\left(\frac{K_m}{K_c}\right)^{\left(\frac{z}{h}+\frac{1}{2}\right)} \tag{2.31}$$

Thus considering porosity the equation of thermal conductivity for e-FGM pretwisted shallow conical shell will be

$$K(z) = K_m \left(\frac{K_c}{K_m}\right)^{\left(\frac{z}{h}+\frac{1}{2}\right)} - \frac{\alpha_p}{2}(K_c + K_m) \tag{2.32}$$

where α_p is the volume fraction of porosities in even and uneven distribution.

So, the equation for temperature distribution for a pretwisted evenly porous shallow conical shell will take the form from Eq. (2.31)

$$T = \frac{T_c - T_m\left(\frac{K_m}{K_c}\right)}{1-\frac{K_m}{K_c}} + \frac{T_m - T_c}{\left(1-\frac{K_m}{K_c}\right)}\left(\frac{K_m}{K_c}\right)^{\left(\frac{z}{h}+\frac{1}{2}\right)} - \frac{\alpha_p}{2}(T_c + T_m) \tag{2.33}$$

Similarly for uneven porosity distribution the equation for temperature distribution will be

$$T = \frac{T_c - T_m\left(\frac{K_m}{K_c}\right)}{1-\frac{K_m}{K_c}} + \frac{T_m - T_c}{\left(1-\frac{K_m}{K_c}\right)}\left(\frac{K_m}{K_c}\right)^{\left(\frac{z}{h}+\frac{1}{2}\right)} - \frac{\alpha_p}{2}(T_c + T_m)\left(1 - \frac{2\,|\,z\,|}{h}\right) \tag{2.34}$$

2.3.3 Equations for s-FGM

In power law FGM, the volume fraction of any of the constituents in the conical shell element vary with the change of power law index but in case of sigmoid FGM the volume fraction only changes in different layers with the change of power law index but the overall volume fraction in the entire shell element always remains equally distributed. That is why for the purpose of realising the smooth distribution of stresses Chi and Chung (2002), proposed this functionally graded material where the distribution of ceramic and metal constituents take place according to the sigmoid law. Here the volume fraction index of upper half ($\frac{h}{2} > z > 0$) and bottom half ($0 > z > -h/2$) are governed by two different equations. The volume fractions of ceramic in different layers are expressed by the following equations.

$$V_{c1}(z) = 1 - \frac{1}{2}\left(1 - \frac{2z}{h}\right)^N \text{ for } 0 \le z \le h/2 \tag{2.35a}$$

$$V_{c2}(z) = \frac{1}{2}\left(1 + \frac{2z}{h}\right)^N \quad \text{for } -h/2 \le z \le 0 \tag{2.35b}$$

where $V_{c1}(z)$ denotes the volume fraction of ceramic from top surface to middle surface whereas $V_{c2}(z)$ denotes from middle surface to bottom surface, h is the thickness of the conical shell, z is the distance in z-axis and N is the power-law index, a positive real number that ranges from zero to infinity.

Both these Eq. (2.35a) and Eq. (2.35b) also satisfies Eq. (2.10) i.e. $Vc + Vm = 1$.

The effective material properties will also vary followed by two different equations for the top half and bottom half respectively. For a pretwisted porous shallow conical shell having even porosity distribution these equations of effective material properties will be

$$P_{eff}(z,T) = P_m(T) + \left(P_c(T) - P_m(T)\right)\left[1 - \frac{1}{2}\left(1 - \frac{2z}{h}\right)^N\right] - \frac{\alpha_p}{2}\left(P_c(T) + P_m(T)\right) \quad \text{for } 0 \le z \le h/2 \tag{2.36a}$$

$$P_{eff}(z,T) = P_m(T) + \left(P_c(T) - P_m(T)\right)\left[\frac{1}{2}\left(1 + \frac{2z}{h}\right)^N\right] - \frac{\alpha_p}{2}\left(P_c(T) + P_m(T)\right) \quad \text{for } -h/2 \le z \le 0 \tag{2.36b}$$

where P_m and P_c are the material properties of metal and ceramic, respectively and both are the functions of temperature and α_p is the volume fraction of porosities.

Similarly for uneven porosity distribution the equations for effective material properties will be

$$P_{eff}(z,T) = P_m(T) + \left(P_c(T) - P_m(T)\right)\left[1 - \tfrac{1}{2}\left(1 - \tfrac{2z}{h}\right)^N\right] - \tfrac{\alpha_p}{2}\left(P_c(T) + P_m(T)\right)\left(1 - \tfrac{2|z|}{h}\right) \quad \text{for } 0 \le z \le h/2 \tag{2.37a}$$

$$P_{eff}(z,T) = P_m(T) + \left(P_c(T) - P_m(T)\right)\left[\frac{1}{2}\left(1 + \frac{2z}{h}\right)^N\right] - \frac{\alpha_p}{2}\left(P_c(T) + P_m(T)\right)\left(1 - \frac{2\,|\,z\,|}{h}\right) \quad \text{for } -h/2 \le z \le 0 \tag{2.37b}$$

Here the temperature dependent material properties (E, υ and α_t) will follow the same relations as Eq. (2.15) and Eq. (2.16)

The equations of thermal conductivity of s-FGM for evenly porous distribution will be

$$K(z) = K_m + (K_c - K_m)\left[1 - \tfrac{1}{2}\left(1 - \tfrac{2z}{h}\right)^N\right] - \tfrac{\alpha_p}{2}(K_c + K_m) \quad \text{for } 0 \le z \le h/2 \tag{2.38a}$$

$$K(z) = K_m + (K_c - K_m)\left[\tfrac{1}{2}\left(1 + \tfrac{2z}{h}\right)^N\right] - \tfrac{\alpha_p}{2}(K_c + K_m) \quad \text{for } -h/2 \le z \le 0 \tag{2.38b}$$

After solving the one-dimensional Fourier heat conduction Eq. (2.17), the equation of temperature distribution will be as follows

$$T(z) = T_m + \frac{\Delta T}{F}\left[\left(1 - \frac{1}{2}\left(1 - \frac{2z}{h}\right)^N\right) - \frac{K_{cm}}{(N+1)K_m}\left(1 - \frac{1}{2}\left(1 - \frac{2z}{h}\right)^{(N+1)}\right)\right.$$
$$+ \frac{{K_{cm}}^2}{(2N+1){K_m}^2}\left(1 - \frac{1}{2}\left(1 - \frac{2z}{h}\right)^{(2N+1)}\right)$$
$$- \frac{{K_{cm}}^3}{(3N+1){K_m}^3}\left(1 - \frac{1}{2}\left(1 - \frac{2z}{h}\right)^{(3N+1)}\right)$$
$$+ \frac{{K_{cm}}^4}{(4N+1){K_m}^4}\left(1 - \frac{1}{2}\left(1 - \frac{2z}{h}\right)^{(4N+1)}\right)$$
$$\left. - \frac{{K_{cm}}^5}{(5N+1){K_m}^5}\left(1 - \frac{1}{2}\left(1 - \frac{2z}{h}\right)^{(5N+1)}\right)\right] - \frac{\alpha_p}{2}(T_c + T_m)$$

for $0 \le z \le h/2$ (2.39a)

$$T(z) = T_m + \frac{\Delta T}{F}\left[\left(\frac{1}{2}\left(1 + \frac{2z}{h}\right)^N\right) - \frac{K_{cm}}{(N+1)K_m}\left(\frac{1}{2}\left(1 + \frac{2z}{h}\right)^{(N+1)}\right)\right.$$
$$+ \frac{{K_{cm}}^2}{(2N+1){K_m}^2}\left(\frac{1}{2}\left(1 + \frac{2z}{h}\right)^{(2N+1)}\right)$$
$$- \frac{{K_{cm}}^3}{(3N+1){K_m}^3}\left(\frac{1}{2}\left(1 + \frac{2z}{h}\right)^{(3N+1)}\right)$$
$$+ \frac{{K_{cm}}^4}{(4N+1){K_m}^4}\left(\frac{1}{2}\left(1 + \frac{2z}{h}\right)^{(4N+1)}\right)$$
$$\left. - \frac{{K_{cm}}^5}{(5N+1){K_m}^5}\left(\frac{1}{2}\left(1 + \frac{2z}{h}\right)^{(5N+1)}\right)\right] - \frac{\alpha_p}{2}(T_c + T_m)$$

(2.39b)

for $-h/2 \le z \le 0$

Similarly for uneven porosity distribution the equation for temperature distribution will be

$$T(z) = T_m + \frac{\Delta T}{F}\left[\left(1 - \frac{1}{2}\left(1 - \frac{2z}{h}\right)^{N}\right) - \frac{K_{cm}}{(N+1)K_m}\left(1 - \frac{1}{2}\left(1 - \frac{2z}{h}\right)^{(N+1)}\right)\right.$$
$$+ \frac{{K_{cm}}^2}{(2N+1){K_m}^2}\left(1 - \frac{1}{2}\left(1 - \frac{2z}{h}\right)^{(2N+1)}\right)$$
$$- \frac{{K_{cm}}^3}{(3N+1){K_m}^3}\left(1 - \frac{1}{2}\left(1 - \frac{2z}{h}\right)^{(3N+1)}\right)$$
$$+ \frac{{K_{cm}}^4}{(4N+1){K_m}^4}\left(1 - \frac{1}{2}\left(1 - \frac{2z}{h}\right)^{(4N+1)}\right)$$
$$\left. - \frac{{K_{cm}}^5}{(5N+1){K_m}^5}\left(1 - \frac{1}{2}\left(1 - \frac{2z}{h}\right)^{(5N+1)}\right)\right]$$
$$- \frac{\alpha_p}{2}(T_c + T_m)\left(1 - \frac{2 \mid z \mid}{h}\right)$$

for $0 \le z \le h/2$ (2.40a)

$$T(z) = T_m + \frac{\Delta T}{F}\left[\left(\frac{1}{2}\left(1 + \frac{2z}{h}\right)^{N}\right) - \frac{K_{cm}}{(N+1)K_m}\left(\frac{1}{2}\left(1 + \frac{2z}{h}\right)^{(N+1)}\right)\right.$$
$$+ \frac{{K_{cm}}^2}{(2N+1){K_m}^2}\left(\frac{1}{2}\left(1 + \frac{2z}{h}\right)^{(2N+1)}\right)$$
$$- \frac{{K_{cm}}^3}{(3N+1){K_m}^3}\left(\frac{1}{2}\left(1 + \frac{2z}{h}\right)^{(3N+1)}\right)$$
$$+ \frac{{K_{cm}}^4}{(4N+1){K_m}^4}\left(\frac{1}{2}\left(1 + \frac{2z}{h}\right)^{(4N+1)}\right)$$
$$\left. - \frac{{K_{cm}}^5}{(5N+1){K_m}^5}\left(\frac{1}{2}\left(1 + \frac{2z}{h}\right)^{(5N+1)}\right)\right] - \frac{\alpha}{2}(T_c + T_m)\left(1 - \frac{2 \mid z \mid}{h}\right)$$

for $-h/2 \le z \le 0$ (2.40b)

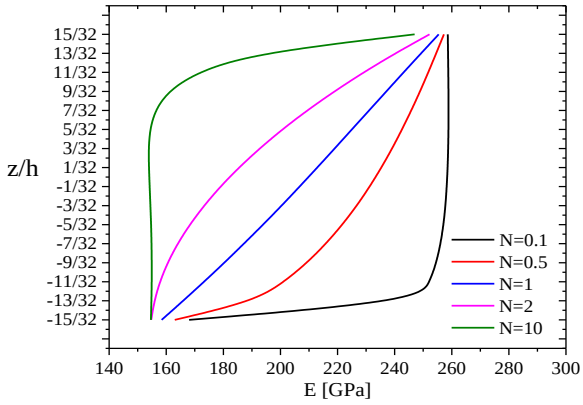

(a) p-FGM with even porosity

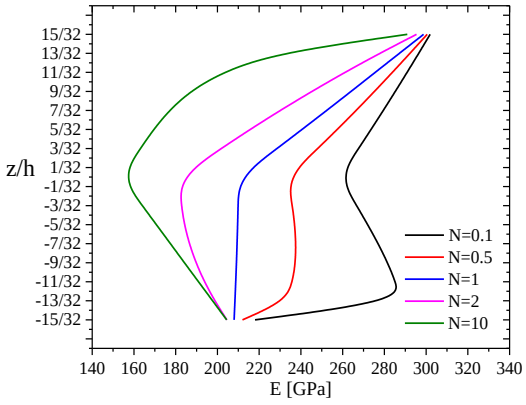

(b) p-FGM with uneven porosity

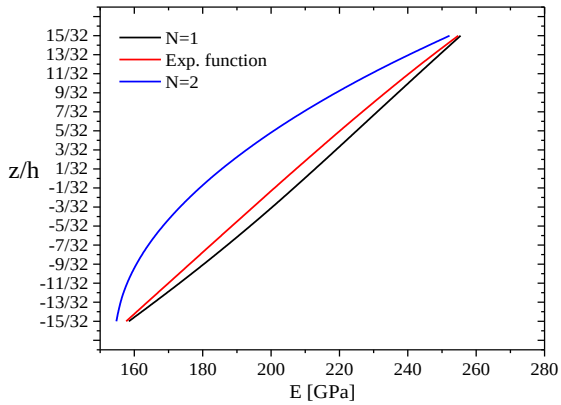

(c) e-FGM with even porosity

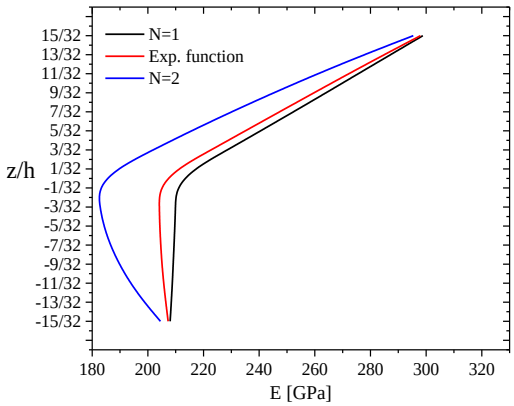

(d) e-FGM with uneven porosity

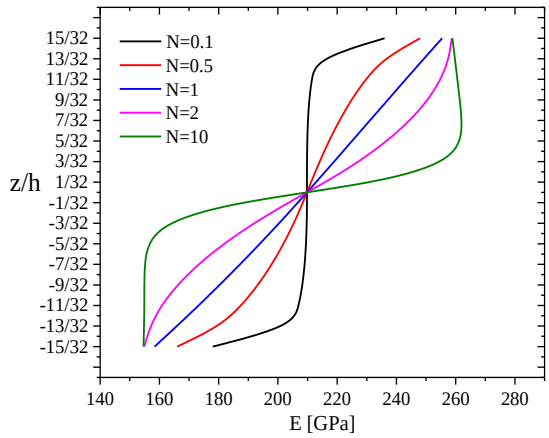

(e) s-FGM with even porosity

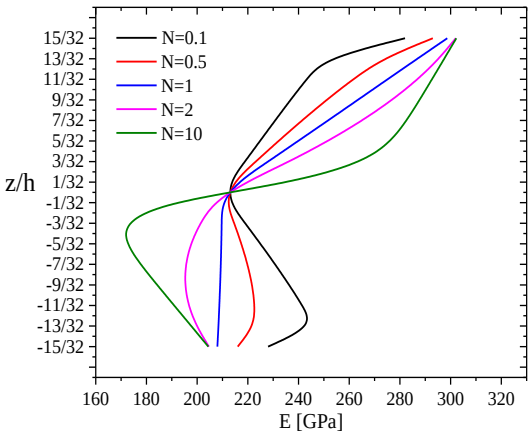

(e) s-FGM with uneven porosity

Figure 2.4 Representation of Young's Modulus across the thickness of p-FGM, e-FGM, s-FGM when (i) volume fraction of porosity (α_p) is 0.2 and (ii) temperatures at the top and bottom surfaces are 300K and 600K respectively

Applying the above formulations of Eqs. (2.13) and (2.14) for p-FGM, Eq. (2.21) for e-FGM and Eqs. (2.36) and (2.37) for s-FGM the values of material properties can be derived. Young's

modulus as an important material property has been calculated from the above mentioned formulations and plotted in Figure 2.4 considering porosity and temperature distribution. It is clearly observed that the material properties strictly obey different distribution laws for current formulations.

2.3.4 Equations of porous BDFGM

The tapered bidirectional FG conical shell is composed of one ceramic and two metal constituents. The gradation of the three constituents follow simple power law along the thickness (z- axis) and longitudinal direction (x-axis). The top surface (z= +h/2) is assumed to have completely ceramic and its volume proportion keeps on decreasing along the depth, where the bottom surface (z= -h/2) is completely metallic in nature as a composition of the two metal constituents. Subsequently, the metallic volume fraction at the fixed end (x= 0) only contains metal-1 and its proportion is gradually replaced by metal-2 with the increase of the length of conical shell. As a result, at the extreme free end (x= L) the volume fraction of metal is found to be completely constituted by metal-2.

With the gradation along the two directions the volume fractions of the constituents can be estimated by applying Voigt's law as

$$V_{m1} = \left[1 - \left(\frac{z}{h} + \frac{1}{2}\right)^{n_z}\right]\left[1 - \left(\frac{x}{L}\right)^{n_x}\right], V_{m2} = \left[1 - \left(\frac{z}{h} + \frac{1}{2}\right)^{n_z}\right]\left(\frac{x}{L}\right)^{n_x},\ V_c = \left(\frac{z}{h} + \frac{1}{2}\right)^{n_z} \quad (2.41)$$

where, the volume fractions of metal-1, metal-2 and ceramic are denoted by V_{m1}, V_{m2}, and V_c respectively, z is the distance from the mid-plane and the power-law index for gradations in the longitudinal and thickness direction are denoted by n_x and n_z respectively.

As per the criteria of Voigt's methodology

$$V_{m1} + V_{m2} + V_c = 1 \quad (2.42)$$

Due to the continuous gradation of three constituents the material properties of the BDFG conical shell also varies through the shell. The expression for any temperature dependent material property like Young's modulus (E), thermal expansion coefficient (α_t) and Poisson's ratio (υ) can be established by the relation

$$P_{eff}(x, z, T) = P_{m1}(T) + P_{m2}(T) + P_c(T) \quad (2.43)$$

where $P_{m1}(T), P_{m2}(T)$ and $P_c(T)$ denote the temperature dependent material properties of metal-1, metal-2 and ceramic constituents respectively.

In the presence of even porosity distribution the Eq. (2.43) will take the form

$$P_{eff}(x,z,T) = P_{m1}(T) + P_{m2}(T) + P_c(T) - \frac{\alpha}{2}\left(P_{m1}(T) + P_{m2}(T) + P_c(T)\right) \tag{2.44}$$

and, when the distribution of porosity is uneven then the equation is expressed by

$$P_{eff}(x,z,T) = P_{m1}(T) + P_{m2}(T) + P_c(T) - \frac{\alpha}{2}\left(P_{m1}(T) + P_{m2}(T) + P_c(T)\right)\left[1 - \frac{2 \mid z \mid}{h}\right] \tag{2.45}$$

where α is the volume fraction of porosity.

These temperature dependent material properties (Young's modulus, thermal expansion coefficient and Poisson's ratio) for metals and ceramic can be estimated by the relation

$$P(T) = P_0(P_{-1}T^{-1} + 1 + P_1T + P_2T^2 + P_3T^3) \tag{2.46}$$

where $P_i(i = -1,0,1,2, \dots)$ are coefficients of temperature and these are specific for individual materials.

The expression for the nonlinear temperature distribution across the porous BDFG conical shell can be obtained by solving the one-dimensional steady state heat conduction equation

$$-\frac{d}{dz}\left[K(z)\frac{dT}{dz}\right] = 0 \tag{2.47}$$

where, thermal conductivity

$$K(z) = K_{m1} + K_{m2} + K_c \tag{2.48}$$

Solving Eq. (2.47) by putting Eq. (2.48) and applying the boundary conditions $T = T_t$ at z= +h/2 and $T = T_b$ at z= -h/2, the equation for nonlinear temperature distribution can be derived.

For even porosity distribution the final equation for temperature distribution is

$$T(z) = T_b + [T_t - T_b]\left[\frac{(\Gamma_1 \times \Gamma_2)}{\left(\frac{z}{h} + \frac{1}{2}\right)}\right] - \frac{\alpha}{2}(K_{m1} + K_{m2} + K_c) \tag{2.49}$$

and, for uneven porosity distribution it will take the form

$$T(z) = T_b + [T_t - T_b]\left[\frac{(\Gamma_1 \times \Gamma_2)}{\left(\frac{z}{h} + \frac{1}{2}\right)}\right] - \frac{\alpha}{2}(K_{m1} + K_{m2} + K_c)\left[1 - \frac{2 \mid z \mid}{h}\right] \tag{2.50}$$

in which

$$\Gamma_1 = \left[\left(\frac{z}{h}+\frac{1}{2}\right) - \frac{K_{cm1}}{(n_z+1)K_{m1}}\left(\frac{z}{h}+\frac{1}{2}\right)^{(n_z+1)} + \frac{{K_{cm1}}^2}{(2n_z+1){K_{m1}}^2}\left(\frac{z}{h}+\frac{1}{2}\right)^{(2n_z+1)} - \frac{{K_{cm1}}^3}{(3n_z+1){K_{m1}}^3}\left(\frac{z}{h}+\frac{1}{2}\right)^{(3n_z+1)} + \frac{{K_{cm1}}^4}{(4n_z+1){K_{m1}}^4}\left(\frac{z}{h}+\frac{1}{2}\right)^{(4n_z+1)} - \frac{{K_{cm1}}^5}{(5n_z+1){K_{m1}}^5}\left(\frac{z}{h}+\frac{1}{2}\right)^{(5n_z+1)}\right]/F_1 \quad (2.51)$$

$$\Gamma_2 = \left[\left(\frac{z}{h}+\frac{1}{2}\right) - \frac{K_{cm2}}{(n_x+1)K_{m2}}\left(\frac{z}{h}+\frac{1}{2}\right)^{(n_x+1)} + \frac{{K_{cm2}}^2}{(2n_x+1){K_{m2}}^2}\left(\frac{z}{h}+\frac{1}{2}\right)^{(2n_x+1)} - \frac{{K_{cm2}}^3}{(3n_x+1){K_{m2}}^3}\left(\frac{z}{h}+\frac{1}{2}\right)^{(3n_x+1)} + \frac{{K_{cm2}}^4}{(4n_x+1){K_{m2}}^4}\left(\frac{z}{h}+\frac{1}{2}\right)^{(4n_x+1)} - \frac{{K_{cm2}}^5}{(5n_x+1){K_{m2}}^5}\left(\frac{z}{h}+\frac{1}{2}\right)^{(5n_x+1)}\right]/F_2 \quad (2.52)$$

$$F_1 = 1 - \frac{K_{cm1}}{(n_z+1)K_{m1}} + \frac{{K_{cm1}}^2}{(2n_z+1){K_{m1}}^2} - \frac{{K_{cm1}}^3}{(3n_z+1){K_{m1}}^3} + \frac{{K_{cm1}}^4}{(4n_z+1){K_{m1}}^4} - \frac{{K_{cm1}}^5}{(5n_z+1){K_{m1}}^5}$$

$$F_2 = 1 - \frac{K_{cm2}}{(n_x+1)K_{m2}} + \frac{{K_{cm2}}^2}{(2n_x+1){K_{m2}}^2} - \frac{{K_{cm2}}^3}{(3n_x+1){K_{m2}}^3} + \frac{{K_{cm2}}^4}{(4n_x+1){K_{m2}}^4} - \frac{{K_{cm2}}^5}{(5n_x+1){K_{m2}}^5}$$

$K_{cm1} = K_c - K_{m1}$ and $K_{cm2} = K_c - K_{m2}$, where K_{m1}, K_{m2} and K_c are the thermal conductivities of metal-1, metal-2 and ceramic respectively.

Due to the bidirectional gradation of the constituents in the conical shell, the thermal conductivity is found to change along both z-axis and x-axis. This effect is reflected in the

equation of temperature distribution with the inclusion of the terms τ_1 and τ_2 (Katiyar and Gupta, 2023).

2.4 FINITE ELEMENT FORMULATION

The finite element formulation is carried out using an eight-noded isoparametric quadratic shell element having seven degrees of freedom (three translation and four rotations) at each node. The interpolation (shape) functions are derived from an interpolation polynomial in terms of the natural co-ordinates so that the displacement fields are satisfactorily represented. In the analysis of thin shells, when the final element is presumed to possess only mid-surface nodes, the interpolation polynomial is a function of ξ and η and represented in the following form.

$$y(\xi,\eta) = C_0 + C_1\xi + C_2\eta + C_3\xi^2 + C_4\xi\eta + C_5\eta^2 + C_6\xi^2\eta + C_7\xi\eta^2 \tag{2.53}$$

where, C_0, C_1, C_2, C_3, C_4, C_5, C_6 and C_7 are the generalized degree of freedom.

The finite element formulation for tapered twisted FG conical shell element have been developed by considering an eight-nodded isoparametric shell element having seven degrees of freedom $(u_0, v_0, w_0, \theta_x, \theta_y, \xi_x \; and \; \xi_y)$ at each node. The generalized displacement vector $\{\delta\}$ at any point in the shell element can be expressed by

$$\{\delta\} = \sum_{i=1}^{8} [N_i]\{\delta_e\}_i \tag{2.54}$$

where, the displacement vector at any point is $\{\delta\} = \left[u_0 v_0 \; w_0 \theta_x \theta_y \xi_x \xi_y\right]^T$, nodal displacement vectors $\{\delta_e\}_i = \left[u_{0i} \;\; v_{0i} \;\; w_{0i} \;\; \theta_{xi}\theta_{yi}\xi_{xi} \;\; \xi_{yi}\right]^T$ and nodal shape functions at any node 'i' is defined in terms of local natural coordinate systems (χ, η) as

$$N_i = \frac{(1+\chi\chi_i)(1+\eta\eta_i)(\chi\chi_i+\eta\eta_i-1)}{4} \qquad \text{(for } i = 1, 2, 3, 4\text{)} \tag{2.55a}$$

$$N_i = \frac{(1-\chi^2)(1+\eta\eta_i)}{2} \qquad \text{(for } i = 5, 7\text{)} \tag{2.55b}$$

$$N_i = \frac{(1-\eta^2)(1+\chi\chi_i)}{2} \qquad \text{(for } i = 6, 8\text{)} \tag{2.55c}$$

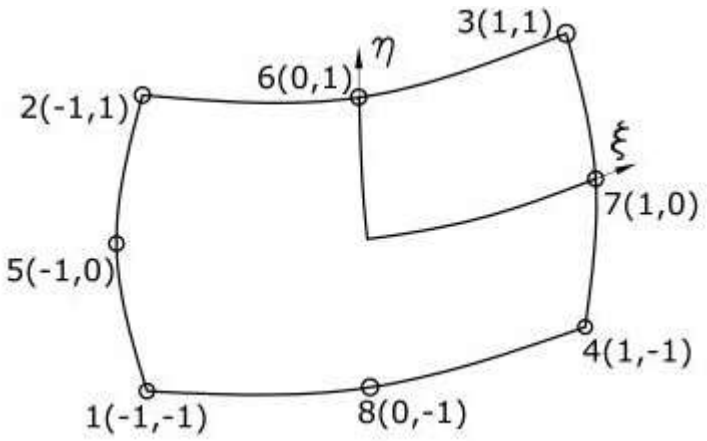

Figure 2.5 An eight-noded isoparametric shell element with nodes

The mid-plane displacement variables within the element can be expressed in terms of the corresponding nodal displacement parameters as

$$\{u_0\} = \sum_{i=1}^{8} [N_i]\{u_{0i}\}; \quad \{v_0\} = \sum_{i=1}^{8} [N_i]\{v_{0i}\}; \quad \{w_0\} = \sum_{i=1}^{8} [N_i]\{w_{0i}\}$$

$$\{\theta_x\} = \sum_{i=1}^{8} [N_i]\{\theta_{xi}\}; \quad \{\theta_y\} = \sum_{i=1}^{8} [N_i]\{\theta_{yi}\}; \quad \{\xi_x\} = \sum_{i=1}^{8} [N_i]\{\xi_{xi}\}; \tag{2.56}$$

$$\{\xi_y\} = \sum_{i=1}^{8} [N_i]\{\xi_{yi}\}$$

The generalized displacements at any point within the element can be interpolated from the nodal values as

$$\{\delta\} = \begin{Bmatrix} u_0 \\ v_0 \\ w_0 \\ \theta_x \\ \theta_y \\ \xi_x \\ \xi_y \end{Bmatrix} = \sum_{i=1}^{8} \begin{bmatrix} N_i & 0 & 0 & 0 & 0 & 0 & 0 \\ 0 & N_i & 0 & 0 & 0 & 0 & 0 \\ 0 & 0 & N_i & 0 & 0 & 0 & 0 \\ 0 & 0 & 0 & N_i & 0 & 0 & 0 \\ 0 & 0 & 0 & 0 & N_i & 0 & 0 \\ 0 & 0 & 0 & 0 & 0 & N_i & 0 \\ 0 & 0 & 0 & 0 & 0 & 0 & N_i \end{bmatrix} \begin{Bmatrix} u_{0i} \\ v_{0i} \\ w_{0i} \\ \theta_{xi} \\ \theta_{yi} \\ \xi_{xi} \\ \xi_{yi} \end{Bmatrix} \tag{2.57}$$

Eq. (2.57) can be written in a compact form

$$\{\delta\} = [N]\{\delta_e\} \tag{2.58}$$

where $[N]$ is the shape function matrix.

2.5 KINEMATICS OF CONICAL SHELL

2.5.1 Applying Trigonometric HSDT

The displacement equation of any point within the porous FG conical shell is derived by applying the trigonometric higher order shear deformation shell theory (THSDT). The displacement variables at any point within the FG conical panel are expressed by

$$u(x,y,z,t) = u_0(x,y,t) + z\theta_x(x,y,t) + z^2\varphi_x(x,y,t) + \tan^{-1} z\,\psi_x(x,y,t) \quad (2.59a)$$

$$v(x,y,z,t) = v_0(x,y,t) + z\theta_y(x,y,t) + z^2\varphi_y(x,y,t) + \tan^{-1} z\,\psi_y(x,y,t) \quad (2.59b)$$

$$w(x,y,z,t) = w_0(x,y,t) \quad (2.59c)$$

where *u*, *v*, and *w* are the displacement variables along x, y, and z –axes, respectively. These are dependent on the three mid-plane displacement variables u_0, v_0, and w_0 and two rotation variables θ_x and θ_y which denote the rotations of the normal to the mid-surface about y- and x-axes, respectively. φ_x, φ_y, ψ_x and ψ_y are the higher order terms in the Taylor series expansion given at the mid plane of the FG conical shell.

The transverse shear stresses at top ($z = h/2$) and bottom ($z = -h/2$) faces of the FG conical shell are zero, so do the corresponding strains. Applying these conditions, the displacement field takes the new form as

$$u(x,y,z,t) = u_0(x,y,t) + z\theta_x(x,y,t) + \tan^{-1}(z)\,\psi_x(x,y,t) \quad (2.60a)$$

$$v(x,y,z,t) = v_0(x,y,t) + z\theta_y(x,y,t) + \tan^{-1}(z)\,\psi_y(x,y,t) \quad (2.60b)$$

$$w(x,y,z,t) = w_0(x,y,t) \quad (2.60c)$$

where $\psi_x = -\left(\frac{4+h^2}{4}\right)\left(\frac{\partial w_0}{\partial x} + \theta_x\right)$ and $\psi_y = -\left(\frac{4+h^2}{4}\right)\left(\frac{\partial w_0}{\partial y} + \theta_y\right)$

Substituting the values of ψ_x and ψ_y in Eq. (2.60), one can get

$$u(x,y,z,t) = u_0(x,y,t) + f_1(z)\theta_x(x,y,t) + f_2(z)\xi_x(x,y,t) \quad (2.61a)$$

$$v(x,y,z,t) = v_0(x,y,t) + f_1(z)\theta_y(x,y,t) + f_2(z)\xi_y(x,y,t) \tag{2.61b}$$

$$w(x,y,z,t) = w_0(x,y,t) \tag{2.61c}$$

where $f_1(z) = z - \frac{4+h^2}{4}\tan^{-1}(z)$, $f_2(z) = -\frac{4+h^2}{4}\tan^{-1}(z)$, $\xi_x = \frac{\partial w_0}{\partial x}$ and $\xi_y = \frac{\partial w_0}{\partial y}$

As we have considered thin conical shell so the mid-plane displacement and rotations variables u_0, v_0, w_0,θ_x, θ_y,ξ_x and ξ_y are not functions of *z*-coordinate.

The displacement vector of the porous tapered FG conical shell can be expressed as

$$\{\bar{\delta}\} = [Z]\{\delta\} \tag{2.62}$$

where $\{\bar{\delta}\} = [u\ v\ w]^T$, $\{\delta\} = \left[u_0\ \ v_0\ \ w_0\ \ \theta_x\ \theta_y\ \ \xi_x\xi_y\right]^T$ and $[Z]$ is the transformation matrix expressed as

$$[Z] = \begin{bmatrix} 1 & 0 & 0 & 0 & 0 & 0 & f_1 & 0 & 0 & 0 & f_2 & 0 & 0 & 0 \\ 0 & 1 & 0 & 0 & 0 & 0 & 0 & f_1 & 0 & 0 & 0 & f_2 & 0 & 0 \\ 0 & 0 & 1 & 0 & 0 & 0 & 0 & 0 & f_1 & 0 & 0 & 0 & f_2 & 0 \\ 0 & 0 & 0 & 1 & 0 & 0 & 0 & 0 & 0 & f_1 & 0 & 0 & 0 & f_2 \\ 0 & 0 & 0 & 0 & 1 & 0 & 0 & 0 & 0 & 0 & 0 & 0 & 0 & 0 \\ 0 & 0 & 0 & 0 & 0 & 1 & 0 & 0 & 0 & 0 & 0 & 0 & 0 & 0 \end{bmatrix} \tag{2.63}$$

The expressions of the linear bending and shear strain components are expressed as

$$\{\varepsilon\} = \begin{Bmatrix} \varepsilon_{xx} \\ \varepsilon_{yy} \\ \gamma_{xy} \end{Bmatrix} = \begin{Bmatrix} \dfrac{\partial u}{\partial x} \\ \dfrac{\partial v}{\partial x} + \dfrac{w}{r_y} \\ \dfrac{\partial u}{\partial y} + \dfrac{\partial v}{\partial x} + \dfrac{2w}{r_{xy}} \end{Bmatrix} \tag{2.64a}$$

$$\begin{Bmatrix} \varepsilon_{xx} \\ \varepsilon_{yy} \\ \gamma_{xy} \end{Bmatrix} = \begin{Bmatrix} \varepsilon_x^0 \\ \varepsilon_y^0 \\ \gamma_{xy}^0 \end{Bmatrix} + f_1 \begin{Bmatrix} \kappa_x^1 \\ \kappa_y^1 \\ \kappa_{xy}^1 \end{Bmatrix} + f_2 \begin{Bmatrix} \kappa_x^2 \\ \kappa_y^2 \\ \kappa_{xy}^2 \end{Bmatrix} \tag{2.64b}$$

$$\{\gamma\} = \begin{Bmatrix} \gamma_{xz} \\ \gamma_{yz} \end{Bmatrix} = \begin{Bmatrix} \dfrac{\partial u}{\partial z} + \dfrac{\partial w}{\partial x} \\ \dfrac{\partial v}{\partial z} + \dfrac{\partial w}{\partial y} \end{Bmatrix} \tag{2.65a}$$

$$\begin{Bmatrix}\gamma_{xz}\\ \gamma_{yz}\end{Bmatrix} = \begin{Bmatrix}\gamma_{xz}^{0}\\ \gamma_{yz}^{0}\end{Bmatrix} + f_1' \begin{Bmatrix}\kappa_{xz}^{1}\\ \kappa_{yz}^{1}\end{Bmatrix} + f_2' \begin{Bmatrix}\kappa_{xz}^{2}\\ \kappa_{yz}^{2}\end{Bmatrix} \tag{2.65b}$$

where $f_1' = \frac{\partial f_1}{\partial z}$ and $f_2' = \frac{\partial f_2}{\partial z}$

The Eq. (2.64b) and (2.65b) are expressed in compact form as

$$\{\varepsilon\} = [Z_b]\{\bar{\varepsilon}\} \tag{2.66}$$

$$\{\gamma\} = [Z_s]\{\bar{\gamma}\} \tag{2.67}$$

where $\{\bar{\varepsilon}\} = \begin{Bmatrix}\varepsilon_x^0 & \varepsilon_y^0 & \gamma_{xy}^0 & \kappa_x^1 & \kappa_y^1 & \kappa_{xy}^1 & \kappa_x^2 & \kappa_y^2 & \kappa_{xy}^2\end{Bmatrix}^T$

$\{\bar{\gamma}\} = \begin{Bmatrix}\gamma_{xz}^0 & \gamma_{yz}^0 & \kappa_{xz}^1 & \kappa_{yz}^1 & \kappa_{xz}^2 & \kappa_{yz}^2\end{Bmatrix}^T$

The mid plane strain and curvature components are expressed as

$$\begin{aligned}
&\varepsilon_x^0 = \frac{\partial u_0}{\partial x},\ \varepsilon_y^0 = \frac{\partial v_0}{\partial y} + \frac{w_0}{R_y},\ \gamma_{xy}^0 = \frac{\partial u_0}{\partial y} + \frac{\partial v_0}{\partial x} + \frac{w_0}{R_{xy}},\\
&\kappa_x^1 = \frac{\partial \theta_x}{\partial x},\ \kappa_y^1 = \frac{\partial \theta_y}{\partial y},\ \kappa_{xy}^1 = \frac{\partial \theta_x}{\partial y} + \frac{\partial \theta_y}{\partial x},\\
&\kappa_x^2 = \frac{\partial \xi_x}{\partial x},\ \kappa_y^2 = \frac{\partial \xi_y}{\partial y},\ \kappa_{xy}^2 = \frac{\partial \xi_x}{\partial y} + \frac{\partial \xi_y}{\partial x}\\
&\gamma_{xz}^0 = \frac{\partial w_0}{\partial x},\ \gamma_{yz}^0 = \frac{\partial w_0}{\partial y},\ \kappa_{xz}^1 = \theta_x,\ \kappa_{yz}^1 = \theta_y,\ \kappa_{xz}^2 = \xi_x,\ \kappa_{yz}^2 = \xi_y
\end{aligned} \tag{2.68}$$

$[Z_b]$ and $[Z_s]$ are the mid-plane bending thickness and mid-plane shear thickness co-ordinate matrices provided as

$$[Z_b] = \begin{bmatrix}1 & 0 & 0 & f_1 & 0 & 0 & f_2 & 0 & 0\\ 0 & 1 & 0 & 0 & f_1 & 0 & 0 & f_2 & 0\\ 0 & 0 & 1 & 0 & 0 & f_1 & 0 & 0 & f_2\end{bmatrix} \tag{2.69}$$

$$[Z_s] = \begin{bmatrix}1 & 0 & f_1' & 0 & f_2' & 0\\ 0 & 1 & 0 & f_1' & 0 & f_2'\end{bmatrix} \tag{2.70}$$

The mid plane strain vector of bending and shear are expressed as

$$\{\bar{\varepsilon}\} = [B_b]\{\delta_e\} \tag{2.71}$$

$$\{\bar{\gamma}\} = [B_s]\{\delta_e\} \tag{2.72}$$

where, $[B_b]$ and $[B_s]$ are the strain-displacement matrices for bending and shear respectively. where

$$[B_b] = \begin{bmatrix} \frac{\partial N_i}{\partial x} & 0 & 0 & 0 & 0 & 0 & 0 \\ 0 & \frac{\partial N_i}{\partial y} & \frac{N_i}{R_y} & 0 & 0 & 0 & 0 \\ \frac{\partial N_i}{\partial y} & \frac{\partial N_i}{\partial x} & \frac{2N_i}{R_{xy}} & 0 & 0 & 0 & 0 \\ 0 & 0 & 0 & \frac{\partial N_i}{\partial x} & 0 & 0 & 0 \\ 0 & 0 & 0 & 0 & \frac{\partial N_i}{\partial y} & 0 & 0 \\ 0 & 0 & 0 & \frac{\partial N_i}{\partial y} & \frac{\partial N_i}{\partial x} & 0 & 0 \\ 0 & 0 & 0 & 0 & 0 & \frac{\partial N_i}{\partial x} & 0 \\ 0 & 0 & 0 & 0 & 0 & 0 & \frac{\partial N_i}{\partial y} \\ 0 & 0 & 0 & 0 & 0 & \frac{\partial N_i}{\partial y} & \frac{\partial N_i}{\partial x} \end{bmatrix} \tag{2.73}$$

and

$$[B_s] = \begin{bmatrix} 0 & 0 & \frac{\partial N_i}{\partial x} & 0 & 0 & 0 & 0 \\ 0 & 0 & \frac{\partial N_i}{\partial y} & 0 & 0 & 0 & 0 \\ 0 & 0 & 0 & N_i & 0 & 0 & 0 \\ 0 & 0 & 0 & 0 & N_i & 0 & 0 \\ 0 & 0 & 0 & 0 & 0 & N_i & 0 \\ 0 & 0 & 0 & 0 & 0 & 0 & N_i \end{bmatrix} \tag{2.74}$$

Putting the values of $\{\bar{\varepsilon}\}$ and $\{\bar{\gamma}\}$ in Eqs. (2.66) and (2.67), the values of $\{\varepsilon\}$ and $\{\gamma\}$ can be obtained.

2.5.2 Applying Polynomial HSDT

The displacement equation of any point within the porous FG conical shell is derived by applying the polynomial higher order shear deformation shell theory (PHSDT). The displacement variables at any point within the FG conical panel are expressed by

$$u(x,y,z,t) = u_0(x,y,t) + z\theta_x(x,y,t) + z^2u_0^*(x,y,t) + z^3\xi_x(x,y,t) \quad (2.75a)$$

$$v(x,y,z,t) = v_0(x,y,t) + z\theta_y(x,y,t) + z^2v_0^*(x,y,t) + z^3\xi_y(x,y,t) \quad (2.75b)$$

$$w(x,y,z,t) = w_0(x,y,t) \quad (2.75c)$$

where *u*, *v*, and *w* are the displacement variables along x, y, and z –axes, respectively. These are dependent on the three mid-plane displacement variables u_0, v_0, and w_0 and two rotation variables θ_x and θ_y which denote the rotations of the normal to the mid-surface about y- and x-axes, respectively. u_0^*, v_0^*, ξ_x and ξ_y are the higher order terms in the Taylor series expansion given at the mid plane of the FG conical shell.

The transverse shear stresses at top ($z = h/2$) and bottom ($z = -h/2$) faces of the FG conical shell are zero, so do the corresponding strains. Applying these conditions, the displacement field takes the new form as

$$u(x,y,z,t) = u_0(x,y,t) + z\theta_x(x,y,t) + z^3\xi_x(x,y,t) \quad (2.76a)$$

$$v(x,y,z,t) = v_0(x,y,t) + z\theta_y(x,y,t) + z^3\xi_y(x,y,t) \quad (2.76b)$$

$$w(x,y,z,t) = w_0(x,y,t) \quad (2.76c)$$

where $\xi_x = -\frac{4}{3h^2}\left(\frac{\partial w_0}{\partial x} + \theta_x\right)$ and $\xi_y = -\frac{4}{3h^2}\left(\frac{\partial w_0}{\partial y} + \theta_y\right)$

The displacement vector of the porous tapered FG conical shell can be expressed as

$$\{\bar{\delta}\} = [Z]\{\delta\} \quad (2.77)$$

where $\{\bar{\delta}\} = [u\ v\ w]^T$, $\{\delta\} = \left[u_0\ \ v_0\ \ w_0\ \ \theta_x\ \theta_y\ \xi_x\ \xi_y\right]^T$ and $[Z]$ is the transformation matrix expressed as

$$[Z] = \begin{bmatrix} 1 & 0 & 0 & 0 & 0 & 0 & z & 0 & 0 & 0 & z^3 & 0 & 0 & 0 \\ 0 & 1 & 0 & 0 & 0 & 0 & 0 & z & 0 & 0 & 0 & z^3 & 0 & 0 \\ 0 & 0 & 1 & 0 & 0 & 0 & 0 & 0 & z & 0 & 0 & 0 & z^3 & 0 \\ 0 & 0 & 0 & 1 & 0 & 0 & 0 & 0 & 0 & z & 0 & 0 & 0 & z^3 \\ 0 & 0 & 0 & 0 & 1 & 0 & 0 & 0 & 0 & 0 & 0 & 0 & 0 & 0 \\ 0 & 0 & 0 & 0 & 0 & 1 & 0 & 0 & 0 & 0 & 0 & 0 & 0 & 0 \end{bmatrix} \tag{2.78}$$

The expressions of the linear bending and shear strain components are expressed as

$$\{\varepsilon\} = \begin{Bmatrix} \varepsilon_{xx} \\ \varepsilon_{yy} \\ \gamma_{xy} \end{Bmatrix} = \begin{Bmatrix} \dfrac{\partial u}{\partial x} \\ \dfrac{\partial v}{\partial x} + \dfrac{w}{r_y} \\ \dfrac{\partial u}{\partial y} + \dfrac{\partial v}{\partial x} + \dfrac{2w}{r_{xy}} \end{Bmatrix} \tag{2.79a}$$

$$\begin{Bmatrix} \varepsilon_{xx} \\ \varepsilon_{yy} \\ \gamma_{xy} \end{Bmatrix} = \begin{Bmatrix} \varepsilon_x^0 \\ \varepsilon_y^0 \\ \gamma_{xy}^0 \end{Bmatrix} + z \begin{Bmatrix} \kappa_x^1 \\ \kappa_y^1 \\ \kappa_{xy}^1 \end{Bmatrix} + z^3 \begin{Bmatrix} \kappa_x^2 \\ \kappa_y^2 \\ \kappa_{xy}^2 \end{Bmatrix} \tag{2.79b}$$

$$\{\gamma\} = \begin{Bmatrix} \gamma_{xz} \\ \gamma_{yz} \end{Bmatrix} = \begin{Bmatrix} \dfrac{\partial u}{\partial z} + \dfrac{\partial w}{\partial x} \\ \dfrac{\partial v}{\partial z} + \dfrac{\partial w}{\partial y} \end{Bmatrix} \tag{2.80a}$$

$$\begin{Bmatrix} \gamma_{xz} \\ \gamma_{yz} \end{Bmatrix} = \begin{Bmatrix} \gamma_{xz}^0 \\ \gamma_{yz}^0 \end{Bmatrix} + z \begin{Bmatrix} \kappa_{xz}^1 \\ \kappa_{yz}^1 \end{Bmatrix} + z^2 \begin{Bmatrix} \gamma_{xz}^1 \\ \gamma_{yz}^1 \end{Bmatrix} + z^3 \begin{Bmatrix} \kappa_{xz}^2 \\ \kappa_{yz}^2 \end{Bmatrix} \tag{2.80b}$$

The Eq. (2.79b) and (2.80b) are expressed in compact form as

$$\{\varepsilon\} = [Z_b]\{\bar{\varepsilon}\} \tag{2.81}$$

$$\{\gamma\} = [Z_s]\{\bar{\gamma}\} \tag{2.82}$$

where $\{\bar{\varepsilon}\} = \begin{Bmatrix} \varepsilon_x^0 & \varepsilon_y^0 & \gamma_{xy}^0 & \kappa_x^1 & \kappa_y^1 & \kappa_{xy}^1 & \kappa_x^2 & \kappa_y^2 & \kappa_{xy}^2 \end{Bmatrix}^T$

$\{\bar{\gamma}\} = \begin{Bmatrix} \gamma_{xz}^0 & \gamma_{yz}^0 & \kappa_{xz}^1 & \kappa_{yz}^1 & \gamma_{xz}^1 & \gamma_{yz}^1 & \kappa_{xz}^2 & \kappa_{yz}^2 \end{Bmatrix}^T$

$[Z_b]$ and $[Z_s]$ are the mid-plane bending thickness and mid-plane shear thickness co-ordinate matrices provided as

$$[Z_b] = \begin{bmatrix} 1 & 0 & 0 & z & 0 & 0 & z^3 & 0 & 0 \\ 0 & 1 & 0 & 0 & z & 0 & 0 & z^3 & 0 \\ 0 & 0 & 1 & 0 & 0 & z & 0 & 0 & z^3 \end{bmatrix} \tag{2.83}$$

$$[Z_s] = \begin{bmatrix} 1 & 0 & z & 0 & z^2 & 0 & z^3 & 0 \\ 0 & 1 & 0 & z & 0 & z^2 & 0 & z^3 \end{bmatrix} \tag{2.84}$$

The mid plane strain and curvature components are expressed as

$\varepsilon_x^0 = \frac{\partial u_0}{\partial x}$, $\varepsilon_y^0 = \frac{\partial v_0}{\partial y} + \frac{w_0}{R_y}$, $\gamma_{xy}^0 = \frac{\partial u_0}{\partial y} + \frac{\partial v_0}{\partial x} + \frac{w_0}{R_{xy}}$,

$\kappa_x^1 = \frac{\partial \theta_x}{\partial x}$, $\kappa_y^1 = \frac{\partial \theta_y}{\partial y}$, $\kappa_{xy}^1 = \frac{\partial \theta_x}{\partial y} + \frac{\partial \theta_y}{\partial x}$,

$\kappa_x^2 = \frac{\partial \xi_x}{\partial x}$, $\kappa_y^2 = \frac{\partial \xi_y}{\partial y}$, $\kappa_{xy}^2 = \frac{\partial \xi_x}{\partial y} + \frac{\partial \xi_y}{\partial x}$

$\gamma_{xz}^0 = \left(\theta_x + \frac{\partial w_0}{\partial x}\right)$, $\gamma_{yz}^0 = \left(\theta_y + \frac{\partial w_0}{\partial y}\right)$, (2.85)

$\kappa_{xz}^1 = 0$, $\kappa_{yz}^1 = -\frac{\theta_y}{R_y}$,

$\gamma_{xz}^1 = 3\xi_x$, $\gamma_{yz}^1 = \xi_y$

$\kappa_{xz}^2 = 0$, $\kappa_{yz}^2 = -\frac{\xi_y}{R_y}$

The mid plane strain vector of bending and shear are expressed as

$$\{\bar{\varepsilon}\} = [B_b]\{\delta_e\} \tag{2.86}$$

$$\{\bar{\gamma}\} = [B_s]\{\delta_e\} \tag{2.87}$$

where, $[B_b]$ and $[B_s]$ are the strain-displacement matrices for bending and shear respectively. where

$$[B_b] = \begin{bmatrix} \frac{\partial N_i}{\partial x} & 0 & 0 & 0 & 0 & 0 & 0 \\ 0 & \frac{\partial N_i}{\partial y} & \frac{N_i}{R_y} & 0 & 0 & 0 & 0 \\ \frac{\partial N_i}{\partial y} & \frac{\partial N_i}{\partial x} & \frac{2N_i}{R_{xy}} & 0 & 0 & 0 & 0 \\ 0 & 0 & 0 & \frac{\partial N_i}{\partial x} & 0 & 0 & 0 \\ 0 & 0 & 0 & 0 & \frac{\partial N_i}{\partial y} & 0 & 0 \\ 0 & 0 & 0 & \frac{\partial N_i}{\partial y} & \frac{\partial N_i}{\partial x} & 0 & 0 \\ 0 & 0 & 0 & 0 & 0 & \frac{\partial N_i}{\partial x} & 0 \\ 0 & 0 & 0 & 0 & 0 & 0 & \frac{\partial N_i}{\partial y} \\ 0 & 0 & 0 & 0 & 0 & \frac{\partial N_i}{\partial y} & \frac{\partial N_i}{\partial x} \end{bmatrix} \tag{2.88}$$

and

$$[B_s] = \begin{bmatrix} 0 & 0 & \frac{\partial N_i}{\partial x} & N_i & 0 & 0 & 0 \\ 0 & -\frac{N_i}{R_y} & \frac{\partial N_i}{\partial y} & 0 & N_i & 0 & 0 \\ 0 & 0 & 0 & 0 & 0 & 0 & 0 \\ 0 & 0 & 0 & 0 & -\frac{N_i}{R_y} & 0 & 0 \\ 0 & 0 & 0 & 0 & 0 & N_i & 0 \\ 0 & 0 & 0 & 0 & 0 & 0 & N_i \\ 0 & 0 & 0 & 0 & 0 & 0 & 0 \\ 0 & 0 & 0 & 0 & 0 & 0 & -\frac{N_i}{R_y} \end{bmatrix} \tag{2.89}$$

Putting the values of $\{\bar{\varepsilon}\}$ and $\{\bar{\gamma}\}$ in Eqs. (2.81) and (2.82), the values of $\{\varepsilon\}$ and $\{\gamma\}$ can be obtained.

The linear thermoelastic constitutive equation for FG conical shell can be represented as

$$\begin{Bmatrix}\sigma_{11}\\ \sigma_{22}\\ \tau_{12}\end{Bmatrix}=\begin{bmatrix}Q_{11} & Q_{12} & 0\\ Q_{21} & Q_{22} & 0\\ 0 & 0 & Q_{66}\end{bmatrix}\left(\begin{Bmatrix}\varepsilon_{xx}\\ \varepsilon_{yy}\\ \gamma_{xy}\end{Bmatrix}-\sigma_t\Delta T\begin{Bmatrix}1\\ 1\\ 0\end{Bmatrix}\right) \tag{2.90a}$$

$$\begin{Bmatrix}\tau_{13}\\ \tau_{23}\end{Bmatrix}=\begin{bmatrix}Q_{44} & 0\\ 0 & Q_{55}\end{bmatrix}\begin{Bmatrix}\gamma_{xz}\\ \gamma_{yz}\end{Bmatrix} \tag{2.90b}$$

where $\Delta T = T_1 - T_0$, T_0 and T_1 indicate the reference temperature and applied temperature respectively and $[Q_{ij}]$ are the stiffness components and can be expressed as

$$Q_{11}=\frac{E_{11}}{1-\nu_{12}\nu_{21}}, Q_{22}=\frac{E_{22}}{1-\nu_{12}\nu_{21}}, Q_{12}=\frac{\nu_{21}E_{11}}{1-\nu_{12}\nu_{21}}, \tag{2.91}$$

$$Q_{66}=G_{12}, Q_{44}=G_{23}, Q_{55}=G_{13}$$

Employing the transformation rule given in Jones (1975), the linear thermo elastic constitutive equation for FGM conical shell for off-axis reduced elastic coefficients can be expressed as

$$\begin{Bmatrix}\sigma_x\\ \sigma_y\\ \tau_{xy}\end{Bmatrix}=\begin{bmatrix}\bar{Q}_{11} & \bar{Q}_{12} & \bar{Q}_{16}\\ \bar{Q}_{21} & \bar{Q}_{22} & \bar{Q}_{26}\\ \bar{Q}_{16} & \bar{Q}_{26} & \bar{Q}_{66}\end{bmatrix}\left(\begin{Bmatrix}\varepsilon_{xx}\\ \varepsilon_{yy}\\ \gamma_{xy}\end{Bmatrix}-\sigma_t\Delta T\begin{Bmatrix}1\\ 1\\ 0\end{Bmatrix}\right) \tag{2.92a}$$

$$\begin{Bmatrix}\tau_{xz}\\ \tau_{yz}\end{Bmatrix}=\begin{bmatrix}\bar{Q}_{44} & \bar{Q}_{45}\\ \bar{Q}_{45} & \bar{Q}_{55}\end{bmatrix}\begin{Bmatrix}\gamma_{xz}\\ \gamma_{yz}\end{Bmatrix} \tag{2.92b}$$

where $\Delta T = T_1 - T_0$, T_0 and T_1 indicate the reference temperature and applied temperature respectively and $\bar{Q}_{ij}$ are the transformed reduced stiffness components.

By integrating the stress equation over the thickness of the shell, the in-plane thermal forces caused by the thermal field in the current FG conical shell are derived and are written as follows:

$$\begin{Bmatrix}N_x^{Th}\\ N_y^{Th}\\ N_{xy}^{Th}\end{Bmatrix}=\int_{-\frac{h}{2}}^{\frac{h}{2}}\begin{bmatrix}\bar{Q}_{11} & \bar{Q}_{12} & \bar{Q}_{16}\\ \bar{Q}_{21} & \bar{Q}_{22} & \bar{Q}_{26}\\ \bar{Q}_{16} & \bar{Q}_{26} & \bar{Q}_{66}\end{bmatrix}\alpha_t(z,T)\Delta T\begin{Bmatrix}1\\ 1\\ 0\end{Bmatrix}dz \tag{2.93}$$

where $[\bar{Q}_{ij}]$ are the transformed reduced stiffness components and can be defined as

$$\begin{Bmatrix} \bar{Q}_{11} \\ \bar{Q}_{12} \\ \bar{Q}_{22} \\ \bar{Q}_{16} \\ \bar{Q}_{26} \\ \bar{Q}_{66} \\ \bar{Q}_{44} \\ \bar{Q}_{45} \\ \bar{Q}_{55} \end{Bmatrix} = \begin{bmatrix} p^4 & 2p^2q^2 & q^4 & 4p^2q^2 & 0 & 0 \\ p^2q^2 & p^4+q^4 & p^2q^2 & -4p^2q^2 & 0 & 0 \\ q^4 & 2p^2q^2 & p^4 & 4p^2q^2 & 0 & 0 \\ p^3q & pq^3-p^3q & -pq^3 & -2p^3q+2pq^3 & 0 & 0 \\ pq^3 & p^3q-pq^3 & -p^3q & 2p^3q-2pq^3 & 0 & 0 \\ p^2q^2 & -2p^2q^2 & p^2q^2 & (p^2-q^2)^2 & 0 & 0 \\ 0 & 0 & 0 & 0 & p^2 & q^2 \\ 0 & 0 & 0 & 0 & pq & -pq \\ 0 & 0 & 0 & 0 & q^2 & p^2 \end{bmatrix} \begin{Bmatrix} Q_{11} \\ Q_{12} \\ Q_{22} \\ Q_{66} \\ Q_{44} \\ Q_{55} \end{Bmatrix} \tag{2.94}$$

where $p = cos\theta$ and $q = sin\theta$, θ is the inclination angle of the layer with positive x-axis.

2.6 ELEMENT STIFFNESS MATRIX

The strain energy of deformation for the element can be computed as

$$U_0 = \frac{1}{2}\left(\int_V \{\varepsilon\}^T\{\sigma\}dV + \int_V \{\gamma\}^T\{\tau\}dV\right) \tag{2.95}$$

Putting the values of $\{\varepsilon\}, \{\gamma\}, \{\sigma\}$ and $\{\tau\}$ in Eq. (2.95)

$$U_0 = \frac{1}{2}\left(\int_V \{\bar{\varepsilon}\}^T[Z_b]^T\left[\bar{Q}_{ij}\right][Z_b]\{\bar{\varepsilon}\}dZdA + \int_V \{\bar{\gamma}\}^T[Z_S]^T\left[\bar{Q}_{ij}\right][Z_S]\{\bar{\gamma}\}dZdA\right) \tag{2.96}$$

which will take the form

$$\begin{aligned} U_0 = \frac{1}{2}\Bigg[\int_A \{\bar{\varepsilon}\}^T\left(\int_Z [Z_b]^T\left[\bar{Q}_{ij}\right][Z_b]dZ\right)\{\bar{\varepsilon}\}dA \\ + \int_A \{\bar{\gamma}\}^T\left(\int_Z [Z_S]^T\left[\bar{Q}_{ij}\right][Z_S]dZ\right)\{\bar{\gamma}\}dA\Bigg] \end{aligned} \tag{2.97}$$

Where the elastic matrices due to bending and shear will be represented by

$$[D_b] = \int_Z [Z_b]^T\left[\bar{Q}_{ij}\right][Z_b]dZ \tag{2.98}$$

$$[D_S] = \int_Z [Z_S]^T \left[\bar{Q}_{ij}\right] [Z_S] dZ \tag{2.99}$$

Putting the values of $\{\bar{\varepsilon}\}$ and $\{\bar{\gamma}\}$ in Eq. (2.97)

$$U_0 = \frac{1}{2}\left(\int_A \{\delta_e\}^T [B_b]^T [D_b][B_b]\{\delta_e\} dA + \int_A \{\delta_e\}^T [B_S]^T [D_S][B_S]\{\delta_e\} dA \right) \tag{2.100}$$

Finally the Equation of the strain energy stored will be

$$U_0 = \frac{1}{2}\{\delta_e\}^T ([K_b] + [K_S])\{\delta_e\} = \frac{1}{2}\{\delta_e\}^T [K_e]\{\delta_e\} \tag{2.101}$$

$[K_b]$ and $[K_S]$ are the stiffness matrix due to bending and shear which are expressed as

$$[K_b] = \int_A [B_b]^T [D_b][B_b] dA \tag{2.102}$$

$$[K_S] = \int_A [B_S]^T [D_S][B_S] dA \tag{2.103}$$

where,$[K_e]$ is the elemental elastic stiffness matrix and it can be derived by using the following equation

$$[K_e] = [K_b] + [K_s] = \int_A [B_b]^T [D_b][B_b] dA + \int_A [B_s]^T [D_s][B_s] dA \tag{2.104}$$

2.7 ELEMENT MASS MATRIX

The kinetic energy of the element can be computed as

$$T = \frac{1}{2} m v^2 = \frac{1}{2} \int_V \rho \left\{\dot{\bar{\delta}}\right\}^T \left\{\dot{\bar{\delta}}\right\} dV \tag{2.105}$$

Putting the values of $\{\bar{\delta}\}$ in Eq. (2.105)

$$T = \frac{1}{2} \int_V \left\{\dot{\delta}\right\}^T [Z]^T \rho [Z] \left\{\dot{\delta}\right\} dV \tag{2.106}$$

The value of $[Z]$ is taken from Eq. (2.63) for trigonometric HSDT and it is taken from Eq. (2.78) for polynomial HSDT

Eq. (2.106) will take the form

$$T = \frac{1}{2}\int_A \{\dot{\delta}\}^T \left(\int_Z [Z]^T \rho [Z] dz\right) \{\dot{\delta}\} dA \tag{2.107}$$

The inertia matrix will be represented by

$$[m] = \int_Z [Z]^T \rho [Z] dz \tag{2.108}$$

Eq. (2.107) will take the form

$$T = \frac{1}{2}\int_A \{\dot{\delta}\}^T [m] \{\dot{\delta}\} dA \tag{2.109}$$

Putting the values of $\{\delta\}$ in Eq. (2.109)

$$T = \frac{1}{2}\int_A \{\dot{\delta}_e\}^T [N]^T [m][N] \{\dot{\delta}_e\} dA \tag{2.110}$$

Finally the Equation of the kinetic energy will be

$$T = \frac{1}{2}\{\dot{\delta}_e\}^T [M_e] \{\dot{\delta}_e\} \tag{2.111}$$

$[M_e]$ is the element mass matrix, which is expressed by

$$[M_e] = \int_A [N]^T [m][N] dA \tag{2.112}$$

2.8 EQUATIONS OF GENERAL DYNAMIC EQUILIBRIUM

2.8.1. Strain Energy of rotating FG conical shell

The elemental strain energy stored due to the thermal and rotational effects of the initial stresses obtained as (Rout et al., 2018)

$$U_2 = \int_V \{\varepsilon_{nl}\}^T \{\sigma_0\}_{Th} dv + \int_V \{\varepsilon_{nl}\}^T \{\sigma_0\}_R dv \tag{2.113}$$

The non-linear strain components according to the Green-Lagrange relations are given as (Cook et al., 1989)

$$\{\varepsilon_{nl}\} = \begin{Bmatrix} \varepsilon_{xnl} \\ \varepsilon_{ynl} \\ \gamma_{xynl} \\ \gamma_{yznl} \\ \gamma_{zxnl} \end{Bmatrix} =$$

$$\frac{1}{2}\begin{Bmatrix} \left[\left(\frac{\partial u}{\partial x}\right)^2 + \left(\frac{\partial v}{\partial x} + \frac{w}{R_{xy}}\right)^2 + \left(\frac{\partial w}{\partial x}\right)^2\right] \\ \left[\left(\frac{\partial u}{\partial y} + \frac{w}{R_{xy}}\right)^2 + \left(\frac{\partial v}{\partial y} + \frac{w}{R_y}\right)^2 + \left(\frac{\partial w}{\partial y} - \frac{v}{R_y}\right)^2\right] \\ 2\left[\frac{\partial u}{\partial x}.\left(\frac{\partial u}{\partial y} + \frac{w}{R_{xy}}\right) + \left(\frac{\partial v}{\partial x} + \frac{w}{R_{xy}}\right).\left(\frac{\partial v}{\partial y} + \frac{w}{R_y}\right) + \frac{\partial w}{\partial x}.\left(\frac{\partial w}{\partial y} - \frac{v}{R_y}\right)\right] \\ 2\left[\frac{\partial u}{\partial x}.\frac{\partial u}{\partial z} + \frac{\partial v}{\partial x}.\frac{\partial v}{\partial z} + \frac{\partial w}{\partial z}.\frac{\partial w}{\partial x}\right] \\ 2\left[\frac{\partial u}{\partial y}.\frac{\partial u}{\partial z} + \left(\frac{\partial v}{\partial y} + \frac{w}{R_y}\right).\frac{\partial v}{\partial z} + \frac{\partial w}{\partial z}.\left(\frac{\partial w}{\partial y} - \frac{v}{R_y}\right)\right] \end{Bmatrix} \tag{2.114}$$

The stress resultants developed due to thermal and centrifugal load are given by

$$\{\sigma_0\}_{Th} = \begin{bmatrix} N_x^{Th} \\ N_y^{Th} \\ N_{xy}^{Th} \end{bmatrix} \tag{2.115a}$$

$$\{\sigma_0\}_R = \begin{bmatrix} N_x^R \\ N_y^R \\ N_{xy}^R \end{bmatrix} \tag{2.115b}$$

Substituting the values on nonlinear strains and initial stress resultants in Equation (2.113), one can get

$$U_2 = \frac{1}{2}\int_V \{H\}^T[A_{GTh}]\{H\}\,dv + \frac{1}{2}\int_V \{H\}^T[A_{GR}]\{H\}dv \tag{2.116}$$

where $\{H\} = [Z][G]\{\delta_e\}$ and $[A_{Gk}] = \begin{bmatrix} N_x^k & N_{xy}^k \\ N_{xy}^k & N_y^k \end{bmatrix}_{k=R\ or\ Th}$

$[G]$ matrix contains the derivatives of shape functions and it is expressed as

$$[G] = \sum_{i=1}^{8} \begin{bmatrix} N_{i,x} & 0 & 0 & 0 & 0 & 0 & 0 \\ N_{i,y} & 0 & N_i/R_{xy} & 0 & 0 & 0 & 0 \\ 0 & N_{i,x} & N_i/R_{xy} & 0 & 0 & 0 & 0 \\ 0 & N_{i,y} & N_i/R_y & 0 & 0 & 0 & 0 \\ 0 & 0 & N_{i,x} & 0 & 0 & 0 & 0 \\ 0 & -N_i/R_y & N_{i,y} & 0 & 0 & 0 & 0 \\ 0 & 0 & 0 & N_{i,x} & 0 & 0 & 0 \\ 0 & 0 & 0 & N_{i,y} & 0 & 0 & 0 \\ 0 & 0 & 0 & 0 & N_{i,x} & 0 & 0 \\ 0 & 0 & 0 & 0 & N_{i,y} & 0 & 0 \\ 0 & 0 & 0 & 0 & 0 & N_{i,x} & 0 \\ 0 & 0 & 0 & 0 & 0 & N_{i,y} & 0 \\ 0 & 0 & 0 & 0 & 0 & 0 & N_{i,x} \\ 0 & 0 & 0 & 0 & 0 & 0 & N_{i,y} \\ 0 & 0 & 0 & 0 & 0 & 0 & 0 \\ 0 & 0 & 0 & 0 & -N_i/R_y & 0 & 0 \\ 0 & 0 & 0 & 0 & 0 & 0 & 0 \\ 0 & 0 & 0 & 0 & 0 & 0 & -N_i/R_y \end{bmatrix} \tag{2.117}$$

After putting the values of $\{H\}$ and $[A_{Gk}]$ in the Equation (2.116), we have

$$U_2 = \frac{1}{2}\int_V \{\delta_e\}^T[G]^T[Z]^T[A_{GTh}][Z][G]\{\delta_e\}\,dv + \frac{1}{2}\int_V \{\delta_e\}^T[G]^T[Z]^T[A_{GR}][Z][G]\{\delta_e\}dv \tag{2.118}$$

The value of $[Z]$ is taken from Eq. (2.63) for trigonometric HSDT and it is taken from Eq. (2.78) for polynomial HSDT

In order to simplify the above expression, the integrations are performed as

$$\int_Z [Z]^T [A_{GTh}][Z]dz = [S]_{Th} \tag{2.119a}$$

$$\int_Z [Z]^T [A_{GR}][Z]dz = [S]_R \tag{2.119b}$$

Where $[S]_R$ and $[S]_{Th}$ denote the matrices that encapsulate the in-plane stress resultants generated by thermal and rotational influences, respectively.

The elemental strain energy due to initial stresses will take the form

$$U_2 = \frac{1}{2}\int_A \{\delta_e\}^T [G]^T [S]_{Th}[G]\{\delta_e\}\, dA + \frac{1}{2}\int_A \{\delta_e\}^T [G]^T [S]_R [G]\{\delta_e\} dA \tag{2.120}$$

Finally, Eq. (2.120) can be reduced as

$$U_2 = \frac{1}{2}\{\delta_e\}^T([K_{GThe}] + [K_{GRe}])\{\delta_e\} \tag{2.121}$$

where $[K_{GThe}]$ and $[K_{GRe}]$ denote the geometrical stiffness matrices due to the thermal effect and rotational effect respectively.

Where

$$[K_{GThe}] = \int_A \{G\}^T [S]_{Th}[G] dA \tag{2.122}$$

$$[K_{GRe}] = \int_A \{G\}^T [S]_R [G] dA \tag{2.123}$$

The integrals in the above expressions are numerically evaluated by using Gaussian quadrature of orders 2 (4 points) (Cook et al., 1989).

Finally the total strain energy stored in the shell is expressed as

$$U = U_1 + U_2 = \frac{1}{2}\{\delta_e\}^T [K_e]\{\delta_e\} + \frac{1}{2}\{\delta_e\}^T([K_{GRe}] + [K_{GThe}])\{\delta_e\} \tag{2.124}$$

2.8.2. Kinetic Energy of rotating FG conical shell

Two coordinate systems, (x′, y′, z′) and (x, y, z), are employed for modeling a rotating conical shell (Fig. 2.6), where (x′, y′, z′) represents the inertial or fixed frame of reference, and (x, y, z) denotes the shell coordinate system (local coordinate system).

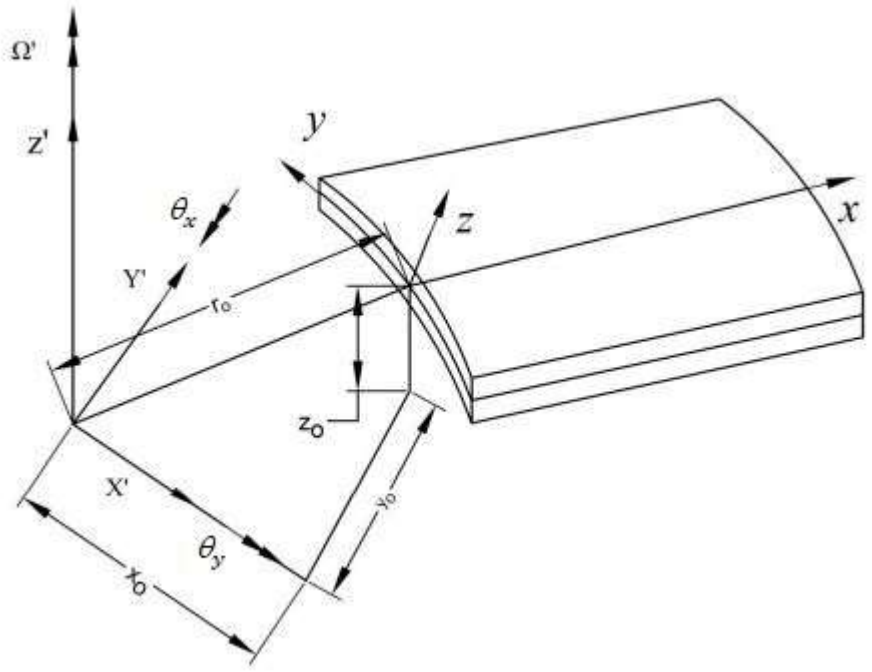

Figure 2.6 Rotating FG conical shell with two reference frames and offsets

The total kinetic energy of a rotating conical shell can be expressed as

$$T = \frac{1}{2}\int_{v} \rho \vec{V}.\vec{V} dv \tag{2.125}$$

where, $\vec{V}$ is the absolute velocity vector of an arbitrary point on the shell with respect to inertial reference frame (x', y', z') and ρ is the mass density of the composite shell. It is assumed that the conical shell rotates about the inertial coordinate system (x', y', z') with an angular velocity component $\Omega = \Omega' k'$ about the Z′ axis, wherein k' is the unit vector along Z′ axis.

The components of angular velocity corresponding to the shell's local coordinate system are specified as

$$\{\Omega'_x, \quad \Omega'_{y,} \quad \Omega'_z\} = \{0, \quad 0, \quad \Omega'\}\left[T_{\theta y}\right]'[T_{\theta x}]' \tag{2.126}$$

where

$$\left[T_{\theta y}\right] = \begin{bmatrix} cos(\theta_y) & 0 & -sin(\theta_y) \\ 0 & 1 & 0 \\ sin(\theta_y) & 0 & cos(\theta_y) \end{bmatrix} \tag{2.127}$$

$$[T_{\theta x}] = \begin{bmatrix} 1 & 0 & 0 \\ 0 & cos(\theta_x) & -sin(\theta_x) \\ 0 & sin(\theta_x) & cos(\theta_x) \end{bmatrix} \tag{2.128}$$

where Ω' is the speed of rotation of the conical shell about z′ axis of the inertial coordinate system (x', y', z'), θ_y is the precone angle and θ_x is the skew angle. The order of rotations is θ_x and θ_y. The fixed translational offsets expressed with reference to conical shell or local coordinate systems are given as

$$\{h_x, \quad h_y, \quad h_z\} = \{x_0, \quad y_0, \quad z_0\}\left[T_{\theta y}\right]'[T_{\theta x}]' \tag{2.129}$$

The unit vectors for the inertial reference frame and local coordinate axes are (i', j', k') and (i, j, k), respectively. Chasle's theorem states that

$$\vec{V} = \frac{d\vec{r}}{dt} + (\Omega' k') \times \vec{r} \tag{2.130}$$

where $\vec{r}$ indicates the position vector of the arbitrary point on the conical shell after deformation from the origin of the inertial reference frame and is given by

$$\vec{r} = (h_x + x + u)i + \left(h_y + y + v\right)j + (h_z + z + w)k \tag{2.131}$$

where (x, y, z) are the coordinates of the point in the shell coordinate system (local coordinate axes), (h_x, h_y, h_z) are the fixed translational offsets of the shell coordinate axes from the inertial axes expressed with reference to the shell coordinate system, (u, v, w) are the elastic deflections of a point.

The angular velocity vector Ω' in Eq. (2.130) is given by

$$\Omega = \Omega' k' = \Omega'_x i + \Omega'_y j + \Omega'_z k \tag{2.132}$$

where $(\Omega'_x, \Omega'_y, \Omega'_z)$ are the components of angular velocity in the shell coordinate system.

Substituting the expressions of $\vec{r}$ and Ω into Eq. (2.130), the absolute velocity $\vec{V}$ can be derived as

$$\begin{aligned} \vec{V} = &\left[\dot{u} + \Omega'_y(h_z + z + \dot{w}) - \Omega'_z\left(h_y + y + v\right)\right] i \\ &+ \left[\dot{v} + \Omega'_z\left(h_y + y + v\right) - \Omega'_x(h_x + x + u)\right] j \\ &+ \left[\dot{w} + \Omega'_x(h_x + x + u) - \Omega'_y(h_z + z + w)\right] k \end{aligned} \tag{2.133}$$

Computing $\left|\vec{V}\right|^2$ and by eliminating the variables that contribute nothing when Lagrange's equation of motion is applied and inserting the resultant expression into the kinetic energy formula, one can obtain,

$$T = \frac{1}{2}\int_v \rho \begin{Bmatrix}\dot{u}\\ \dot{v}\\ \dot{w}\end{Bmatrix}^T \begin{Bmatrix}\dot{u}\\ \dot{v}\\ \dot{w}\end{Bmatrix} dv + \frac{1}{2}\int_v \rho \begin{Bmatrix}\dot{u}\\ \dot{v}\\ \dot{w}\end{Bmatrix}^T [A_1] \begin{Bmatrix}u\\ v\\ w\end{Bmatrix} dv + \frac{1}{2}\int_v \rho \begin{Bmatrix}u\\ v\\ w\end{Bmatrix}^T [A_2] \begin{Bmatrix}u\\ v\\ w\end{Bmatrix} dv + \frac{1}{2}\int_v \rho \begin{Bmatrix}h_x + x\\ h_y + y\\ h_z + z\end{Bmatrix}^T [A_2] \begin{Bmatrix}u\\ v\\ w\end{Bmatrix}^T dv \tag{2.134}$$

where the matrices $[A_1]$ and $[A_2]$ are given by

$$[A_1] = \begin{bmatrix} 0 & -2\Omega'_z & 2\Omega'_y \\ 2\Omega'_z & 0 & -2\Omega'_x \\ -2\Omega'_y & 2\Omega'_x & 0 \end{bmatrix} \tag{2.135}$$

$$[A_2] = \begin{bmatrix} {\Omega'_y}^2 + {\Omega'_z}^2 & -\Omega'_x\Omega'_y & -\Omega'_x\Omega'_z \\ -\Omega'_x\Omega'_y & {\Omega'_z}^2 + {\Omega'_x}^2 & -\Omega'_y\Omega'_z \\ -\Omega'_x\Omega'_z & -\Omega'_y\Omega'_z & {\Omega'_x}^2 + {\Omega'_y}^2 \end{bmatrix} \tag{2.136}$$

The displacement vector $\{\delta\}$ at any point in the element can be written as

$$\{\delta\} = \begin{Bmatrix}u\\ v\\ w\end{Bmatrix} = [N]\{\delta_e\} \tag{2.137}$$

where $[N]$ stands for the shape function matrix and $\{\delta_e\}$ stands for the element nodal displacement vector.

The expression for the kinetic energy of an element is derived by substituting the aforementioned relation as

$$T = \frac{1}{2}\int_v \rho\{\dot{\delta}_e\}^T [N]^T [N]\{\dot{\delta}_e\} dv + \frac{1}{2}\int_v \rho\{\dot{\delta}_e\}^T [N]^T [A_1][N]\{\delta_e\} dv + \frac{1}{2}\int_v \rho\{\delta_e\}^T [N]^T [A_2][N]\{\delta_e\} dv + \frac{1}{2}\int_v \rho \begin{Bmatrix}h_x + x\\ h_y + y\\ h_z + z\end{Bmatrix}^T [A_2][N]^T\{\delta_e\}^T dv \tag{2.138}$$

Finally, which can be expressed as

$$T = \frac{1}{2}\{\dot{\delta}_e\}^T [M_e]\{\dot{\delta}_e\} + \frac{1}{2}\{\dot{\delta}_e\}^T [C_e]\{\delta_e\} + \frac{1}{2}\{\delta_e\}^T [K_R]\{\delta_e\} + \frac{1}{2}\{\delta_e\}^T \{F_{cfe}\} \tag{2.139}$$

where, the element mass matrix of the conical shell is (by putting the values of inertia matrix $[m]$)

$$[M_e] = \int_v [N]^T [m][N] dA \tag{2.140}$$

The element Coriolis matrix (skew symmetric) is

$$[C_e] = \rho \int_v [N]^T [A_1][N] dv \tag{2.141}$$

The element rotational stiffness matrix (symmetric and positive definite) is

$$[K_R] = \rho \int_v [N]^T [A_2][N] dv \tag{2.142}$$

The element centrifugal force vector is

$$[F_{cfe}] = \rho \int_v [N]^T [A_2] \begin{Bmatrix} h_x + x \\ h_y + y \\ h_z + z \end{Bmatrix}^T dv \tag{2.143}$$

2.9 GOVERNING EQUATION OF MOTION

The dynamic equilibrium equation of the tapered pretwisted FG conical shell element will be obtained using Lagrange's equation of motion.

$$\frac{d}{dt}\left(\frac{\partial T_e}{\partial \dot{\delta}_e}\right) - \frac{\partial T_e}{\partial \delta_e} + \frac{\partial V_e}{\partial \delta_e} = 0 \tag{2.144}$$

On substitution of the expressions of the elemental kinetic energy and strain energy, the governing equation of motion of FG conical shell element becomes

$$[M_e]\{\ddot{\delta}_e\} + [C_e]\{\dot{\delta}_e\} + ([K_e] + [K_{GRe}] + [K_{GThe}] - [K_R])\{\delta_e\} = \left[F_{cfe}\right] \quad (2.145)$$

For moderate rotational speeds, the Coriolis matrix and rotational stiffness matrix are disregarded, resulting in the simplification of the dynamic equilibrium equation to

$$[M_e]\{\ddot{\delta}_e\} + ([K_e] + [K_{GRe}] + [K_{GThe}])\{\delta_e\} = \left[F_{cfe}\right] \quad (2.146)$$

Upon assembling all elemental matrices and force vectors in relation to the global coordinates, the resultant dynamic equilibrium equation is expressed as

$$[M]\{\ddot{\delta}\} + ([K] + [K_{GT}] + [K_{GR}])\{\delta\} = \{F_{cf}\} \quad (2.147)$$

where $[M]$, $[K]$, $[K_{GR}]$ and $[K_{GT}]$ represent the global mass matrix, global elastic stiffness matrix, global geometric rotational stiffness matrix and global geometric thermal stiffness matrix, respectively. $\left[F_{cf}\right]$ is the vector of nodal equivalent due to centrifugal forces and $\{\delta\}$ is the global displacement vector.

In the aforementioned equation, $[K_{GR}]$ is contingent upon the initial stress distribution induced by the rotating action and is ascertained by an iterative approach (Sreenivasamurthy and Ramamurti, 1981) upon solving

$$([K] + [K_{GR}] + [K_{GTh}])\{\delta\} = \left[F_{cf}\right] \quad (2.148)$$

Initially, the stresses due to rotation are taken as zero and Eq. (2.149) turns into

$$([K] + [K_{GTh}])\{\delta\} = \left[F_{cf}\right] \quad (2.149)$$

After solving the above equation, the initial form of stress distribution is as follows

$$([K] + [K_{GTh}] + [K_{GR1}])\{\delta\} = \left[F_{cf}\right] \quad (2.150)$$

The solution of the above equation derives another new set of stress distributions $[K_{GR2}]$ and the stresses are found to converge within two iterations. Finally, Eq. (2.147) can be obtained as

$$[M]\{\ddot{\delta}\} + ([K] + [K_{GT}] + [K_{GR}])\{\delta\} = 0 \quad (2.151)$$

The natural frequencies are derived from the standard eigenvalue problem utilizing the QR iteration approach (Bathe, 1990) as follows:

$$[A]\{\delta\} = \lambda\,\{\delta\} \quad (2.152)$$

where

$$[A] = ([K] + [K_{GT}] + [K_{GR}])^{-1}[M] \text{ and } \lambda = \frac{1}{\omega^2} \quad (2.153)$$

where ω is the vector of Eigen values of the porous taper FG conical shell with pretwist.

CHAPTER 3

FREE VIBRATION ANALYSIS OF ROTATING POROUS FG CONICAL SHELLS (p-FGM, e-FGM and s-FGM) IN THERMAL ENVIRONMENT

3.1 INTRODUCTION

Aviation engines rely on turbomachinery blades in order to transform the pressure and kinetic energy of a gas flow into extremely high spinning speeds. These blades frequently experience high speeds, intense temperature loads, and tremendous pressure. When developing the rotating blades for a gas turbine or aero engine, a significant issue is the endurance of the blade materials to withstand the high temperature and high-velocity gaseous flow. Initially, functionally graded materials (FGMs) were proposed as a solution for this problem. Specialized, cutting-edge composite materials consisting metal and ceramic constituents have been designed as FGMs. The ceramic component's role is to protect the blades from extreme temperature gradients while the metal component provides structural support. FGMs are resistant to all types of interlaminar debonding or delamination as well as fibre breaking at high temperatures as compared to laminated composites. Therefore, it is highly relevant to study the vibration characteristics of rotating FGM blades operating in a thermal environment.

There has been much research on the free vibration response of functionally graded conical shells, but no studies that account for the porosity and rotating nature of the FG pretwisted conical shell in thermal environment have been reported so far. This challenge has been taken into account using a finite element approach based on polynomial and non-polynomial HSDT to find a free vibration solution. Three varieties of functionally graded conical shells (p-FGM, e-FGM and s-FGM) are included with porosities under nonlinear temperature distributions, which will make the study more idealised with the practical scenario. The pretwisted FG conical shell with cantilever boundary condition might be considered a turbomachinery blade. This blade's rotation speed is thought to be moderate, thus the Coriolis effects are disregarded (Sreenivasamurthy and Ramamurti, 1981). Lagrange's equation is used to derive the governing equation of motion. In order to verify the convergence and accuracy of the formulation, benchmark problems are addressed. Regarding the free vibration behaviour of the FG porous conical shell, the impact of a number of variables including porosity, temperature, twist angle

and rotational speed has been studied. The effect of twist angle, temperature and rotating speed on the mode shapes of the conical shell is also examined.

3.2 NUMERICAL RESULTS AND DISCUSSIONS

The mathematical analysis based on finite element formulations are employed to develop an in-house computer code to evaluate the natural frequencies of rotating porous conical shell in thermal environments for three different types of functionally graded materials i.e., p-FGM, e-FGM, and s-FGM. Here, the ceramic portion of FGM shell is made of silicon nitride (Si_3N_4) and the metallic portion is made of stainless steel (SUS304). The variation of the ceramic and metallic portion of the FGM shells follows three different patterns (p-FGM, e-FGM, s-FGM) as discussed in Chapter-2. The material properties of the metal and ceramic constituents are considered as temperature dependent. The Young's modulus, Poisson's ratio and thermal expansion coefficient and the effective material properties are computed by using respective equations as discussed earlier wherein the temperature-dependent coefficients of Si_3N_4 and SUS304 are shown in Table 3.1.

Table 3.1 Temperature-dependent material properties of ceramic and metal (unit of E in Pa, α_t in 1/K, suffix m and c refer to metal and ceramic, respectively)

Material	Properties	P_{-1}	P_0	P_1	P_2	P_3
SUS304	E_m	0	201.04×10^9	3.079×10^{-4}	-6.534×10^{-7}	0
	α_{tm}	0	12.330×10^{-6}	8.086×10^{-6}	0	0
	υ_m	0	0.3262	-2.002×10^{-4}	3.797×10^{-7}	0
Si_3N_4	E_c	0	348.43×10^9	-3.070×10^{-4}	2.160×10^{-7}	-8.946×10^{-11}
	α_{tc}	0	5.8723×10^{-6}	9.095×10^{-6}	0	0
	υ_c	0	0.24	0	0	0

The two temperature independent material properties of SUS304 and Si_3N_4 are as follows

$\rho_m = 8166$ kg/m^3

$K_m = 12.04$W/mK

$\rho_c = 2370$ kg/m^3

$K_c = 9.19$W/mK

where suffix m and c indicate metal and ceramic, respectively.

Unless and otherwise stated, the geometric dimensions and other parameters adopted for the porous FG conical shell are as follows

s = 0.5 m, ϕ_0 = 75°, ϕ_v = 50°, L/s = 0.4, s/h = 20

where length of the shell is L, cone length is s, reference width is b_0, vertex angle is ϕ_v, and base subtended angle is ϕ_0 (Figure 2.1).

The cantilever boundary condition is expressed as:

At x=0, $u = v = w = \theta_x = \theta_y = \xi_x = \xi_y = 0$ (3.1)

where $u, v,$ and w are the displacement variables along $x, y,$ and z axes and two rotational variables θ_x, θ_y which denote the rotations of the normal to the mid-surface about y and x −axes respectively.

The variation of Young's modulus across the thickness of the FG conical shell of p- FGM, e-FGM and s-FGM having different temperature at top surface are shown in Fig 3.1 to 3.6.

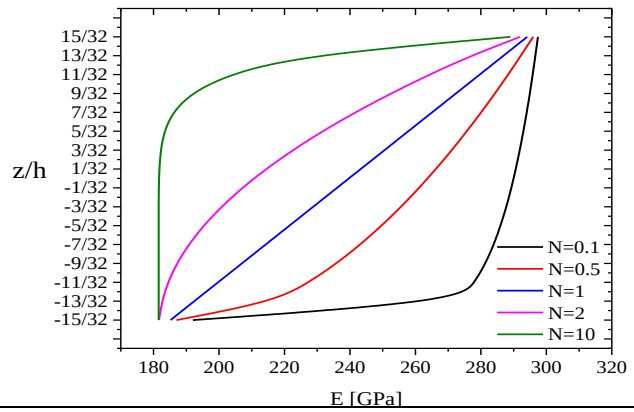

(a) Even porosity with T_t = 300K

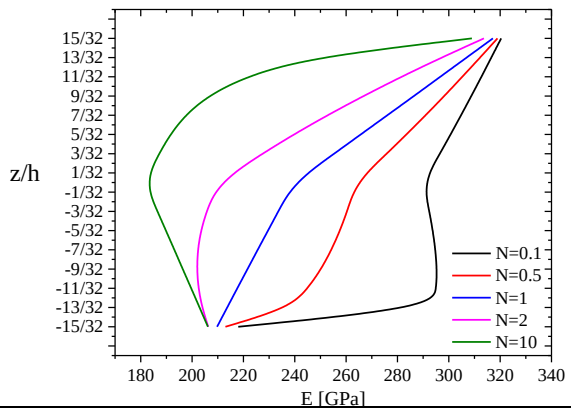

(b) Uneven porosity with T_t = 300K

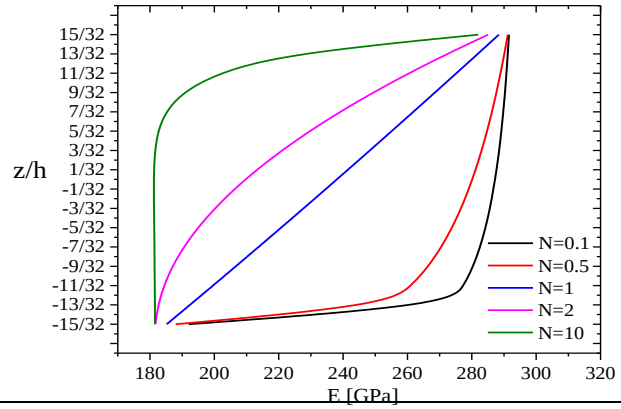

(c) Even porosity with T_t = 400K

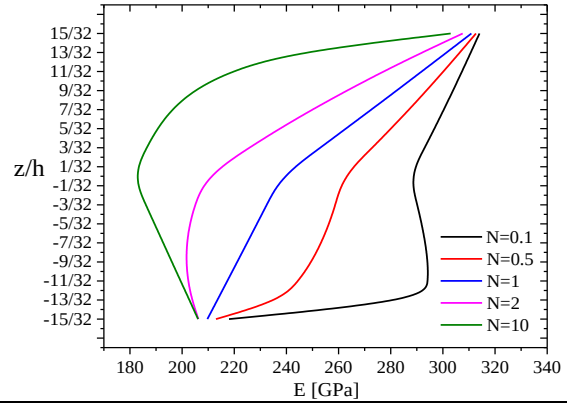

(d) Uneven porosity with T_t =400K

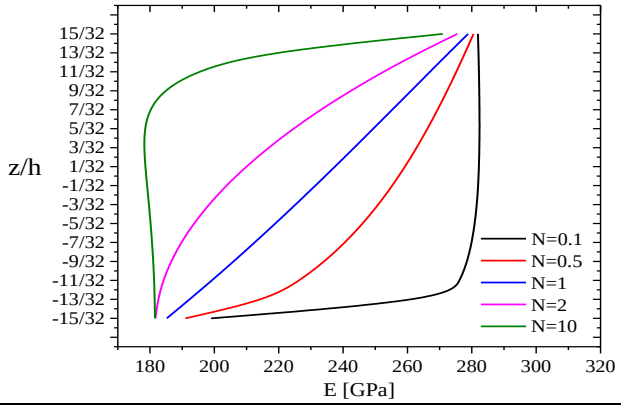

(e) Even porosity with T_t = 600K

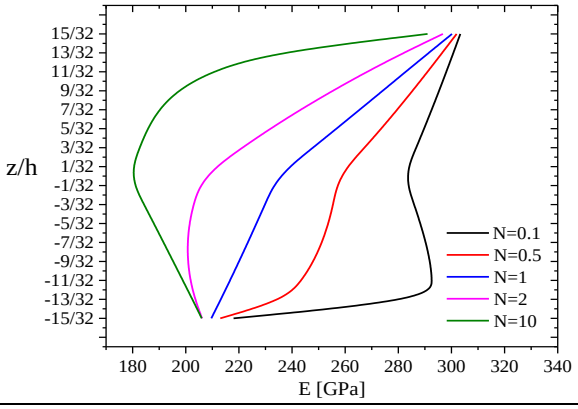

(e) Uneven porosity with T_t = 600K

Figure 3.1 Representation of Young's Modulus across the thickness of p-FGM for different temperature distribution (T_t) when volume fraction of porosity (α) is 0.1

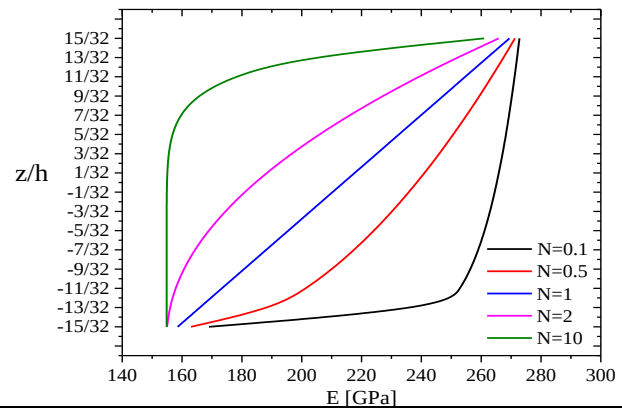

(a) Even porosity with T_t = 300K

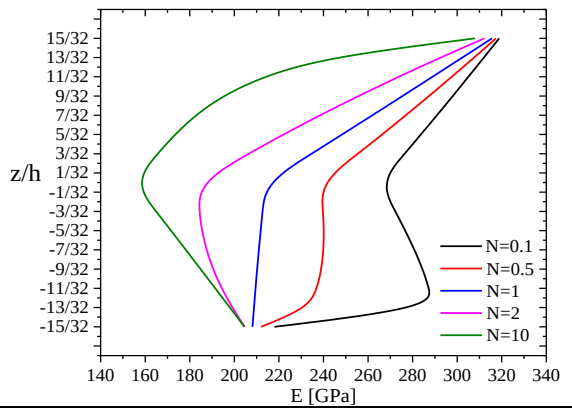

(b) Uneven porosity with T_t = 300K

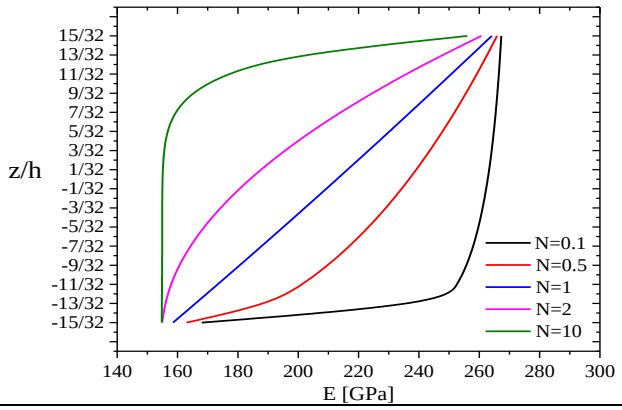

(c) Even porosity with T_t = 400K

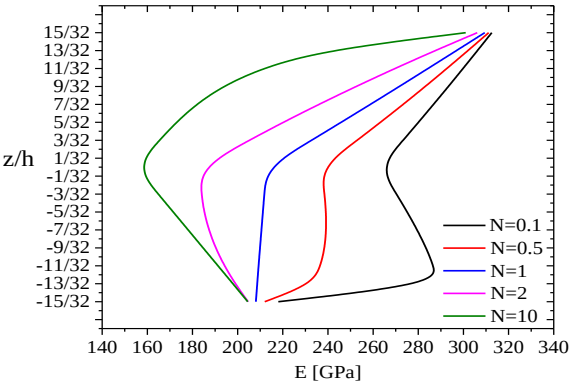

(d) Uneven porosity with T_t =400K

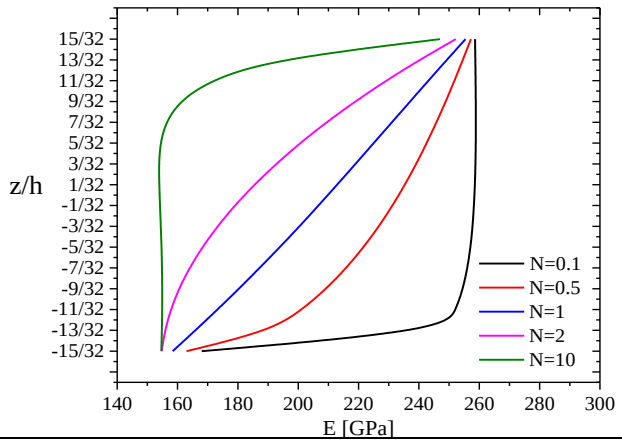

(e) Even porosity with T_t = 600K

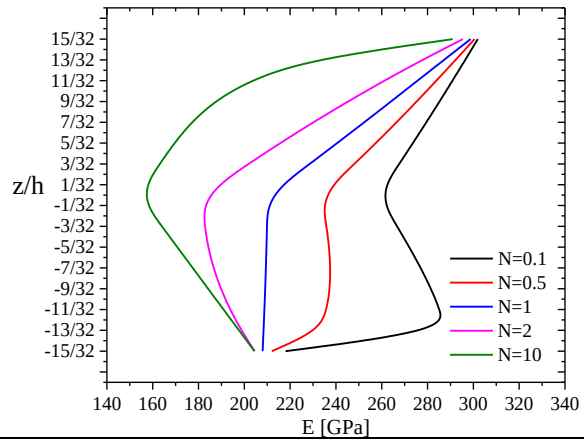

(e) Uneven porosity with T_t = 600K

Figure 3.2 Representation of Young's Modulus across the thickness of p-FGM for different temperature distribution (T_t) when volume fraction of porosity (α) is 0.2

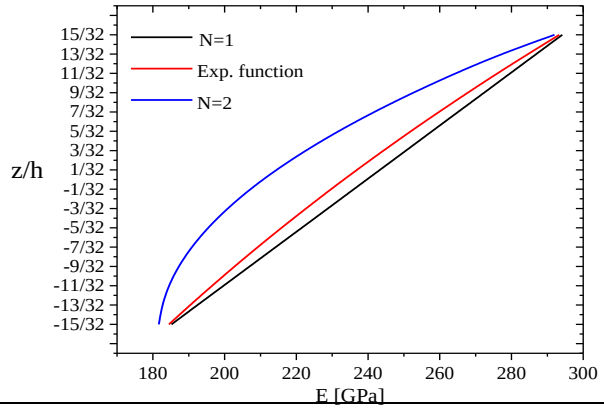

(a) Even porosity with T_t = 300K

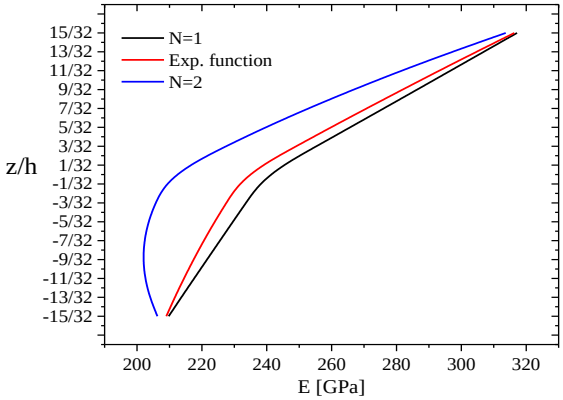

(b) Uneven porosity with T_t = 300K

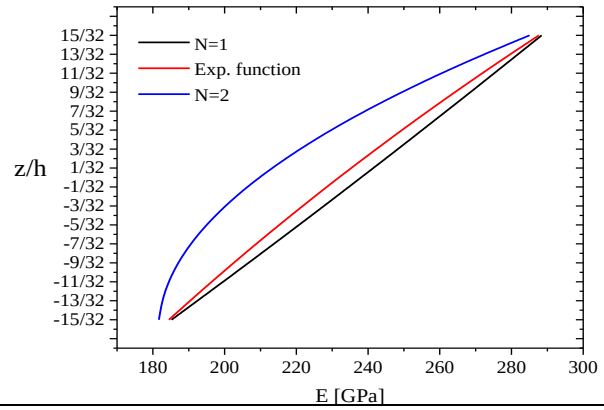

(c) Even porosity with T_t = 400K

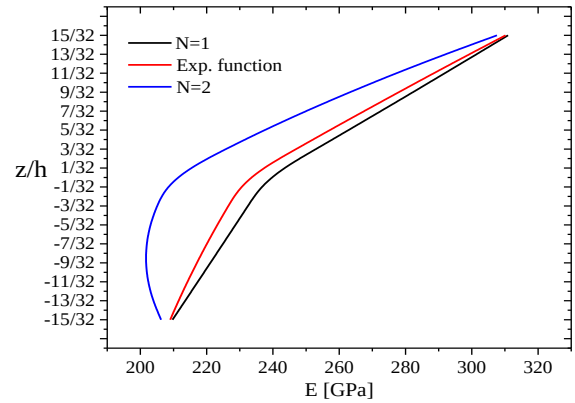

(d) Uneven porosity with T_t =400K

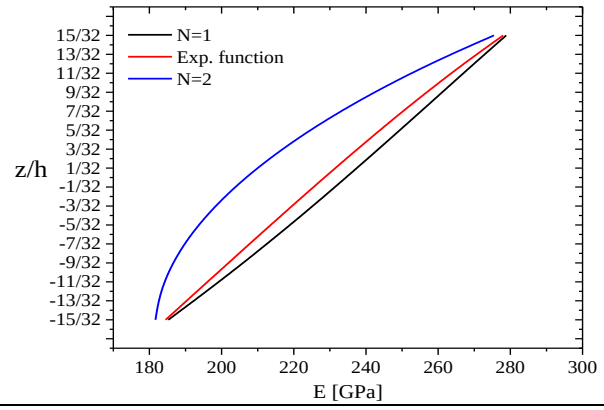

(e) Even porosity with T_t = 600K

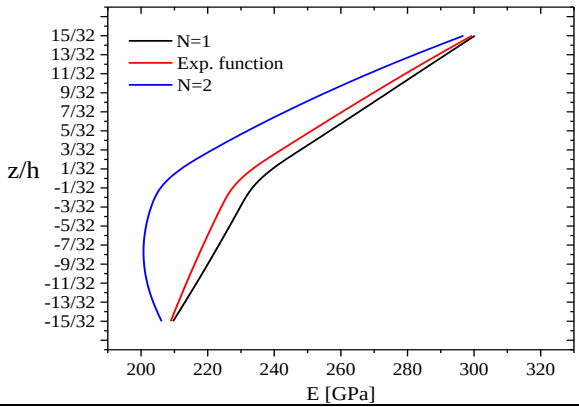

(e) Uneven porosity with T_t = 600K

Figure 3.3 Representation of Young's Modulus across the thickness of e-FGM for different temperature distribution (T_t) when volume fraction of porosity (α) is 0.1

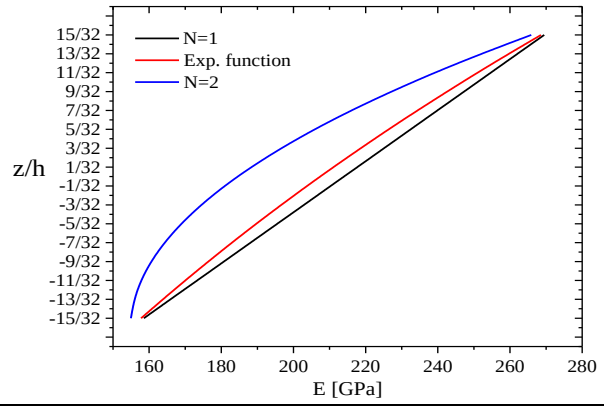

(a) Even porosity with T_t = 300K

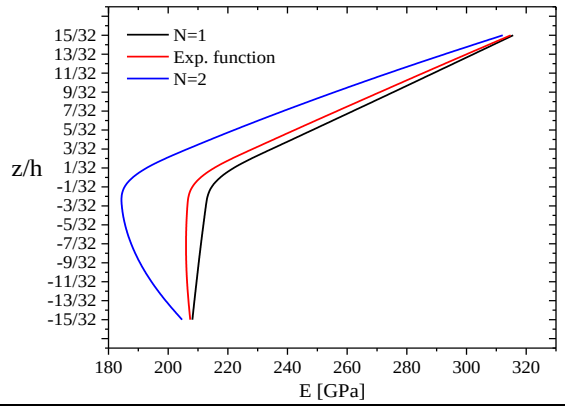

(b) Uneven porosity with T_t = 300K

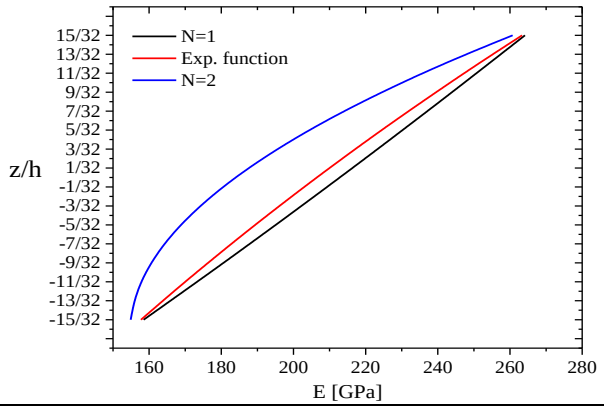

(c) Even porosity with T_t = 400K

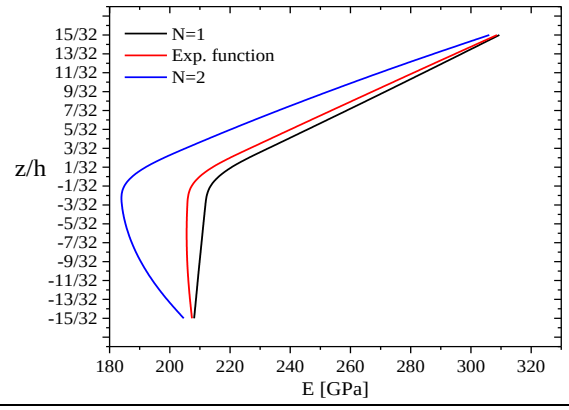

(d) Uneven porosity with T_t =400K

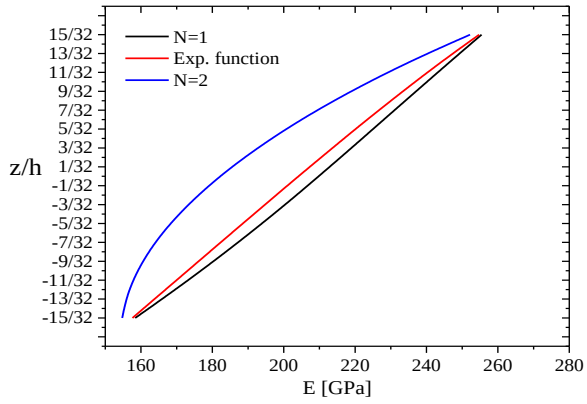

(e) Even porosity with T_t = 600K

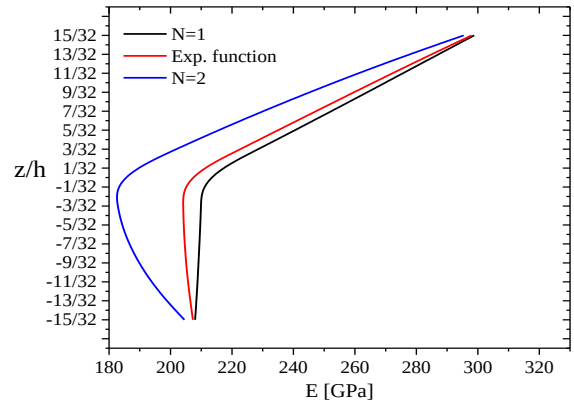

(e) Uneven porosity with T_t = 600K

Figure 3.4 Representation of Young's Modulus across the thickness of e-FGM for different temperature distribution (T_t) when volume fraction of porosity (α) is 0.2

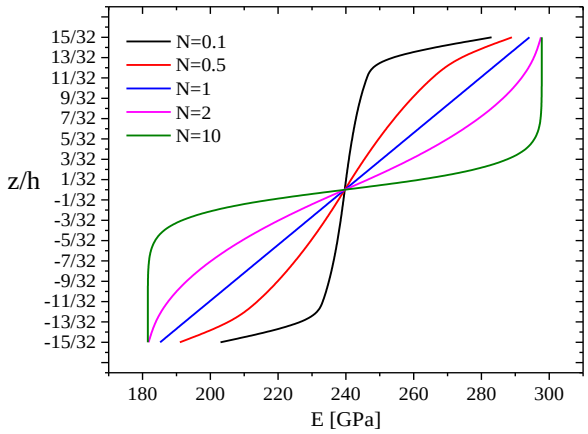

(a) Even porosity with T_t = 300K

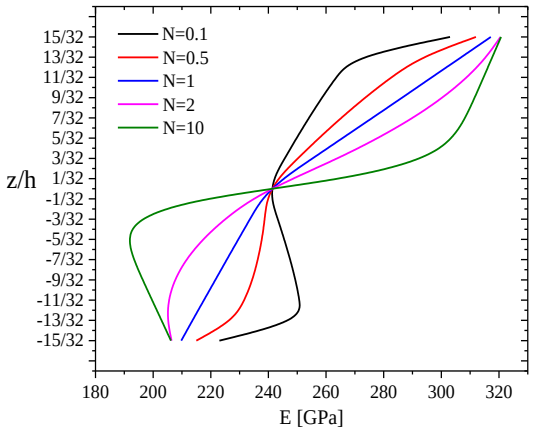

(b) Uneven porosity with T_t = 300K

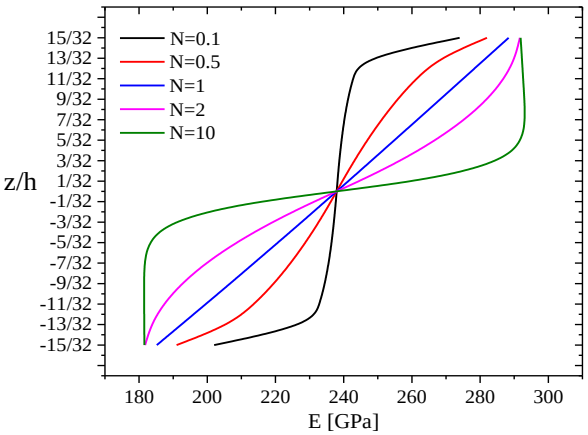

(c) Even porosity with T_t = 400K

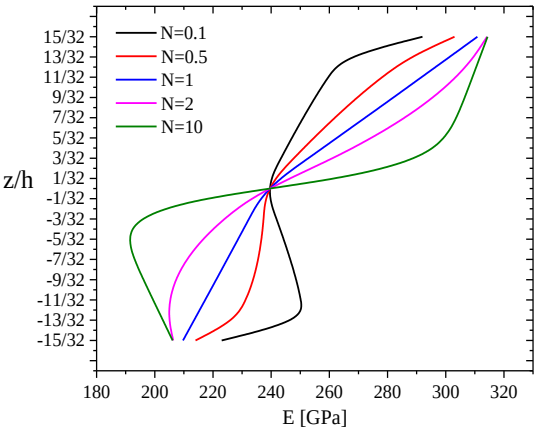

(d) Uneven porosity with T_t =400K

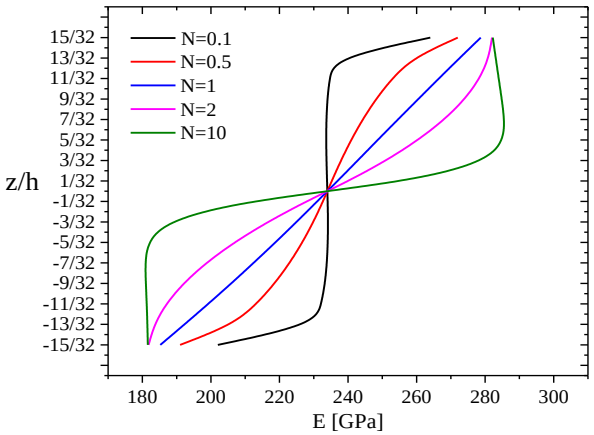

(e) Even porosity with T_t = 600K

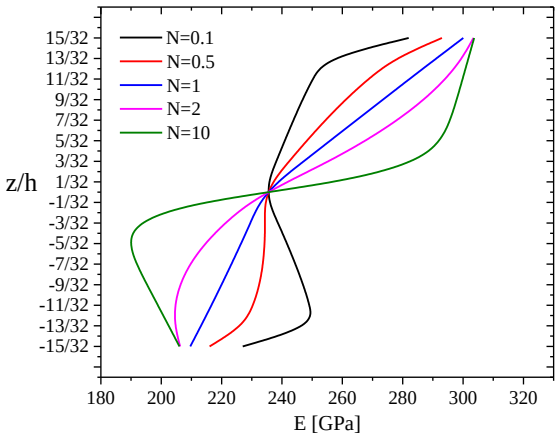

(e) Uneven porosity with T_t = 600K

Figure 3.5 Representation of Young's Modulus across the thickness of s-FGM for different temperature distribution (T_t) when volume fraction of porosity (α) is 0.1

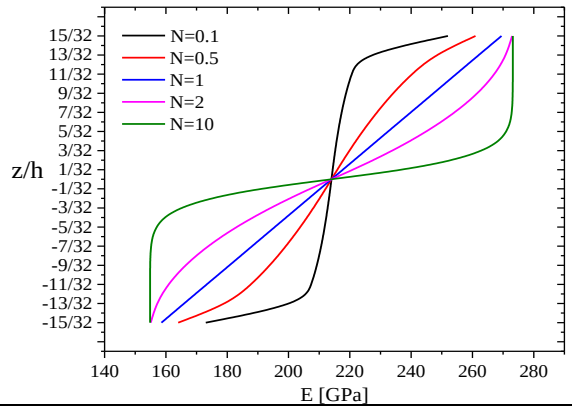

(a) Even porosity with T_t = 300K

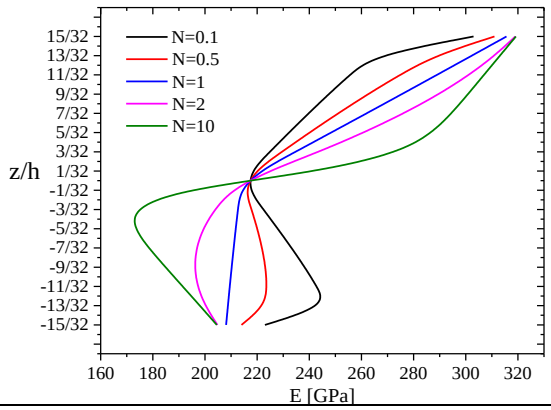

(b) Uneven porosity with T_t = 300K

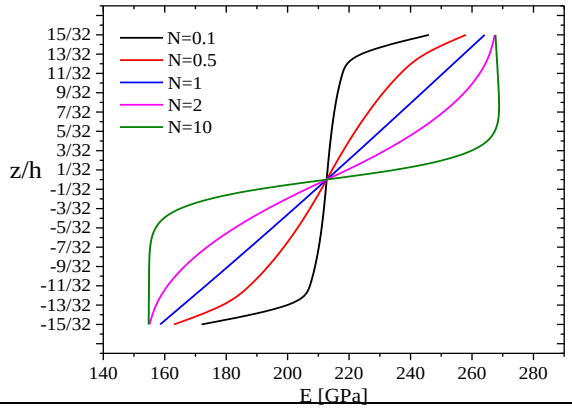

(c) Even porosity with T_t = 400K

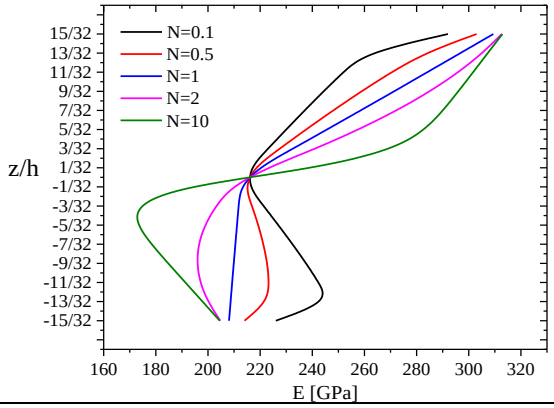

(d) Uneven porosity with T_t =400K

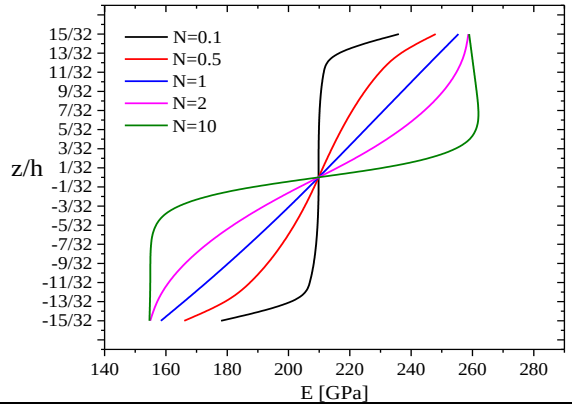

(e) Even porosity with T_t = 600K

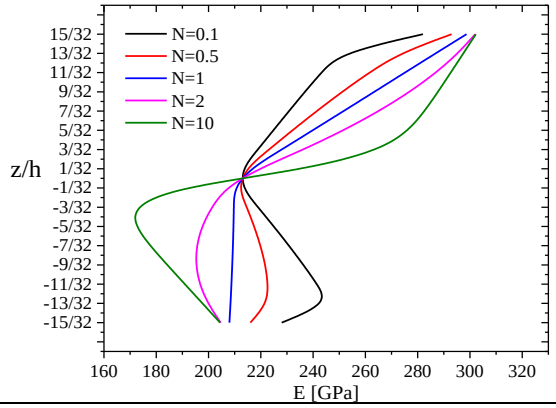

(e) Uneven porosity with T_t = 600K

Figure 3.6 Representation of Young's Modulus across the thickness of s-FGM for different temperature distribution (T_t) when volume fraction of porosity (α) is 0.2

So it is observed from the Figure 3.1 to Figure 3.6 that with the increase of temperature at the top surface the value of Young's modulus reduces and for uneven porosity distribution the value of Young's modulus is greater than even porosity at same temperature distribution.

3.3 VALIDATION AND CONVERGENCE STUDIES

The numerical findings from the in-house computer programme are compared to those found in the literature, which are provided in Table 3.2 to Table 3.9. The validation of the code is carried out to ensure that the formulation is accurate. In Table 3.2, which compares the non-dimensional frequency of pretwisted shallow conical shells with Liew et al. (1994), validity of the formulation in relation to the pretwisted conical shell is shown. Table 3.3 displays the accuracy of the code in comparison to free vibration of rotating plates (Sreenivasamurthy and Ramamurti, 1981). Table 3.4 shows the confirmation of the first four natural frequencies for various power-law indices of p-FGM plates. While Table 3.5 provides the first six natural frequencies of e-FGM plates for various aspect ratios, the same problem was reported by Kumar and Jana (2019). There is a slight discrepancy in the outcomes, which may be the consequence of Kumar and Jana (2019) not taking into account the effect of rotational inertia. The comparisons of the natural frequencies for porous p-FGM (Rezaei et al. 2017) and s-FGM (Wang and Zu, 2018) plates, respectively, for various porosity volume fractions are shown in Tables 3.6 and 3.7. Last but not the least, Table 3.8 compares natural frequencies in the presence of a temperature distribution (Huang and Shen, 2004; Parida and Mohanty 2017). Based on the findings of the comparison, it shows a strong agreement with results that have already been published, demonstrating the effectiveness of the developed computer code and the precision of the analyses.

A convergence study is carried out using the mesh sizes of 2×2, 4×4, 6×6, 8×8, and 10×10 as shown in Table 3.9. One can see that the findings conversed at 8×8 mesh size. As a result, the entire study uses a mesh size of 8×8 with 64 elements and 225 nodes.

Table 3.2 Non-dimensional frequency parameters [$\lambda' = \omega_n b_0^2\sqrt{(\rho h/D)}$, $D = Eh^3/12(1-\nu^2)$] for the pretwisted shallow conical shell with $\nu = 0.3$, s/h =1000, $\phi_v = 15°$ and ϕ_0 =30°

Ψ	L/s	1st Mode		2nd Mode	
		Liew et al. (1994)	Present FEM	Liew et al. (1994)	Present FEM
0°	0.3	1.0274	1.02783	2.1768	2.16932
	0.4	0.63879	0.63909	1.7850	1.78094
	0.5	0.45689	0.45711	1.5872	1.58703
	0.3	0.84448	0.84425	2.5766	2.56895

15°	0.4	0.56767	0.56795	1.9704	1.96537
	0.5	0.42308	0.42346	1.6244	1.62634
	0.3	0.58204	0.58173	2.6746	2.67132
30°	0.4	0.42558	0.42592	1.8747	1.87469
	0.5	0.33981	0.34046	1.3660	1.36872
	0.3	0.37519	0.37518	1.8930	1.89384
45°	0.4	0.28260	0.28305	1.3385	1.34063
	0.5	0.23615	0.23695	1.0280	1.03109

Table 3.3 Non-dimensional fundamental frequencies ($\varpi = \omega_n L^2\sqrt{\rho h / D}$) of an isotropic rotating cantilever plate. [L/b =1, $h/L = 0.12$, $D = Eh^3/12(1-\nu^2)$,$\nu = 0.3$]

Nondimensional rotational speed ($\overline{\Omega}$)	Sreenivasamurthy and Ramamurthi (1981)	Present FEM
0.0	3.43685	3.41749
0.2	3.51858	3.49109
0.4	3.75280	3.70191
0.6	4.12875	4.02542
0.8	4.56786	4.43319
1.0	5.09167	4.90043

Table 3.4 Non-dimensional frequency parameters ($\lambda' = \omega_n L^2\sqrt{\rho_c / E_c}$) with the volume fraction exponent N for square Al/Al_2O_3 p-FGM plates (L/h =10) for simply supported boundary condition.

Mode	$N = 1$	$N = 2$	$N = 5$

	Zhao et al. (2009)	Present FEM	Zhao et al. (2009)	Present FEM	Zhao et al. (2009)	Present FEM
1st	4.3474	4.6074	3.9474	4.3656	4.1671	3.7218
2nd	10.4160	10.4384	9.4434	9.6138	9.1616	8.8448
3rd	10.4160	10.4384	9.4434	9.6138	9.1616	8.8448
4th	15.9360	16.1969	14.4310	14.9566	14.1815	13.4450

Table 3.5 Non-dimensional natural frequencies ($\lambda' = \omega_n a^2\sqrt{\rho_c h\ /\ D_c}$) with $D_c = E_c h^3/\ 12(1-\nu^2)$ for all Levy type edge conditions of rectangular **e-FGM** plate for $h/L = 0.005$.

Mode	$L/b = 0.5$		$L/b = 1$		$L/b = 1.5$		$L/b = 2$	
	Kumar and Jana (2019)	Present FEM	Kumar and Jana (2019)	Present FEM	Kumar and Jana (2019)	Present FEM	Kumar and Jana (2019)	Present FEM
1st	8.6856	9.3436	13.897	14.794	22.582	23.975	34.7425	36.7574
2nd	13.897	14.197	34.742	34.215	43.428	43.027	55.588	55.251
3rd	22.569	22.756	34.742	34.215	69.485	66.521	90.3305	87.4388
4th	29.507	28.912	55.588	54.539	78.170	75.815	118.124	109.540
5th	34.742	34.187	69.485	67.221	90.330	86.452	138.969	128.571
6th	34.742	34.505	69.485	67.773	125.07	117.99	138.97	128.57

Table 3.6 Non-dimensional fundamental frequencies ($\varpi = \omega_n h\sqrt{\rho_m\ /\ E_m}$) of simply supported porous **p-FGM** plate for porosity parameters, power law indices and porosity distributions. [$h/L = 0.05, L/b = 0.5$]

Power-law index (N)	Porosity volume fraction (α)	Even		Uneven	
		Rezaei et al. (2017)	Present FEM	Rezaei et al. (2017)	Present FEM
0	0.0	0.018257	0.018256	0.018257	0.018256

	0.2	0.018829	0.018507	0.018804	0.018304
	0.4	0.019669	0.019084	0.019444	0.018408
0.1	0.0	0.017565	0.017713	0.017565	0.017713
	0.2	0.018026	0.017896	0.018082	0.017729
	0.4	0.018712	0.018371	0.018688	0.017790
0.5	0.0	0.015465	0.016103	0.015465	0.016103
	0.2	0.015392	0.015985	0.015820	0.015989
	0.4	0.015184	0.015983	0.016235	0.015909
1	0.0	0.013937	0.014982	0.013937	0.014982
	0.2	0.013184	0.014507	0.014087	0.014749
	0.4	0.011384	0.013716	0.014227	0.014519

Table 3.7 First natural frequencies (in rad/s) of simply supported evenly porous Nickel/Alumina **s-FGM** plate ($L = 0.4$ m, $b = 0.1$ m, $h = 0.001$ m)

Power-law index (N)	Porosity volume fraction (α)	Wang and Zu (2018)	Present FEM
0.3	0.0	2019.8	2016.3
	0.1	2003.3	1999.1
	0.2	1989.3	1983.9
1	0.0	2018.6	2012.9
	0.1	2002.2	1995.0
	0.2	1987.9	1978.7
3	0.0	2017.7	2009.4
	0.1	2001.2	1990.7
	0.2	1986.9	1973.4
5	0.0	1933.9	2008.6
	0.1	1921.6	1989.7
	0.2	1910.9	1972.1

Table 3.8 Non-dimensional fundamental frequency $\left(\varpi = \omega_n L^2/h\sqrt{\rho_0(1-\nu^2)/E_0}\right)$ of simply supported Si_3N_4/SUS304 FGM square plates in **thermal environments**. [L/b=1, L=8h, ρ_c=2370 kg/m^3, ρ_m=8166 kg/m^3, ν_c=0.28,ν_m=0.28, K_c=9.19 W/m K, K_m=12.04 W/m K]

Temperature (T)	Power-law index (N)	Huang and Shen (2004)	Parida and Mohanty (2017)	Present FEM
T_c=300 K	$Si_3N_4(N=0)$	12.495	12.587	12.508
T_m=300 K	0.5	8.675	9.094	8.625
	1.0	7.555	7.656	7.552
	2.0	6.777	6.78	6.778
	SUS304 $(N=\infty)$	5.405	5.445	5.411
T_c=400 K	$Si_3N_4(N=0)$	12.397	12.387	12.308
T_m=300 K	0.5	8.615	8.615	8.468
	1.0	7.474	7.51	7.406
	2.0	6.693	6.642	6.638
	SUS304 $(N=\infty)$	5.311	5.311	5.273
T_c=600 K	$Si_3N_4(N=0)$	11.984	11.971	11.888
T_m=300 K	0.5	8.269	8.272	8.131
	1.0	7.171	7.186	7.087
	2.0	6.398	6.327	6.327
	SUS304 $(N=\infty)$	4.971	4.989	4.923

Table 3.9 Convergence study for fundamental natural frequency (Hz) of pretwisted p-FGM conical shallow shell in thermal environment (s = 0.5 m, ϕ_0 = 75°, ϕ_v = 50°, L/s = 0.4, s/h = 20, T_t = 600 K, Ψ=30°, Even porosity with α = 0.2)

Power-law index (N)	Mesh size				
	2×2	4×4	6×6	8×8	10×10

0	15387.17	15386.31	15384.77	15384.12	15383.92
0.5	8935.90	8934.09	8933.15	8932.75	8932.63
1	7446.83	7445.24	7444.45	7444.12	7444.01
2	6377.31	6376.39	6375.73	6375.45	6375.36
∞	4536.44	4533.69	4533.10	4532.87	4532.80

3.4 RESULTS AND DISCUSSIONS

Even and uneven porosity distributions having volume fraction of porosities 0.1 and 0.2 for both the cases have been considered. Three different temperature distributions are considered for both types of porosity distributions. The temperature of bottom surface is always maintained at 300K but for the top surface at three different instances of temperature distribution 300K, 400K and 600K have been considered. As the porous conical shell element is pretwisted so four values of twist angle (Ψ) is also chosen and these are 0°, 15°, 30° and 45°. For each values of pretwist angle, the natural frequency is calculated for seven different power law indices ($N = 0$, 0.1, 0.5, 1, 2, 10 and ∞). As the natural frequencies in different rotation consequences were also studied, so five different values of normalized rotational speeds are considered and these are 0, 0.25, 0.5, 0.75 and 1.

The top and bottom surface temperatures are denoted by the T_t and T_b, respectively. First, the natural frequencies of p-FGM have been tabulated in Table 3.10 for different porosity distributions. Next, the frequencies of e-FGM are shown in Table 3.11 and lastly the frequencies of s-FGM are tabulated in Table 3.12 for various porosity distributions.

Table 3.10 Non-dimensional fundamental frequencies $\left(\bar{\omega} = \frac{\omega L^2}{2\pi h}\sqrt{\frac{\rho_c}{E_c}}\right)$ of p-FGM cantilever conical shell

Porosity	Temperature	Twist angle (ψ)	$(\bar{\omega})$						
			Si_3N_4 (N=0)	N=0.1	N=0.5	N=1	N=2	N=10	SUS304 (N= ∞)
No porosity	T_t = 300K T_b = 300K	ψ=0	6.11309	5.44219	4.25318	3.71308	3.29793	2.81431	2.64441
		ψ=15	5.56606	4.95109	3.86488	3.37761	3.00906	2.57581	2.40778
		ψ=30	4.65344	4.13685	3.22665	2.82222	2.52039	2.16299	2.01299
		ψ=45	3.65153	3.2447	2.5299	2.21318	1.9799	1.7025	1.57959
	T_t = 400K T_b = 300K	ψ=0	5.91241	5.25287	4.07889	3.54161	3.12507	2.63102	2.45378
		ψ=15	5.31846	4.71678	3.64809	3.16491	2.79666	2.35283	2.17166
		ψ=30	4.35375	3.85346	2.96487	2.5655	2.26402	1.89341	1.72674

		ψ=45	3.27451	2.88811	2.19915	1.88918	1.65562	1.35896	1.21146
	T_t = 600K T_b = 300K	ψ=0	5.39412	4.76269	3.62261	3.08729	2.65908	2.1154	1.90144
		ψ=15	4.65471	4.08431	3.04829	2.56348	2.18036	1.6619	1.38986
		ψ=30	3.52543	3.06214	2.20675	1.79691	1.46379	0.94866	0.56899
		ψ=45	2.10934	1.75765	1.04291	0.60653	0.53402	0.44471	0.40618
Even porosity with volume fraction of porosity α = 0.1	T_t = 300K T_b = 300K	ψ=0	6.74931	5.86021	4.41772	3.80361	3.34468	2.822	2.6401
		ψ=15	6.18183	5.36593	4.0456	3.48948	3.0799	2.60996	2.43122
		ψ=30	5.21107	4.52444	3.41545	2.9524	2.61579	2.22749	2.06807
		ψ=45	4.14716	3.60477	2.72965	2.36632	2.10459	1.80206	1.67204
	T_t = 400K T_b = 300K	ψ=0	6.61129	5.73268	5.18186	3.69054	3.23062	2.70119	2.51511
		ψ=15	6.01209	5.20898	4.70561	3.35129	2.94219	2.4661	2.28013
		ψ=30	5.00405	4.33352	3.9131	2.78592	2.4503	2.05492	1.8865
		ψ=45	3.88886	3.36725	3.03975	2.16137	1.90134	1.59023	1.44857
	T_t = 600K T_b = 300K	ψ=0	6.25824	5.40635	4.0067	3.39765	2.93106	2.37099	2.16326
		ψ=15	5.57294	4.80181	3.53246	2.984	2.56996	2.05872	1.83296
		ψ=30	4.4641	3.83341	2.78853	2.33501	1.99228	1.54939	1.32611
		ψ=45	3.18639	2.71593	1.92051	1.56482	1.28751	0.88297	0.61633
Uneven porosity with volume fraction of porosity α = 0.1	T_t = 300K T_b = 300K	ψ=0	6.42821	5.66037	4.35369	3.77788	3.34081	2.83649	2.66059
		ψ=15	5.88121	5.17639	3.98087	3.46004	3.07034	2.61686	2.44414
		ψ=30	4.94691	4.35357	3.34988	2.91678	2.59686	2.22193	2.06781
		ψ=45	3.9176	3.44896	2.65792	2.31896	2.0709	1.77882	1.65269
	T_t = 400K T_b = 300K	ψ=0	6.26008	5.5032	4.21072	3.63774	3.19979	2.68687	2.50464
		ψ=15	5.67577	4.98402	3.80568	3.28917	2.9003	2.43868	2.25574
		ψ=30	4.6978	4.12067	3.13855	2.71107	2.39247	2.00793	1.84107
		ψ=45	3.60635	3.15835	2.39504	2.06345	1.8172	1.51261	1.36935
	T_t = 600K T_b = 300K	ψ=0	5.82772	5.09852	3.83981	3.27071	2.825	2.27355	2.06281
		ψ=15	5.13579	4.47624	3.33557	2.82355	2.42795	1.91827	1.67921
		ψ=30	4.03143	3.49362	2.55607	2.13171	1.80105	1.34366	1.08903
		ψ=45	2.71687	2.31656	1.59606	1.25097	0.9605	0.39476	0.21514
Even porosity with volume fraction of porosity α = 0.2	T_t = 300K T_b = 300K	ψ=0	7.68888	6.39638	4.56934	3.85913	3.34672	2.77799	2.58161
		ψ=15	7.0663	5.87878	4.20333	3.55814	3.09904	2.58656	2.3941
		ψ=30	5.98205	4.98106	3.57092	3.03221	2.65389	2.23006	2.0582
		ψ=45	4.79199	3.99912	2.88311	2.4588	2.16332	1.83212	1.69198
	T_t = 400K T_b = 300K	ψ=0	7.59915	6.31608	4.49797	3.78855	3.27504	2.70226	2.50425
		ψ=15	6.9538	5.77837	4.11487	3.47155	3.01245	2.49655	2.30073
		ψ=30	5.84112	4.85599	3.46225	2.9266	2.54879	2.12107	1.94478
		ψ=45	4.6136	3.84179	2.7485	2.32901	2.03485	1.69926	1.5534
	T_t = 600K T_b = 300K	ψ=0	7.36607	6.10796	4.31356	3.60547	3.08676	2.4933	2.28157
		ψ=15	6.66446	5.52016	3.88666	3.24649	2.78421	2.24731	2.02955
		ψ=30	5.48208	4.53689	3.1829	2.65237	2.27151	1.81891	1.61527
		ψ=45	4.15383	3.43491	2.39534	1.98332	1.6854	1.3162	1.13199
Uneven porosity	T_t = 300K	ψ=0	6.78886	5.89507	4.44677	3.83047	3.36904	2.84224	2.65999
		ψ=15	6.23471	5.41311	4.8998	3.52698	3.11391	2.6386	2.46058

with volume fraction of porosity α = 0.2	T_b = 300K	ψ=30	5.2682	4.57523	3.45894	2.99328	2.65336	2.25953	2.10068
		ψ=45	4.19782	3.64916	2.76757	2.40235	2.13795	1.83009	1.70008
	T_t = 400K T_b = 300K	ψ=0	6.64684	5.76383	4.32896	3.71537	3.25339	2.71935	2.53153
		ψ=15	6.06212	5.25357	3.943	3.38836	2.97634	2.49449	2.30815
		ψ=30	5.05785	4.38121	3.28619	2.82624	2.48806	2.08681	1.91769
		ψ=45	3.93513	3.40748	2.55376	2.19634	1.93459	1.61776	1.47459
	T_t = 600K T_b = 300K	ψ=0	6.28086	5.42557	4.02402	3.41523	2.94781	2.38218	2.17034
		ψ=15	5.61272	4.83713	3.56601	3.0184	2.60335	2.08638	1.85984
		ψ=30	4.50564	3.86978	2.82349	2.37184	2.02913	1.58078	1.35607
		ψ=45	3.21614	2.74049	1.94604	1.5948	1.31993	0.91126	0.64437

Table 3.11 Non-dimensional fundamental frequencies $\left(\bar{\omega} = \frac{\omega L^2}{2\pi h}\sqrt{\frac{\rho_c}{E_c}}\right)$ of e-FGM cantilever conical shell

Temperature	Twist angle (ψ)	$(\bar{\omega})$				
		No Porosity	α=0.1		α=0.2	
			Even	Uneven	Even	Uneven
T_t = 300K T_b = 300K	ψ=0	3.90862	4.02292	3.98482	4.10821	4.05023
	ψ=15	3.55756	3.69153	3.65086	3.78783	3.73012
	ψ=30	2.97411	3.12321	3.07810	3.22662	3.16541
	ψ=45	2.33325	2.50167	2.44649	2.61312	2.53853
T_t = 400K T_b = 300K	ψ=0	3.73784	3.91116	3.84526	4.03967	3.93565
	ψ=15	3.3459	3.55458	3.48056	3.70306	3.59180
	ψ=30	2.71833	2.95756	2.87256	3.12231	2.99807
	ψ=45	2.0105	2.29706	2.19070	2.48398	2.33142
T_t = 600K T_b = 300K	ψ=0	3.28461	3.61917	3.47791	3.85856	3.63438
	ψ=15	2.751224	3.18966	3.01697	3.48018	3.22150
	ψ=30	1.962953	2.50983	2.29706	2.84987	2.54337
	ψ=45	0.814435	1.70766	1.39298	2.13994	1.73173

Table 3.12 Non-dimensional fundamental frequencies $\left(\bar{\omega} = \frac{\omega L^2}{2\pi h}\sqrt{\frac{\rho_c}{E_c}}\right)$ of s-FGM cantilever conical shell

Porosity	Temperature	Twist angle (ψ)	$(\bar{\omega})$						
			Si_3N_4 (N=0)	N=0.1	N=0.5	N=1	N=2	N=10	SUS304 (N= ∞)
No porosity	T_t = 300K T_b = 300K	ψ=0	3.71833	3.71832	3.71606	3.71308	3.70971	3.70596	3.70551
		ψ=15	3.3856	3.38584	3.38251	3.37761	3.37189	3.36539	3.36462

		ψ=30	2.83049	2.83096	2.8276	2.82222	2.81585	2.80856	2.80768
		ψ=45	2.22107	2.2215	2.21828	2.21318	2.20715	2.20026	2.19944
	T_t = 400K	ψ=0	3.52363	3.52528	3.52921	3.53132	3.53315	3.53642	3.53811
	T_b = 300K	ψ=15	3.14572	3.14796	3.1517	3.15245	3.15249	3.15398	3.15575
		ψ=30	2.54079	2.54378	2.54919	2.55078	2.55146	2.55387	2.55604
		ψ=45	1.85396	1.85784	1.86639	1.87047	1.87363	1.87922	1.88227
	T_t = 600K	ψ=0	2.99482	3.00214	3.02664	3.0452	3.06336	3.08787	3.09577
	T_b = 300K	ψ=15	2.44311	2.45342	2.48427	2.50568	2.526	2.55469	2.56503
		ψ=30	1.62766	1.64249	1.68741	1.71873	1.74833	1.78906	1.80322
		ψ=45	0.60391	0.60393	0.04241	0.33295	0.46624	0.60346	0.64295
Even porosity with volume fraction of porosity α = 0.1	T_t = 300K	ψ=0	3.8131	3.81296	3.80882	3.80361	3.79761	3.78992	3.78815
	T_b = 300K	ψ=15	3.50223	3.50241	3.49702	3.48948	3.48061	3.46932	3.46696
		ψ=30	2.96607	2.96651	2.96081	2.9524	2.94238	2.92957	2.92686
		ψ=45	2.38006	2.38042	2.37466	2.36632	2.35639	2.34346	2.34054
	T_t = 400K	ψ=0	3.68188	3.68295	3.68357	3.68241	3.68068	3.67893	3.67904
	T_b = 300K	ψ=15	3.34317	3.34482	3.34483	3.34179	3.33762	3.33303	3.33281
		ψ=30	2.77452	2.77683	2.77785	2.77494	2.77062	2.76576	2.76554
		ψ=45	2.14373	2.1466	2.14955	2.14815	2.14529	2.14201	2.14204
	T_t = 600K	ψ=0	3.33251	3.33806	3.3548	3.36657	3.37772	3.3928	3.39776
	T_b = 300K	ψ=15	2.90676	2.91414	2.9335	2.94537	2.95597	2.97111	2.97689
		ψ=30	2.23665	2.2463	2.27193	2.28785	2.3021	2.32186	2.32906
		ψ=45	1.4169	1.43124	1.47171	1.49832	1.52261	1.55472	1.56528
Uneven porosity with volume fraction of porosity α = 0.1	T_t = 300K	ψ=0	3.78428	3.78427	3.78157	3.77788	3.77346	3.76741	3.76587
	T_b = 300K	ψ=15	3.46907	3.46934	3.46564	3.46004	3.4532	3.44412	3.44204
		ψ=30	2.92628	2.9268	2.92299	2.91678	2.90908	2.89877	2.89639
		ψ=45	2.32824	2.3287	2.32498	2.31896	2.31147	2.30117	2.29858
	T_t = 400K	ψ=0	3.6229	3.6245	3.62776	3.62891	3.62931	3.62954	3.62981
	T_b = 300K	ψ=15	3.27372	3.27591	3.279	3.27877	3.27727	3.27522	3.27524
		ψ=30	2.69121	2.69411	2.69862	2.69894	2.69771	2.69581	2.69587
		ψ=45	2.03551	2.03913	2.04621	2.04854	2.0492	2.04929	2.04964
	T_t = 600K	ψ=0	3.19004	3.19701	3.21955	3.23588	3.25103	3.26954	3.27477
	T_b = 300K	ψ=15	2.72474	2.73403	2.7611	2.779	2.79489	2.81476	2.82102
		ψ=30	2.00272	2.01505	2.05129	2.07543	2.0969	2.12341	2.13149
		ψ=45	1.02484	1.04703	1.11388	1.15903	1.19916	1.24697	1.26044
Even porosity with volume fraction of porosity α = 0.2	T_t = 300K	ψ=0	3.8739	3.8736	3.86713	3.85913	3.8499	3.83745	3.83416
	T_b = 300K	ψ=15	3.57722	3.57729	3.56914	3.55814	3.54515	3.52786	3.52365
		ψ=30	3.05306	3.0534	3.0446	3.03221	3.01746	2.99774	2.99293
		ψ=45	2.48006	2.4803	2.47127	2.4588	2.44395	2.4237	2.41843
	T_t = 400K	ψ=0	3.78969	3.79012	3.787	3.78211	3.7763	3.76894	3.76735
	T_b = 300K	ψ=15	3.47497	3.47596	3.47169	3.46418	3.45503	3.44353	3.44125
		ψ=30	2.9284	2.93002	2.92624	2.91821	2.90817	2.89533	2.89271
		ψ=45	2.32649	2.32855	2.32615	2.31919	2.31012	2.29801	2.29525
	T_t = 600K	ψ=0	3.5634	3.5672	3.57657	3.5819	3.58648	3.59304	3.59556

	T_b = 300K	ψ=15	3.19934	3.20452	3.2147	3.21863	3.22109	3.22544	3.22798
		ψ=30	2.59289	2.59974	2.61377	2.6197	2.62371	2.62986	2.63293
		ψ=45	1.90079	1.90992	1.93117	1.94239	1.95137	1.96321	1.9675
Uneven porosity with volume fraction of porosity α = 0.2	T_t = 300K T_b = 300K	ψ=0	3.83816	3.83815	3.83495	3.83047	3.82487	3.81641	3.81374
		ψ=15	3.53731	3.5376	3.53342	3.52698	3.51887	3.50704	3.50366
		ψ=30	3.00432	3.00487	3.00049	2.99328	2.98409	2.9706	2.96673
		ψ=45	2.4133	2.41378	2.40942	2.40235	2.39324	2.3794	2.37509
	T_t = 400K T_b = 300K	ψ=0	3.70353	3.70507	3.70762	3.70777	3.70669	3.70384	3.70273
		ψ=15	3.37638	3.37852	3.38089	3.37959	3.37647	3.3709	3.36927
		ψ=30	2.81066	2.8135	2.81711	2.81612	2.81294	2.80687	2.80499
		ψ=45	2.17415	2.1776	2.18344	2.18416	2.18248	2.17758	2.17559
	T_t = 600K T_b = 300K	ψ=0	3.34388	3.3506	3.37158	3.38601	3.39849	3.41166	3.4146
		ψ=15	2.9343	2.94299	2.96748	2.98274	2.99514	3.00805	3.01121
		ψ=30	2.26589	2.27702	2.30855	2.32835	2.34457	2.36142	2.36541
		ψ=45	1.4377	1.45393	1.50207	1.53362	1.56021	1.58788	1.59392

3.4.1 Effects of porosity

In this study, both even and uneven porosity distributions with two distinct porosity volume fractions in each case are taken into account. The non-dimensional frequencies of various porosity distributions are displayed in Figure 3.7. To keep the discussion concise, the charts with no twist are only shown for the p-FGM and s-FGM at T_t = 300K and N=1. Figure 3.7 (a) shows a graphical comparison of the frequencies of conical shells with even and uneven porosity distributions made using p-FGM and s-FGM. Figure 3.7 (b) displays the plot for the e-FGM.

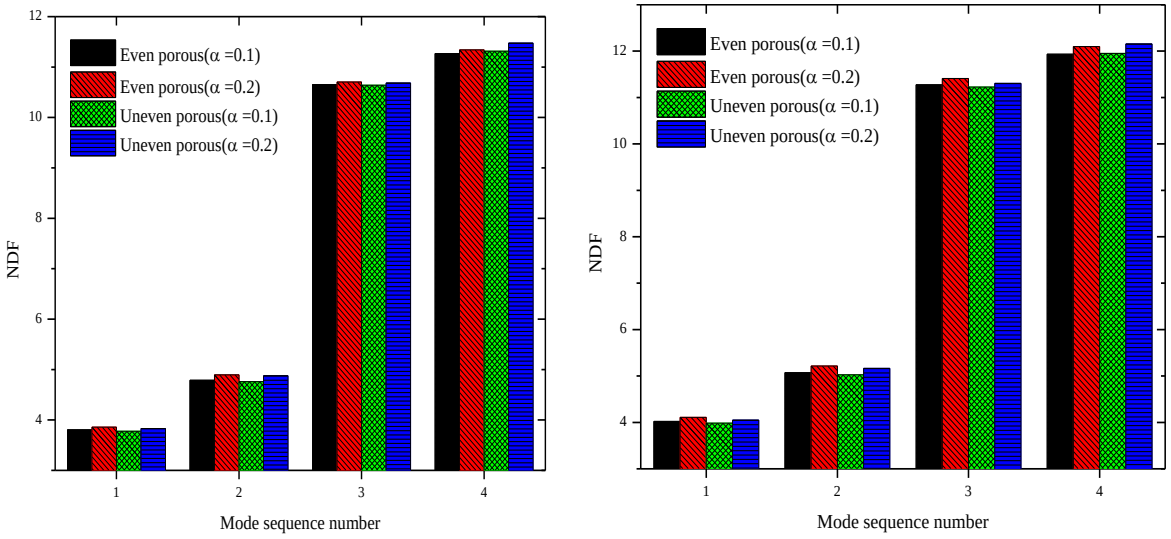

(a) p-FGM and s-FGM (N=1) (b) e-FGM

Figure 3.7 Effect of porosity on the first four non-dimensional frequencies of different types of FG conical shells [T_t = 300K, Ψ=0°]

Table 3.10 to Table 3.12 only list the non-dimensional fundamental frequencies, however the values of higher modes of frequencies are also estimated in the current investigation. The horizontal axis in Figure 3.7 represents the four mode shapes while the vertical axis represents the first four non-dimensional frequencies (NDF) that have been taken into consideration. While the values of the first to fourth modes are steadily rising, there are four distinct porosity distributions represented by four obviously distinct trends in their values. The value of non-dimensional frequencies increases when the functionally graded material has more porosity, or when the volume percentage of porosity (α) is larger. This trend can be explained by the fact that the presence of porosity always decreases the density of the conical shell which results in the increase of non-dimensional natural frequencies. Therefore the value of NDF rises with the increase of volume fraction porosity. Figure 3.7 makes it obvious that the columns with values of α =0.2 are higher than those with values of α =0.1. The NDF values of even distribution stay bigger than uneven for lower modes, but for higher modes it reflects the reverse tendency, according to a comparison between even and uneven distribution in the presence of the same amount of porosity. The uneven porosity distribution always exhibits more similarity to the nonporous FGM in the two surface regions and the unevenly distributed pores remain more concentrated in the middle region of the shell. From the mode shapes (Figure 3.11) it is evident that only higher torsion is observed in the top and bottom regions for fourth mode of natural frequencies, which results in the decrease of the structural stiffness for uneven porosity distributions but for the first three modes the stiffness is greater for uneven porosity distributions. However, it is noted that their differences are marginal.

3.4.2 Effects of pretwist angle

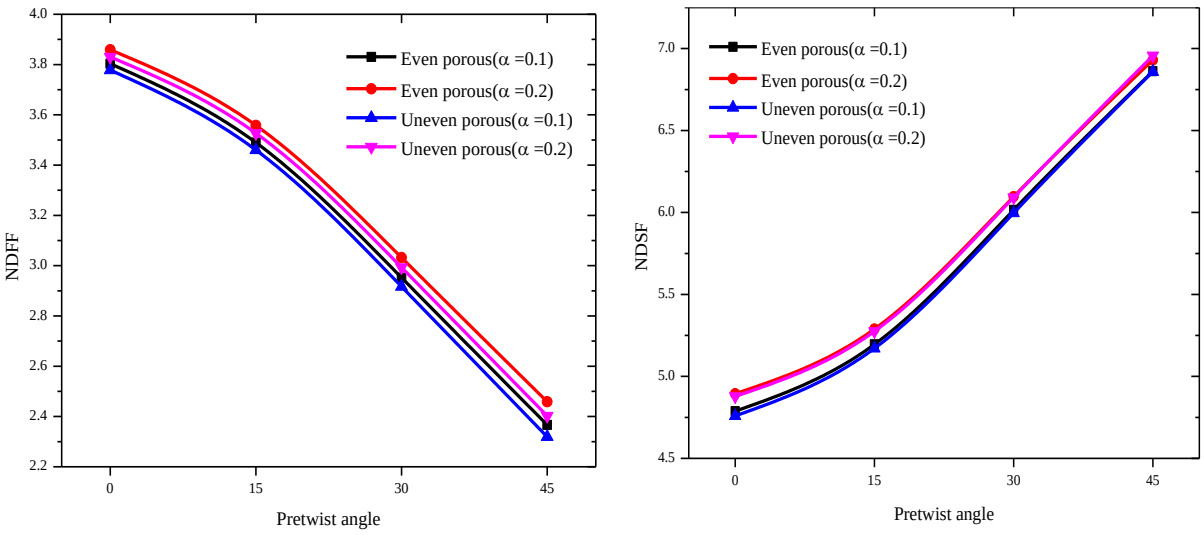

1st mode 2nd mode

(a) p-FGM and s-FGM (N=1)

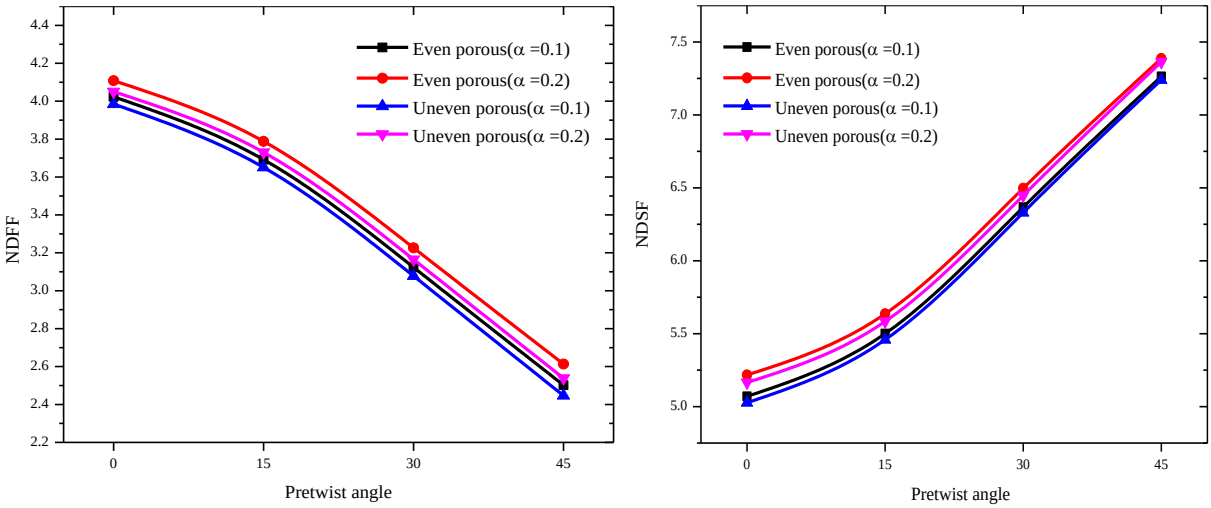

(b) e-FGM

Figure 3.8 Effect of pretwist angle on the fundamental and second frequencies of pretwisted FG conical shells at T_t=300 K for different types of porosity distributions and porosity volume fractions**.**

Figure 3.8 shows how the fundamental frequencies of pretwisted FG shallow conical shells with pretwist angles of 0°, 15°, 30°, and 45° vary at various porosity distributions (even and uneven), which correspond to porosity volume fractions (α) 0.1 and 0.2. A specific outcome with T_t = 300K, N=1 is taken into consideration for p-FGM and s-FGM and is shown in Figure 3.8 (a). Here, it is shown that as the twist angle increases, the values of non-dimensional fundamental frequencies steadily decrease. The non-dimensional fundamental frequency is detected to have a maximum value for untwisted FG conical shells, whereas the lowest is

observed at twist angle 45°. This appears due to fact that the increase in pretwist angle always reduces the structural stiffness of the conical shell. Similar patterns can be seen for all other top surface temperatures (T_t=300 K, 400 K, and 600 K) and power law indices (N=0, 0.1, 0.5, 1, 2, 10, and ∞). The top surface temperature for e-FGM has been considered to be 300K. Similar trends may be seen in the graphs that compare non-dimensional fundamental frequencies to four different pretwist angles. The four different porosity distributions are also shown, and it can be seen that for first-mode, non-dimensional frequencies for α =0.2 are greater than values for α =0.1 for all pretwist angles. Additionally, values for even porosities are greater than values for uneven porosities irrespective of pretwist angles. It should be noted that regardless of the porosity volume fraction, increasing the twist angle always results in a rise in the non-dimensional second frequencies (NDSF). It can be explained by the induction of the coupling effect due to bending and torsion in second mode (Figure 3.12) which increases the structural stiffness of the conical shell.

3.4.3 Effects of temperature

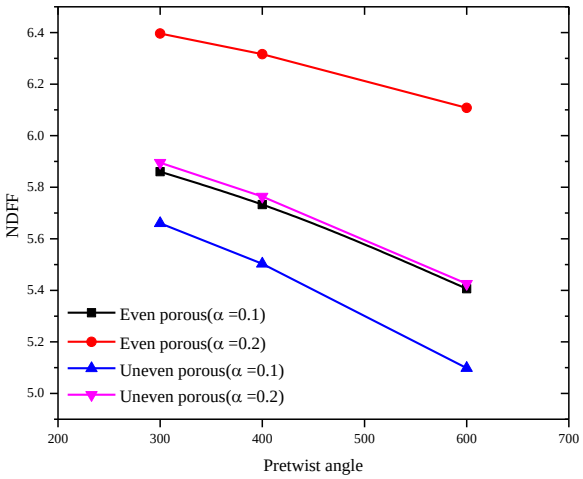

(a) For N=0.1 (p-FGM) & no twist

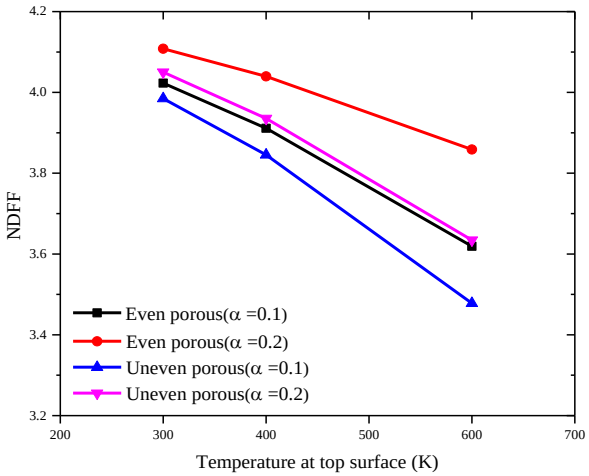

(b) For e-FGM & no twist

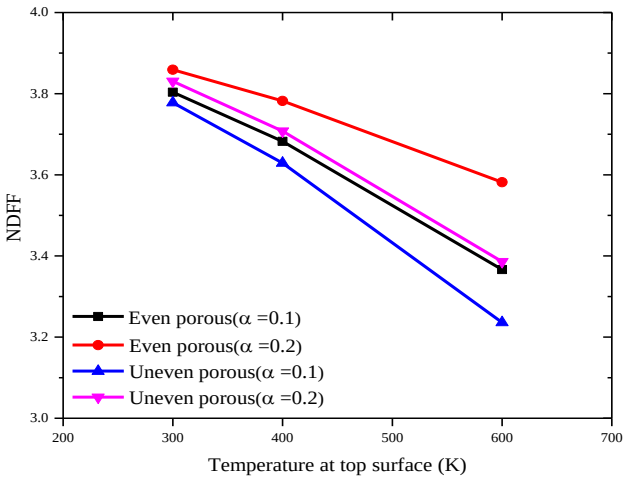

(c) For *N*=1 (s-FGM) & no twist

Figure 3.9 Representation of non-dimensional fundamental frequencies at three different temperature distributions at top surface for all four types of porosity distributions.

In the current assessment, the temperature at the bottom surface is held constant at room temperature (300 K) while the non-dimensional fundamental frequencies corresponding to three distinct temperature distributions at the top surface 300K, 400K, and 600K have been computed. Figure 3.9 shows three distinct plots for p-FGM, e-FGM, and s-FGM, respectively. The horizontal axis denotes the temperature distribution on the top surface, while the vertical axis denotes the non-dimensional fundamental frequencies. The study considers untwisted FGM conical shells and for p-FGM *N*=0.1 whereas for s-FGM *N*=1. As the temperature difference increases for p-FGM, e-FGM, and s-FGM, respectively, it is evident from the three graphs in Figures 3.9(a), 3.9(b), and 3.9(c) that the first mode frequency is steadily lowering. This is because the stiffness of the material decreases with the rise of temperature. Moreover, as the effective material properties in this formulation are considered temperature dependent, so when the temperature of the top surface increases, the natural frequency decreases as a result of the decrease in modulus of elasticity of the material. Additionally, it can be seen from the plots that all three of the functionally graded materials exhibit the same tendency, with the rate of decline of first mode frequencies being higher for the uneven than the even porosity distributions. Even porosity with α=0.2 exhibits maximum value of natural frequency. Then uneven porosity with α=0.2 comes in the order and uneven porosity with α=0.1 shows minimum values of natural frequencies for all temperature distributions. This pattern is explained in the parametric study of porosity and this similar trend appears for all the three types of FG conical shells.

3.4.4 Effects of rotational speed

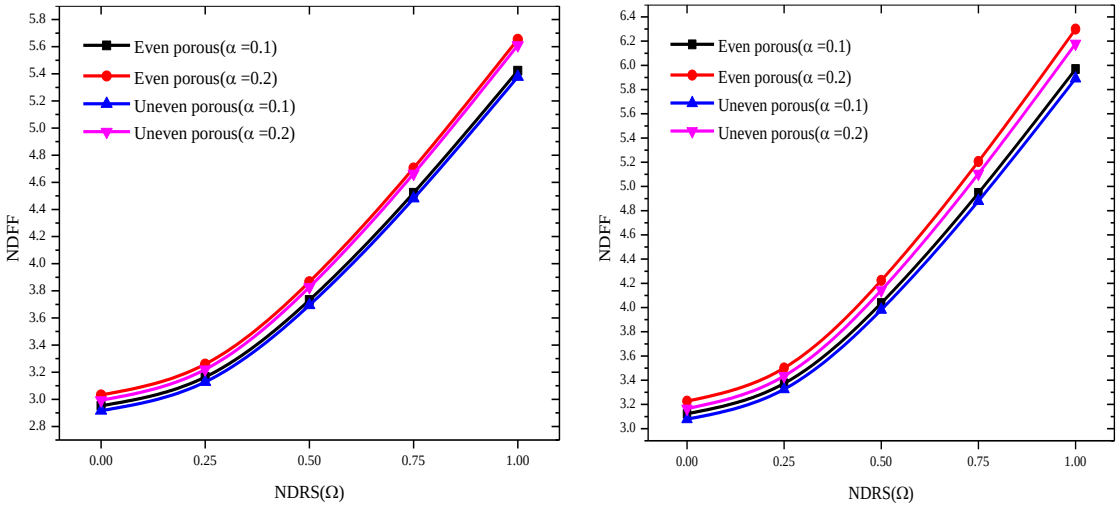

(a) For N=1(p-FGM and s-FGM), T_t = 300K & twist angle = 30^0

(b) For e-FGM, T_t = 300K & twist angle =30^0

Figure 3.10 Representation of non-dimensional fundamental frequencies of the porous FG conical shells corresponding to five non-dimensional rotational speeds.

Figure 3.10 illustrates the variations of non-dimensional fundamental frequencies for various porous FGM conical shells corresponding to various rotating speeds. Here, five distinct non-dimensional rotational speed values ($\Omega = \frac{\Omega'}{\omega_n}$, where Ω' is the actual rotational speed and ω_n is the frequency of the FG conical shell at rest) have been taken into account as 0, 0.25, 0.5, 0.75, and 1. N is assumed to have a value of 1, making p-FGM and s-FGM equivalent. Figure 3.10 (a) illustrates the NDF of p-type and s-type FGMs at room temperature (300K) with a pretwist angle (ψ) of 30^0, whereas Figure 3.10 (b) shows the frequency response of e-FGM. It is obvious that the fundamental frequency of the conical shell increases with the escalation of its rotational speed. This is observed due to the effect of centrifugal force generated by the rotating shells, which then manifests as geometric stiffness and raises the fundamental frequency. This effect is referred as centrifugal stiffening. The curve becomes stiffer as the volume fraction of porosity rises as discussed earlier.

3.5 MODE SHAPES

Types of porosity distribution	Mode 1	Mode 2	Mode 3	Mode 4

Even porosity with α = 0.1	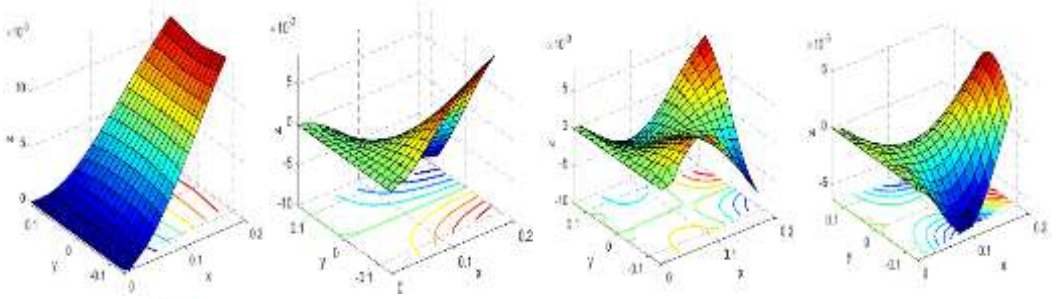
Uneven porosity with α = 0.1	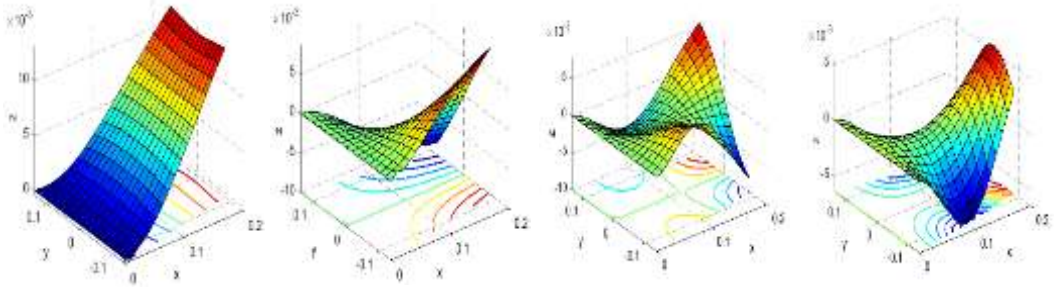
Even porosity with α = 0.2	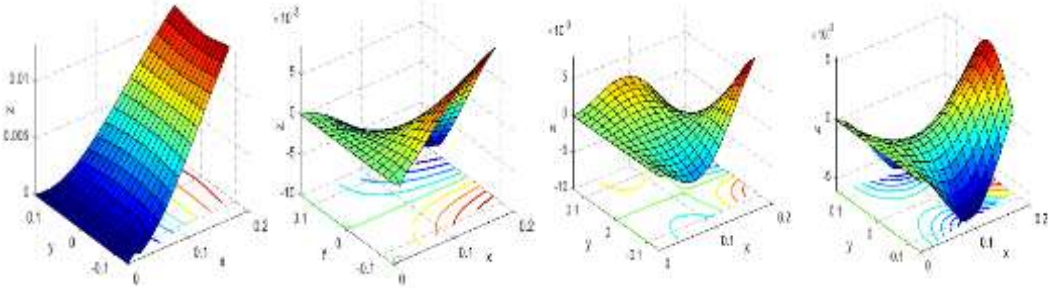
Uneven porosity with α = 0.2	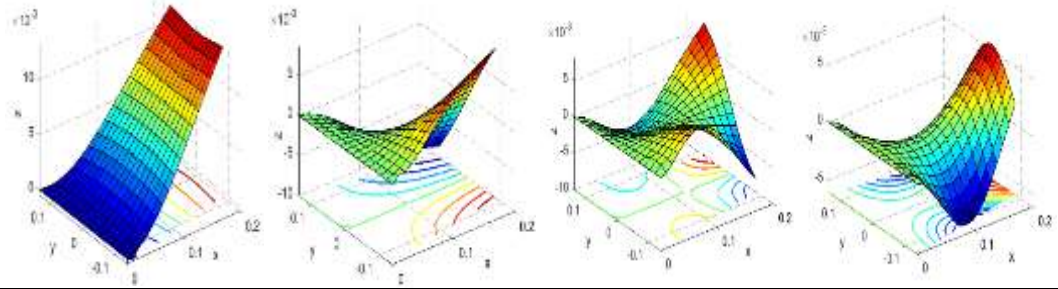

Table 3.13 Effect of porosity distributions on mode shapes of a functionally graded twisted conical shell for N=1 (p-FGM and s-FGM), T_t = 300K & no twist

Tables 3.13, 3.14, 3.15, and 3.16 show, respectively, the mode shapes of the pretwisted functionally graded porous conical shells with regard to porosity distribution, pretwist angle, nonlinear temperature change, and rotational speed. By taking into account the normalized displacement (*w*) through Z-axis, where the negative value denotes downward displacement and the positive value represents upward displacement, the first four mode shapes are displayed. The first four mode shapes in Table 3.13 are, respectively, the first span-wise bending mode (1B), the first torsional mode (1T), the first cord-wise bending mode (1C), and the second torsional mode (2T). When the shells vibrate at various frequencies, the mode shapes show the deformed shapes. Table 3.13 demonstrates that the various porosity

distributions have insignificant influence on mode shape. However, Table 3.14 demonstrates that the pretwist angle significantly affects mode shapes.

Pretwist angle	Mode 1	Mode 2	Mode 3	Mode 4
$\psi = 0^0$	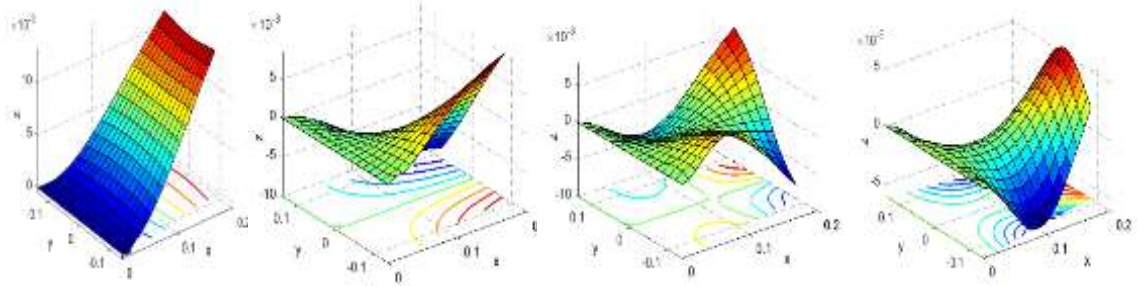			
$\psi = 15^0$	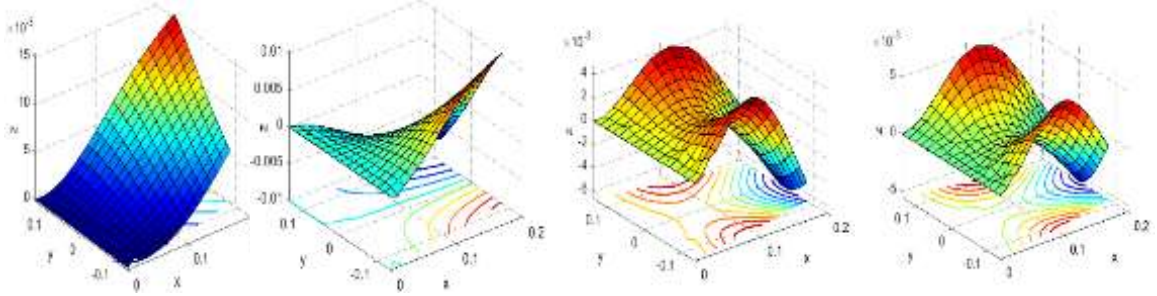			
$\psi = 30^0$	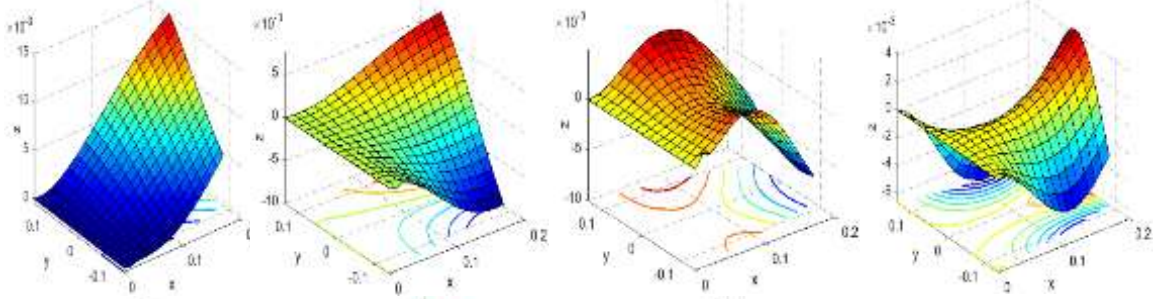			
$\psi = 45^0$	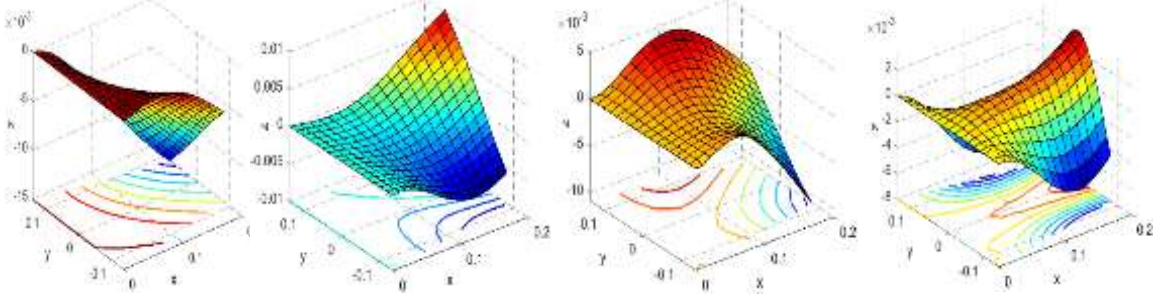			

Table 3.14 Effect of pretwist angle on mode shapes of a functionally graded twisted conical shell for N=1 (p-FGM and s-FGM), T_t = 300K & uneven porosity with α = 0.2

The third mode of the untwisted shell has the shape 1C, but if the pretwist angle is present, it takes on the shape 1C but the shell is much more influenced by torsion. For the fourth mode, the 2T mode is converted into 2C at twist angle 15^0. Unsymmetrical mode shapes are obtained in the presence of twist angles.

Temperature at top surface	Mode 1	Mode 2	Mode 3	Mode 4
T_t = 300K	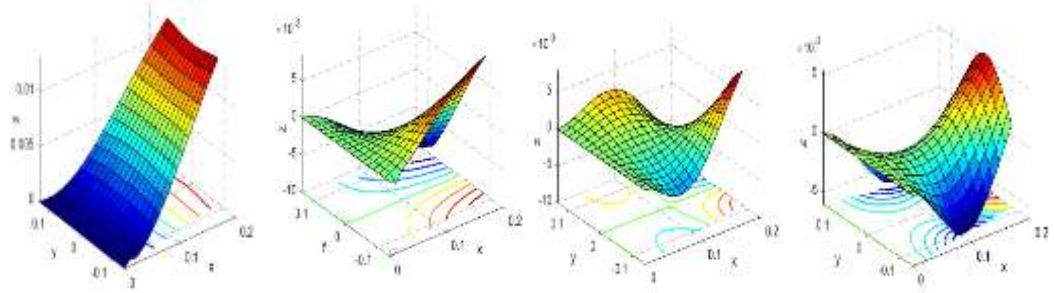			
T_t = 400K	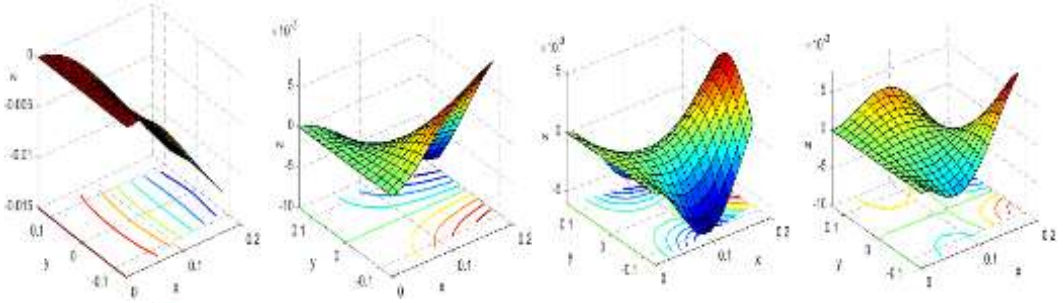			
T_t = 600K	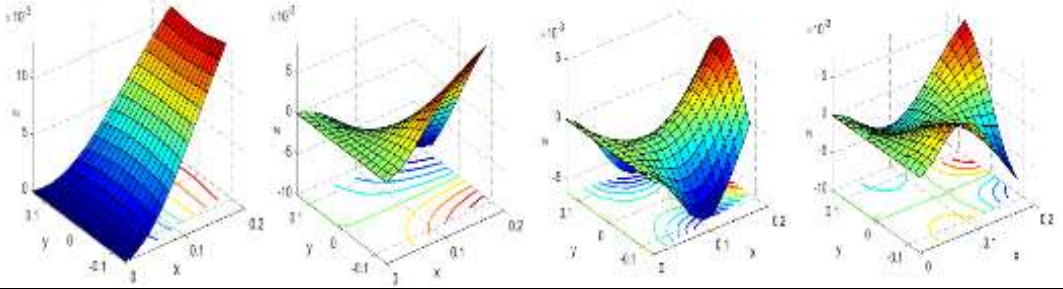			

Table 3.15 Effect of top surface temperature on mode shapes of a functionally graded twisted conical shell for N=1 (p-FGM and s-FGM), no twist & even porosity with $\alpha = 0.2$

Table 3.15 shows that the temperature has a negligible impact on the mode shapes, and Table 3.16 shows that the rotational speed has little impact on the mode shapes. However, the symmetry of the modes changes dramatically for the third and fourth modes at high speeds.

Rotation	Mode 1	Mode 2	Mode 3	Mode 4
Ω= 0	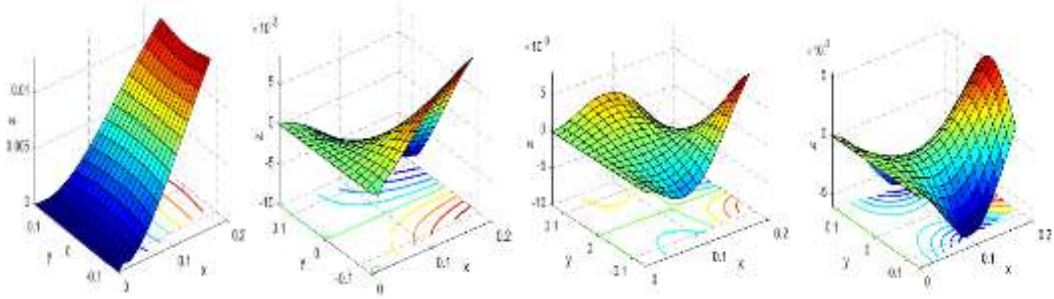			

Ω= 0.25

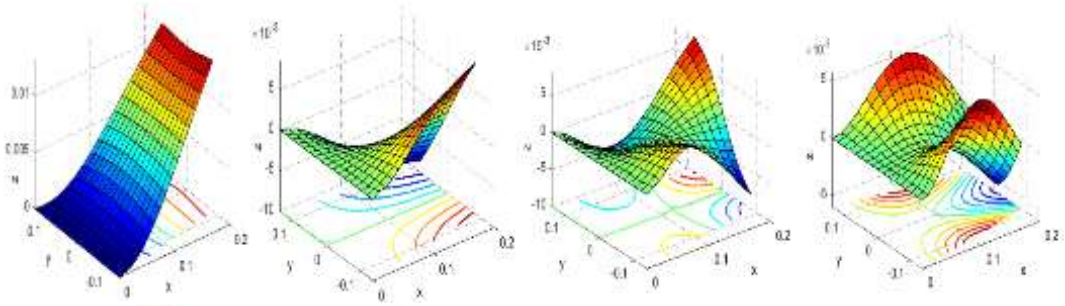

Ω= 0.5

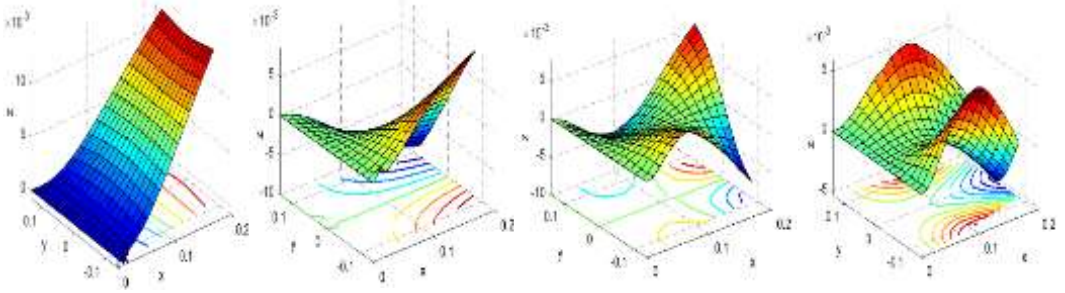

Ω= 0.75

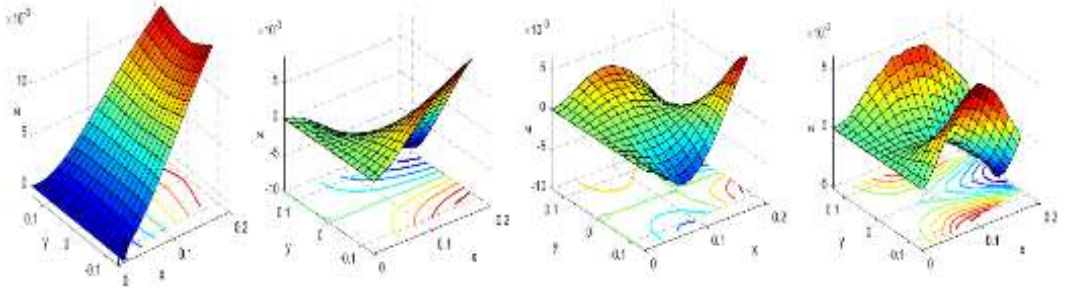

Ω= 1

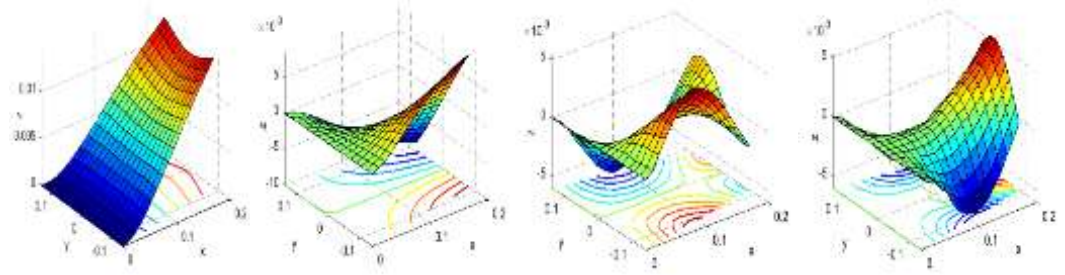

Table 3.16 Effect of rotation on mode shapes of a functionally graded twisted conical shell for N=1 (p-FGM and s-FGM), T_t = 300K, no twist & even porosity with α = 0.2

CHAPTER 4

FREE VIBRATION ANALYSIS OF ROTATING TAPERED POROUS FG CONICAL SHELL BASED ON TRIGONOMETRIC HIGHER-ORDER SHEAR DEFORMATION THEORY

4.1 INTRODUCTION

Turbomachines, which have applications in gas, steam, wind, hydraulic turbines, helicopter fans, and aeroplane engines, rely on structural stiffness of the FG blades. When a gas or steam turbine's hub rotates rapidly under high-pressure flow, the turbine's FG blades endure centrifugal force, pressure force, and elevated thermal stresses, leading to considerable vibration amplitude. The blades can be modeled as plates or shell structures due to their low aspect ratio, rather than as beams. 2D modelling can also be used to capture chord-wise mode shapes as well as the coupling impact of span-wise and chord-wise mode shapes. Again, shells outperform plates when it comes to matching blade curvature and twist angle. In order to minimise weight and maximise strength, these are also practically constructed as cantilevers functionally graded shells with different cross-sections. FG conical shells with reducing width and thickness towards the free tip may be the optimal choice for turbo blade design when all relevant criteria are considered.

In order to optimise the design of FG tubromachinery blades, a thorough understanding of their deformation properties is required. It is well known that FSDT overestimates the results as compared to HSDT. The current study will investigate the free vibration behaviour of laminated composite plates utilising trigonometric higher order shear deformation theories (THSDT). In this novel trigonometric higher order shear deformation theory, the transverse displacement is assumed to remain constant throughout the thickness, while the middle surface's displacement is expanded as inverse tangential trigonometric functions of the thickness coordinate. The primary goal of this chapter is to provide an appropriate solution methodology using the finite element method for vibration analysis of the FG conical shell using THSDT in thermal environment. The shear correction factor is not necessary because this theory takes into account the proper distribution of the transverse shear stresses through the thickness direction of FG conical shell with boundary conditions having tangential stress-free on the shell boundary surface.

In general, FGM is the combination of metal and ceramic components. The metal component contributes to the material properties of the FGM, while the ceramic component serves as a protective barrier against extreme temperatures and pressures. This material will be useful in tubromachinery blade applications since the blades rotate at high speeds and are exposed to high temperatures and dampness. Regarding the advanced features of this functionally graded material, predicting applicability of FGM in turbomachinery applications requires a study of free vibration response of the blades. The utilization of a twisted tapering conical shell composed of functionally graded material with a certain level of porosity would enhance the practicality and realism of the model. This is because the manufacturing of FGM without porosity is not possible.

The finite element formulation is used to calculate the fundamental frequency of the rotating FG porous taper conical shell using a non-polynomial higher-order shear deformation theory under nonlinear thermal gradient. The tapered FG porous conical shell is discretized based on eight noded isoparametric shell elements with seven degrees of freedom at each node. The metal and ceramic constituents of the conical shell are graded along the thickness using a simple power law, which is commonly referred to as p-FGM. The precision and accuracy of the formulation are validated and compared to known benchmark solutions. The analysis shows how temperature distribution, taper ratio, volume fraction of porosity, power law index, pretwist angle, and rotational speed affect the fundamental frequency of the FG conical shell. The impacts of some factors on the mode shapes of the tapering FG porous conical shell are also examined.

4.2 NUMERICAL RESULTS AND DISCUSSIONS

In the present work, pretwisted tapered FG conical shell made of silicon nitride (Si_3N_4) and stainless steel (SUS304) are considered as ceramic and metal constituent, respectively. The material properties of the metal and ceramic constituents i.e. Young's modulus, Poison's ratio and thermal expansion coefficient are temperature dependent in nature and these effective material properties are computed as discussed earlier. The temperature-dependent coefficients of Si_3N_4 and SUS304 are taken form Table 4.1.

Table 4.1 Temperature-dependent material properties of ceramic and metal (unit of E in Pa, α_t in 1/K, suffix m and c refer to metal and ceramic, respectively).

Material	Properties	P_{-1}	P_0	P_1	P_2	P_3

SUS304	E_m	0	201.04×10^9	3.079×10^{-4}	-6.534×10^{-7}	0
	α_{tm}	0	12.330×10^{-6}	8.086×10^{-6}	0	0
	υ_m	0	0.3262	-2.002×10^{-4}	3.797×10^{-7}	0
Si_3N_4	E_c	0	348.43×10^9	-3.070×10^{-4}	2.160×10^{-7}	-8.946×10^{-11}
	α_{tc}	0	5.8723×10^{-6}	9.095×10^{-6}	0	0
	υ_c	0	0.24	0	0	0

In addition to the aforementioned three material parameters, density (ρ) and thermal conductivity (*K*) exhibit temperature independence. The values corresponding to SUS304 and Si_3N_4 are as follows:

$\rho_m = 8166$ kg/m^3, $K_m = 12.04$W/mK, $\rho_c = 2370$ kg/m^3, $K_c = 9.19$W/mK

The suffix "*m*" is used to signify a metal, while the suffix "*c*" is used to denote a ceramic material.

The geometric dimensions and parameters of the conical shell are considered as follows:

$s = 0.5$ m, $\theta_0 = 75°$, $\theta_v = 50°$, $L/s = 0.4$, $s/h_0 = 20$

The cantilever boundary condition is considered for the entire study as

At x= 0, $u = v = w = \theta_x = \theta_y = \xi_x = \xi_y = 0$ (4.1)

4.3 VALIDATION AND CONVERGENCE STUDIES

On the basis of the current finite element formulation, a unique computer code is developed. The numerical findings from the code are provided in Table 4.2 to Table 4.6, where they are validated and compared to those found in benchmark literature. Based on the proximity of the comparison investigation, it shows extremely good agreement with the results from earlier publications, revealing the precision of the produced computer code and proving the veracity of the studies. Table 4.2 shows the verification of the non-dimensional natural frequency of a cantilever conical shell, which was previously reported by Liew et al. (1994). In Table 4.3, the natural frequency of the variable-thickness Mindlin plates is compared to that of Cheung and Zhou (2003) and Fang & Zhou (2017). Table 4.4 compares the results of Sreenivasamurthy and Ramamurthi (1981) with the accuracy of the code for the application of rotational speeds. Table 4.5 displays the comparison of natural frequencies of FG plates consisting of both even and uneven porosity distributions with that of Rezaei et al. (2017). Last but not least, Table 4.6

compares the natural frequencies of FG plates in the presence of nonlinear temperature distribution with Huang and Shen (2004) and Parida and Mohanty (2017).

Table 4.2 Frequency parameter $\grave{\lambda} = \omega b_0^2\sqrt{\frac{\rho h}{D}}, D = Eh^3/12(1-\nu^2)$for the pretwisted shallow conical shell with ν = 0.3, *s*/*h* = 1000, θ_v = 15° and θ_0 = 30°

Ψ	*L*/*s*	Liew et al. (1994) ($\grave{\lambda}$)	Present FEM ($\grave{\lambda}$)
0	0.6	0.35997	0.35713
	0.7	0.30608	0.30419
15	0.6	0.34116	0.34053
	0.7	0.29410	0.29389
30	0.6	0.28828	0.28798
	0.7	0.25752	0.25674

Table 4.3 Comparison of the first five dimensionless natural frequencies ($\bar{\omega} = \omega L^2\sqrt{\rho h/D}$) of stationary tapered square Mindlin plates with simply supported boundary conditions.c_h = -1, *L*=*b*=1 m, $D = Eh^3/12(1-v^2)$.

h_0 / *L*	References	Dimensionless natural frequencies				
		$\bar{\omega}_1$	$\bar{\omega}_2$	$\bar{\omega}_3$	$\bar{\omega}_4$	$\bar{\omega}_5$
0.1	Fang & Zhou (2017)	27.1176	61.3818	61.7365	92.0113	108.3339
	Cheung and Zhou (2003)	27.118	61.382	61.737	92.011	108.340
	Present FEM	27.1165	61.3544	61.7257	92.0098	108.3039
0.2	Fang & Zhou (2017)	23.0246	46.5902	46.6580	64.8338	74.8950
	Cheung and Zhou (2003)	23.025	46.590	46.658	64.834	74.896
	Present FEM	23.0237	46.3313	46.6369	64.8206	71.8188

Table 4.4 Non-dimensional fundamental frequencies ($\beta = \omega L^2\sqrt{\rho h\ /\ D}$) of an isotropic rotating cantilever plate. (*L*/*b* = 1, *h*/*L* = 0.12, $D = Eh^3/12(1-\nu^2)$, ν = 0.3)

NDRS (Ω)	Sreenivasamurthy and Ramamurthi (1981)	Present FEM
0.0	3.43685	3.41683
0.2	3.51858	3.49704
0.4	3.75280	3.72663
0.6	4.12875	4.07865
0.8	4.56786	4.52205
1.0	5.09167	5.02988

Table 4.5 Non-dimensional fundamental frequencies ($\varpi = \omega_n h\sqrt{\rho_m\ /\ E_m}$)of a simply supported porous p-FGM plate. $h/L = 0.05, L/b = 0.5$

Power-law index (N)	Porosity volume fraction (α)	Even		Uneven	
		Rezaei et al. (2017)	Present FEM	Rezaei et al. (2017)	Present FEM
0	0.0	0.018257	0.018226	0.018257	0.018246
	0.2	0.018829	0.018507	0.018804	0.018704
	0.4	0.019669	0.019084	0.019444	0.019408
0.1	0.0	0.017565	0.017413	0.017565	0.017513
	0.2	0.018026	0.017996	0.018082	0.018029
	0.4	0.018712	0.018571	0.018688	0.018590
0.5	0.0	0.015465	0.015103	0.015465	0.015103
	0.2	0.015392	0.015185	0.015820	0.015789
	0.4	0.015184	0.015083	0.016235	0.016109
1	0.0	0.013937	0.013912	0.013937	0.013882
	0.2	0.013184	0.014507	0.014087	0.014049
	0.4	0.011384	0.011216	0.014227	0.014219

Table 4.6 Natural frequency parameter, $\bar{\omega} = \omega(L^2/h)\sqrt{\rho_0(1-\upsilon^2)/E_0}$of a simply supported Si_3N_4/SUS304 square plate in thermal environment. $\rho_0$and$E_0$are the density and modulus of elasticity of metal at 300 K. L/b=1, L=8h, ρ_c=2370 kg/m^3, ρ_m=8166 kg/m^3, ν_c=0.28,ν_m=0.28, K_c=9.19 W/m K, K_m=12.04 W/m K.

	Power-law index	Huang and Shen (2004)	Parida and Mohanty (2017)	Present FEM
T_b=300 K	Si_3N_4 (N=0)	12.495	12.587	12.483
T_t=300 K	0.5	8.675	9.094	8.625
	1.0	7.555	7.656	7.542
	2.0	6.777	6.78	6.768
	SUS304 (N=∞)	5.405	5.445	5.401
T_b=400 K	Si_3N_4 (N=0)	12.397	12.387	12.308
T_t=300 K	0.5	8.615	8.615	8.468
	1.0	7.474	7.51	7.406
	2.0	6.693	6.642	6.638
	SUS304 (N=∞)	5.311	5.311	5.273
T_b=600 K	Si_3N_4 (N=0)	11.984	11.971	11.888
T_t=300 K	0.5	8.269	8.272	8.131
	1.0	7.171	7.186	7.087
	2.0	6.398	6.327	6.307
	SUS304 (N=∞)	4.971	4.989	4.923

The study of mesh convergence is also conducted and shown in Table 4.7 for the initial four modes of natural frequencies in order to ascertain the accuracy and reliability of the results obtained. For the test, we are considering mesh sizes of 2×2, 4×4, 6×6, 8×8, and 10×10. The minor and insignificant disparity in outcomes between the mesh sizes of 8 × 8 and 10 × 10 has

led to the selection of a mesh size of 8 × 8, which comprises 64 elements and 225 nodes, for computational purposes. Unless explicitly specified, the non-dimensional fundamental frequency (NDFF) that has been calculated is $\bar{\omega} = \frac{\omega L^2}{2\pi h}\sqrt{\frac{\rho_c}{E_c}}$.

Table 4.7 Non-dimensional fundamental frequency$\left(\bar{\omega} = \frac{\omega L^2}{2\pi h}\sqrt{\frac{\rho_c}{E_c}}\right)$of a tapered pretwisted FG conical shell with varying thickness in thermal environment.(s = 0.5 m, ϕ_0= 75°, ϕ_v = 50°, L/s = 0.4, s/h = 20, T_t= 600 K, Ψ=30°, uneven porosity with α= 0.2,C_h=0.5, N=1)

Mode	Mesh size				
	2×2	4×4	6×6	8×8	10×10
1	2.69711	2.71631	2.72279	2.72608	2.72810
2	6.26943	6.31477	6.32952	6.33723	6.34192
3	11.51048	11.17068	11.17200	11.18142	11.18854
4	13.92489	13.39054	13.37320	13.38156	13.38937

4.4 RESULTS AND DISCUSSIONS

4.4.1. Effects of volume fraction of porosity (α)

Fig. 4.1 shows how porosity volume fraction affects the non-dimensional fundamental frequencies (NDF) as well as the impact of both even and uneven porosity corresponding to N=0.5. At standard temperature (300K), three distinct values of the porosity volume fraction are taken into consideration for both even and uneven types FG conical shells. For the purpose of this investigation, the porous untwisted (0^0) and twisted (15^0) FG conical shells are presented in Fig 4.1 (a) and (b), respectively having two taper ratios of 0.5 and 0.1.

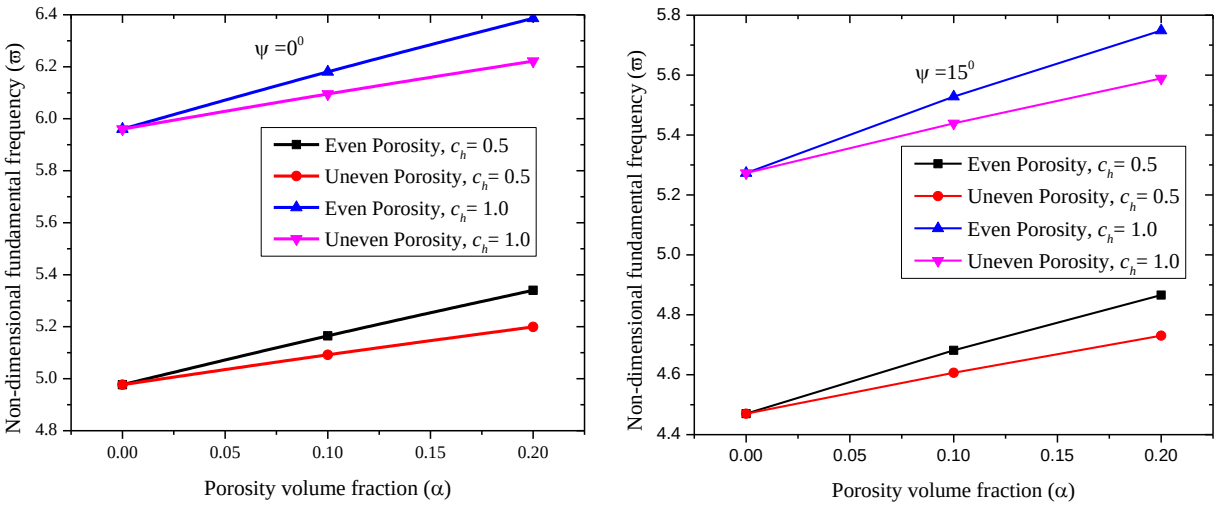

(a) **(b)**

Figure 4.1 Effect of porosity on the non-dimensional fundamental frequencies of different types of tapered FG conical shells [T_t=T_b = 300K, N=0.5] (a)Ψ=0^0 (b)Ψ=15^0.

It may be seen that the NDF of the taper shells increases linearly as the porosity volume percentage increases. This might be as a result of the FG conical shell becoming less rigid and dense as its porosity increases. The mass suffers as a result, which raises the fundamental frequency of the FG conical shell. The predominance of mass over stiffness may be the cause. Further, the even porosity has larger magnitude of NDF as compared with uneven porous FG conical shell. The cause of this result can be attributed to the fact that an uneven porosity distribution lacks a regular pattern, making it appear more like non-porous shell, particularly in the layers that are close to the top and bottom surfaces. Table 4.8 shows the variation of NDF with respect to volume fraction of porosity for taper FG conical shell at N=1. The similar conclusion may be drawn from this table.

Table 4.8 Effect of porosity volume fraction on non-dimensional fundamental frequency of the taper FG conical shell.T_b=300 K,T_t=300 K, Ψ=0^0, N=1

Volume fraction of porosity	Non-dimensional fundamental frequency					
	Even porosity			Uneven porosity		
	C_r =0	C_r =0.5	C_r =1.0	C_r =0	C_r =0.5	C_r =1.0
0	3.71308	4.34475	5.20347	3.71308	4.34475	5.20347

0.1	3.80333	4.44646	5.31977	3.77788	4.41815	5.28826
0.2	3.85913	4.50892	5.39129	3.83046	4.47789	5.35755

4.4.2. Effects of taper ratio (C_r)

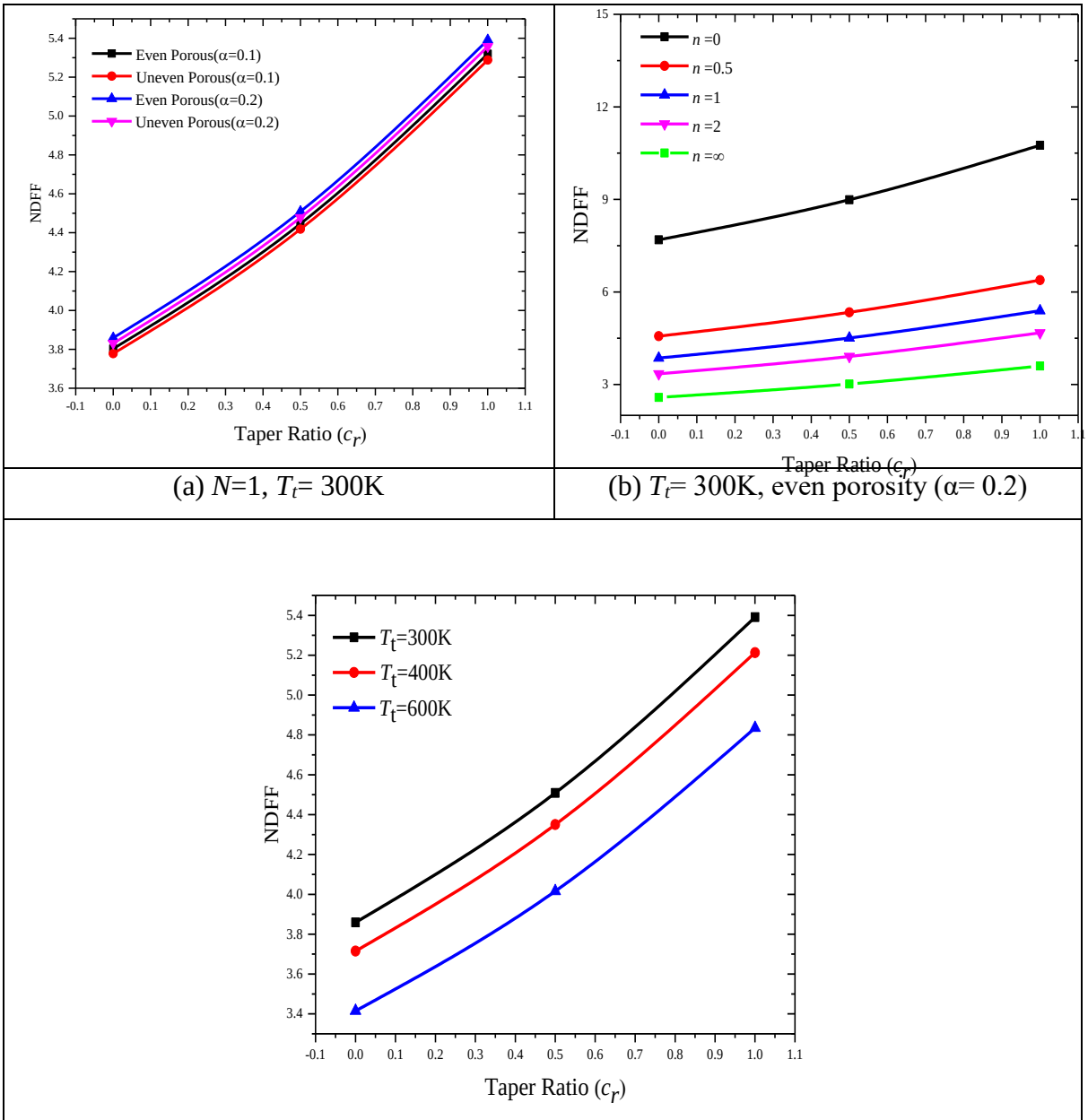

(a) N=1, T_t= 300K

(b) T_t= 300K, even porosity (α= 0.2)

(c) N=1, uneven porosity(α= 0.2)

Figure 4.2 Effect of taper ratio on the non-dimensional fundamental frequencies associated with (a) porosity distribution, (b) power law index, & (c) nonlinear temperature distribution

Figure 4.2 depicts the influence of taper ratio on the fundamental frequency of the porous FG conical shells. Figure 4.2(a) illustrates the natural frequency variation with taper ratio of even and uneven porous FG conical shells. For both even and uneven porous untwisted conical shells, two porosity volume fractions (0.1 and 0.2) are studied while the temperature is kept constant at 300 K and N=1. The fundamental frequency rises as the taper ratio increases because the mass of the conical shell is inversely proportional to the taper ratio. This pattern is clear and consistent across all types of porosity distributions. Figure 4.2(b) depicts the variation of natural frequency with taper ratio of the untwisted even porous (α= 0.2) FG conical shells corresponding to five values of power index at room temperature (300K). The natural frequency increases with rise in taper ratio irrespective of the value of power index (N). The similar trend is observed corresponding to all five values of power index. Figure 4.2 (c) illustrates the variation of non-dimensional fundamental frequency with taper ratio of an uneven porosity (α= 0.2) untwisted FG conical shell in a thermal environment with the bottom surface temperature held constant at 300 K and the top surface temperature altered. Three scenarios are explored, with top surface temperatures of 300 K, 400 K, and 600 K, respectively. In this case, the rise of NDFF in relation to the taper ratio is substantially faster. As the temperature of the top surface rises, the fundamental frequency decreases, and the highest NDFF is attained at T_t=300 K.

4.4.3 Effects of pretwist angle (Ψ)

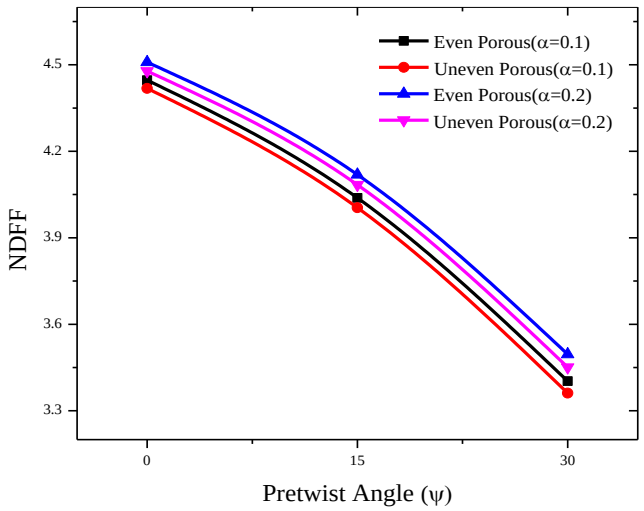

Figure 4.3 Effect of pretwist angle on the non-dimensional fundamental frequenciesof taper FG conical shell having different types of porosity distributions and volume fractions**.** [T_t = 300K, N=1, C_r = 0.5]

Figure 4.3 depicts the variation of the fundamental frequency of tapered FG conical shells with respect to pretwist angle for different porosity distributions and porosity volume fractions at normal temperature (300K), C_r = 0.5, and N =1. In this study, three values of pretwist angle are considered: 0^0, 15°, and 30°. The natural frequency of the FG conical shells decreases with increasing pretwist angle, regardless of porosity distribution type or porosity volume fraction. Thus, an untwisted conical shell always has the highest natural frequency, but a shell with a higher pretwist angle has the lowest fundamental frequency. This could be due to a decrease in the value of the twisted radius of curvature, which is directly related to flexural rigidity. The stiffness of the porous FG conical shell reduces as flexural rigidity diminishes, leading to a decrease in nonlinear fundamental frequency.

4.4.4 Effects of nonlinear temperature distribution

Figure 4.4 depicts the influence of nonlinear temperature distribution on the fundamental frequency of the FG conical shell with taper ratio, C_r = 0.5 and even and uneven porosity distribution. Two values of porosity fraction (α=0.1 and 0.2) is considered for even and uneven porosity distribution. The temperature at the bottom surface of the FG conical shell is always kept at 300 K, whereas the temperature at the top surface has three values: 300 K, 400 K, and 600 K for three different cases.

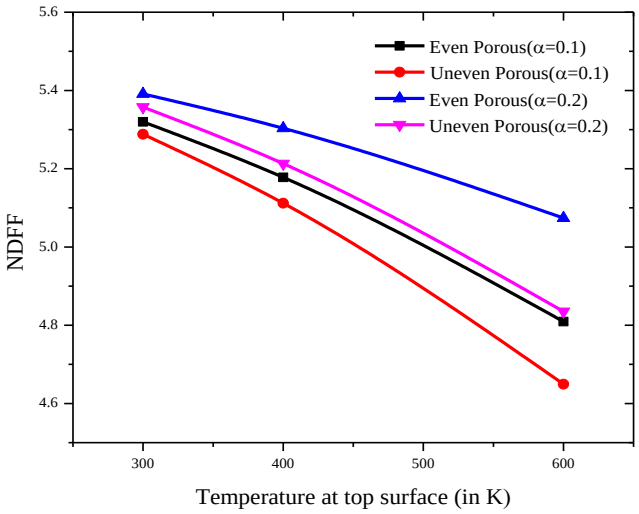

Figure 4.4 Representation of non-dimensional fundamental frequencies at three different temperature distributions at top surface for all four types of porosity distributions. [T_t= 300K, C_r = 0.5, Ψ=0°]

When the top surface temperature is 300K, the highest natural frequency is seen. The natural frequency of the FG conical shell is observed to decrease as the temperature of the top surface rises. This is because, in the formulation discussed earlier, Young's modulus is regarded a temperature dependant material, and it decreases as the nonlinear temperature distribution increases, which in turn reduces the stiffness of the porous FG conical shell.

4.4.5 Effects of rotational speed

Figure 4.5 illustrates the variations of non-dimensional fundamental frequencies for various porous FGM conical shells with variable thickness corresponding to various rotating speeds. Here, five distinct non-dimensional rotational speed values ($\Omega = \frac{\Omega'}{\omega_n}$, where ω_n is the static fundamental frequency and $\Omega'$is the actual rotational speed) have been taken into account as 0, 0.25, 0.5, 0.75, and 1. The temperature of the top surface is assumed to be 600K with N=1 and pretwist angle 30^0.It is obvious that the fundamental frequency of the conical shell increases with the escalation of its rotational speed. This is observed due to the effect of centrifugal force generated by the rotating shells, which then manifests itself through geometric stiffness and raises the fundamental frequency. This effect is referred as centrifugal stiffening. The curve becomes stiffer as the volume fraction of porosity rises.

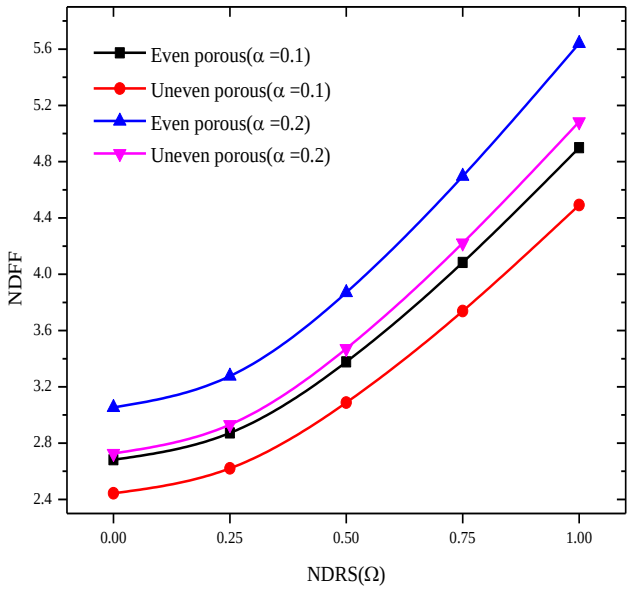

Figure 4.5 Non-dimensional fundamental frequencies of the porous FG conical shell with respect to variation of rotational speed. [T_t= 600K, C_r = 0.5, Ψ=30°, N=1]

4.5 MODE SHAPES

The presentation of the mode shape variations of the porous FG conical shell is conducted in relation to various factors outlined in Table 4.9 to 4.12. Table 4.9 illustrates mode shapes for the variation of taper ratio of an uneven porous FG conical shell having $\alpha = 0.1$, N=1, T_t= 300K and Ψ=0°. The initial mode observed in all taper ratios is the first span-wise bending (1B), followed by the first torsional mode (1T), the first chord-wise bending (1CB), and finally the second torsional mode (2T), in sequential order. There is a lack of significant changes observed in the modal displacements across various modes when considering variations in the taper ratio.

Table 4.9 Effect of taper ratio on mode shapes of a functionally graded conical shell for N=1, T_t= 300K, Ψ=0°,uneven porosity with $\alpha = 0.1$

Taper Ratio	Mode 1	Mode 2	Mode 3	Mode 4
C_r=-1	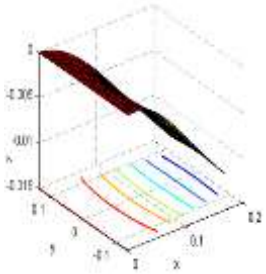	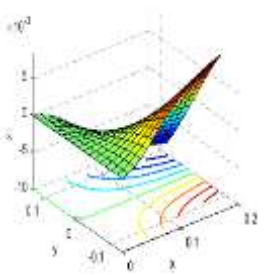	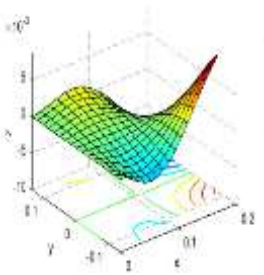	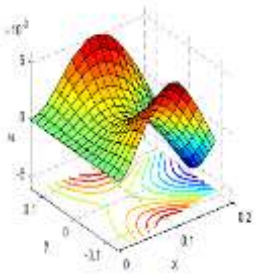
C_r=0	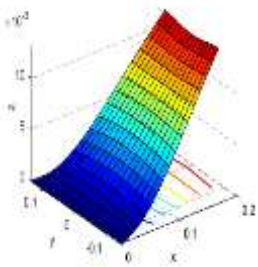	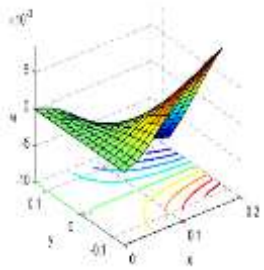	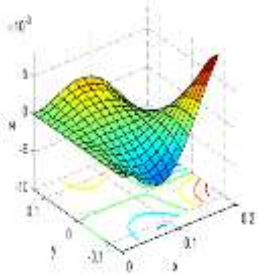	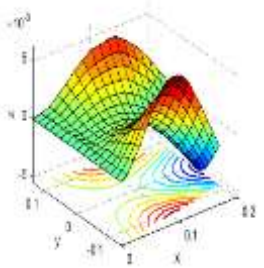
C_r=0.5	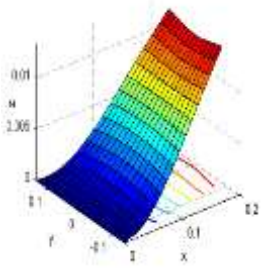	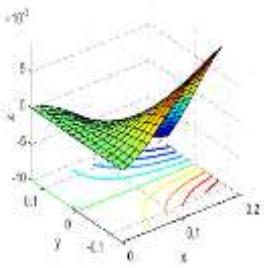	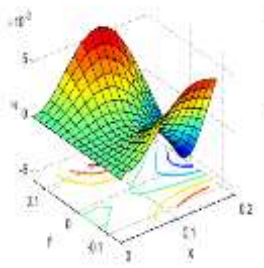	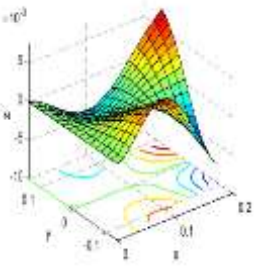

C_r=1	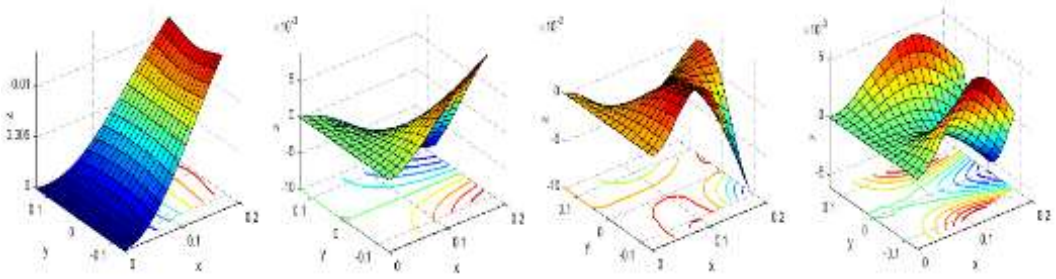			

Table 4.10 and 4.11 provide a description of the modes pertaining to the alteration of nonlinear temperature distribution and power law index, respectively. The analysis of the two tables reveals that variations in the top surface temperature and power law index have minimal impact on modal displacement. Nevertheless, the symmetry of the mode structure undergoes a change at extremely elevated temperatures for the third and fourth modes.

Table 4.10 Effect of top surface temperature on mode shapes of a functionally graded twisted conical shell for C_r=1, N=1, $\Psi=0^0$, even porosity with $\alpha = 0.2$

Temperature at top surface	Mode 1	Mode 2	Mode 3	Mode 4
T_t = 300K	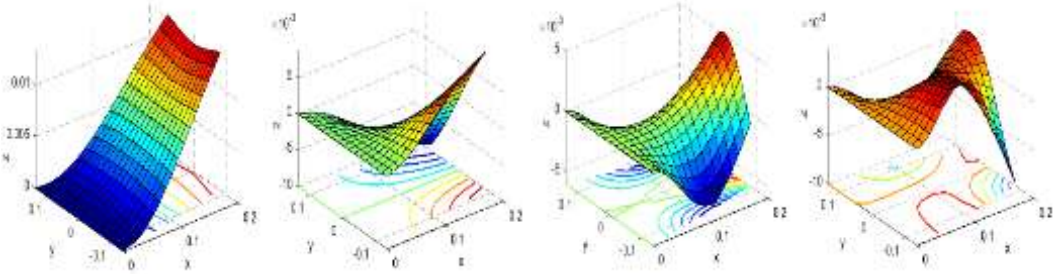			
T_t = 400K	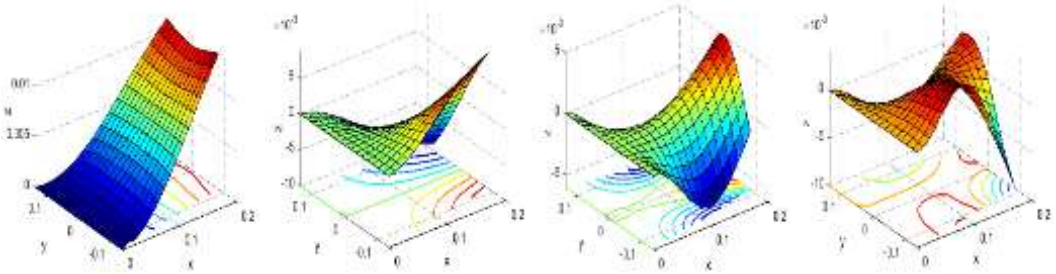			
T_t = 600K	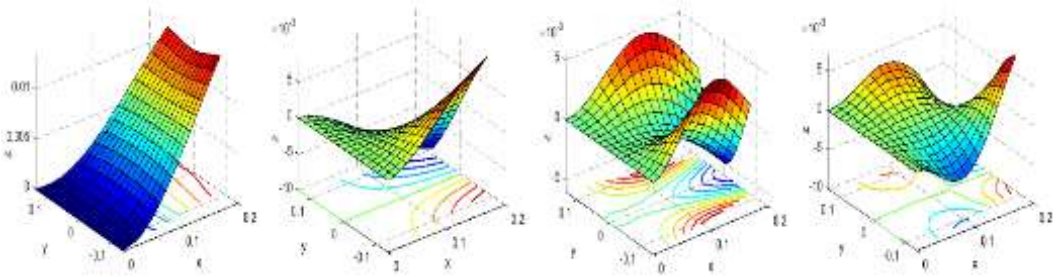			

Table 4.11 Effect of power law index on mode shapes of a functionally graded twisted conical shell for C_r=1, T_t= 300K, $\Psi=0^0$, uneven porosity with $\alpha = 0.2$

Power Law Index	Mode 1	Mode 2	Mode 3	Mode 4
N=0	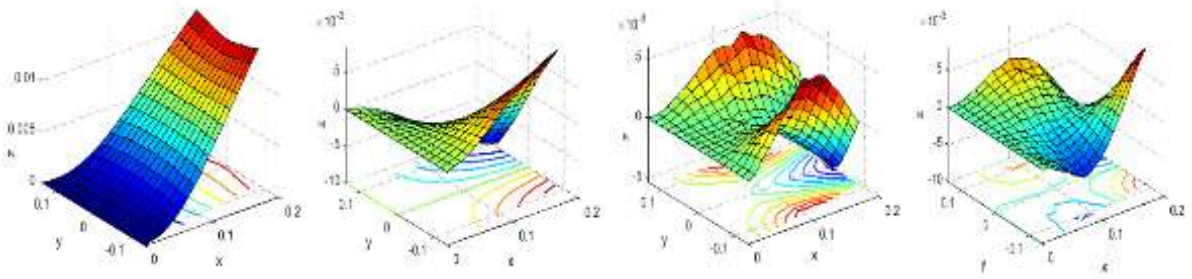			
N=0.5	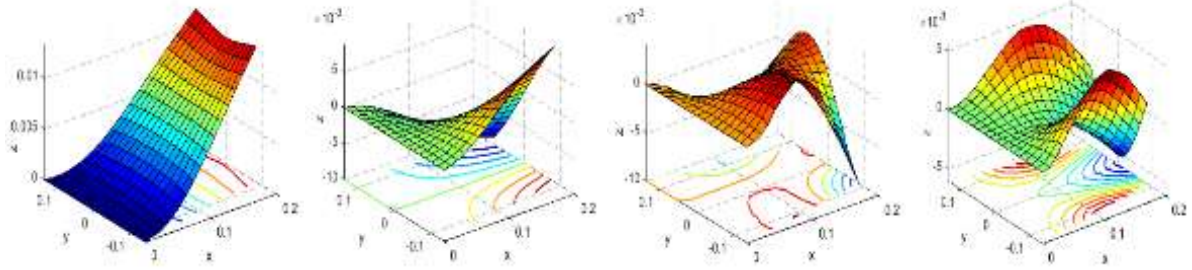			
N=1	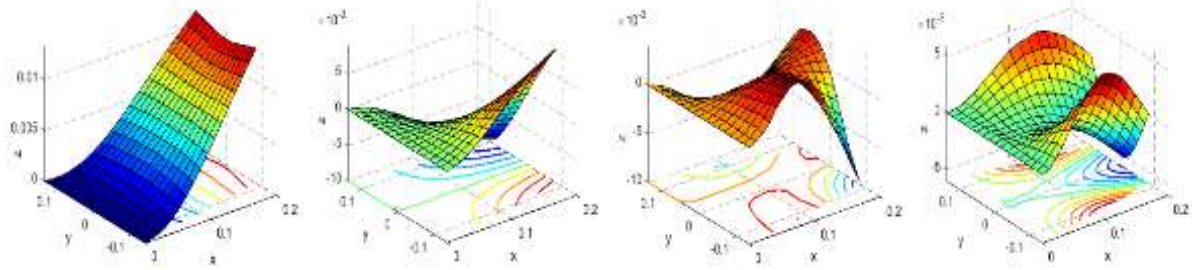			
N=2	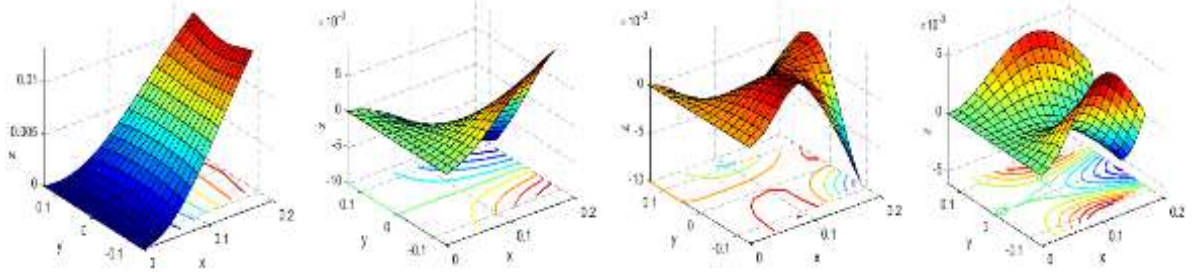			
N=∞	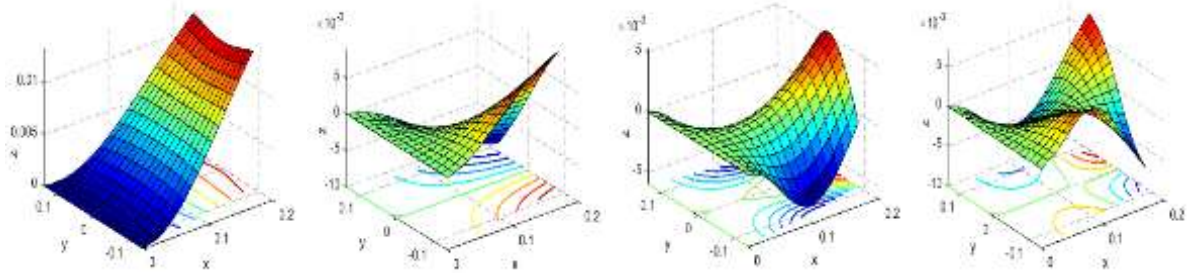			

The mode shapes, as presented in Table 4.12, demonstrate a clear and intelligible relationship with the variation in pretwist angles. It is evident that alterations in the pretwist angle significantly impact the mode shapes. The torsional behavior of the shell is notably affected by the inclusion of a pretwist angle. The initial mode is characterized by the first torsional mode (1T) occurring at a phase angle of 30 degrees relative to the first span-wise bending (1B) of an untwisted shell. The fourth mode of the untwisted shell has the characteristic shape of first cord-wise bending (1CB), but it assumes the form of second torsion (2T) due to the inclusion of a pretwist angle.

Table 4.12 Effect of pretwist angle on mode shapes of a functionally graded twisted conical shell for C_r=1, N=1, T_t= 300K & uneven porosity with α = 0.2

Pretwist angle	Mode 1	Mode 2	Mode 3	Mode 4
$\psi = 0^0$	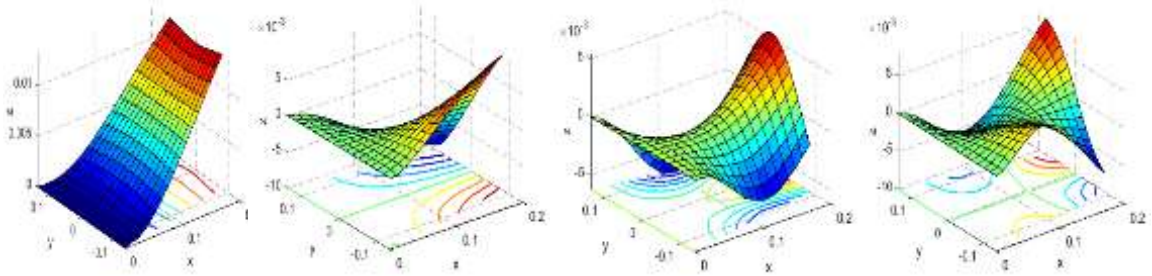			
$\psi = 15^0$	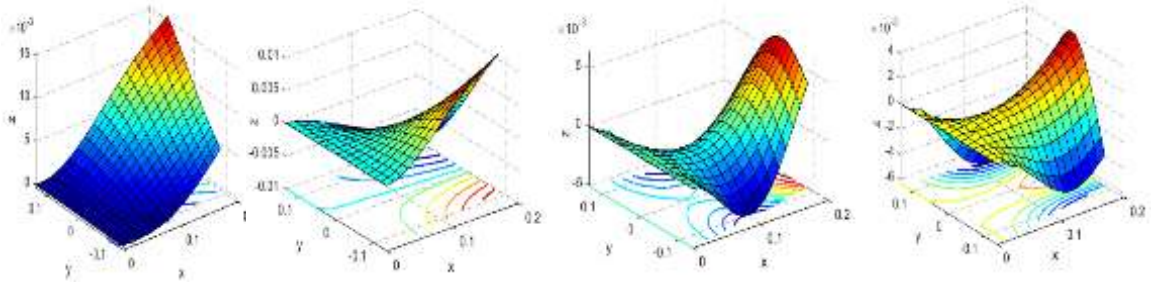			
$\psi = 30^0$	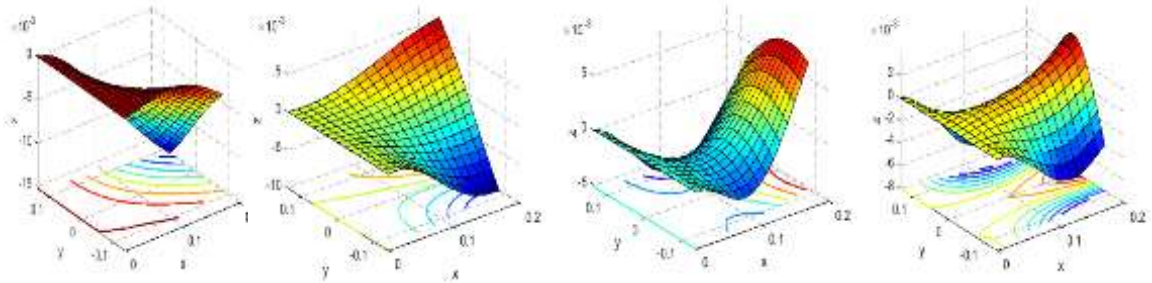			

CHAPTER 5

FREE VIBRATION ANALYSIS OF TAPERED POROUS BIDIRECTIONAL FG CONICAL SHELL IN THERMAL ENVIRONMENT

5.1 INTRODUCTION

Earlier the concept of FGMs were implemented by grading two constituents ceramic and metal across the thickness unidirectional, where the metal part was placed to provide the mechanical strength and toughness and the role of the ceramic constituent was to protect the metal from high temperature and high velocity impact. With the grading of the constituents, the material properties also keep changing through the dimension. In recent times, further advancements were carried out in the field of FGMs by grading the constituents in two directions that is termed as bi-directional functionally graded materials (BDFGM). This can effectively enable the contribution of mechanical properties from three constituents to construct the FGM. In most of the cases, two different metals are used to develop the desired mechanical properties and one ceramic constituent protects the structure from the hostile thermal environment.

It is already discussed in Chapter-1 that most of the works regarding the free vibration of bidirectional functionally graded materials were carried out based on the plate and beam structures with simply supported boundary conditions and some of the studies considered porosity distribution. However, none of the researchers had focussed on the free vibration of rotating porous BDFGM in twisted conical shell structure with cantilever boundary conditions. In light of turbomachinery and aerospace based applications, the incorporation of thermal environment with nonlinear temperature distribution may bring the situation extremely close to the reality. Moreover, the variable thickness model of the BDFG conical shell with twisting effect will justify the objectives extensively. An exploratory feature of the study will be provided by the application of non-polynomial higher order shear deformation theory, which behaves more computationally efficiently compared to standard FSDT and HSDT since it uses trigonometric function to express deformation. Finite element method is employed to discretize the conical shell into eight-noded isoparametric elements having seven degrees of freedom at each node. The bidirectional FG conical shell is composed of two metals and one ceramic constituent where the ceramic is graded across the thickness direction and both the metals are graded along the longitudinal direction. Both the metals having diversity in Young's modulus or thermal conductivity can meet the requirements of the FGM shell as per the situation.

Benchmark solutions from the already published articles are used to validate and examine the accuracy of the present formulation. The present investigation analyses the impact of porosity distribution, power law indexes along both the directions, nonlinear temperature distribution, rotational speed, taper ratio and pretwist angle on the non-dimensional fundamental frequency of the BDFG conical shell. Last but not the least, the characteristics of the initial mode shapes and the effects of some factors on the mode shapes are also analysed.

5.2 NUMERICAL RESULTS AND DISCUSSIONS

As stated in the theoretical formulation, the porous BDFG conical shell that is considered is made by one ceramic and two metal constituents and the two metal constituents are differentiated and specified by metal-1 and metal-2 in the equations. In the present study, silicon nitride (Si_3N_4) is used as the single ceramic constituent that is concentrated mainly in the upper part of the shell. Whereas, stainless steel (SUS304) is considered as metal-1 that concentrates near the fixed end and on the contrary, Nickel (Ni) is chosen as metal-2 which appears prominently at the free end of the conical shell. The two metal constituents combinedly make the lower part of the shell metal rich. The variations of all three constituent materials across the conical shell are pictorially illustrated in Figure 5.1.

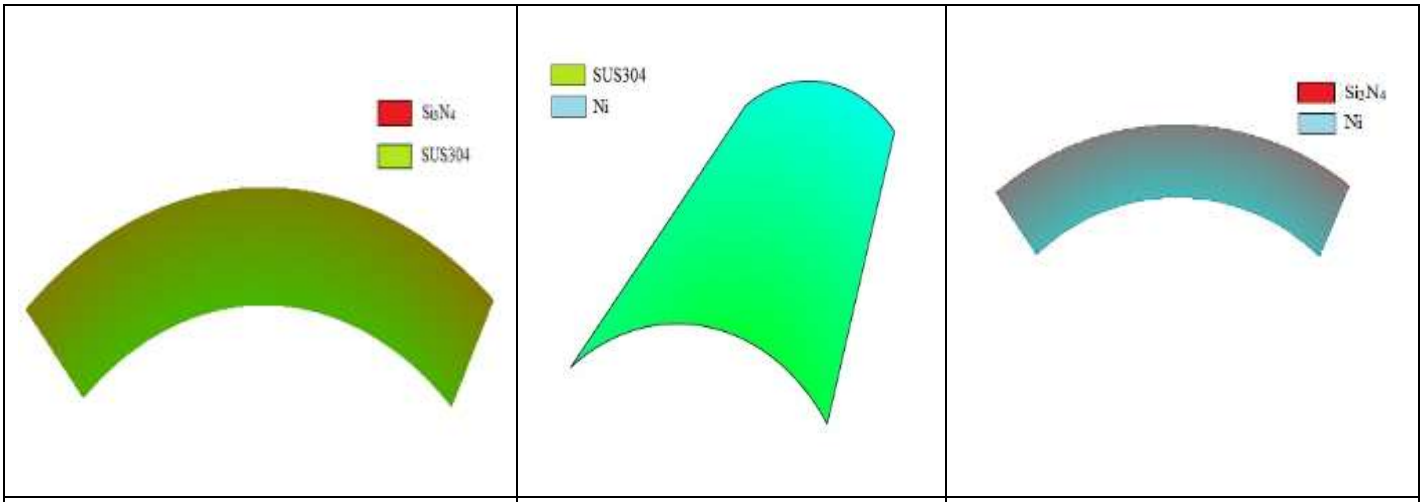

(a)	(b)	(c)

Figure 5.1 The material grading throughout the BDFG conical shell: (a) transverse direction at the fixed end, (b) longitudinal direction, (c) transverse direction at the free end

The temperature dependent material properties of these three constituents i.e. Young's modulus, Poison's ratio and thermal expansion coefficient are furnished in Table 5.1.

Moreover, the two temperature independent material properties used for the formulation are density (ρ) and thermal conductivity (K) and their values are as follows:

$\rho_c = 2370$ kg/m^3, $K_c = 9.19$ W/mK, $\rho_{m1} = 8900$ kg/m^3, $K_{m1} = 83.7$ W/mK, $\rho_{m2} = 8166$ kg/m^3, $K_{m2} = 12.04$ W/mK

Table 5.1 Temperature-dependent material properties of ceramic and metal constituents (unit of E in Pa, α_t in 1/K, suffix c, m1 and m2 refer to ceramic, metal-1 and metal-2, respectively).

Material	Properties	P_{-1}	P_0	P_1	P_2	P_3
Si_3N_4	E_c	0	348.43×10^9	-3.070×10^{-4}	2.160×10^{-7}	-8.946×10^{-11}
	α_{tc}	0	5.8723×10^{-6}	9.095×10^{-6}	0	0
	υ_c	0	0.24	0	0	0
Ni	E_{m1}	0	223.95×10^9	-2.794×10^{-4}	-4.06×10^{-9}	0
	α_{tm1}	0	9.9209×10^{-6}	8.705×10^{-6}	0	0
	υ_{m1}	0	0.31	0	0	0
SUS304	E_{m2}	0	201.04×10^9	3.079×10^{-4}	-6.534×10^{-7}	0
	α_{tm2}	0	12.330×10^{-6}	8.086×10^{-6}	0	0
	υ_{m2}	0	0.3262	-2.002×10^{-4}	3.797×10^{-7}	0

The relevant geometric dimensions and parameters of the BDFG conical shell considered for the convergence study and parametric study as well are

$s = 0.5$ m, $\phi_0 = 75°$, $\phi_v = 50°$, $L/s = 0.4$, $s/h = 20$

The cantilever boundary conditions adopted for the entire study are as follows:

At x= 0, $u = v = w = \theta_x = \theta_y = \xi_x = \xi_y = 0$ (5.1)

5.3 VALIDATION AND CONVERGENCE STUDIES

Based on the above finite element formulation and non-polynomial higher order shear deformation theory, a distinct computer code was developed to assess the free vibration of porous BDFG conical shell in thermal environment. The results generated from the code are validated with the available benchmark publications to establish the authenticity and correctness of the code. The code has already been validated in Chapter 4 with regard to the pretwisted conical shell with Liew et al. (1994), the nonlinear temperature distribution with Parida and Mohanty (2017) and Huang and Shen (2004), and the rotational speed of the shell with Sreenivasamurthy and Ramamurthi (1981). Furthermore, the NDF of the tapper shell is validated with Fang and Zhou (2017) and Cheung and Zhou (2003), and is provided in Chapter 4. The dimensionless natural frequencies of the bidirectional functionally graded structure are finally presented in Table 5.1 and Table 5.2 and compared with the findings of Kumar et al. (2023), Sekkal et al. (2017), and Xiang et al. (2014). It is clear from the tables that the findings closely match those of the investigations while using FSDT but in NPHSDT the result shows a little bit variation. This may be due to the fact that FSDT over estimates the frequency value as compared to HSDT. So the code can effectively analyse the free vibration characteristics of the rotating porous bidirectional functionally graded (BDFG) twisted conical shell.

Table 5.2 Non-dimensional natural frequencies ($\varpi = \omega_n(a/\pi)^2\sqrt{12(1-\nu^2)\rho_c\,/\,E_c h^2}$) for **BDFG** plate with simply supported boundary conditions for $a/h = 10$, $E_c = 151$ GPa, $\rho_c = 3000$ kg\m^3, $\nu = 0.3$.

n_x	n_z	Kumar et al. (2023)	Sekkal et al. (2017)	Present (FSDT)	Present (NPHSDT)
0	0	1.9313	1.9388	1.9311	1.8942
	0.2	1.8339	1.8424	1.8360	1.8019
	0.5	1.7402	1.7504	1.7408	1.7090
	1	1.6595	1.6708	1.6579	1.6274
	5	1.5503	1.5575	1.5494	1.5163

Table 5.3 Non-dimensional natural frequencies ($\varpi = \omega_n(a/\pi)^2\sqrt{12(1-\nu^2)\rho_c\,/\,E_c h^2}$) for **BDFG** plate with simply supported boundary conditions for $a/h = 50$, $E_c = 348.43$ GPa, $\rho_c = 2370$ kg\m^3, $\nu = 0.24$.

n_x	n_z	Kumar et al. (2023)	Xiang et al. (2014)	Present (FSDT)	Present (NPHSDT)

0		1.9955	1.9978	1.9973	1.9817
0.5		1.3811	1.3960	1.3960	1.3865
1	0	1.2004	1.1851	1.1848	1.1819
2		1.0579	1.0200	1.0198	1.0119
5		0.9399	0.9011	0.9008	0.8931

A convergence study is carried out for the first four modes of the natural frequencies using the mesh sizes of 2×2, 4×4, 6×6, 8×8, and 10×10 as shown in Table 5.3. One can see that the findings conversed at 8×8 mesh size. As a result, the entire study uses a mesh size of 8×8 with 64 elements and 225 nodes. For this convergence study the natural frequency has been taken in non-dimentionalized form and the same form is applied for the parametric study also.

Table 5.4 Convergence study for non-dimensional fundamental frequency $\left(\bar{\omega} = \frac{\omega L^2}{h}\sqrt{\frac{\rho_{m1}}{E_{m1}}}\right)$ of a porous pretwisted BDFG conical shell in thermal environment. (T_t= 400 K, Ψ=30°, uneven porosity with α= 0.2, C_h=0.0, Ω=0, n_x=0.5, n_z=1.0)

Mode	Mesh size				
	2×2	4×4	6×6	8×8	10×10
1	2.98967	2.99041	2.99032	2.99046	2.99062
2	6.72449	6.70224	6.70122	6.70146	6.70173
3	10.08620	9.86689	9.85253	9.85000	9.84930
4	13.47815	12.79526	12.74789	12.74031	12.73840

5.4 RESULTS AND DISCUSSIONS

5.4.1. Effects of volume fraction of porosity (α)

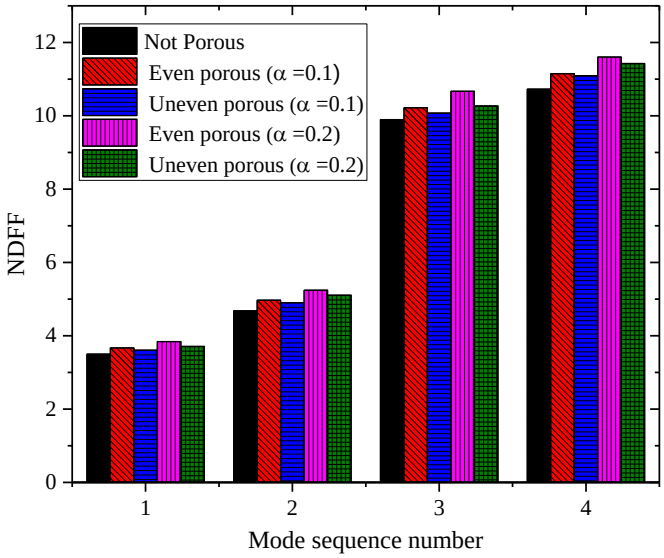

Figure 5.2 Effect of porosity on the first four non-dimensional frequencies of different types of BDFG conical shells [T_t = 300K, C_r =0.0, Ψ=0°, n_x= n_z=1.0]

Figure 5.2 shows the impact of porosity distribution on the non-dimensional frequencies of the first four modes for BDFG conical shell without taper and twist at room temperature. In order to preserve consistency over the distribution of porosity, the power law index values for both the x-axis (n_x) and z-axis (n_z) are regarded as 1. Even and uneven porosity distributions are considered with volume fraction of porosity (α) 0.1 & 0.2, while the equivalent modes of non-dimensional frequencies are also compared with nonporous BDFG conical shell to study the variations of porosity distribution.

The plot clearly demonstrates that increasing volume fraction of porosity proportionally enhances magnitude of fundamental frequency. This pattern is influenced by the existence of porosity, which consistently decreases the density of the conical shell while simultaneously diminishing its rigidity. Moreover, is observable between the corresponding columns in the graph that an even porosity distribution consistently produces greater frequency values than uneven porosity distribution. This is due to the reason that uneven porosity distribution may concentrate at any particular region by not adhering to any regular pattern. Thus, the uniform pattern of even porosity distribution always has prominent effect compared to uneven porosity distribution for the same volume fraction of porosity.

5.4.2. Effects of Power Law Indexes (n_x,n_z)

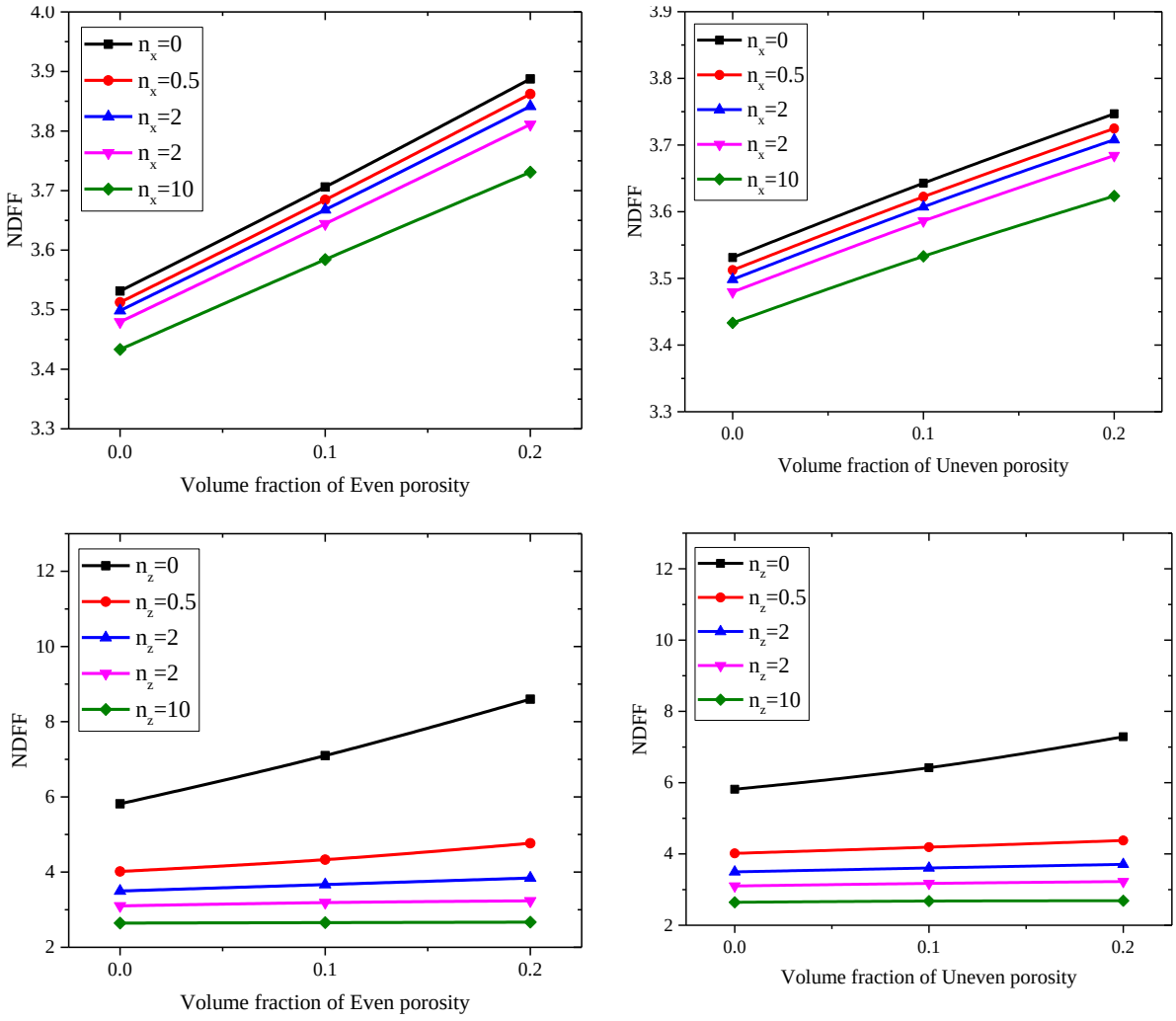

Figure 5.3 Effect of power law indexes (n_x, n_z) on the non-dimensional fundamental frequencies of porous BDFG conical shell [T_t = 300K, C_r =0.0, Ψ=0°]

Figure 5.3 represents the change of non-dimensional fundamental frequencies (NDFF) depending on power law indexes for porous BDFG conical shell with no taper and pretwist at room temperature (300K) for various porosity distributions. Both the power law indexes at longitudinal (n_x) and thickness (n_z) directions are considered for even and uneven porosity distributions separately and the trend was found to be exactly equivalent. When n_x was chosen as a function of NDFF then the value of n_z was regarded constant as $n_z = 1$ and vice versa. Here, n_x=0 signifies that the entire metallic portion is formed by SUS304 (metal-2) and with the increase of n_x, the volume fraction of stainless steel (SUS304) is replaced by nickel (metal-1) where the volume fraction of ceramic remains unchanged. On the other hand, n_z=0 implies that the entire shell is made by ceramic and the increase of n_z replaces the quantity of ceramic by both the metals equally. It is observed from the plot that the change in NDFF due to the

change of n_x is negligible compared to the change of n_z. As n_z increases, the stiffness of the BDFG conical shell substantially drops due to the decrease in ceramic volume fraction, which in turn instigates an extensive decrease in NDFF. The similar impact of porosity distribution with even and uneven patterns and increasing volume fraction is repeatedly observed as discussed in the previous section.

5.4.3. Effects of top surface temperature (T_t)

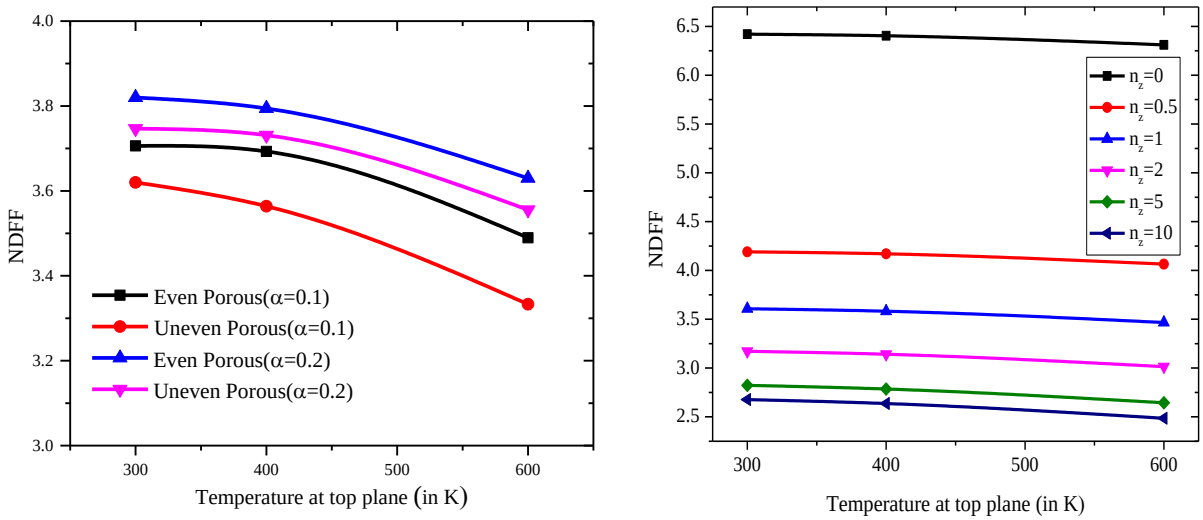

(a) at C_r =0.0, Ψ=0°, n_x= n_z=1.0

(b) at C_r =0.0, Ψ=0°, n_x=1.0, Uneven porosity (α=0.1)

Figure 5.4 Representation of non-dimensional fundamental frequencies at different top surface temperature.

Figure 5.4 illustrates the variation of non-dimensional fundamental frequencies (NDFF) when the BDFG conical shell is subjected to different temperature distributions without taper and pretwist. Figure 5.4(a) depicts the changes of NDFF due to temperature gradient of different porosity distributed shells and Figure 5.4(b) exhibits the NDFF variation with change in temperature of shells having different power law indexes along the thickness (n_z). The metal rich bottom surface is always assumed to be maintained at room temperature (300K) and the ceramic rich top surface is subjected to steady temperature rise, as the main role of the ceramic constituent is to protect the shell from high temperature environment. It can be seen from both the figures that the NDFF decreases as the temperature difference between the two extreme surfaces of the conical shell increases. This observation can be explained by the temperature-dependent behaviour of Young's modulus. The values of Young's modulus of all three constituents declines with the rise of temperature and this leads to a simultaneous reduction of

stiffness, which eventually results in the decrease of NDFF. The decrease in NDFF is not uniform and it increases at higher temperature ranges because it depends on the Fourier's equation of temperature distribution which is nonlinear.

5.4.4. Effects of rotational speed (Ω)

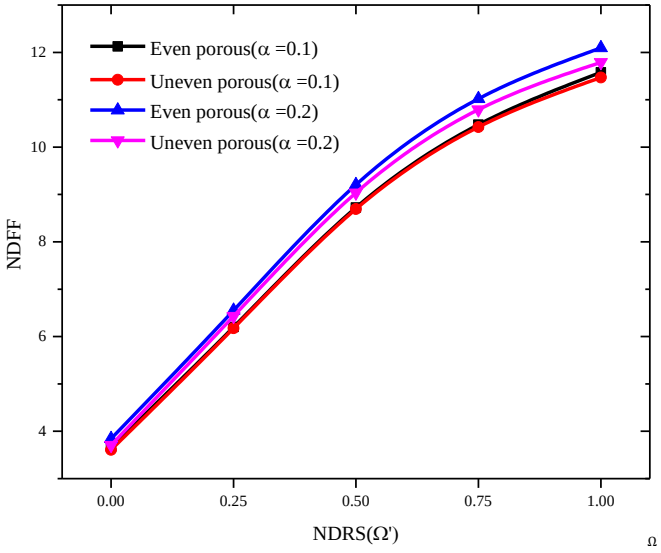

at T_t = 300K, C_r =0.0, Ψ=0°, n_x= n_z=1.0

Figure 5.5 Representation of non-dimensional fundamental frequencies at different non-dimensional rotational speeds.

Figure 5.5 displays the effect of non-dimensional rotational speeds (Ω′) on non-dimensional fundamental frequencies (NDFF) of BDFG conical shell with no taper and pretwist at room temperature (300K) for different porosity distributions. Here five different non-dimensional rotational speeds (Ω′) are considered as 0, 0.25, 0.5, 0.75 and 1 ($\Omega' = \frac{\Omega}{\omega_n}$, where ω_n is the static fundamental frequency and Ω is the rotational speed). The plot substantially demonstrates the trend that NDFF rises proportionally with the increase of NDRS. This is due to the increase of stiffness that is manifested by the development of centrifugal force generated by the rotation and is termed as centrifugal stiffening.

5.4.5. Effects of taper ratio (C_r)

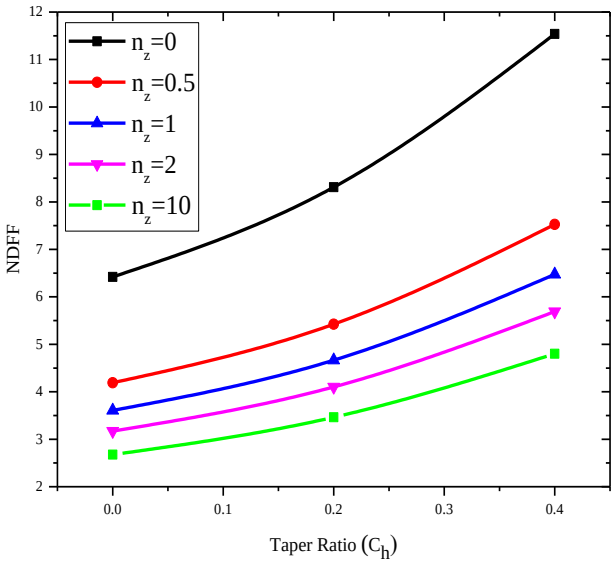

(a) at T_t = 300K, Ψ=0°, n_x=1.0, Uneven porosity (α=0.1)

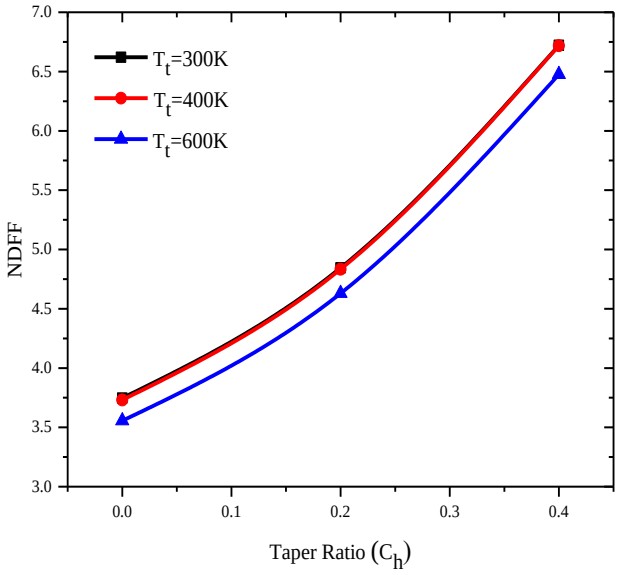

(b) at T_t = 300K, Ψ=0°, n_x= n_z=1.0, Uneven porosity (α=0.2)

Figure 5.6 Representation of non-dimensional fundamental frequencies with the change of taper ratio

Figure 5.6 depicts the impact of taper ratio on the non-dimensional fundamental frequencies (NDFF) of porous untwisted BDFG conical shell at room temperature. Figure 5.6(a) shows variation of non-dimensional fundamental frequencies with respect to taper ratio of the shells having different values of n_z of uneven porous shell with the volume fraction of porosity 0.1 while Figure 5.6(b) describes the changes of NDFF with taper ratio of shells having three different top surface temperatures with volume fraction of porosity 0.2. From both the plots, it is clearly observed that NDFF always rises with the increase of taper ratio. As increase of taper ratio means reduction of mass and NDFF is always inversely proportional to the mass of the shell. This reduction of mass takes place in the thickness direction due to taper and here in Figure 5.6(a) the effect of thickness reduction with different compositions of the constituents is displayed and it is found that for all the values of n_z the increase of NDFF is throughout consistent.

5.4.6. Effects of pretwist angle (Ψ)

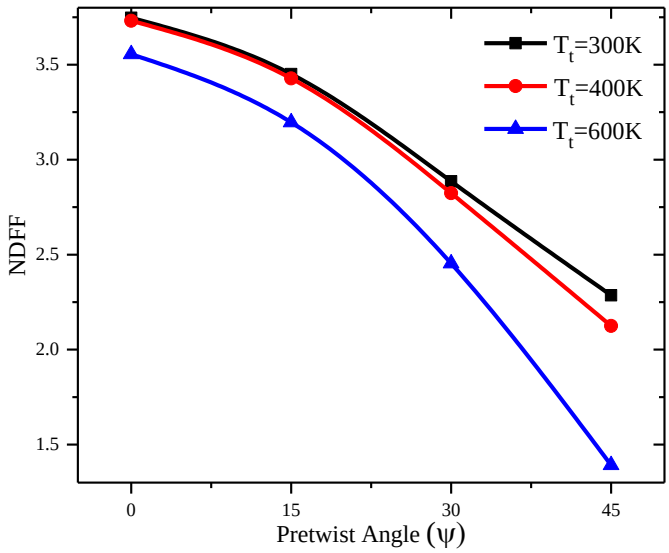

at T_t = 300K, C_r =0, n_x= n_z=1.0, Uneven porosity (α=0.2)

Figure 5.7 Representation of non-dimensional fundamental frequencies with the change of pretwist angle

Figure 5.7 illustrates the effect of pretwist angle (Ψ) on the non-dimensional fundamental frequencies (NDFF) of uneven porous BDFG conical shell without taper. It represents the variation of the NDFF with pretwist angles of conical shells having different nonlinear temperature distributions at n_x=n_z=1.0 with volume fraction of porosity 0.2. From the figure, it is proved that the NDFF decreases with the increase of pretwist angle (Ψ). This is simply because the increase of pretwist angle (Ψ) always reduces the structural stiffness of the shell which simultaneously lowers the NDFF also. The depletion of the NDFF with the rise of pretwist angle (Ψ) is observed to be more prominent for the higher values of top surface temperature of the conical shell.

5.5 MODE SHAPES

The variations in the modal displacements are represented in Table 5.4 to Table 5.9 for uneven porous BDFG conical shell at T_t = 300K. Table 5.4 consists the mode shapes with the change of power law indexes along the thickness (n_z) and for the first four modes the mode shapes are found to be first span-wise bending (1B), first torsional mode (1T), first chord-wise bending (1C) and second torsional mode (2T) sequentially. The impact of different power law indexes along the thickness (n_z) on the mode shapes of initial modes are appeared to be negligible. Table 5.5 presents the first four mode shapes with the alteration of different power law indexes along the length (n_x) and exactly same results are found with Table 5.4 However

the compositions of the conical shell vary with the changes of n_x and n_z but no significant impact of the power law indexes are observed in the mode shapes throughout different values.

Table 5.6 constitutes the different mode shapes for the alterations of pretwist angle. With the addition of twisting effect, the torsional behaviour emerges across all the modes and it increases proportionally with the rise in pretwist angle. Subsequently the first span-wise bending (1B) and first chord-wise bending (1C) disappear from the first mode and third mode respectively.

Table 5.7 displays the initial mode shapes due to the change of thickness of the BDFG conical shell and like pretwist angle, taper ratio is also proved to have a significant impacts on the mode shapes. With the rise of taper ratio from 0.5 to 1, the first span-wise bending (1B) and first torsional mode (1T) interchange between first mode and second mode while the symmetry changes for third mode.

Table 5.8 and 5.9 exhibit that volume fraction of porosity and top surface temperature have very minimal effect on the order of modal displacements.

Power Law Index along the thickness (n_z)	Mode 1	Mode 2	Mode 3	Mode 4
n_z=0	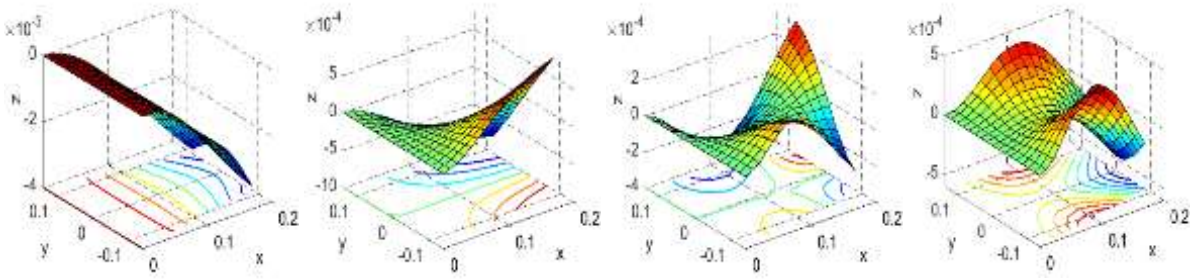			
n_z=1	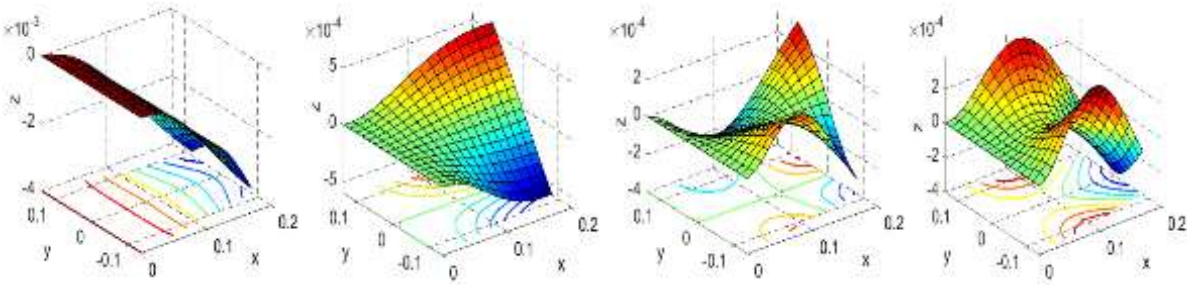			

n_z=10

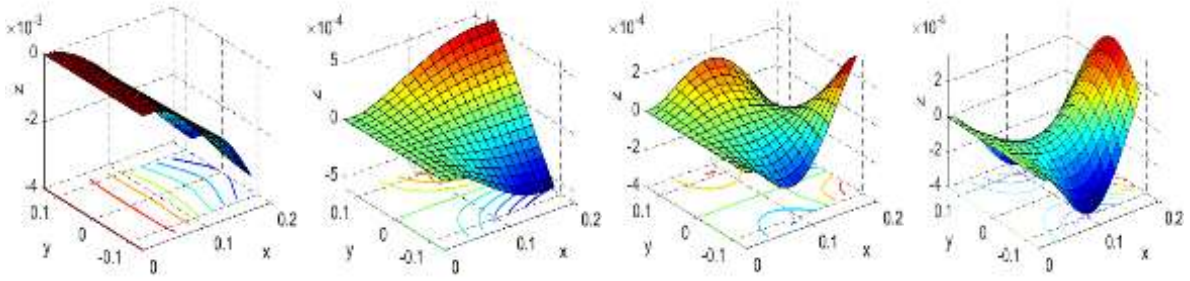

Table 5.5 Effect of power law index in the thickness direction on mode shapes of a BDFG conical shell for n_x=1 , T_t = 300K, C_r =0, ψ= 0^0 & uneven porosity with α = 0.1

Power Law Index along the length (n_x)	Mode 1	Mode 2	Mode 3	Mode 4

n_x=0

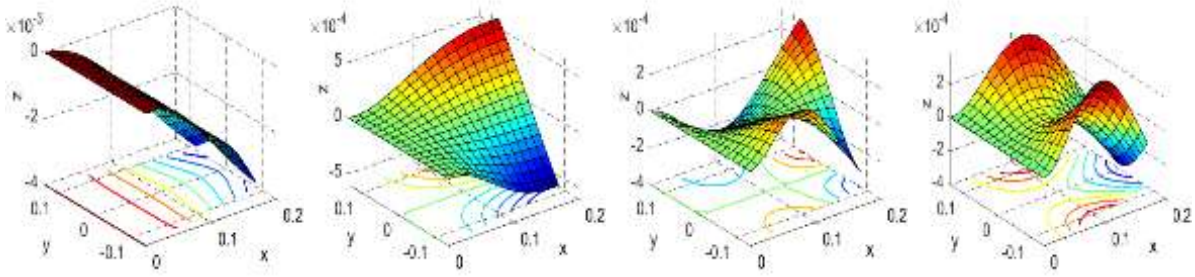

n_x=1

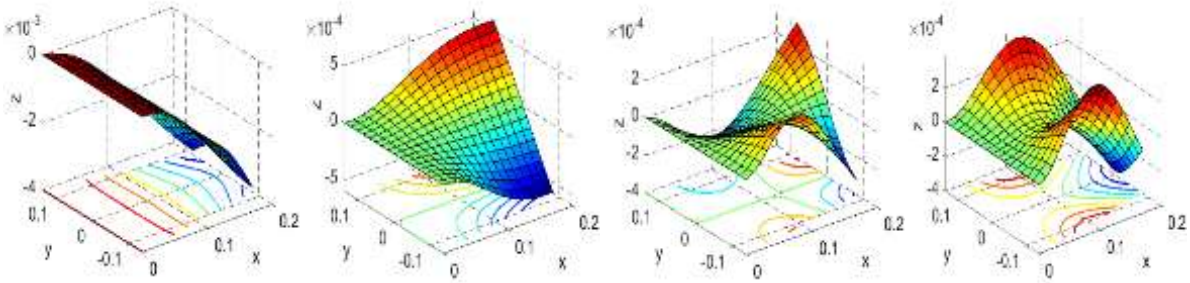

n_x=10

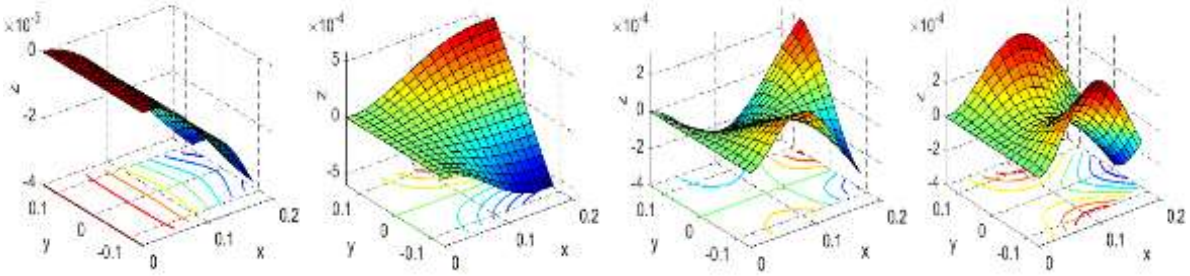

Table 5.6 Effect of power law index in the thickness direction on mode shapes of a BDFG conical shell for n_z=1 , T_t = 300K, C_r =0, ψ= 0^0 & uneven porosity with α = 0.1

Pretwist angle	Mode 1	Mode 2	Mode 3	Mode 4
$\psi = 0^0$	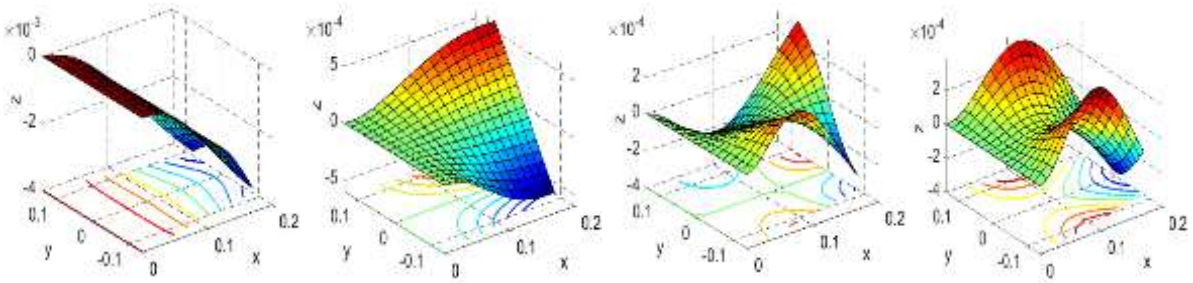			
$\psi = 15^0$	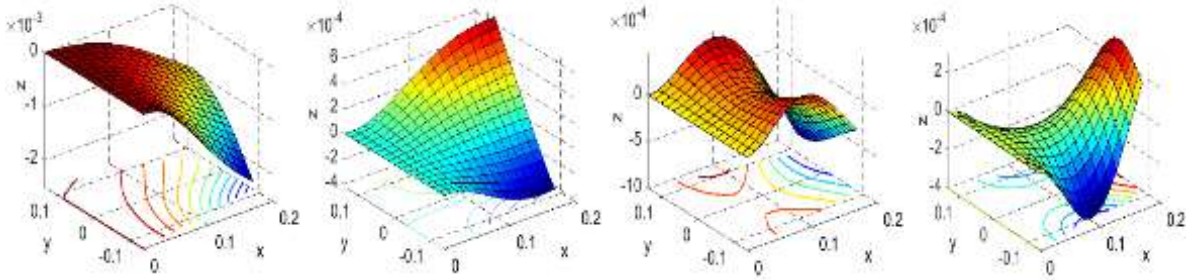			
$\psi = 30^0$	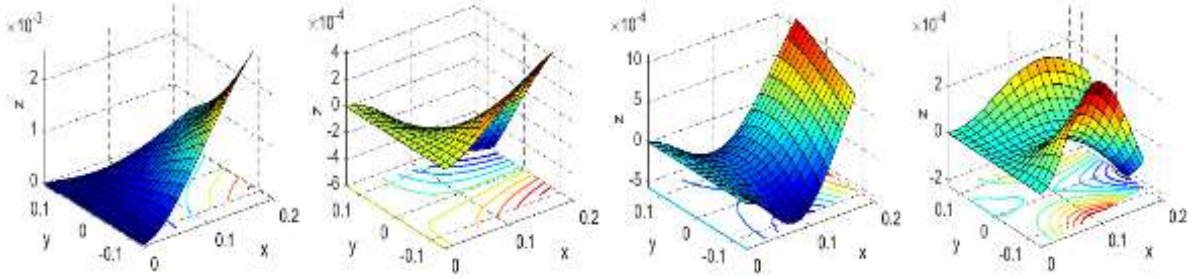			

Table 5.7 Effect of pretwist angle on mode shapes of a BDFG conical shell for $n_x = n_z = 1$, $T_t = 300$K, $C_r = 0$ & uneven porosity with $\alpha = 0.2$

Taper Ratio	Mode 1	Mode 2	Mode 3	Mode 4
$C_r = 0$	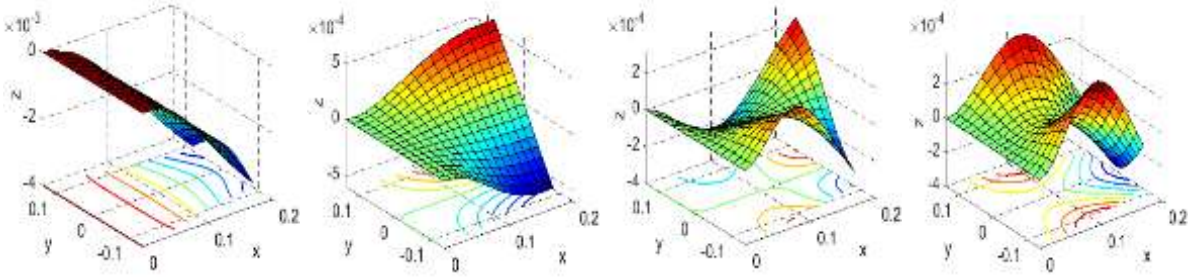			

C_r =0.5	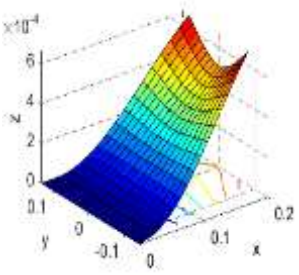	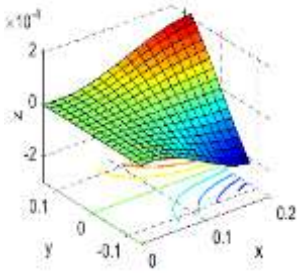	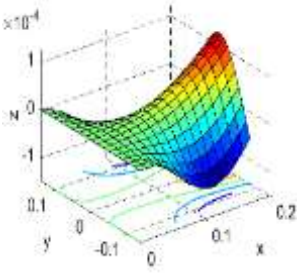	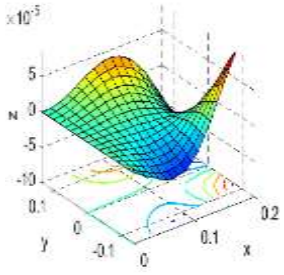
C_r =1	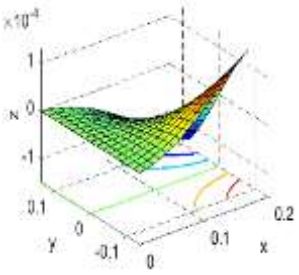	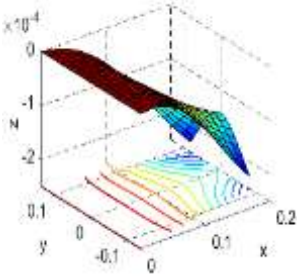	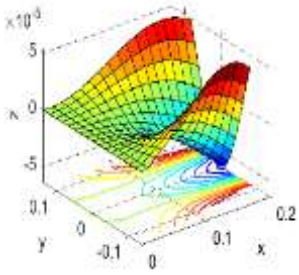	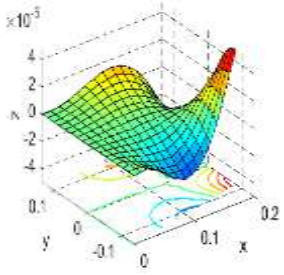

Table 5.8 Effect of taper ratio on mode shapes of a BDFG conical shell for n_x= n_z=1, T_t = 300K, ψ =0 & uneven porosity with α = 0.2

Porosity	Mode 1	Mode 2	Mode 3	Mode 4
α=0	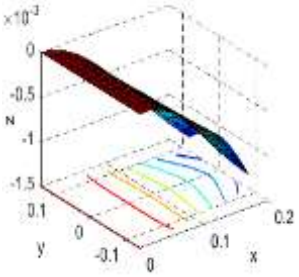	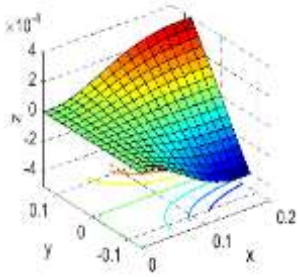	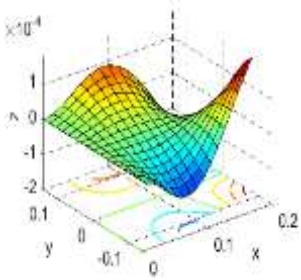	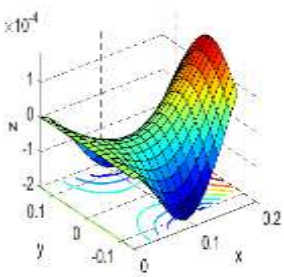
α=0.1	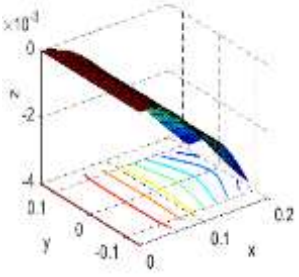	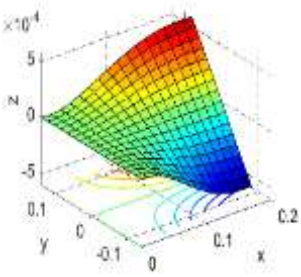	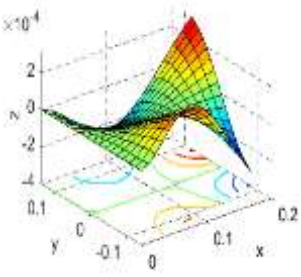	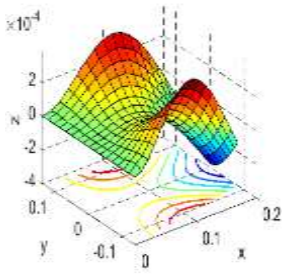
α=0.2	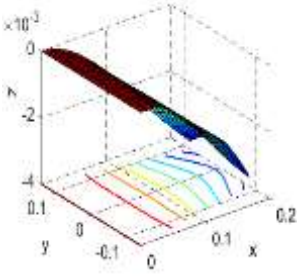	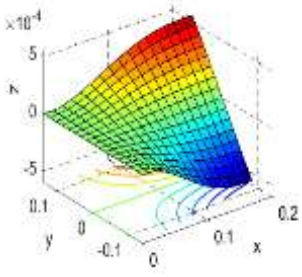	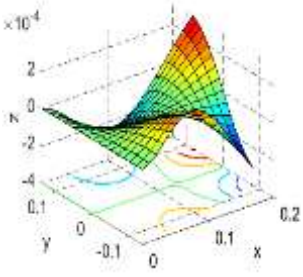	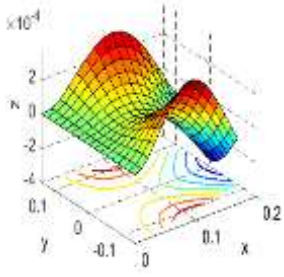

Table 5.9 Effect of porosity on mode shapes of an evenly porous BDFG conical shell for n_x= n_z=1, T_t = 300K, ψ =0 & C_r =0

Temperature at top surface	Mode 1	Mode 2	Mode 3	Mode 4
T_t= 300K	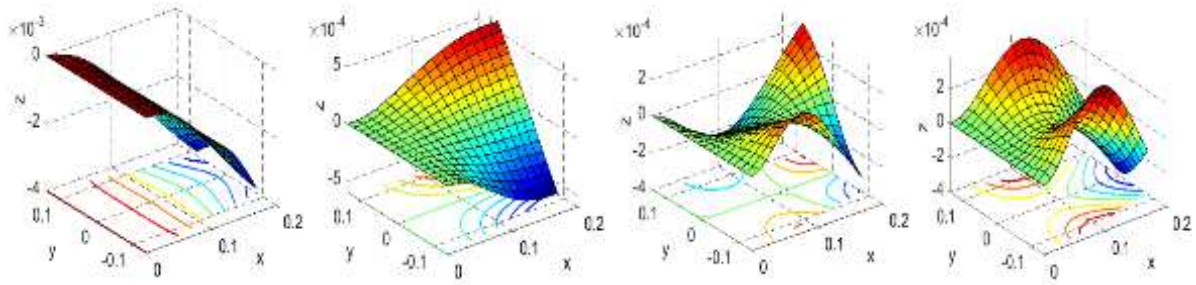			
T_t= 400K	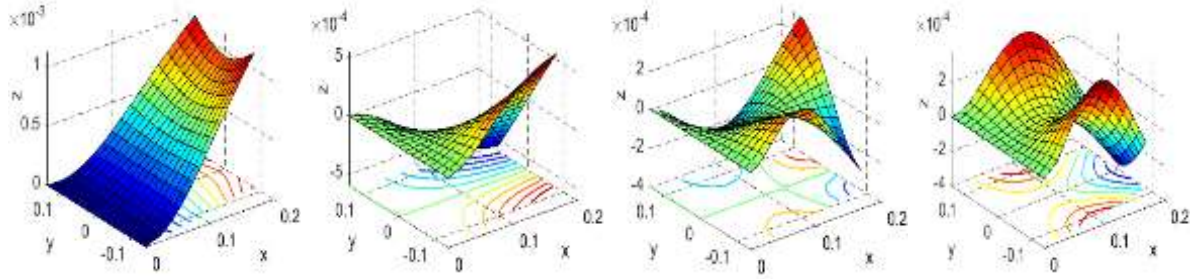			
T_t= 400K	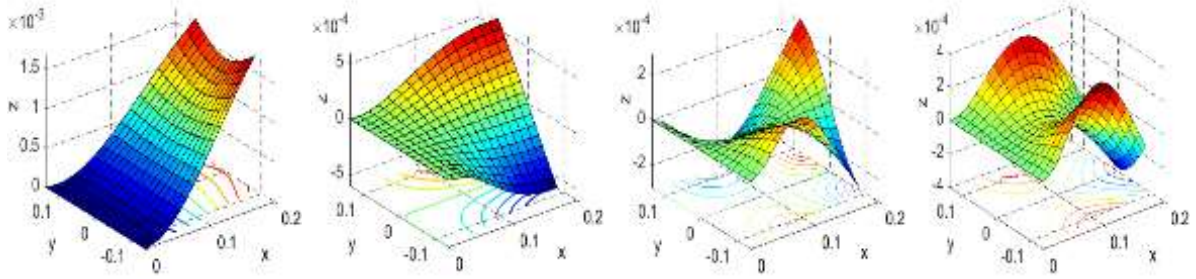			

Table 5.10 Effect of top surface temperature on mode shapes of a BDFG conical shell for n_x= n_z=1, ψ =0 & C_r =0 & uneven porosity with α = 0.1

CHAPTER 6
CONCLUSIONS

6.1 INTRODUCTION

This chapter summarizes the results, presented as tables and graphs, regarding the free vibration characteristics of the rotating pretwisted FGM conical shell within the current scope of work employing trigonometric and polynomial higher order shear deformation theory. Finite element-based computer programs are created to get numerical findings for the free vibration characteristics of different types (p-FGM, e-FGM, s-FGM, BDFGM) of functionally graded conical shells. The convergence studies of the finite element method are conducted by altering mesh sizes for free vibration analysis. This investigation aims to examine the influence of different triggering factors on the free vibration characteristics of functionally graded shallow conical shells. Parametric investigations are conducted for free vibration, as detailed in Chapter 3, Chapter 4 and Chapter 5, respectively. This chapter enumerates the key conclusions derived from the current analysis. The outcomes produced represent the inaugural findings of the studies conducted in this investigation and serve as benchmark solutions for future researchers. This chapter also outlines the potential for future extensions of the current study or new investigations related to similar problem areas.

6.2 CONCLUDING REMARKS

6.2.1 FREE VIBRATION ANALYSIS OF ROTATING POROUS FG CONICAL SHELLS (p-FGM, e-FGM and s-FGM) IN THERMAL ENVIRONMENT

(1) Pretwisted FG conical shells with even porosity have frequency that is always higher than shells with uneven porosity distribution. The fundamental frequency rises as the volume fraction of porosity rises, indicating that porosity plays a substantial role in modelling the material.

(2) The non-dimensional frequency of the conical shell decreases as the top surface temperature rises, keeping bottom surface temperature constant.

(3) The non-dimensional frequency of the porous FG conical shells is significantly influenced by the pretwist angle. The non-dimensional fundamental frequency decreases as the pretwist angle value rises.

(4) The non-dimensional fundamental frequency of the porous FG conical shell has a magnitude that is precisely related to the rotational speed, suggesting that frequency increases as rotational speed increases. This is due to centrifugal stiffening.

(5) The nature and symmetry of the mode shapes are significantly influenced by the pretwist angle, although the effects of temperature and porosity distribution are minimal.

6.2.2 FREE VIBRATION ANALYSIS OF ROTATING TAPERED POROUS FG CONICAL SHELL IN THERMAL ENVIRONMENT

1. The fundamental frequency of the FG conical shell is significantly influenced by the taper ratio. It continues to rise as the taper ratio increases.
2. The fundamental frequency is always increased by the presence of porosity, and the even distribution of porosity always exhibits a greater fundamental frequency than uneven distribution.
3. The greatest fundamental frequency is always initiated by the untwisted shell, and as the pretwist angle is increased, the natural frequency value decreases.
4. While keeping the temperature at the metal surface constant, an increase in the top surface temperature of the FG porous conical shell produces a drop in its fundamental frequency.
5. The fundamental frequency continues to decline as the power law index rises, which has a significant impact on it.
6. The fundamental frequency of the FG porous conical shell increases with rotating speed, which can be due to centrifugal stiffening.

6.2.3 FREE VIBRATION ANALYSIS OF ROTATING TAPERED POROUS BIDIRECTIONAL FUNCTIONALLY GRADED CONICAL SHELL IN THERMAL ENVIRONMENT

1) Being an integral property, porosity always plays a significant impact on the fundamental frequency. Inclusion of the porosity level always increases the fundamental frequency. Uneven porosity distribution always ensues lower fundamental frequency compared to evenly distributed pattern for the same amount of volume fraction of porosity.

2) Both the power law indexes along the longitudinal and thickness direction affects identically on the fundamental frequency. Fundamental frequency decreases with the increase of both power law indexes while the change of power law indexes have marginal effects on the modal displacements of the conical shell.
3) Fundamental frequency always drops with the increase of nonlinear temperature distribution across the thickness of the conical shell.
4) Rotational speed always acts as an agent to introduce centrifugal stiffening to the conical shell that ultimately increases the fundamental frequency by raising the stiffness.
5) The tapered thickness always reduces the mass uniformly in the thickness direction which proportionally declines the fundamental frequency. It influences the modal displacements for the corresponding modes unlike power law indexes.
6) The fundamental frequency always drops as the pretwist angle increases. Besides disrupting the symmetry, it also inducts more torsions to the mode shapes of the BDFG conical shell.

6.3 SIGNIFICANT CONTRIBUTIONS OF THE THESIS

The contributions of the current work and the objective assessment of the thesis are delineated as follows

(1) The pretwisted FG conical shell with cantilever boundary condition might be considered as one of the most appropriate options for turbomachinery blade. However, no studies that account for the porosity and rotating nature of the FG pretwisted conical shell have been reported so far in thermal condition. Though the expression of nonlinear temperature distribution for p-FGM and s-FGM is available in open literature but the expression for e-FGM has been presented in this thesis for the first time. The volume fraction of the metal and ceramic constituents of different FG conical shells (p-FGM, e-FGM, s-FGM, BDFGM) are estimated by using Voigt's law. The temperature-dependent material properties are obtained by considering the expression of non-linear temperature distribution derived from the one-dimensional steady-state heat conduction equation of Fourier.
(2) As discussed in the literature survey, it is clear that the majority of the investigators have worked on FG porous plates and shells based on FSDT or HSDT, with only a handful on CPT. Based on polynomial shear deformation theories, a few researchers

also recorded the free vibration response of porous FG plates/shells with varying thickness. The free vibration response of a rotating twisted porous FG conical shell with varying thickness along the axial direction is an entirely new area of investigation. It is well known that the accuracy of the FSDT cannot be ensured due to the dependence of the shear correction factor, whereas the polynomial HSDT incorporates the shear deformation using Taylor series coefficients. Moreover, Non-polynomial HSDTs have been proposed, in which the shear strain function is employed to show the shear deformation, to get over the aforementioned limits. The non-polynomial functions allow for accurate structural behaviour prediction, nonlinear in-plane displacement variation, parabolic transverse shear stress variation over the thickness, and fulfilment of traction-free boundary conditions. Thus, polynomial and non-polynomial HSDT, together with the subject matter, is very much worthwhile in the field of free vibration analysis. Finite element method (FEM) is used to calculate the natural frequency of the rotating FG porous tapered conical shell based on polynomial and non-polynomial HSDT under nonlinear thermal gradient. The finite element formulation for this tapered pretwisted FG conical shell have been developed by considering an eight-nodded isoparametric shell element having seven degrees of freedom at each node.

(3) Most of the works regarding the free vibration of bidirectional functionally graded materials were carried out based on the plate and beam structures with simply supported boundary conditions and few of them considered porosity distribution. However, none of the researchers had focussed on the free vibration of porous BDFGM in conical shell structure with cantilever boundary conditions. In addition, the incorporation of thermal environment with nonlinear temperature distribution may bring the situation extremely close to the reality for turbomachinery and aerospace based applications. Moreover, the variable thickness model of the BDFG conical shell with twisting effect will justify the objectives extensively.

6.4 FUTURE SCOPE OF WORK

This thesis addresses and resolves several significant features of rotating pretwisted functionally graded conical shells. However, owing to their technological importance and demand, additional study is required for the diverse uses of functionally graded conical shells concerning design, analysis, modeling, and production. Additional research may be conducted to thoroughly investigate the dynamic behavior of these specific

FGM structures, thereby expanding the current work or presenting a new set of challenges. The following possible areas for the extension of the current effort are identified:

(1) The current study, centred on linear elastic analysis, can be expanded to include the nonlinear analysis of moderately thick conical shells and can also integrate structural damping.
(2) The current study can be expanded to examine the conical shell structure in relation to the hygrothermal effect, which encompasses the combined influences of moisture and temperature.
(3) The current study may be expanded to include stiffened shells or shells featuring different geometrical structures.
(4) CNTs/Graphene-reinforced shallow conical shells can be considered for further investigation to enhance structural rigidity.
(5) A functionally graded graphene/CNTs-reinforced cylindrical or conical shell with fluid interaction may be considered for the exploration of free vibration analysis.

REFERENCES

[1] Ahmad M, Naeem MN. Vibration characteristics of rotating FGM circular cylindrical shells using wave propagation method. European Journal of Scientific Research. 2009;36(2):184-235.

[2] Alijani F, Amabili M, Karagiozis K, Bakhtiari-Nejad F. Nonlinear vibrations of functionally graded doubly curved shallow shells. Journal of Sound and Vibration. 2011;330(7):1432-54.

[3] Alijani F, Amabili M. Non-linear vibrations of shells: A literature review from 2003 to 2013. International Journal of Non-Linear Mechanics. 2014; 58:233-57.

[4] Alijani F, Bakhtiari-Nejad F, Amabili M. Nonlinear vibrations of FGM rectangular plates in thermal environments. Nonlinear Dynamics. 2011:66: 251–270.

[5] Amine DA, Abd El Kader M. Thermal behavior of functionally graded materials. In: 7th African conference on non destructive testing ACNDT 2016 & the 5th international conference on NDT and materials industry and alloys 2016. IC-WNDT-MI.

[6] Amoozgar M, Gelman L. Vibration analysis of rotating porous functionally graded material beams using exact formulation. Journal of Vibration and Control. 2022:28(21-22): 3195–3206.

[7] Ansari MI, Kumar A, Chakrabarti A. Static analysis of doubly curved singly ruled truncated FGM cone. Composite Structures. 2018; 184:523-35.

[8] Arciniega RA, Reddy JN. Large deformation analysis of functionally graded shells. International Journal of Solids and Structures. 2007; 44(6):2036-52.

[9] Aris H, Ahmadi H. "Nonlinear forced vibration and resonance analysis of rotating stiffened FGM truncated conical shells in a thermal environment." Mechanics Based Design of Structures and Machines. 2023: 51(7): 4063-4087.

[10] Arshad SH, Naeem MN, Sultana N. Frequency analysis of functionally graded material cylindrical shells with various volume fraction laws. Proc Inst Mech Eng, Part C: J Mech Eng Sci 2007; 221(12):1483–95.

[11] Atmane HA, Tounsi A, Bernard F. Effect of thickness stretching and porosity on mechanical response of a functionally graded beams resting on elastic foundations. International Journal of Mechanics and Materials in Design. 2017;13(1):71-84.

[12] Ayoubi P, Alibeigloo A. Three-dimensional transient analysis of FGM cylindrical shell subjected to thermal and mechanical loading. Journal of Thermal Stresses. 2017;40(9):1166-83.

[13] Bagheri H, Kiani Y, and Eslami M R. "Thermally induced large amplitude vibrations of FGM conical–cylindrical–conical shells." Journal of Vibration Engineering & Technologies. 2024: 12(3): 4655-4671.

[14] Barati MR, Shahverdi H. Aero-hygro-thermal stability analysis of higher-order refined supersonic FGM panels with even and uneven porosity distributions. Journal of Fluids and Structures. 2017;73:125-36.

[15] Barbosa JA, Ferreira AJ. Geometrically nonlinear analysis of functionally graded plates and shells. Mechanics of Advanced Materials and Structures. 2009;17(1):40-8.

[16] Bathe KJ. Finite Element Procedures in Engineering Analysis, New Delhi: Prentice Hall of India. 1990.

[17] Batra RC, Jin J. Natural frequencies of a functionally graded anisotropic rectangular plate. Journal of Sound and Vibration. 2005;282(1):509-16.

[18] Behjat B, Salehi M, Sadighi M, Armin A, Abbasi M. Static, dynamic, and free vibration analysis of functionally graded piezoelectric panels using finite element method. Journal of Intelligent Material Systems and Structures. 2009;20(13):1635-46.

[19] Beldjelili Y, Tounsi A, Mahmoud SR. Hygro-thermo-mechanical bending of S-FGM plates resting on variable elastic foundations using a four-variable trigonometric plate theory. Smart Structures and Systems. 2016;18(4):755-86.

[20] Beni YT, Mehralian F, Razavi H. Free vibration analysis of size-dependent shear deformable functionally graded cylindrical shell on the basis of modified couple stress theory. Composite Structures. 2015;120:65-78.

[21] Bharti I, Gupta N, Gupta KM. Novel applications of functionally graded nano, optoelectronic and thermoelectric materials. Int J Mater Mech Manuf 2013; 1:221–4.

[22] Bich DH, Nam VH, Phuong NT. Nonlinear postbuckling of eccentrically stiffened functionally graded plates and shallow shells. Vietnam Journal of Mechanics. 2011;33(3):131-47.

[23] Birman V, Byrd LW. Modeling and analysis of functionally graded materials and structures. Applied mechanics reviews. 2007;60(5):195-216.

[24] Bohidar SK, Sharma R, Mishra PR. Functionally graded materials: A critical review. Int J Res 2014; 1:289–301.

[25] Bouderba B, Houari MS, Tounsi A. Thermomechanical bending response of FGM thick plates resting on Winkler-Pasternak elastic foundations. Steel and Composite Structures. 2013;14(1):85-104.

[26] Cao D, Liu B, Yao M, Zhang W. Free vibration analysis of a pre-twisted sandwich blade with thermal barrier coatings layers. Science China Technological Sciences. 2017;60(11): 1747-1761.

[27] Chakraverty S, Pradhan KK. Free vibration of exponential functionally graded rectangular plates in thermal environment with general boundary conditions. Aerospace Science and Technology. 2014:36: 132–156.

[28] Che, Y, Ye T, Jin G, Li S, Yang, C. Vibration analysis of rotating pretwist FG sandwich blades operating in thermal environment. International Journal of Mechanical Sciences. 2021:205: 106596.

[29] Chen H, Wang A, Hao Y, Zhang W. Free vibration of FGM sandwich doubly-curved shallow shell based on a new shear deformation theory with stretching effects. Composite Structures. 2017;179:50-60.

[30] Chen M, Jin G, Ma X, Zhang Y, Ye T, Liu Z. Vibration analysis for sector cylindrical shells with bi-directional functionally graded materials and elastically restrained edges. Composites Part B: Engineering 2018:153: 346-363.

[31] Chen M, Ye T, Zhang J, Jin G, Zhang Y, Xue Y, Ma X, Liu Z. Isogeometric three-dimensional vibration of variable thickness parallelogram plates with in-plane functionally graded porous materials. Int. J. Mech. Sci. 2020:169.

[32] Chen Y, Jin G, Ye T, Lee HP. "Three-dimensional vibration analysis of rotating pre-twisted cylindrical isotropic and functionally graded shell panels." Journal of Sound and Vibration. 2022:517:116581.

[33] Cheung YK, Zhou D. Vibration of tapered Mindlin plates in terms of static Timoshenko beam functions. Journal of Sound and Vibration. 2003:260(4): 693-709.

[34] Cheung YK, Zhou D. Vibration of tapered Mindlin plates in terms of static Timoshenko beam functions, J. Sound Vib. 2003:260(4):693–709.

[35] Chi SH, Chung YL. Cracking in sigmoid functionally graded coating. Journal of Mechanisms. 2002:18: 41–53.

[36] Chung YL, Chi SH. The residual stress of functionally graded materials. Journal of the Chinese Institute of Civil and Hydraulic Engineering. 2001:13: 1–9.

[37] Cook RD, Malkus DS, Plesha ME. Concepts and Applications of Finite Element Analysis, John Wiley & Sons, New York. 1989.

[38] Dey T, Bandyopadhyay T. "Free vibration response of porous FGM plates using finite element analysis in thermal environment." Journal of Vibration Engineering & Technologies. 2024: 12(3): 4593-4615.

[39] Du C, Li Y, Jin X. Nonlinear forced vibration of functionally graded cylindrical thin shells. Thin-Walled Structures. 2014;78:26-36.

[40] Du C, Li Y. Nonlinear resonance behavior of functionally graded cylindrical shells in thermal environments. Composite Structures. 2013;102:164-74.

[41] Duc ND, Quan TQ. Nonlinear dynamic analysis of imperfect functionally graded material double curved thin shallow shells with temperature-dependent properties on elastic foundation. Journal of Vibration and Control. 2015;21(7):1340-62.

[42] Duc ND, Quan TQ. Nonlinear stability analysis of double-curved shallow FGM panels on elastic foundations in thermal environments. Mechanics of Composite Materials. 2012;48(4):435-48.

[43] Duc ND, Thang PT. Nonlinear buckling of imperfect eccentrically stiffened metal–ceramic–metal S-FGM thin circular cylindrical shells with temperature-dependent properties in thermal environments. International Journal of Mechanical Sciences. 2014:81: 17–25.

[44] Ebrahimi F, Ghasemi F, Salari E. Investigating thermal effects on vibration behavior of temperature-dependent compositionally graded Euler beams with porosities. Meccanica. 2016;51(1):223-49.

[45] Ebrahimi F, Mokhtari M. Transverse vibration analysis of rotating porous beam with functionally graded microstructure using the differential transform method. Journal of the Brazilian Society of Mechanical Sciences and Engineering. 2015;37(4):1435-44.

[46] Ebrahimi F, Zia M. Large amplitude nonlinear vibration analysis of functionally graded Timoshenko beams with porosities. Acta Astronautica. 2015;116:117-25.

[47] Ebrahimi MJ, Najafizadeh MM. Free vibration analysis of two-dimensional functionally graded cylindrical shells. Applied Mathematical Modelling. 2014;38(1):308-24.

[48] Ebrahimi MJ, Najafizadeh MM. Free vibration analysis of two-dimensional functionally graded cylindrical shells. Applied Mathematical Modelling. 2014:38(1): 308-324.

[49] Fang JS, Zhou D. Free vibration analysis of rotating Mindlin plates with variable thickness. International Journal of Structural Stability and Dynamics. 2017:17(04): 1750046.

[50] Fang JS, Zhou D. Free vibration analysis of rotating Mindlin plates with variable thickness. Int. J. Struct. Stab. Dyn. 2017:17 (04): 1750046.

[51] Farsani SR, Saadat Z, Jafari-Talookolaei RA, Tikani R, Ziaei-Rad S. Free vibrational analysis of variable thickness plate made of functionally graded porous materials using internal supports in contact with bounded fluid. Ocean Eng. 2022:263.

[52] Fazzolari FA. Modal characteristics of P-and S-FGM plates with temperature-dependent materials in thermal environment. Journal of Thermal Stresses. 2016:39(7): 854–873.

[53] Frikha A, Trabelsi S, Zghal S. A Four-Node Shell Element for Geometrically Nonlinear Analysis of Thin FGM Plates and Shells. International Conference Design and Modeling of Mechanical Systems 2017 pp. 209-215. Springer, Cham.

[54] Gupta A, Talha M. Recent development in modeling and analysis of functionally graded materials and structures. Progress in Aerospace Sciences. 2015;79:1-4.

[55] Han SC, Lee WH, Park WT. Non-linear analysis of laminated composite and sigmoid functionally graded anisotropic structures using a higher-order shear deformable natural Lagrangian shell element. Composite Structures. 89(1): 8–19.

[56] Han Y, Zhu X, Li T, Yu Y. Vibration analysis of submerged orthogonally stiffened FGM cylindrical shells. In INTER-NOISE and NOISE-CON Congress and Conference Proceedings 2017.(Vol. 255, No. 4, pp. 3355-3363). Institute of Noise Control Engineering.

[57] Hashemi, S, Jafari AA. Nonlinear free and forced vibrations of in-plane bi-directional functionally graded rectangular plate with temperature-dependent properties. International Journal of Structural Stability and Dynamics. 2020:20(08): 2050097.

[58] Heydarpour Y, Aghdam MM, Malekzadeh P. Free vibration analysis of rotating functionally graded carbon nanotube-reinforced composite truncated conical shells. Composite structures. 2014;117:187-200.

[59] Heydarpour Y, Malekzadeh P, Haghighi MG, Vaghefi M. Thermoelastic analysis of rotating laminated functionally graded cylindrical shells using layerwise differential quadrature method. Acta Mechanica. 2012;223(1):81-93.

[60] Hong CC. "Advanced dynamic thermal vibration of thick FGM plates-cylindrical shells." Ocean Engineering. 2022: 266: 112701.

[61] Hosseini Kordkheili SA, Naghdabadi R. Geometrically nonlinear thermoelastic analysis of functionally graded shells using finite element method. International journal for numerical methods in Engineering. 2007;72(8):964-86.

[62] Hu Y, Zhou Q, Yang T. "Magneto-thermo-elastic coupled free vibration and nonlinear frequency analytical solutions of FGM cylindrical shell." Thin-Walled Structures. 2024:195:111406.

[63] Huang XL, Shen HS. Nonlinear vibration and dynamic response of functionally graded plates in thermal environments. International Journal of Solids and Structures. 2004:41(9–10): 2403–2427.

[64] Isvandzibaei MR, Jamaluddin H, Raja Hamzah RI. Vibration analysis of supported thick-walled cylindrical shell made of functionally graded material under pressure loading. Journal of Vibration and Control. 2016;22(4):1023-36.

[65] Jha DK, Kant T, Singh RK. A critical review of recent research on functionally graded plates. Composite Structures. 2013;96:833-49.

[66] Jiammeepreecha W, Chaidachatorn K, Phungpaingam B, Klaycham K, Chucheepsakul S. "Free vibration analysis of FGM spherical and elliptical shells under nonlinear thermal environments." Thin-Walled Structures. 2024: 196: 111497.

[67] Jin ZH, Batra RC. Stress intensity relaxation at the tip of an edge crack in a functionally graded material subjected to a thermal shock. Journal of Thermal Stresses. 1996:19(4): 317–339.

[68] Jones RM. Mechanics of Composite Materials, McGraw Hill Kogakusha Limited. 1975.

[69] Kant T, Khare RK. A higher-order facet quadrilateral composite shell element. International Journal for Numerical Methods in Engineering. 1997;40(24):4477-99.

[70] Kapuria S, Patni M, Yasin MY. A quadrilateral shallow shell element based on the third-order theory for functionally graded plates and shells and the inaccuracy of rule of mixtures. Eur J Mech A Solids 2015;49:268–82.

[71] Kar VR, Mahapatra TR, Panda SK. Effect of different temperature load on thermal postbuckling behaviour of functionally graded shallow curved shell panels. Composite Structures. 2017;160:1236-47.

[72] Katiyar V, Gupta A. Vibration response of a geometrically discontinuous bi-directional functionally graded plate resting on elastic foundations in thermal environment with initial imperfections. Mechanics Based Design of Structures and Machines. 2023:51(6): 3480-3508.

[73] Khor KA, Gu YW. Effects of residual stress on the performance of plasma sprayed functionally graded ZrO2/NiCoCrAlY coatings. Materials Science and Engineering: A. 2000;277(1-2):64-76.

[74] Kiani Y, Shakeri M, Eslami MR. Thermoelastic free vibration and dynamic behaviour of an FGM doubly curved panel via the analytical hybrid Laplace–Fourier transformation. Acta Mechanica. 2012;223(6):1199-218.

[75] Kohli GS, Singh T. Review of functionally graded materials. J Prod Eng 2015; 18:1–4.

[76] Kumar PR, Rao KM, Rao NM. Effect of taper on free vibration of functionally graded rotating beam by Mori-Tanaka method. Journal of The Institution of Engineers (India): Series C. 2019:100: 729-736.

[77] Kumar R, Gupta KK, Singh J, Singh, J. Radial basis collocation method for free vibration analysis of elastically supported porous bi-directional FGM plate under various types of porosity distribution. Advances in Materials and Processing Technologies. 2023:9(2):368-390.

[78] Kumar S, Jana P. Application of dynamic stiffness method for accurate free vibration analysis of sigmoid and exponential functionally graded rectangular plates. International Journal of Mechanical Sciences. 2019:163: 105105.

[79] Kumar V, Singh SJ, Saran VH, Harsha SP. Vibration characteristics of porous FGM plate with variable thickness resting on Pasternak's foundation. Eur. J. Mech.-A/Solids. 2021:85.

[80] Kumar V, Singh SJ, Saran VH. Vibration characteristics of porous FGM plate with variable thickness resting on Pasternak's foundation. European Journal of Mechanics. - A: Solids 2021:85: 104124.

[81] Lakhdar Z, Chorfi SM, Belalia SA, Khedher KM, Alluqmani AE, Tounsi A, Yaylacı M. "Free vibration and bending analysis of porous bi-directional FGM sandwich shell using a TSDT p-version finite element method." Acta Mechanica. 2024: 235(6): 3657-3686.

[82] Lal R, Saini R. Vibration analysis of FGM circular plates under non-linear temperature variation using generalized differential quadrature rule. Applied Acoustics. 2020:158: 107027.

[83] Lam KY, Hua L. Influence of boundary conditions on the frequency characteristics of a rotating truncated circular conical shell. Journal of Sound and Vibration. 1999;223(2):171-95.

[84] Lee CY, Kim JH. Degradation of thermal postbuckling behaviors of functionally graded material in aero-hygrothermal environments. Composite Structures. 2014;118:228-33.

[85] Lee CY, Kim JH. Hygrothermal postbuckling behavior of functionally graded plates. Composite Structures. 2013;95:278-82.

[86] Lee WH, Han SC, Park W T. A refined higher order shear and normal deformation theory for E-, P-, and S-FGM plates on Pasternak elastic foundation. Composite Structures. 2015:122: 330–342.

[87] Leissa A.W., Vibration of shells, NASA SP388, The Government Printing Office, Washington DC, 1973.

[88] Levy M. Mémoire sur la théorie des plaques élastiques planes. Journal de mathématiques pures et appliquées. 1877:219-306.

[89] Li F, Chen Y, Lv M. Vibro-acoustic characteristics of sigmoid functionally graded sandwich plates with temperature-dependent materials. Thin-Walled Structures. 2021:159: 107310.

[90] Li HC, Ke LL, Yang J, Kitipornchai S, Wang YS. Free vibration of variable thickness FGM beam submerged in fluid. Composite Structures. 2020:233: 111582.

[91] Li Y, Yang C, Zhao H, Qu S, Li X, Li Y. New developments of Ti-based alloys for biomedical applications. Materials (Basel) 2014; 7:1709–800.

[92] Liew KM, Lei ZX, Zhang LW. Mechanical analysis of functionally graded carbon nanotube reinforced composites: a review. Composite Structures. 2015;120:90-7.

[93] Liew KM, Lim CW, Ong LS. Vibration of pretwisted cantilever shallow conical shells. Int. J. Solids Struct. 1994:31 (18): 2463–2476.

[94] Liew KM, Ng TY, Zhao X. Free vibration analysis of conical shells via the element-free kp-Ritz method. Journal of Sound and Vibration. 2005;281(3):627-45.

[95] Liew KM, Zhao X, Ferreira AJ. A review of meshless methods for laminated and functionally graded plates and shells. Composite Structures. 2011;93(8):2031-41.

[96] Liu CS, Fang JC, Chen QC. Fabrication and Performance Evaluation of Functionally Graded Materials. Materials for Mechanical Engineering. 2006;10:001.

[97] Liu M, Liu J, Cheng Y. Free vibration of a fluid loaded ring-stiffened conical shell with variable thickness. Journal of Vibration and Acoustics. 2014:136(5).

[98] Loy CT, Lam KY, Reddy JN. Vibration of functionally graded cylindrical shells. International Journal of Mechanical Sciences. 1999;41(3):309-24.

[99] Malekzadeh P, Heydarpour Y. Free vibration analysis of rotating functionally graded truncated conical shells. Composite structures. 2013;97:176-88.

[100] Malekzadeh P, Heydarpour Y. Free vibration analysis of rotating functionally graded cylindrical shells in thermal environment. Composite Structures. 2012;94(9):2971-81.

[101] Malekzadeh P, Shojaee SA. Dynamic response of functionally graded plates under moving heat source. Composites Part B: Engineering. 2013;44(1):295-303.

[102] Mantari JL, Oktem AS, Soares CG. Bending and free vibration analysis of isotropic and multilayered plates and shells by using a new accurate higher-order shear deformation theory. Composites Part B: Engineering. 2012;43(8):3348-60.

[103] Mantari JL, Oktem AS, Soares CG. Bending response of functionally graded plates by using a new higher order shear deformation theory. Composite Structures. 2012a;94(2):714-23.

[104] Marzavan S, Nastasescu V. "Free vibration analysis of a functionally graded plate by finite element method." Ain Shams Engineering Journal. 2023: 14(8):102024.

[105] Matsunaga H. Free vibration and stability of functionally graded shallow shells according to a 2D higher-order deformation theory. Composite structures. 2008;84(2):132-46.

[106] Matsunaga H. Free vibration and stability of functionally graded circular cylindrical shells according to a 2D higher-order deformation theory. Composite Structures. 2009;88(4):519-31.

[107] Mechab I, Mechab B, Benaissa S, Serier B, Bouiadjra BB. Free vibration analysis of FGM nanoplate with porosities resting on Winkler Pasternak elastic foundations based on two-variable refined plate theories. Journal of the Brazilian Society of Mechanical Sciences and Engineering. 2016;38(8):2193-211.

[108] Meirovitch L. Principles and techniques of vibrations. New Jersey: Prentice Hall; 1997.

[109] Miao XY, Li CF, Jiang YL, Zhang ZX. Free vibration analysis of three-layer thin cylindrical shell with variable thickness two-dimensional FGM middle layer under arbitrary boundary conditions. Journal of Sandwich Structures & Materials. 2022:24(2): 973-1003.

[110] Mohammadi R, Hosseini M. "Modeling and free vibration analysis of a rotating functionally graded thin-walled hub-blade system under aerothermoelastic loading." Aerospace Science and Technology. 2024:146: 108935.

[111] Mohammadimehr M, Rostami R. Bending and vibration analyses of a rotating sandwich cylindrical shell considering nanocomposite core and piezoelectric layers subjected to thermal and magnetic fields. Applied Mathematics and Mechanics. 2018:1-22.

[112] Monge JC, Mantari JL. 3D elasticity numerical solution for the static behavior of FGM shells. Engineering Structures. 2020:208: 110159.

[113] Naeem MN, Arshad SH, Sharma CB. The Ritz formulation applied to the study of the vibration frequency characteristics of functionally graded circular cylindrical shells. Proceedings of the Institution of Mechanical Engineers, Part C: Journal of Mechanical Engineering Science. 2010;224(1):43-54.

[114] Naghdabadi R, Kordkheili SH. A finite element formulation for analysis of functionally graded plates and shells. Archive of applied mechanics. 2005;74(5-6):375-86.

[115] Naj R, Boroujerdy MS, Eslami MR. Thermal and mechanical instability of functionally graded truncated conical shells. Thin-Walled Structures. 2008;46(1):65-78.

[116] Najafizadeh MM, Isvandzibaei MR. Vibration of functionally graded cylindrical shells based on higher order shear deformation plate theory with ring support. Acta Mechanica. 2007;191(1-2):75-91.

[117] Ng TY, Lam KY, Liew KM, Reddy JN. Dynamic stability analysis of functionally graded cylindrical shells under periodic axial loading. International Journal of Solids and Structures. 2001;38(8):1295-309.

[118] Nguyen DD, Tran QQ. Nonlinear postbuckling of imperfect eccentrically stiffened P-FGM double curved thin shallow shells on elastic foundations in thermal environments. Compos Struct 2013;106:590–600.

[119] Nguyen Dinh D, Nguyen PD. The dynamic response and vibration of functionally graded carbon nanotube-reinforced composite (FG-CNTRC) truncated conical shells resting on elastic foundations. Materials. 2017;10(10):1194.

[120] Nguyen NV, Phan DH. "Nonlinear free vibration of bi-directional functionally graded porous plates." Thin-Walled Structures. 2023: 192: 111198.

[121] Parida S, Mohanty SC. Free vibration analysis of rotating functionally graded material plate under nonlinear thermal environment using higher order shear deformation theory. Proceedings of the Institution of Mechanical Engineers - Part C: Journal of Mechanical Engineering Science. 2019:233(6): 2056–2073.

[122] Patel BP, Gupta SS, Loknath MS, Kadu CP. Free vibration analysis of functionally graded elliptical cylindrical shells using higher-order theory. Composite structures. 2005;69(3):259-70.

[123] Pompe W, Worch H, Epple M, Friess W, Gelinsky M, Greil P, Hempel U, Scharnweber D, Schulte K. Functionally graded materials for biomedical applications. Materials Science and Engineering: A. 2003;362(1-2):40-60.

[124] Pradhan SC, Loy CT, Lam KY, Reddy JN. Vibration characteristics of functionally graded cylindrical shells under various boundary conditions. Applied Acoustics. 2000;61(1):111-29.

[125] Pradyumna S, Bandyopadhyay JN. Free vibration analysis of functionally graded curved panels using a higher-order finite element formulation. Journal of Sound and Vibration. 2008;318(1):176-92.

[126] Pradyumna S, Nanda N. Geometrically nonlinear transient response of functionally graded shell panels with initial geometric imperfection. Mechanics of Advanced Materials and Structures. 2013;20(3):217-26.

[127] Rahmani F, Kamgar R, Rahgozar R. Optimum material distribution of porous functionally graded plates using Carrera unified formulation based on isogeometric analysis. Mechanics of Advanced Materials and Structures. 2022:29(20): 2927–2941.

[128] Rao JS. Turbomachine blade vibration. New Age International; 1991.

[129] Reddy JN, Chin CD. Thermomechanical analysis of functionally graded cylinders and plates. Journal of thermal Stresses. 1998;21(6):593-626.

[130] Reddy JN, Chin CD. Thermomechanical analysis of functionally graded cylinders and plates. Journal of Thermal Stresses 1998:21(6): 593–626.

[131] Reddy JN. Mechanics of laminated composite plates and shells: theory and analysis. CRC Press; 2004.

[132] Reddy KSZ, Kant T. Three-dimensional elasticity solution for free vibrations of exponentially graded plates. Journal of Engineering Mechanics. 2014:140(7): 04014047.

[133] Rezaei AS, Saidi AR, Abrishamdari M. Natural frequencies of functionally graded plates with porosities via a simple four variable plate theory: an analytical approach. Thin-Walled Structures. 2017:120: 366–377.

[134] Rezaiee-Pajand M, Masoodi AR. Hygro-thermo-elastic nonlinear analysis of functionally graded porous composite thin and moderately thick shallow panels. Mechanics of Advanced Materials and Structures. 2022:29(4): 594–612.

[135] Rotter JM. Shell structures: the new European standard and current research needs. Thin-walled structures. 1998;31(1-3):3-23.

[136] Rout M, Hota SS, Karmakar A. Free vibration characteristics of delaminated composite pretwisted stiffened cylindrical shell. Proceedings of the Institution of Mechanical Engineers, Part C: Journal of Mechanical Engineering Science. 2018:232(4): 595-611.

[137] Sah SK, Ghosh A. Influence of porosity distribution on free vibration and buckling analysis of multi-directional functionally graded sandwich plates. Composite Structures. 2022:279: 114795.

[138] Santos H, Soares CM, Soares CA, Reddy JN. A semi-analytical finite element model for the analysis of cylindrical shells made of functionally graded materials. Composite Structures. 2009;91(4):427-32.

[139] Seifried S, Winterer M, Hahn H. Nanocrystalline gradient films through chemical vapor synthesis. Scripta materialia. 2001;44(8-9):2165-8.

[140] Sekkal M, Fahsi B, Tounsi A, Mahmoud SR. A new quasi-3D HSDT for buckling and vibration of FG plate. Structural Engineering and Mechanics, An Int'l Journal. 2017:64(6): 737-749.

[141] Sekkal M, Fahsi B, Tounsi A, Mahmoud SR. A new quasi-3D HSDT for buckling and vibration of FG plate. Structural Engineering and Mechanics, An Int'l Journal. 2017:64(6):737-749.

[142] Shahsiah R, Eslami MR. Functionally graded cylindrical shell thermal instability based on improved Donnell equations. AIAA journal. 2003;41(9):1819-26..

[143] Shahsiah R, Eslami MR. Thermal buckling of functionally graded cylindrical shell. Journal of Thermal Stresses. 2003a;26(3):277-94.

[144] Shariyat M. Vibration and dynamic buckling control of imperfect hybrid FGM plates with temperature-dependent material properties subjected to thermo-electro-mechanical loading conditions. Composite Structures. 2009;88(2):240-52.

[145] Shen HS. Functionally graded materials: nonlinear analysis of plates and shells. CRC press; 2016.

[146] Sheng GG, Wang X. Non-linear response of functionally graded cylindrical shells under mechanical and thermal loads. Journal of Thermal Stresses. 2011;34(11):1105-18.

[147] Sheng GG, Wang X. The non-linear vibrations of rotating functionally graded cylindrical shells. Nonlinear Dynamics. 2017;87(2):1095-109.

[148] Şimşek M. Bi-directional functionally graded materials (BDFGMs) for free and forced vibration of Timoshenko beams with various boundary conditions. Composite Structures. 2015:133: 968-978.

[149] Sivadas KR, Ganesan N. Free vibration of cantilever conical shells with variable thickness. Computers & structures. 1990:36(3): 559-566.

[150] Sobhy M. An accurate shear deformation theory for vibration and buckling of FGM sandwich plates in hygrothermal environment. International Journal of Mechanical Sciences. 2016;110:62-77.

[151] Sofiyev AH, Kuruoglu N. Domains of dynamic instability of FGM conical shells under time dependent periodic loads. Composite Structures. 2016;136:139-48.

[152] Sofiyev AH. On the vibration and stability of shear deformable FGM truncated conical shells subjected to an axial load. Composites Part B: Engineering. 2015;80:53-62.

[153] Sofiyev AH. Parametric vibration of FGM conical shells under periodic lateral pressure within the shear deformation theory. Composites Part B: Engineering. 2016;89:282-94.

[154] Sofiyev AH. The vibration and stability behavior of freely supported FGM conical shells subjected to external pressure. Composite Structures. 2009;89(3):356-66.

[155] Song C, Xu Z, Li J. Structure of in situ Al/Si functionally graded materials by electromagnetic separation method. Materials & design. 2007;28(3):1012-5.

[156] Sreenivasamurthy S, Ramamurti V. Coriolis effect on the vibration of flat rotating low aspect ratio cantilever plates. The Journal of Strain Analysis for Engineering Design. 1981:16(2): 97-106.

[157] Stein M. Nonlinear theory for plates and shells including the effects of transverse shearing. AIAA journal. 1986;24(9):1537-44.

[158] Su Z, Jin G, Shi S, Ye T, Jia X. A unified solution for vibration analysis of functionally graded cylindrical, conical shells and annular plates with general boundary conditions. International Journal of Mechanical Sciences. 2014;80:62-80.

[159] Sundararajan N, Prakash T, Ganapathi M. Nonlinear free flexural vibrations of functionally graded rectangular and skew plates under thermal environments. Finite Elements in Analysis and Design. 2005;42(2):152-68.

[160] Swaminathan K, Naveenkumar DT, Zenkour AM, Carrera E. Stress, vibration and buckling analyses of FGM plates—a state-of-the-art review. Composite Structures. 2015;120:10-31.

[161] Swaminathan K, Sangeetha DM. Thermal analysis of FGM plates–A critical review of various modeling techniques and solution methods. Composite Structures. 2017;160:43-60.

[162] Talebitooti M. Thermal effect on free vibration of ringstiffened rotating functionally graded conical shell with clamped ends. Mechanics of Advanced Materials and Structures. 2018:25(2): 155–165.

[163] Talebitooti M. Thermal effect on free vibration of ring-stiffened rotating functionally graded conical shell with clamped ends. Mechanics of Advanced Materials and Structures. 2018;25(2):155-65.

[164] Talha M, Singh BN. Large amplitude free flexural vibration analysis of shear deformable FGM plates using nonlinear finite element method. Finite Elements in Analysis and Design. 2011;47(4):394-401.

[165] Talha M, Singh BN. Static response and free vibration analysis of FGM plates using higher order shear deformation theory. Applied Mathematical Modelling. 2010;34(12):3991-4011.

[166] Thai HT, Kim SE. A review of theories for the modeling and analysis of functionally graded plates and shells. Composite Structures. 2015;128:70-86.

[167] Thi HN. Thermal vibration analysis of functionally graded porous plates with variable thickness resting on elastic foundations using finite element method. Mech. Based Des. Struct. Mach. 2022:1–29.

[168] Tornabene F, Fantuzzi N, Bacciocchi M. Free vibrations of free-form doubly-curved shells made of functionally graded materials using higher-order equivalent single layer theories. Composites Part B: Engineering. 2014;67:490-509.

[169] Tornabene F. Free vibration analysis of functionally graded conical, cylindrical shell and annular plate structures with a four-parameter power-law distribution. Computer Methods in Applied Mechanics and Engineering. 2009;198(37):2911-35.

[170] Touratier M. An efficient standard plate theory. International journal of engineering science. 1991;29(8):901-16.

[171] Tran TT, Pham QH, Nguyen-Thoi T. Static and free vibration analyses of functionally graded porous variable-thickness plates using an edge-based smoothed finite element method. Defence Technol. 2021:17 (3), 971–986.

[172] Van Do T, Nguyen D K, Duc ND, Doan DH, Bui TQ. Analysis of bi-directional functionally graded plates by FEM and a new third-order shear deformation plate theory. Thin-Walled Structures. 2017:119: 687-699.

[173] Van Do VN, Ong TH, Lee CH. Isogeometric analysis for nonlinear buckling of FGM plates under various types of thermal gradients. Thin-Walled Structures. 2019:137: 448–462.

[174] Van Thinh N, Van Tung H. "Free vibration and dynamical analyses of FGM plates with porosity and tangential edge constraints." Journal of Vibration Engineering & Technologies. 2024: 12(3): 5291-5305.

[175] Van Tung H, Van Thinh N. "Nonlinear free vibration of geometrically imperfect porous FGM shell panels on nonlinear foundations including elastic edge restraints and elevated temperatures." Acta Mechanica. 2025: 1-25.

[176] Van Tung H. Nonlinear axisymmetric response of FGM shallow spherical shells with tangential edge constraints and resting on elastic foundations. Composite Structures. 2016:149:231-8.

[177] Wang YQ, Zu JW. Vibration behaviors of functionally graded rectangular plates with porosities and moving in thermal environment. Aerospace Science and Technology. 2017:69:550-62.

[178] Wang YQ, Zu JW. Vibration characteristics of moving sigmoid functionally graded plates containing porosities. International Journal of Mechanics and Materials in Design. 2018:14: 473–489.

[179] Watanabe Y, Eryu H, Matsuura K. Evaluation of three-dimensional orientation of Al3Ti platelet in Al-based functionally graded materials fabricated by a centrifugal casting technique. Acta Materialia. 2001:49(5):775-83.

[180] Watanabe Y, Yamanaka N, Fukui Y. Control of composition gradient in a metal-ceramic functionally graded material manufactured by the centrifugal method. Composites Part A: Applied Science and Manufacturing. 1998:29(5-6):595-601.

[181] Watari F, Yokoyama A, Saso F, Uo M, Kawasaki T. Fabrication and properties of functionally graded dental implant. Compos Part B Eng 1997; 28:5–11.

[182] Wattanasakulpong N, Prusty BG, Kelly DW, Hoffman M. Free vibration analysis of layered functionally graded beams with experimental validation. Materials & Design (1980-2015). 2012:36:182-90.

[183] Wattanasakulpong N, Ungbhakorn V. Linear and nonlinear vibration analysis of elastically restrained ends FGM beams with porosities. Aerospace Science and Technology. 2014:32(1):111-20.

[184] Wu H, Yang J, Kitipornchai S. Mechanical analysis of functionally graded porous structures: a review. International Journal of Structural Stability and Dynamics. 2020:20(13): 2041015.

[185] Xiang S, Chen YT, Kang GW. Local collocation method for prediction of natural frequency of functionally graded cylindrical shells. Mechanics of Advanced Materials and Structures. 2015 2:22(12):969-77.

[186] Xiang T, Natarajan S, Man H, Song C, Gao W. Free vibration and mechanical buckling of plates with in-plane material inhomogeneity–A three dimensional consistent approach. Composite Structures. 2014:118: 634-642.

[187] Xiang T, Natarajan S, Man H, Song C, Gao W. Free vibration and mechanical buckling of plates with in-plane material inhomogeneity–A three dimensional consistent approach. Composite Structures. 2014:118:634-642.

[188] Xu H, Wang YQ. "Nonlinear free vibration of spinning pre-twisted functionally graded material plates in thermal environment." International Journal of Structural Stability and Dynamics. 2024:24(11):2450131.

[189] Yahia SA, Atmane HA, Houari MS, Tounsi A. Wave propagation in functionally graded plates with porosities using various higher-order shear deformation plate theories. Structural Engineering and Mechanics. 2015:53(6):1143-65.

[190] Yang J, Liew KM, Wu YF, Kitipornchai S. Thermo-mechanical post-buckling of FGM cylindrical panels with temperature-dependent properties. International Journal of Solids and Structures. 2006:43(2):307-24.

[191] Yang J, Shen HS. Free vibration and parametric resonance of shear deformable functionally graded cylindrical panels. Journal of Sound and Vibration. 2003:261(5): 871–893.

[192] Yin LL, Lo KH, Wang SS. Structural dynamics and load analysis of large offshore wind turbines in western gulf of Mexico shallow water. In International Conference on Offshore Mechanics and Arctic Engineering 2014. (Vol. 45547, p. V09BT09A036). American Society of Mechanical Engineers.

[193] Zang Q, Liu J, Ye W, Yang F, Hao C, Lin G. "Static and free vibration analyses of functionally graded plates based on an isogeometric scaled boundary finite element method." Composite Structures. 2022:288: 115398.

[194] Zare Jouneghani F, Dimitri R, Bacciocchi M, Tornabene F. Free Vibration Analysis of Functionally Graded Porous Doubly-Curved Shells Based on the First-Order Shear Deformation Theory. Applied Sciences. 2017:7(12):1252.

[195] Zare Jouneghani F, Dimitri R, Bacciocchi M. Free vibration analysis of functionally graded porous doubly-curved shells based on the first-order shear deformation theory. Applied Sciences. 2017:7(12): 1252.

[196] Zenkour AM, Sobhy M. Thermal buckling of functionally graded plates resting on elastic foundations using the trigonometric theory. Journal of Thermal Stresses. 2011:34(11):1119-38.

[197] Zenkour AM. Exact relationships between classical and sinusoidal theories for FGM plates. Mechanics of Advanced Materials and Structures. 2012:19(7):551-67.

[198] Zenkour AM. Generalized shear deformation theory for bending analysis of functionally graded plates. Applied Mathematical Modelling. 2006:30(1):67-84.

[199] Zenkour AM. Hygro-thermo-mechanical effects on FGM plates resting on elastic foundations. Composite Structures. 2010:93(1):234-8.

[200] Zenkour AM. On vibration of functionally graded plates according to a refined trigonometric plate theory. International Journal of Structural Stability and Dynamics. 2005:5(02):279-97.

[201] Zghal S, Frikha A, Dammak F. Free vibration analysis of carbon nanotube-reinforced functionally graded composite shell structures. Applied Mathematical Modelling. 2018: 53:132-55.

[202] Zhang DG, Zhou YH. A theoretical analysis of FGM thin plates based on physical neutral surface. Computational Materials Science. 2008: 44(2):716-20.

[203] Zhang YF, Niu Y, Zhang W. Nonlinear vibrations and internal resonance of pretwisted rotating cantilever rectangular plate with varying cross-section and aerodynamic force. Engineering Structures. 2020:225: 111259.

[204] Zhao X, Lee YY, Liew KM. Free vibration analysis of functionally graded plates using the element-free kp-Ritz method. Journal of Sound and Vibration. 2009:319(3-5): 918–939.

[205] Zhao X, Liew KM. Free vibration analysis of functionally graded conical shell panels by a meshless method. Composite Structures. 2011a: 93(2):649-64.

[206] Zhou L. A novel similitude method for predicting natural frequency of FG porous plates under thermal environment. Mechanics of Advanced Materials and Structures. 2022:29(27): 6786–6802.

[207] Zhu J, Lai Z, Yin Z, Jeon J, Lee S. Fabrication of ZrO_2–NiCr functionally graded material by powder metallurgy. Materials chemistry and physics. 2001: 68(1-3):130-5.

Appendix:

The flowchart outlines the steps followed in the present finite element formulation

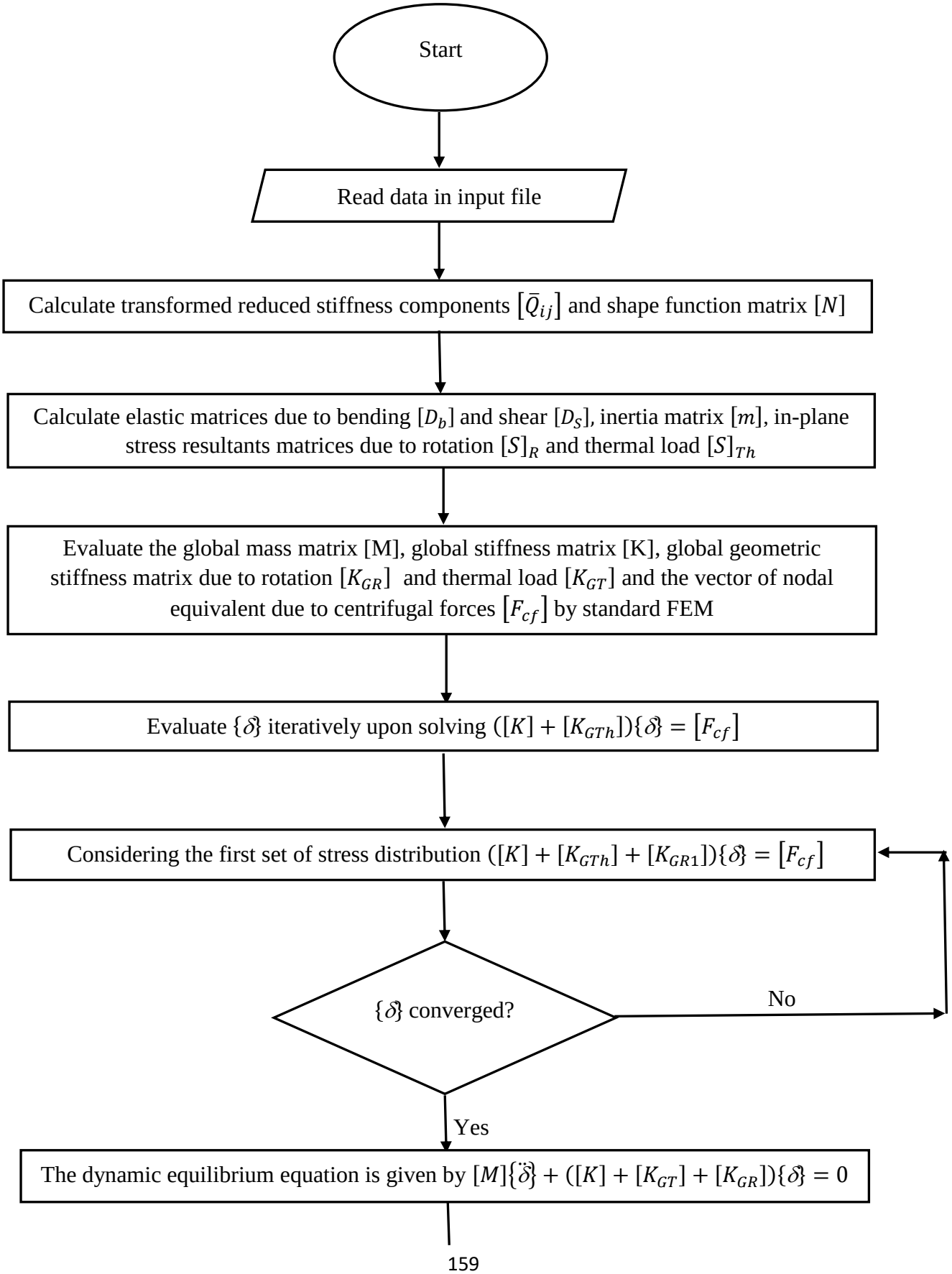

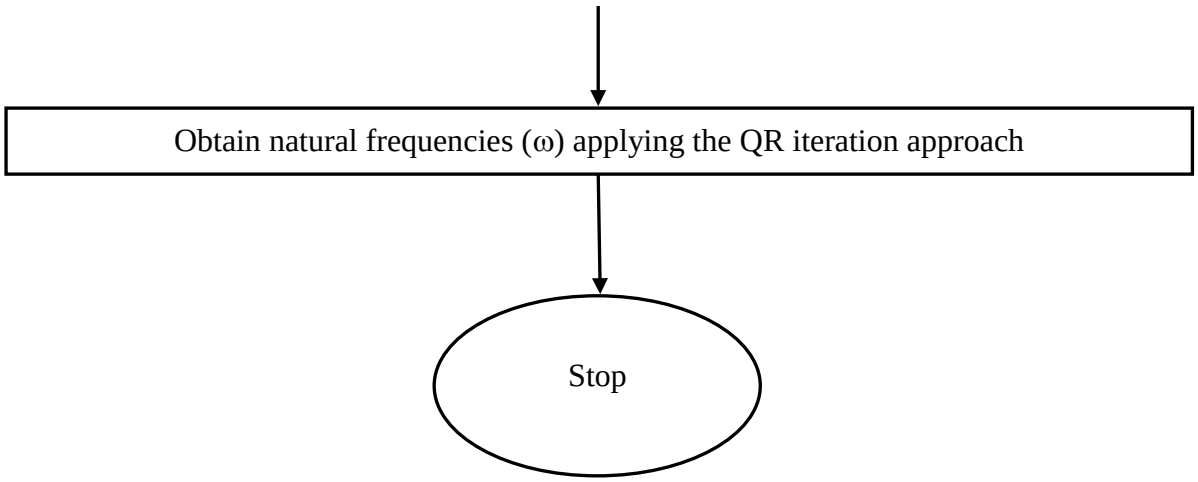
Obtain natural frequencies (ω) applying the QR iteration approach
Stop